Technische Universität München
Chair for Computer-Aided Medical Procedures & Augmented Reality

Challenges in Multimodality Imaging using Positron Emission Tomography

Axel Martínez Möller

Vollständiger Abdruck der von der Fakultät für Informatik der Technischen Universität München zur Erlangung des akademischen Grades eines

Doktors der Naturwissenschaften (Dr. rer. nat.)

genehmigten Dissertation.

Vorsitzender: Univ.-Prof. Dr. M. H. Gerndt

Prüfer der Dissertation:

1. Univ.-Prof. Nassir Navab, Ph.D.
2. Univ.-Prof. Dr. M. Schwaiger
3. Univ.-Prof. Dr. B. Pichler,
   Eberhard-Karls-Universität Tübingen

Die Dissertation wurde am 29. Juni 2009 bei der Technischen Universität München eingereicht und durch die Fakultät für Informatik am 3. Dezember 2009 angenommen.

Abstract

The combination of Positron Emission Tomography (PET) and Computed Tomography (CT) has resulted in improved diagnostic accuracy and enhanced clinical workflows, demonstrating the potential of multimodality imaging and raising the interest for the combination of PET with Magnetic Resonance Imaging (MRI). This thesis focus on the problems of patient motion and photon attenuation, relevant to PET imaging and its combination with CT and MRI. Three specific applications are addressed.

Respiratory motion results in image blurring and does not allow full exploitation of the spatial resolution offered by state-of-the-art PET scanners (below 5 mm). In order to implement respiratory gating, different respiratory sensors were compared for assessing the optimum way to determine the respiratory phase at each point in time. Furthermore, the feasibility of simultaneous cardiac-respiratory gating was shown, providing images of the heart with virtually no motion.

Patient motion does not only affect the acquired PET data, but also jeopardizes the diagnostic accuracy of PET/CT scanners, in which perfect spatial co-registration between both modalities is assumed. In the course of this work, a relevant issue for cardiac imaging was found concerning the CT-based photon attenuation correction, which was biased when misregistration between PET and CT data occurred. Analysis of clinical examinations demonstrated severe artifacts taking place in nearly 30% of the cases and resulting in false positive defects, indicating that realignment of the images was necessary. As an alternative to manual registration, an automatic emission-driven correction was proposed which was able to eliminate the artifacts.

Finally, attenuation correction poses additional problems for combined MRI/PET imaging, which require the development of novel techniques to generate an attenuation map from the MRI data. A method based on the segmentation of MRI images in four different attenuation classes (air, lung, fat and soft tissue) was developed. Application of the segmented attenuation map to PET/CT oncological data was found to result only in a slight decrease of the observed uptake, particularly for osseous lesions (avg. 8%), and this change did not result in any differences in the clinical interpretation. Furthermore, it was shown with PET/CT and MRI data of the same subjects that such tissue segmentation could be robustly obtained from one single MRI acquisition.

Multimodality imaging has profoundly changed the practice of clinical PET despite being less than one decade old. This thesis is a step forward by investigating three relevant issues and proposing solutions which are being adopted by major PET manufacturers and contribute to provide improved diagnosis.

Keywords:
Positron Emission Tomography, Medical Imaging, Attenuation Correction, Motion Correction

Zusammenfassung

Die Kombination aus Positronen-Emissions-Tomographie (PET) und Computertomographie (CT) hat zu einer höheren Genauigkeit bei der Diagnose und zudem zu verbesserten klinischen Arbeitsabläufen geführt. Des Weiteren zeigten hybride PET/CT-Geräte das Potenzial der multimodalen Bildgebung auf und weckten das Interesse für die Kombination von PET mit Magnetresonanztomographie (MRT). Diese Dissertation behandelt die entstehenden Probleme bei der Patientenbewegung und der Photonenschwächung, welche für die PET- sowie für die kombinierte PET/CT- und PET/MRT-Bildgebung relevant sind. Hierbei werden drei verschiedene Anwendungen betrachtet.

Die Atembewegung führt zu einer Bildverwischung und verhindert die optimale Nutzung der Ortsauflösung, die jetzige PET-Tomographen liefern (unter 5 mm). Zur Implementierung einer Atemtriggerung wurden verschiedene Atemsensoren verglichen, um eine optimale Methode zur Bestimmung der Atemphase in jedem Zeitpunkt zu finden. Darüber hinaus wurde die Durchführbarkeit der simultanen Herz-Atem-Triggerung bewiesen, bei der das Herz mit nahezu keiner Bewegung aufgenommen werden kann.

Die Patientenbewegung hat nicht nur einen Einfluss auf die aufgenommenen PET-Daten, sondern beeinträchtigt auch die Genauigkeit der PET/CT Bildgebung, bei der eine perfekte Ortsregistrierung vorausgesetzt wird. Im Laufe dieser Doktorarbeit wurde ein wichtiges Problem in der Herzbildgebung identifiziert, welches die CT-basierte Korrektur der Photon-Abschwächung betrifft. Diese Korrektur wurde ungenau, sobald eine falsche Registrierung zwischen PET und CT Daten stattfand. Bei nahezu 30% der Aufnahmen trat hierdurch ein Artefakt auf, welches zu falsch positiven Defekten führte und eine erneute Abgleichung der PET und CT Bilder nötig machte. Als Alternative zur manuellen Bildregistrierung wurde hierzu eine automatische emissionsbasierte Korrekturmethode entwickelt, welche die auftretenden Artefakte unterdrücken konnte.

Die Schwächungskorrektur führt darüber hinaus zu weiteren Problemen bei kombinierten MRT/PET Tomographen. Hier ist die Entwicklung neuer Techniken zur Erzeugung von MRT-basierten Schwächungskarten nötig. Eine Methode, welche die MRT Bilder in vier verschiedene Schwächungsklassen (Luft, Lungen, Fett und Weichgewebe) segmentiert, wurde entwickelt. Die Anwendung solch einer segmentierten Schwächungskarte auf onkologische PET/CT Daten führte zu einer leichten Verminderung der beobachteten Traceraufnahme, insbesondere bei Knochenmetastasen (Durchschnittswert 8%). Dies führte allerdings zu keinem Unterschied in der klinischen Interpretation. Des Weiteren wurde mittels PET/CT- und MRT-Daten gleicher Patienten bewiesen, dass die vorgeschlagene Gewebesegmentierung zuverlässig aus einer einzigen MR-Aufnahme bestimmt werden kann.

Die Multimodale Bildgebung hat die klinische PET Praxis tiefgreifend verändert, obwohl sie erst seit weniger als einem Jahrzehnt zur Verfügung steht. Im Rahmen dieser Doktorarbeit wurden drei relevante Probleme in der PET Praxis analysiert und entsprechende Lösungen entwickelt. Diese wurden von den führenden PET-Herstellern implementiert und tragen somit einen kleinen Teil zu einer verbesserten Diagnose bei.

Schlagwörter:
Positronen-Emissions-Tomographie, Medizinische Bildgebung, Schwächungskorrektur, Bewegungskorrektur

Para Rafa

Gracias por enseñarme aprendiendo

Acknowledgments

This thesis would not have been possible without Stephan Nekolla, who gave me scientific advice and personal support all along the thesis. I am deeply thankful for everything he taught me, all the time and knowledge he patiently shared with me, and particularly for his friendly and generous help throughout this work. I am also grateful to my advisor Nassir Navab for this opportunity and for being a model in high level research management, creating an incredibly exciting academic environment. I would also like to thank Markus Schwaiger for his permanent support, as well as Sibylle Ziegler for sharing her immense knowledge on nuclear physics and instrumentation.

I am indebted to all colleagues at CAMP for the time together and for so many fruitful CAMPing meetings: it has been great working with the *older* generation (Jörg Traub, Wolfgang Wein, Martin Groher, Marco Feuerstein, Ruxandra Micu, Nicolas Padoy, Martin Horn, Thomas Wendler, Tobias Lasser, Darko Zikic, Ben Glocker, Pierre Georgel, Moritz Blume, and many more), and also seeing the newer students come up with novel projects and fresh ideas.

And special thanks to the colleagues from the Department of Nuclear Medicine for these years working together: Sandra van Marwick, Ralph Bundschuh, Irene Torres, María-José Martínez, Isabelle Miederer, Virginia Spanoudaki, Axel Weber, Sybille Reder, Gaspar Delso, Jasmine Schirmer, Arne Tapfer, Melanie Hohberg, Jozef Pulko, Dominik Schulz, Martina Marinelli, Katharina McGuire... it has been a unique experience working with such an interdisciplinary group. I also thank the MTAs working with PET (Brigitte Dzewas, Anna Winter, Coletta Kruschke, Helga Fernolendt, Sylvia Schachoff), who always supported me with all measurements, and the physicians and research fellows with whom I had the opportunity to share my office for these years, in particular Takahiro Higuchi, Michael Souvatzoglou, Antti Saraste and Hossam Sherif, for the many valuable discussions and for their patience and kindness answering my numerous medical questions and giving me a great insight into cardiovascular research.

Thanks also go to Siemens Healthcare, for the essential financial support for this thesis and for many fruitful collaborations.

I am thankful to all my friends in Munich, who have made me feel at home here, and to my friends abroad, for the trips and visits in all directions reminding me that friendship remains despite the distance.

I would also like to thank my parents and my siblings for their support. And in a very special way my son Raphael, to whom I dedicate this thesis.

Contents

Acknowledgments **ix**

1 Introduction **1**
1.1 From the discovery of X-rays to multimodality imaging 1
1.2 Challenges of multimodality imaging with PET addressed in this thesis . . 3
1.3 Particularities of the work 4

2 Positron Emission Tomography **5**
2.1 Physics and Instrumentation 5
2.1.1 Positron-emitters 5
2.1.2 Synthesis and administration of radiotracers 5
2.1.3 From positrons to gamma rays 6
2.1.4 Interactions between gamma rays and surrounding matter 7
2.1.5 Detection of gamma rays 8
2.1.6 Image reconstruction 11
2.1.7 Attenuation correction in-depth 15
2.2 Clinical role in oncology and neurology 19
2.2.1 Oncology 19
2.2.2 Neurology 20
2.3 Cardiac imaging with PET/CT 21
2.3.1 Pathophysiology of the heart 21
2.3.2 Overview of PET and PET/CT cardiac applications 21
2.3.3 Myocardial perfusion imaging 22
2.3.4 Viability imaging 23
2.3.5 Calcium score 25
2.3.6 Computed Tomography Angiography 26

3 Advances in PET respiratory gating **31**
3.1 State of the art and method of respiratory gating 31

3.2 Measuring a respiratory signal . . . 34
3.2.1 Methods . . . 34
3.2.1.1 Anzai respiratory belt . . . 34
3.2.1.2 PMM spirometer . . . 35
3.2.1.3 BioVet temperature sensor . . . 36
3.2.1.4 ART Stereo Infrared Camera . . . 36
3.2.1.5 Sensor-less approach . . . 37
3.2.1.6 Measurements with volunteers and patients . . . 37
3.2.2 Results . . . 39
3.2.2.1 Measurements with volunteers . . . 39
3.2.2.2 Measurements with patients . . . 40
3.2.2.3 Sensor-less approach . . . 40
3.2.3 Discussion . . . 41
3.3 Dual cardiac-respiratory gating . . . 45
3.3.1 Methods . . . 45
3.3.1.1 MRI acquisition for validation of the respiratory triggering 45
3.3.1.2 Patient population . . . 46
3.3.1.3 PET/CT acquisition . . . 46
3.3.1.4 Definition of the gates . . . 48
3.3.1.5 Motion analysis . . . 49
3.3.2 Results . . . 50
3.3.2.1 Validity of the respiratory trigger . . . 50
3.3.2.2 Variability of the respiratory signals . . . 50
3.3.2.3 Respiratory motion of the heart . . . 50
3.3.3 Discussion . . . 52
3.4 Conclusion . . . 55

4 Cardiac PET/CT misregistration 57
4.1 Introduction . . . 57
4.2 Methods . . . 60
4.2.1 Patient population . . . 60
4.2.2 Protocol . . . 60
4.2.3 Data analysis . . . 60
4.2.3.1 PET-CT Registration . . . 61
4.2.3.2 Emission Driven Correction . . . 62
4.3 Results . . . 65
4.3.1 Simulated misalignment . . . 65
4.3.2 Manual registration . . . 66
4.3.3 Automatic registration . . . 68
4.3.4 Emission-driven algorithm . . . 69
4.4 Discussion . . . 72
4.4.1 Limitations . . . 73
4.5 Conclusion . . . 76

5 Attenuation correction in combined MRI/PET scanners 77
5.1 Strengths and challenges of combined MRI/PET . . . 77
5.2 State of the art . . . 81
5.3 Initial investigation and observations . . . 84
5.3.1 Limited MRI Field of View . . . 87
5.3.2 Cortical bone in MRI . . . 88
5.4 Segmentation of the attenuation map on PET/CT data . . . 90
5.4.1 Methods . . . 90
5.4.1.1 Patient population . . . 90
5.4.1.2 PET/CT acquisition . . . 90
5.4.1.3 Data processing . . . 90
5.4.1.4 Image Analysis . . . 92
5.4.2 Results . . . 92
5.4.3 Discussion . . . 92
5.5 MRI-derived attenuation maps . . . 97
5.5.1 Methods . . . 97
5.5.1.1 Acquisition of the PET/CT . . . 98
5.5.1.2 Acquisition of the MRI . . . 98
5.5.1.3 MRI-CT Spatial registration . . . 99
5.5.1.4 Segmentation of the registered MRI . . . 99
5.5.1.5 Addition of the PET/CT patient bed to the MRI-based attenuation map . . . 100
5.5.1.6 Re-reconstruction of the PET data using the MRI-based attenuation map . . . 100
5.5.1.7 Comparison of the PET images with MRI-based and CT-based AC . . . 101
5.5.2 Results . . . 101
5.5.2.1 Proton-weighted sequence . . . 101
5.5.2.2 VIBE Dixon . . . 103
5.5.2.3 Dual-echo Dixon . . . 103
5.5.3 Discussion . . . 104
5.6 Conclusion . . . 110

6 Conclusions 113

A Computed Tomography 115

B Magnetic Resonance Imaging 119

C Medical hardware used for the data acquisition 127

D Respiratory signal acquisition using an infrared stereovision camera 131

E Authored and Co-Authored Publications **133**
E.1 Publications in peer-reviewed journals 133
E.2 Publications in conferences 134

References **139**

CHAPTER 1

Introduction

1.1 From the discovery of X-rays to multimodality imaging

Medical imaging was a quickly evolving field and continues to be so. The first Nobel prize in physics, awarded to W. C. Röntgen in 1901 for his discovery of X-rays, represents the start of a course during which many fundamental physical phenomena were discovered, understood, and its application for diagnostic imaging envisioned.

Positron Emission Tomography (PET), which is at the core of this thesis, reflects these rapid changes. In 1928, Paul AM Dirac postulated the existence of a subatomic particle with the same mass as the electron but a positive charge. Four years later, Carl D. Anderson experimentally observed these particles in cosmic rays and called them positrons [8]. Both received Nobel prizes for their contributions. Positron emission from radioactive nuclei was first described in 1933 [133, 288].

The first human acquisitions using positron-emitters were performed in the 1940's and 1950's [291, 308, 44]. Shortly after the introduction of tomographical reconstruction techniques in SPECT by Kuhl [156, 157] and in CT by Hounsfield [122], the first PET three-dimensional images were acquired in the mid 1970's [46].

Since then, advances in material engineering and electronics have resulted in major breakthroughs in sensitivity and spatial resolution; research in radiochemistry has brought new radiotracers with a wide variety of biological targets and clinical applications; new image reconstruction algorithms exploiting the increasing computing power produce images with less noise and better diagnostic quality; and, finally, modern image analysis software with the availability of three-dimensional and fused views have made computer-aided diagnosis an essential tool in the daily practice. All these factors have contributed to establish PET as a mainstream noninvasive imaging modality.

This last decade has seen a new evolution in medical imaging, namely the emergence

of multimodality imaging. PET is probably the best representative of this trend: its combination with Computed Tomography (CT) has resulted in an important diagnostic benefit, and has also resulted in an impressive commercial success. Furthermore, the combination with Magnetic Resonance Imaging (MRI) has been investigated in preclinical scanners, and the first prototypes of clinical MRI/PET scanners are currently under evaluation.

PET/CT is the proof that multimodality imaging can result in higher diagnostic accuracy, reduced acquisition time and improved patient comfort. As a result, PET/CT scanners have virtually made standalone PET scanners obsolete. This trend continues with MRI/PET, which might be better adapted for several clinical questions and will allow new research opportunities by exploiting its truly simultaneous acquisition.

1.2 Challenges of multimodality imaging with PET addressed in this thesis

Multimodality imaging with PET does not only result in significant clinical advantages, but also poses new challenges. PET is a nuclear imaging modality, based on the decay of small amounts of radiolabelled molecules, and therefore requires sufficient acquisition time in order to acquire enough data to provide a diagnostic image. Modalities such as CT and MRI, by contrast, usually acquire images much faster; in particular, each single voxel in CT results from data acquired within a fraction of a second, as opposed to data acquired for some minutes as is usual in PET imaging.

This difference in acquisition time results in a variable impact from physiological motion, such as cardiac contraction and breathing motion. Moreover, CT and MRI can provide submillimetric resolution, whereas the resolution of PET is about 5 mm. For this reason, until now, physiological motion was often ignored in PET, with the exception of cardiac gated acquisitions for the purpose of estimating the cardiac function.

In this work, methods to measure and process a respiratory signal for respiratory gating in PET were investigated, as well as the influence of respiratory gating on cardiac acquisitions when combined with cardiac gating. Chapter 3 deals with these topics.

Furthermore, one advantage of combined PET/CT is the possibility of using the CT data for correction of the photon attenuation in the acquired PET data. The time-consuming transmission scans with rod sources, which were usually done before the advent of PET/CT, become thus unnecessary. This advantage, however, is intrinsically coupled to a potential source of error: any misregistration in the PET and CT data can potentially produce artifacts in the PET images. And misregistration is likely to happen in the thorax and abdomen due to the different acquisition times. In chapter 4, the misregistration between PET and CT images for cardiac acquisitions is investigated, the effects on the PET data are analyzed, and possible solutions are proposed.

In MRI/PET scanners the MRI data provide an anatomical view which could be useful for attenuation correction, just like it is done in combined PET/CT scanners. However, the physics of MRI are fundamentally different, and the images do not a priori contain any information on the stopping power of the tissues for high-energy photons. Therefore, new methods are necessary to extract suitable attenuation information out of MRI acquisitions. In chapter 5, the limitations of MRI and the requirements for MRI-based attenuation maps are analyzed; a solution based on an adapted MRI sequence followed by an automatic tissue segmentation is proposed.

1.3 Particularities of the work

Medical imaging merges four different disciplines: medicine, physics, engineering and computer science. Also biology and chemistry, essential to develop suitable contrast agents, are strongly involved. Successful research in medical imaging results from a close cooperation between all parts.

This thesis reflects this particular situation, being a multidisciplinary work. In this regard, it is convenient to know the physics and the clinical role of the different imaging modalities involved. The physics of PET and its clinical applications are presented in chapter 2, being fundamental for the understanding of the research work described in this thesis. The basics of CT and MRI are also described in the appendices A and B and its lecture is recommended to understand several parts of this work. Moreover, the most relevant features of the medical hardware used throughout this thesis (PET, PET/CT and MRI scanners) are presented in the appendix C.

Another particularity of this thesis is its clinical context. Clinical usability of the proposed solutions has been a permanent concern all along the thesis. For the work to be integrated into clinical use and result in a benefit for the patient, only highly reliable methods can succeed. Therefore, robustness was a permanent criterion for the choices made, and the validation of any proposed approach became a fundamental part of the research.

CHAPTER 2

Positron Emission Tomography

2.1 Physics and Instrumentation

Positron Emission Tomography (PET) produces three-dimensional images of the distribution of a radiolabeled molecule. It is typically used to image functional processes in the body, finding applications in areas such as oncology, cardiology and neurology. In this section, an overview of PET is provided; particular attention is paid to the photon attenuation within the body, relevant for some of the research presented in the thesis.

2.1.1 Positron-emitters

PET is based on the radioactive decay of positron-emitter isotopes by beta plus decay, according to the following process:

$$\mathrm{p} \rightarrow \mathrm{n} + \mathrm{e}^{+} + \nu_e.$$

That is, a proton p is converted into a neutron n, a positron (e^{+}) and a neutrino (ν_e).

Among the positron-emitting isotopes which can be produced, the most commonly used in PET are those having a short half-life and which are present naturally in many biological compounds, such as ^{11}C, ^{18}F, ^{15}O, and ^{13}N (see Table 2.1).

2.1.2 Synthesis and administration of radiotracers

Due to the short half-lives of the isotopes, the radionuclides are typically produced on-site using a cyclotron. One significant exception is ^{82}Rb, which can be produced using a generator. The fact that positron-emitters include nuclides common in biological compounds allows the development of a wide variety of radiotracers and also their synthesis by direct isotopic substitution in biologically important molecules without altering their function

Nuclide	Half-life (min)	E_{max} (MeV)	Mean positron range (mm)
^{18}F	109.8	0.63	0.6
^{15}O	2.0	1.74	2.5
^{13}N	10.0	1.12	1.5
^{11}C	20.4	0.96	1.1
^{82}Rb	1.25	3.40	5.9

Table 2.1: Positron-emitting radionuclides most commonly used in PET, together with their half-life, their positron maximum energy, and their average positron range in water prior to annihilation (data from [296]).

[77, 82]. Once the radiotracer is synthesized, it is injected into the patient or administered by inhalation in the case of gases.

The most commonly used radiopharmaceutical in PET is 2-[^{18}F]fluoro-2-deoxy-D-glucose (^{18}F-FDG), a compound which was synthesized and administered to patients for the first time in the late 1970's [129, 130, 3] and which is now used in over 90% of the total PET scans. It is an analog of glucose allowing quantification of glucose metabolism, and it is most commonly used for cancer detection, staging and monitoring, being considered the gold standard for the in vivo assessment of many tumor types. Since it is fluor-labelled, with a half-life of 110 minutes, it can be regionally distributed, so that an on-site cyclotron is not indispensable.

2.1.3 From positrons to gamma rays

When the positron is emitted from the nucleus, it has an initial kinetic energy up to a maximum dependent on the radionuclide (Table 2.1). The positron loses its kinetic energy by interactions with the surrounding matter, suffering several deflections which result in a tortuous path. The average path of the positron until losing its energy can be determined depending on the specific material, and is shown for water in the last column of Table 2.1.

After losing its kinetic energy, the positron annihilates with an electron from the matter[1]. The most probable outcome of the annihilation, occurring in over 99% of the cases, is radiation in form of two photons with an energy of 511 keV each[2], emitted in opposed directions to conserve momentum (Fig 2.1). However, because of some residual momentum of the positron at the moment of the annihilation, the angle formed by the two photons has some variability and is approximately 180±0.25°.

[1] There is a certain probability (30% in water) that the positrons combine first with an electron forming a short-lived bound state called positronium prior to annihilation [55].

[2] Annihilation can also result in emission of three (approx. 0.5% of the cases) or more photons, with the probability quickly decreasing with the number of photons. The idea of doing three-photon PET has been recently proposed [137]; by using detectors with high energy resolution and the conservation of momentum, the exact location of the annihilation could be determined. Since the presence of oxygen results in decreased chances of emission of three photons, this approach could potentially provide information on local concentration of oxygen and hypoxic conditions.

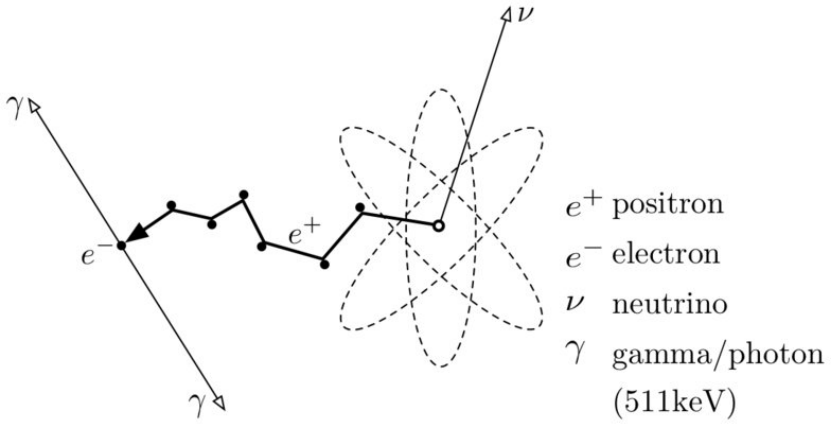

Figure 2.1: Beta plus decay of a radionuclide: the emitted positron slows down by interacting with the surrounding matter and, after collision with an electron, they both annihilate, resulting in two photons of 511 keV each emitted in opposite directions. Image reproduced from [162].

Positron range and non collinearity of the emitted photons represent a fundamental lower limit of the spatial resolution which can be achieved in PET[3].

2.1.4 Interactions between gamma rays and surrounding matter

High-energy photons in the range of 50 keV - 1 MeV interact with matter mainly by photoelectric absorption and Compton scattering[4].

In the photoelectric absorption, the photon interacts with an orbital electron in the atom, transferring all of its energy to the electron. As a result, the electron is ejected from the atom, and the atom where the interaction occurred is ionized. The photoelectric absorption usually occurs with electrons from the inner-shell, so that outer electrons may drop down to occupy the vacancy emitting either radiation in the form of x-rays or a second (Auger) electron.

The photoelectric absorption dominates in human tissue at energies below 100 keV; it has thus little impact for the 511 keV gamma rays resulting from the positron-electron annihilation, but is relevant for X-ray imaging and therefore for CT-based attenuation correction.

Compton scatter refers to the interaction between a photon and a loosely bound orbital electron. As a result of this interaction, the photon undergoes a change in direction and looses part of its energy, and the electron is ejected from the atom (Fig 2.2). The energy of the deflected photon E'_γ can be expressed as:

[3]The uncertainty produced by the positron range can be potentially diminished by application of a strong magnetic field [107].

[4]There are two additional interaction mechanisms: pair-production, which occurs only at energies above 1 MeV, and coherent scatter (also called Rayleigh, Thomson or elastic scatter), which has only a very minor contribution to total scatter, virtually inexistent for 511 keV photons.

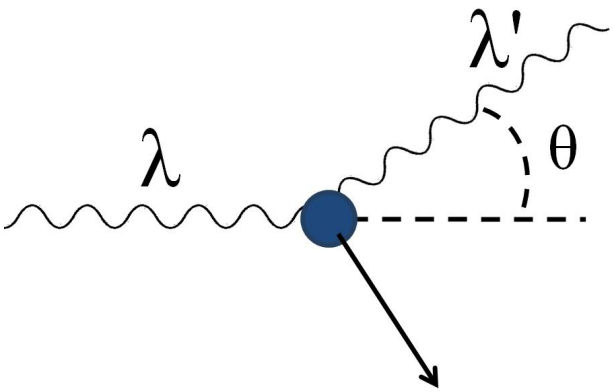

Figure 2.2: Compton scattering: a photon interacts with an electron undergoing a change in direction by an angle θ and a loss of energy.

$$E'_\gamma = \frac{E_\gamma}{1 + \frac{E_\gamma}{m_e c^2}(1 - \cos\theta)}$$

With m_e being the mass of the electron and c the speed of light. At the PET energy with $E_\gamma = 511$ keV, this can be simplified as:

$$E'_\gamma = \frac{E_\gamma}{2 - \cos\theta}$$

If the captured energy of the photon reaching the PET detectors -as explained in the following subsection- is below a certain threshold[5], the photon is considered to have suffered scatter. A relatively low threshold is typically used, so that this energy discrimination is most efficient in rejecting low energy, large angle scatter. Photons scattered with small angles are occasionally accepted and contribute to the image degradation. Scatter correction algorithms are common in clinical routine and help minimizing this impact.

2.1.5 Detection of gamma rays

The detection of 511 keV gamma rays is the basis of PET. Radiation detectors try to measure the energy deposited by radiation upon passage through the detector and usually convert it into an electrical signal. Several types of radiation detectors have been tested for PET. The three most relevant types will be presented here, sorted from least to most commonly used in PET imaging:

Proportional (gas) chambers When high-energy photons pass through a gas, free electrons and positive ions are produced along its track. Under normal conditions, electrons and ions recombine without producing any signal. If a small electric field is

[5]The lowest energy threshold used for clinical scanners is typically about 350-400 keV. This is due to the fact that a significant fraction of the 511 keV photons will only deposit a fraction of their energy within the detectors, so if the threshold is set too close to 511 keV, the overall detection efficiency of the system would be very poor.

applied, the electrons drift to the cathode producing an electric signal corresponding to the initial ionization. By increasing the electric field, the electrons drift towards the cathode with enough speed to become ionizing themselves, producing secondary ionization and resulting in a cascade of electrons, proportionally increasing the electric signal produced. This is the working principle of proportional chambers. Instead of using one single cathode, a grid of fine wires can be used, resulting in position-sensitive proportional chambers called Multi-wire Proportional Chambers (MWPC). Animal PET scanners using MWPC have been tested [292] and shown to provide excellent spatial resolution. However, they suffer from a poor energy resolution, a limited stopping efficiency for 511 keV photons and a slow detector response.

Semiconductor detectors When high-energy photons pass through a semiconductor, they can excite electrons from the valence band into the conduction band, generating electron-hole pairs. The application of an electric field results in a flow of charge following the energy deposition by the photons. Detectors based on Silicium and Germanium are not well adapted for high-energy photons due to their low stopping power, and compound semiconductor detectors with higher atomic number such as mercuric iodide (HgI_2), cadmium telluride (CdTe) and cadmium zinc telluride (CZT) have been developed. Although semiconductor detectors have great potential and an excellent energy resolution [146, 275], their poor timing performance and low sensitivity (due to a bad photopeak efficiency) are still suboptimal for application in clinical PET scanners.

Scintillation detectors When high-energy photons pass through a scintillator and interact with it, electrons from the scintillator are excited into higher energy levels; when they return to lower energy levels, the energy they absorbed is released in form of visible light. The light photons are then measured by photo-detectors in order to determine the energy deposited within the scintillator. Several scintillation crystals are available, and for PET imaging they are commonly chosen to have high atomic numbers (to increase the photoelectric fraction) and high density, resulting in the highest stopping efficiency for 511 keV photons as compared to the other detection schemes while offering a good energy resolution. Therefore, this is the most commonly used approach for PET imaging: all clinical PET scanners and most preclinical scanners use this detection approach.

Since most PET scanners use scintillation detectors coupled to photo-detectors, the working principle of scintillators in PET will be presented with more detail.

The performance of a PET scanner is tightly tied to the properties of the scintillation crystals used (Table 2.2). A scintillator for application in PET should have high stopping power for 511 keV photons, good intrinsic energy resolution, high light output and fast decay time, among other desirable properties.

The first PET scanners in the 1970's used sodium iodide (NaI) as scintillation crystals, but from 1980 through the year 2000, most PET scanners used bismuth germanate (BGO) because of its good detection efficiency, at the expense of a limited light yield and slow decay. Since 2001, clinical PET scanners using other scintillator materials such as

Property	NaI(Tl)	BGO	LSO	GSO	BaF_2
Density (g/cm^3)	3.67	7.13	7.4	6.71	4.89
Effective Z	50.6	74.2	65.5	58.6	52.2
Attenuation length at 511 keV	2.88	1.05	1.16	1.43	2.2
Primary decay constant (ns)	230	300	40	60	0.6
Light output (photons/keV)	38	6	29	10	2
Energy resolution (%)	6.6	10.2	10	8.5	11.4

Table 2.2: Properties of selected scintillators in PET, data from [296].

lutetium oxyorthosylicate (LSO), lutetium yttrium orthosilicate (LYSO) and gadolinium oxyorthosilicate (GSO) have been introduced. They provide a high stopping power combined with short decay times, being therefore better suited for high count rates and 3D imaging without septa[6]. Most clinical scanners developed now use these scintillators.

The light output from the scintillator is converted into an electric signal using a photo-detector. Ideal photo-detectors should have a high quantum energy to ensure a high signal amplitude, a fast readout speed to allow good time resolution and a good amplitude resolution that leads to a good energy resolution [237].

At present, most clinical PET scanners use photo-multiplier tubes (PMTs) as photo-detectors, which are stable to small temperature changes and provide a high gain. Since PMTs are usually quite large and high spatial resolution requires the use of small scintillator crystals, the coupling between the scintillator and the PMT is not done one-to-one for most clinical scanners, but rather in a block design using a coding scheme to determine the crystal of interaction, so that the signal between neighboring PMTs is compared to determine the scintillator crystal emitting the photons [51].

Although PMTs offer good performance for most applications, they are bulky, they have a rather low quantum efficiency (approx. 25%), and they do not work adequately under the influence of strong magnetic fields; this last property makes them unsuitable for use in hybrid MRI/PET scanners. For these reasons, alternative light readout systems have been introduced in preclinical PET scanners, as described in section 5.1, and are planned to be used in combined MRI/PET scanners.

The usual design of PET scanners consists of rings of scintillator crystals, often arranged in detector blocks as mentioned above, and coupled to light readout systems which are used to detect the emitted gamma rays. When two gamma rays are detected within a short time window, they are assumed to come from the same annihilation taking place somewhere in the parallelepiped joining the two detectors, as shown in Fig 2.3. For the sake of simplicity, this parallelepiped is often represented as a line, which will be further referred to as *line of response* (LOR).

In state-of-the-art scanners with suitable scintillators and fast electronics, a time resolution below 1 nanosecond can be achieved, so that the possible location of the annihilation within the LOR is limited by measuring the time difference between the detection of the

[6] Although uncommon in state-of-the-art scanners, older PET scanners often acquire in the so-called 2D mode, with axial collimators (septa) separating each row of detectors avoiding oblique coincidences.

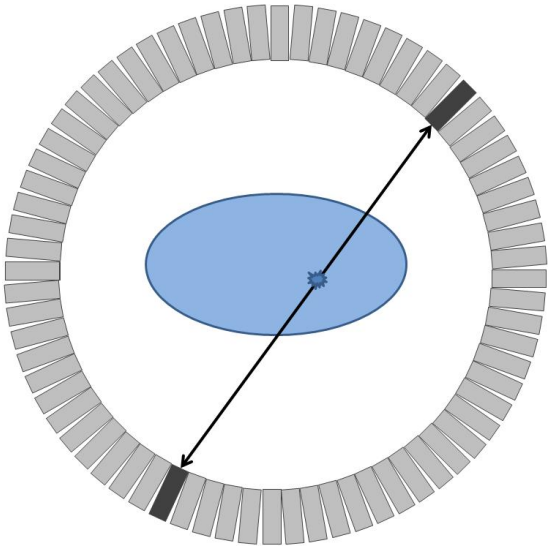

Figure 2.3: Section of a PET scanner showing the arrangement of detectors forming a ring and the detection of two colinear photons in a 2D plane. The photons arise from an annihilation taking place somewhere in the line between both detectors (line of response).

two gamma rays; this receives the name of *time-of-flight* PET (TOF-PET), and serves to improve the spatial resolution of the images. The spatial accuracy Δx with which the location of the annihilation can be measured along the LOR is determined by:

$$\Delta x = \frac{c \times \Delta t}{2}$$

where Δt is the timing accuracy of the system and c the speed of light. As an example, if a timing resolution of 500 ps is achieved, the location of the annihilation can be resolved to a 7.5 cm segment [210]. This additional information can be used in the image reconstruction process to improve the spatial resolution of PET scanners.

A PET scanner -whether TOF or not- is yet not able to determine accurately the position of the annihilation, but provides only information about the LOR where the annihilation happened. In order to estimate the spatial distribution of the radiotracer based on this information, tomographical reconstruction techniques are used.

2.1.6 Image reconstruction

There is no single optimal reconstruction algorithm for PET, but a variety of image reconstruction algorithms is available. Different algorithms may be preferred depending on the specific clinical task for which the image is reconstructed and the properties of the acquired data. It is out of the scope of this introduction to present the variety of algorithms in detail. Only some general concepts will be presented, and two important algorithms which are used in this thesis will be outlined: filtered backprojection (FBP) and ordered subsets expectation maximization (OSEM).

The data processing and particularities of TOF reconstruction will also not be presented in this thesis, since the PET scanners used for this investigation did not yet provide this acquisition mode. For information on this topic, please refer to [181, 67, 298, 58].

For the sake of simplicity, two assumptions will be made:

- It will be assumed that the two-dimensional data are acquired with one single ring of detectors. Although 3D algorithms are available, 3D PET data is often reconstructed by reconstructing each transaxial slice separately using 2D reconstruction algorithms.
- It will be assumed that the data are free of physical effects such as attenuation, scatter, radiotracer half-life, variations in detector efficiency, etc. Different correction methods exist for each effect but will not be presented in this work, with the exception of correction for attenuation, which will be described in the next subsection.

Before introducing the reconstruction algorithms, it is necessary to analyze the information provided by the acquired data. The PET raw data indicates how many events were detected in each LOR during the acquisition. Each LOR can be characterized by its angle of orientation (ϕ) as well as the distance between the LOR and the center of the detector ring (s); the PET raw data consists therefore in the line integrals of the activity distribution (assuming absence of physical effects), defined as:

$$p(s,\phi) = \int_{-\infty}^{\infty} f(x = s\ \cos\phi - t\ \sin\phi, y = s\ \sin\phi + t\ \cos\phi)\ dt$$

where the integration variable t is the coordinate along the LOR (Fig 2.4). The collection of all projections as a two-dimensional function $p(s,\phi)$ is given the name of *sinogram*, since the LORs passing through a fixed point in space x_0, y_0 lie along a sinusoid described by:

$$s = x_0 \cos\phi + y_0 \sin\phi$$

The transform $f(x,y) \rightarrow p(s,\phi)$ which converts the image in its sinogram is called the *X-ray transform*, which in 2D is the same as the *Radon transform* [239]. In PET, as well as in other imaging modalities such as SPECT and CT, the data measured are projections of the original imaged object; therefore, the measurements are in the sinogram space, so that an estimate of the Radon transform of the activity distribution (with some additional noise) is the starting point in order to get back to the original data.

Tomographic reconstruction algorithms can be classified into two large families: analytic and iterative methods. Analytic methods perform basically the inverse of the Radon transform on the projection data. In contrast, iterative algorithms use models able to deal with the behavior of the imaging system, resulting in solutions which cannot be written explicitly or, when they can be written, the analytic form is impractical to compute.

Filtered backprojection (FBP) The *central section theorem* states that the Fourier transform of a one-dimensional projection is equivalent to a section at the same angle through the center of the two-dimensional Fourier transform of the image. The implication for reconstruction is that, if all projections $\phi \in [0,\pi]$ are measured,

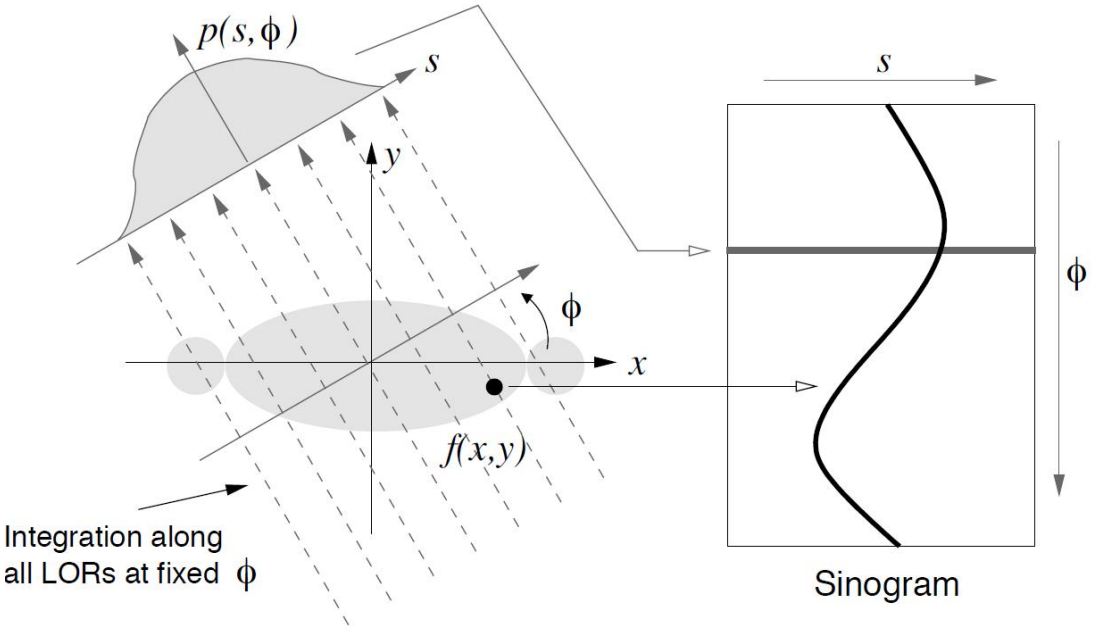

Figure 2.4: A projection, $p(s, \phi)$, formed from integration along all parallel LORs at an angle ϕ. All projections are arranged into a sinogram such that a single point in $f(x, y)$ corresponds to a sinusoid in the sinogram. Figure reproduced from [5], with permission from the copyright-holder Elsevier.

the Fourier transform of the image and then the image itself can be recovered. This way, the inverse Radon transform can be analytically computed, with an algorithm called filtered backprojection.

An essential point is the backprojection step, defined as:

$$b(x, y) = \int_0^{\Pi} p(s = x \cos\phi + y \sin\phi, \phi) d\phi$$

Intuitively, it can be seen that the backprojection of the projections for all angles will interact constructively in regions that correspond to high intensity in the original image. However, backprojection is not yet the inverse of the Radon transform, since it amplifies low frequencies and damps high frequencies, resulting in blurring of the backprojected image. To recover the original image, a ramp filter must be applied to each projection before backprojection, therefore the name of filtered backprojection.

The inverse Radon transform is an ill-posed problem, where a small perturbation of the projections p due to measurement noise can cause an arbitrarily large error on the reconstructed image f. This is due to the fact that the ramp filter amplifies the high frequencies, usually containing noise in them. Therefore, the FBP reconstruction is usually stabilized by filtering out the high frequencies, using a kernel such as Hamming, Butterworth or Shepp-Logan rather than the ramp filter.

Ordered Subsets Expectation Maximization (OSEM) The *expectation maximization* (EM) algorithm [71] offers a numerical method to determine the *maximum*

likelihood (ML) estimate. It was introduced in the field of tomographic image reconstruction in 1982 [274], in order to find the image f which was most likely to have happened given the measured projections p. The MLEM algorithm works by updating the image estimate f through the following iteration:

$$f_j^{(n+1)} = \frac{f_j^{(n)}}{\sum_{i'} H_{i'j}} \sum_i H_{ij} \frac{p_i}{\sum_k H_{ik} f_k^{(n)}}$$

where H_{ij} is the so-called *system matrix* which characterizes the imaging system and represents the probability that an emission from the pixel j (respectively voxel in 3D reconstruction) is detected in the LOR i.

Implicit in the equation above are a forward projection of the image estimate $f^{(n)}$, a comparison (ratio) with the measured projections and a backprojection into the image space in order to update the estimate. For a detailed explanation on how to derive this equation and the theoretical background of iterative reconstruction please refer to [238].

In PET reconstruction, the system matrix H should determine the likelihood of detection of an annihilation at a given voxel by a given pair of detectors with the maximum accuracy, taking into account any physical effects present during the acquisition which are reflected in the input p. The accuracy of H will be determinant in the correctness of the reconstructed image f.

The MLEM algorithm progressively converges to the image estimate with the maximum likelihood, showing first the low frequency components of the image and later the high frequency components; since the high frequency adds significant image variance, the algorithm is usually stopped before convergence and the resulting image is eventually smoothed. Still, the algorithm requires several iterations to reach a satisfactory image, with each iteration involving a projection and backprojection of the estimate, making it considerably slower than the FBP algorithm.

A modification of the algorithm, called OSEM, was proposed in 1994 [125]: it was observed that using subsets of the projections to update the image resulted practically in a much faster convergence. This acceleration contributed notably to the popularization of iterative reconstruction algorithms. In this thesis, a modified OSEM including the photon attenuation within the system matrix H will be often used and referred to as attenuation weighted OSEM (AW-OSEM) [61].

There are relevant differences between both reconstruction algorithms. For its execution, FBP is much faster than OSEM. Regarding the reconstructed images, they have different appearance and different noise distribution. Images reconstructed with OSEM appear less noisier and easier to interpret (Fig 2.5), and the studies comparing their diagnostic accuracy for oncological use conclude that they result in improved tumor detectability as compared to FBP [165, 83]. Therefore, iterative algorithms are currently more often used in clinical routine. FBP, by contrast, is a linear algorithm and allows an

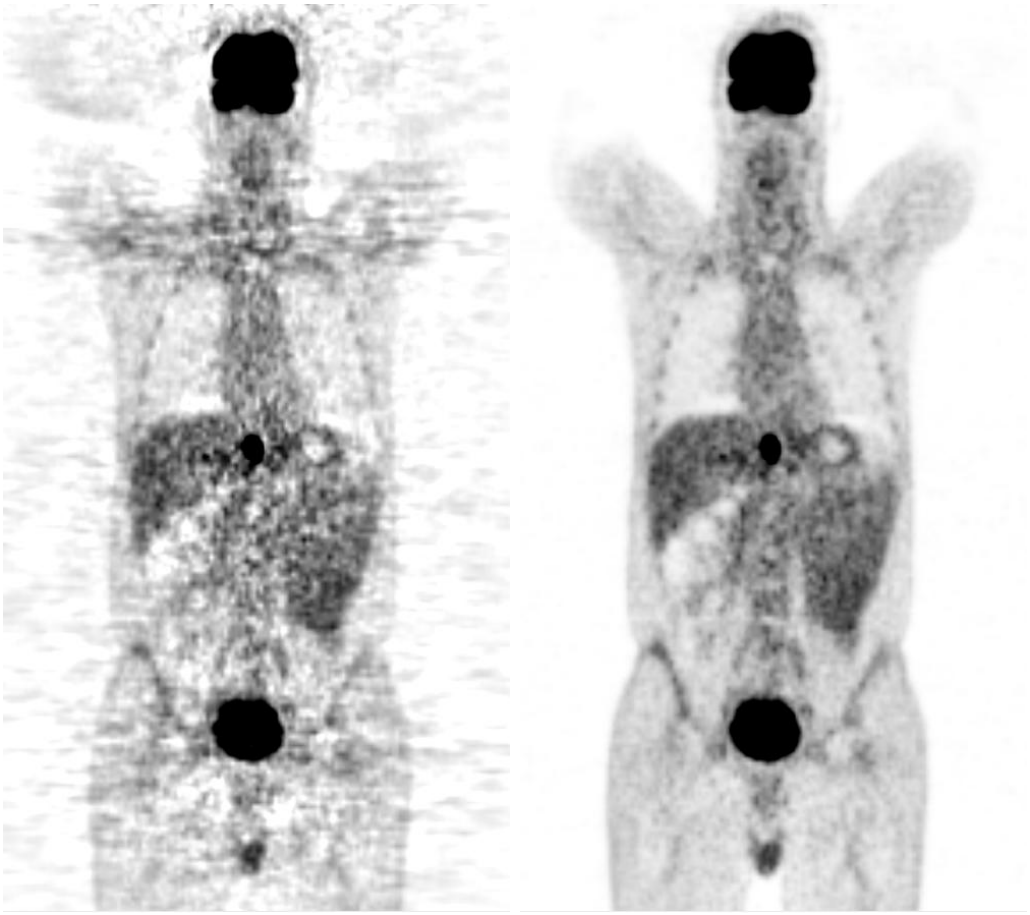

(a) (b)

Figure 2.5: Coronal slice of a ^{18}F-FDG PET image reconstructed using the FBP (a) and the AW-OSEM (b) algorithm. The FBP reconstruction appears noisier, with streaking artifacts, and harder to interpret as compared to the OSEM reconstruction.

easier control of the spatial resolution, remaining thus an important alternative approach. Moreover, there is no consensus yet regarding the accuracy of iterative algorithms for quantitative data analysis [57, 131].

2.1.7 Attenuation correction in-depth

A significant part of this thesis deals with attenuation correction for PET data. Therefore, a more detailed explanation of this correction is provided in this section.

For a given photon energy, each material can be characterized with a linear attenuation factor μ which indicates the chances of interaction and is commonly expressed in cm^{-1} (Table 2.3). The attenuation of a flux of photons I traveling an infinitesimal distance dx through a region with an attenuation coefficient μ is:

Tissue	μ [cm^{-1}]
Lungs	0.01 – 0.04
Adipose tissue	0.086
Water	0.096
Muscle	0.1
Cortical bone	∼0.17

Table 2.3: Attenuation coefficients at 511 keV for common biological tissues, expressing the likelihood of interaction per unity of distance traveled by the photon.

$$dI/dx = -\mu I$$

Integrating the equation for a uniformly attenuating medium, we obtain:

$$I = I_0 \cdot e^{-\mu x}$$

With I_0 being the number of incoming photons, I the number of photons going through the medium without suffering attenuation. Generalizing to a non-uniformly attenuating medium, we obtain:

$$I = I_0 \cdot e^{\int -\mu(x)dx}$$

As PET is based on the detection of coincident photons, the LOR includes the paths taken by both photons. Therefore, the attenuation for events occurring within a LOR does not depend on their location within the LOR, but only on the total attenuation for this LOR (Fig 2.6).

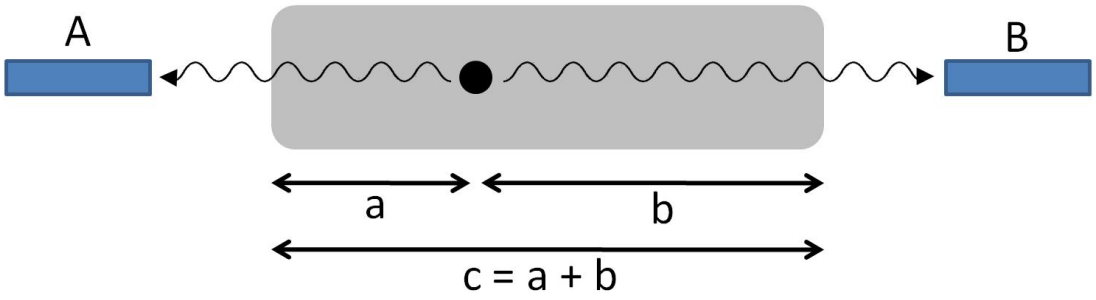

Figure 2.6: Detectors A and B record attenuated count rates from a radioactive source. For each annihilation, the probability of detecting both photons is the product of the individual probability of detecting each photon, so that $I = I_0 \cdot e^{-\mu a} \cdot e^{-\mu b} = I_0 \cdot e^{-\mu(a+b)} = I_0 \cdot e^{-\mu c}$. Therefore, the probability of detecting both photons is independent of the location within the LOR.

Thanks to this property, accurate correction for photon attenuation in PET can be performed by multiplying the measured coincidences in each LOR by a factor specific for

each LOR, the so-called *attenuation correction factor* (ACF). The ACFs are computed as the inverse of the attenuation, so that:

$$ACF_{LOR} = \frac{1}{e^{\int_{LOR} -\mu(x)dx}}$$

Weighting the events detected in each LOR by the ACFs can be done either in the sinogram space before reconstruction, or within the reconstruction itself, as in the AW-OSEM algorithm.

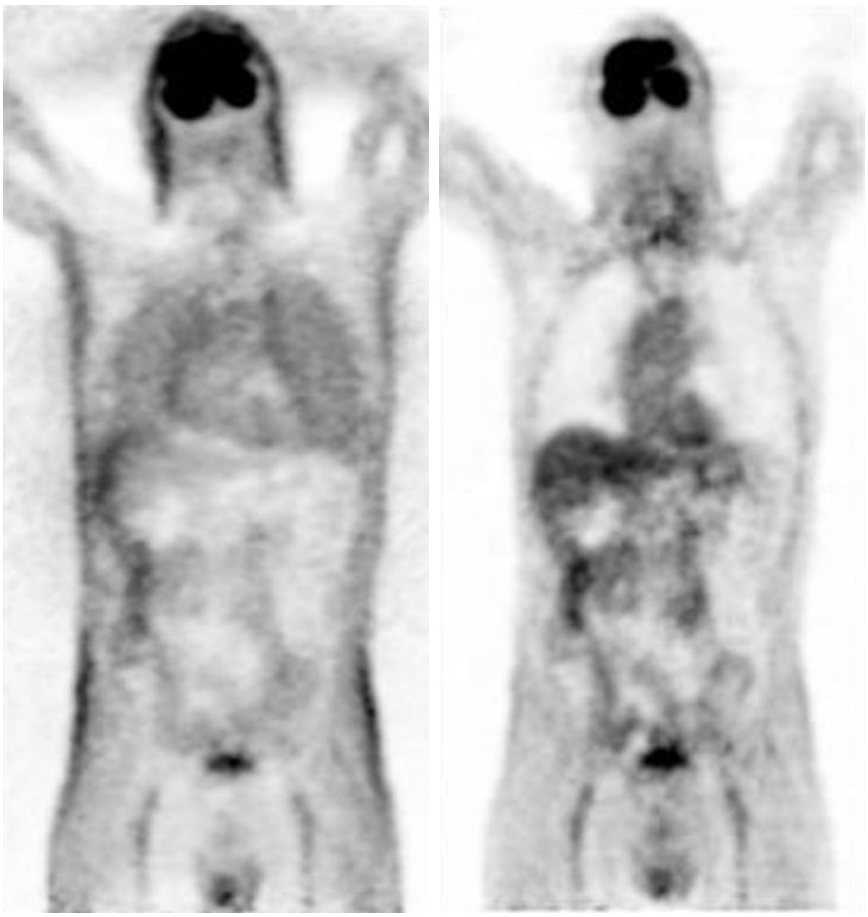

(a) (b)

Figure 2.7: Coronal slice of a ^{18}F-FDG PET image reconstructed without (a) and with (b) attenuation correction. In non-attenuation corrected images, the activity distribution is distorted; among other effects, there is an increased contrast between the surface and inner structures as well as an erroneously high-count density in the lungs.

To get an idea of the relevance of attenuation correction, the attenuation for 20 cm of human tissue (0.1 cm^{-1}) can be computed using the formula indicated above. The results is that only 14% of the annihilations are being detected as a coincident event, so that such an LOR would have an ACF of 7.4. Since ACFs increase exponentially with the

diameter of the imaged object, higher ACFs are common in clinical studies, especially for 3D acquisitions with oblique LORs, where ACFs above 50 are not rare [316]. The influence of attenuation correction is also visible when comparing an attenuation corrected versus a non-attenuation corrected image (Fig 2.7). Clinically, lack of attenuation correction results in harder interpretation and eventually reduced diagnosis accuracy [14, 127].

The challenge for attenuation correction is to accurately determine the ACFs. Since the ACFs are usually determined by first computing the integral of the attenuation factors μ, the problem is usually addressed as how to determine the attenuation factors for the imaged object. The methods which have been proposed can be divided in four classes:

Transmissionless techniques No attenuation map is acquired. The attenuation map can be calculated (or estimated) in different ways: applying a model (geometrical model or atlas), with manual delineation or using consistency criteria [316]. These approaches are still occasionally used for neurological studies in standalone PET scanners.

Radionuclide transmission scan A radionuclide source (typically ^{68}Ga/^{68}Ge or ^{127}Cs) rotating around the patient is used to measure the attenuation map, by *transmitting* gamma rays through the body (transmission scan). Since noise from the transmission scan is propagated into the reconstructed image, transmission maps with reduced noise are preferable, achieved either by performing long acquisitions (10-15 minutes per bed position) or by segmenting the low-statistics data acquired with a short scan (in less than 5 minutes). Radionuclide transmission scans are currently used in standalone PET scanners, and are becoming obsolete with the success of combined PET/CT scanners.

CT-based attenuation map In combined PET/CT scanners, the CT images are used to correct the PET emission data for photon attenuation. Since the CT scanner operates at much lower energies (60-140 keV photons), a bilinear transformation is used to convert from CT Hounsfield units to attenuation factors at 511 keV [148]. CT-based attenuation maps are acquired much faster than radionuclide transmission scans and contain also much less noise; this has contributed to the success of combined PET/CT scanners and has made CT-based attenuation correction the most common approach nowadays (see section 4.1 for further details).

MRI-based attenuation map In combined MRI/PET scanners, methods are currently under development to derive an attenuation map out of the MRI data. Please refer to Chapter 5 and Fig. 5.1 for more information on this topic.

2.2 Clinical role in oncology and neurology

PET is able to image in vivo the distribution of very small amounts (pico to nanomolar range) of radiolabeled molecules. The application areas are very wide: it can be used to study the pharmacokinetic behavior of drugs as well as to depict functional processes in the body. Until the 1990's, partly due to the elevated cost of establishing a PET unit, PET was dominated by research applications. In the last decade, the situation has changed dramatically, also in parallel to the introduction of combined PET/CT scanners, which have resulted in faster acquisition times and increased diagnostic accuracy. PET/CT is now a mainstream diagnostic imaging tool with a major role in patient management.

A large spectrum of radiomolecules has been set up to target different biochemical pathways. The main clinical applications of PET can be divided in three areas: oncology, neurology and cardiology. Other less extended applications of PET exist but will not be addressed here, such as imaging of gene expression, assessment of infectious diseases and pulmonary function. In this section, the applications in oncology and neurology will be introduced. Applications in cardiovascular imaging will be presented with more detail in the following section.

2.2.1 Oncology

The current success of PET is tightly associated to its great potential for oncological imaging [92, 244, 307], and in particular to one molecule: 2-[^{18}F]fluoro-2-deoxy-D-glucose (^{18}F-FDG). ^{18}F-FDG is an analog of glucose, allowing quantification of glucose metabolism. Since tumorous cells have an increased glucose consumption as compared to normal tissue [231, 96, 98], they also have an increased ^{18}F-FDG uptake and can thus be identified in the PET images (Fig 2.8). This has led PET and PET/CT using ^{18}F-FDG to be considered the gold standard for the in vivo detection of many tumor entities. Furthermore, due to the quantitative nature of PET, the tumor malignancy and its response after therapy can be assessed [136].

FDG-PET images are often assessed semiquantitatively using the *Standardized Uptake Value* (SUV). The SUV is a dimensionless index determined according to the following formula:

$$SUV = \frac{Decay\ corrected\ activity\ /\ Volume}{Injected\ dose\ /\ Body\ weight}$$

Although SUV is often used to perform both intrapatient (malignancy of lesions and therapy monitoring) as well as interpatient comparisons, its value as a quantitative index is discussed [143, 289]. Among its criticisms, the formula above assumes that the distribution volume of FDG is dependent only on the patient's body weight; this ignores the effects of the body composition and results in an undesired positive correlation between SUV and patient weight for many tissues [319]. To improve this aspect, alternative definitions of the SUV which normalize the value using the lean body mass or the body surface area have been proposed [147, 290, 187].

^{18}F-FDG is by 2009 the only oncologic PET tracer approved by the Food and Drug Administration (FDA) and is currently used in over 90% of the clinical PET examinations.

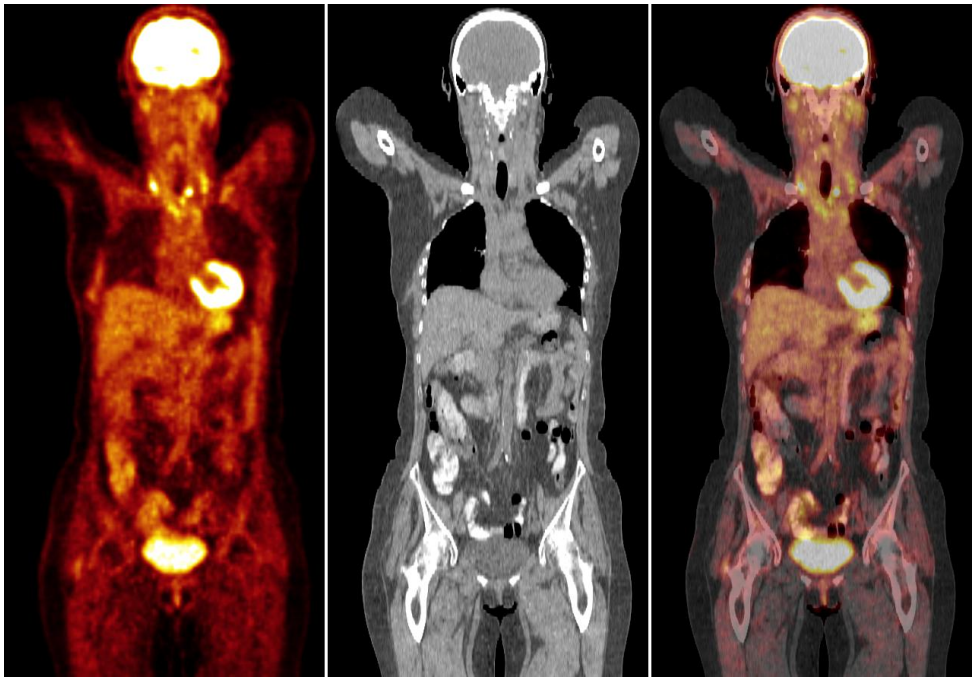

Figure 2.8: Coronal views of PET, CT and fused PET/CT from a patient with bronchial carcinoma examined with ^{18}F-FDG on a PET/CT scanner. Increased focal ^{18}F-FDG uptake allows the localization of the lesions throughout the body.

However, false positive and false negative results can appear in some clinical settings. For example, some organs have a naturally increased ^{18}F-FDG uptake even under fasting conditions, so that the normal tissue can eventually mask the tumors; the most obvious example of this is the brain. Also, some tumors can have a relatively low ^{18}F-FDG uptake, such as bone metastases from prostate cancer, which are therefore often not detected with PET. False positive results are also observed, occurring in benign conditions such as inflammatory or granulomatous lesions.

For these reasons, other tracers have been set up to target processes such as cellular proliferation, tumor hypoxia and amino acid transport. For information on these tracers, please refer to [116, 136].

2.2.2 Neurology

Before the advent of oncologic imaging with ^{18}F-FDG, neurology was the main focus of most PET examinations. Many tracers target cerebral blood flow, oxygen and glucose metabolism, amino acid uptake as well as receptor density and binding of neurotransmitters.

PET applications in clinical neurology include the study of epilepsy, neurooncology, dementia, stroke and movement disorders. This thesis does not directly deal with any application related to neurology, but an overview of these applications can be found in [285, 115, 199].

2.3 Cardiac imaging with PET/CT

2.3.1 Pathophysiology of the heart

A brief introduction to the pathophysiology of the heart is necessary to understand the usefulness of PET/CT for cardiac examinations.

The heart pumps oxygenated blood to the body and deoxygenated blood to the lungs, with one atrium and one ventricle for each circulation. The left ventricle (LV), which pumps oxygenated blood to the body, is thicker and more muscular than the right ventricle, pumping blood at much higher pressure. It is thus the main blood pump, and the target of most PET/CT cardiac examinations.

The LV gets its blood supply through the coronary arteries. In patients with *coronary artery disease* (CAD), atheromatous plaques accumulate within the walls of the coronary arteries, progressively reducing the coronary lumen and somewhat occluding the artery (*stenosis*); moreover, a plaque rupture can occur, causing the formation of a thrombus and eventually occluding completely the blood flow to the corresponding part of the LV, resulting in a *myocardial infarction*.

Some coronary stenoses are large enough to have a functional impact, with the arteries being unable to warrant an adequate myocardial perfusion [295]. The part of the LV perfused by the stenotic artery is therefore unable to function properly; especially under stress conditions (e.g. while doing exercise), the blood flow does not properly respond to the increased metabolic demand of the LV. This condition, with a restricted myocardial blood supply under stress conditions, is called *ischemic heart disease* or *cardiac ischemia*. Although cardiac ischemia is often caused by a stenotic artery, it can also be due to other reasons such as impairment of the microcirculatory function or severe hypotension. An ischemic condition can be asymptomatic or produce chest pain (*angina pectoris*); moreover, it can result in cardiomyopathy, leading to cardiac arrhythmia or eventually to a cardiac arrest.

2.3.2 Overview of PET and PET/CT cardiac applications

PET and combined PET/CT offer a powerful tool for the diagnosis and prognosis of cardiovascular diseases. A number of PET tracers allow the assessment of different physiological processes in the heart and the vascular system (Table 2.4), with two applications leading the clinical use of cardiac PET: quantitative assessment of myocardial perfusion and assessment of myocardial viability.

Furthermore, CT does not only offer an anatomical reference and a way of performing efficient attenuation correction, but it also has an important diagnostic value providing noninvasive coronary angiography (CTA) and information on the coronary calcification. In addition, gated PET or gated CT studies provide information on the local wall motion and cardiac function.

PET and PET/CT are used for cardiac imaging in many research applications such as myocardial innervation imaging [22, 253], late-enhancement CT for viability assessment in acute myocardial infarction [229, 104], hot spot imaging of atherosclerosis [247, 161] or imaging gene expression and monitoring gene therapy with PET [309, 30, 234, 203].

Target	Tracers
Perfusion	$^{13}NH_3$, ^{82}Rb, $H_2^{15}O$, ^{62}Cu-PTSM, ^{18}F-BMS-747158-02
Metabolism	^{18}FDG, ^{11}C-palmitate, ^{11}C-acetate
Myocardial innervation	^{11}C-HED, ^{11}C-EPI, ^{18}F-Fluoronorepinephrine
Gene expression	^{18}FHBG, F^{124}IAU, ^{124}I-hNIS
Apoptosis	^{18}F-Annexin V
Angiogenesis	^{18}F-Galacto-RGD
Hypoxia	^{18}F-Misonidazole
Vulnerable plaque	^{18}FDG (inflammation), ^{18}F-Annexin V (apoptosis)

Table 2.4: Some of the PET tracers used for cardiovascular applications. Well-established clinical applications are shown in the first three rows, whereas the lower rows show research applications and their associated tracers.

However, the mainstream clinical applications of cardiac PET and PET/CT are myocardial perfusion imaging and viability assessment (with PET) as well as CTA and calcium scoring (with CT) [268]. They will be introduced here.

2.3.3 Myocardial perfusion imaging

The presence of high-grade coronary stenoses in anatomical images is a sign of obstructive CAD. However, it is increasingly emphasized that therapy and intervention of CAD cannot be based on symptoms and morphological detection of coronary stenoses alone [106, 172]; low-grade stenoses can have a significant functional impact, whereas other high-grade stenoses can be hemodynamically less relevant and not produce ischemic syndromes.

A normal perfusion scan is associated with a very low risk of cardiovascular events, whereas an abnormal perfusion scan is associated with higher risk of cardiac events [105]. Therefore, *myocardial perfusion imaging* (MPI) offers better diagnostic and prognostic value for CAD patients than morphologic imaging alone, serving as a gatekeeper to conventional coronary angiography and guiding the choice of the therapy.

PET perfusion imaging is widely accepted as the gold standard for non-invasive quantification of absolute regional myocardial blood flow. It is usually done using ^{13}N-NH_3, ^{82}Rb or ^{15}O-H_2O, although newly developed fluor-based tracers such as ^{18}F-BMS-747158-02 are progressively gaining interest [118, 219]. A typical PET perfusion examination consists of two PET scans, one at rest and one at pharmacologically induced stress, which increases blood flow 3-4 fold in normal healthy regions (Fig 2.9). Depending on the isotope used, a pause between both scans is done to allow the tracer to decay before the new injection. Regional comparison of the perfusion between the rest and stress scans allows to draw conclusions about the state of the different myocardial segments (Table 2.5).

PET offers the potential of quantitative measurement of the regional myocardial blood flow, thus allowing the evaluation of multi-vessel disease; this is an important advantage as compared to SPECT perfusion imaging [267, 17]. For rigorous quantification, a dynamic acquisition must be performed followed by the application of a kinetic model [142]. Alternatively, simpler -although less accurate- approaches are used, such as measuring

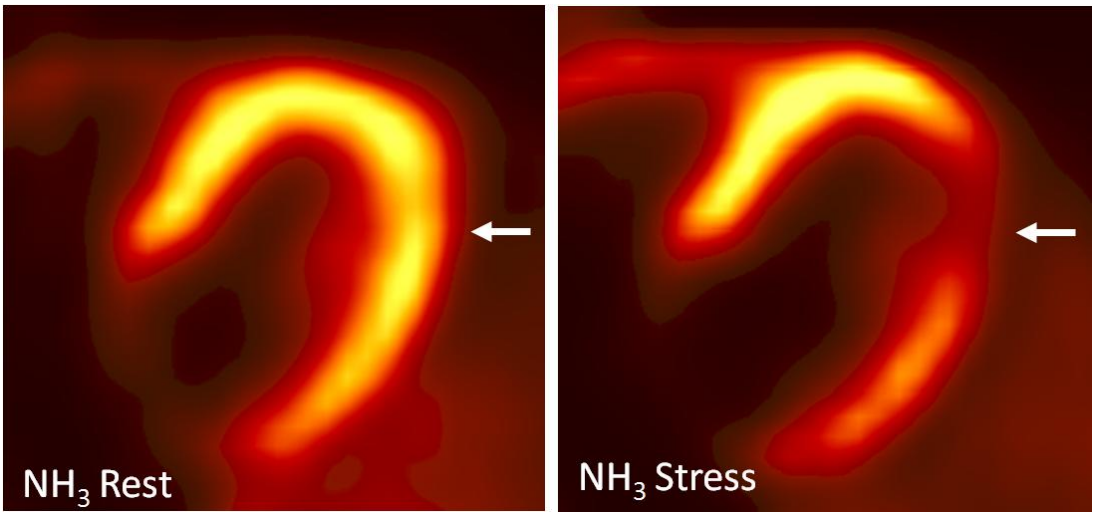

Figure 2.9: ^{13}N-NH_3-PET perfusion images of a patient acquired in rest condition (left) and under pharmacological stress (right). The presence of cardiac ischemia is visible, with a part of the lateral wall (white arrow) hypoperfused under pharmacological stress.

Rest	Stress	Classification
Normal	Normal	Normal
Normal	Reduced	Ischemic
Reduced/absent	Reduced/absent	Hibernating/scarred (see 2.3.4)

Table 2.5: Classification of the myocardial tissue according to its rest an stress perfusion.

the flow reserve, that is, the ratio between uptake during stress and rest.

2.3.4 Viability imaging

The hypoperfused parts of the myocardium can suffer temporary or permanent damage after acute cardiac events or ischemic episodes. When a region of the LV is hypoperfused, it may downregulate its function (by decreasing its contractile performance) to survive despite the reduced flow, entering a status where the tissue is said to be *hibernating*. In this case, once the flow to this region is restored, the myocardium enters first a *stunned* status, still with impaired contractile function, resulting from alterations in contractile proteins in response to the ischemic conditions [39, 152]; after some time, typically a few days or weeks, the heart recovers its normal contractile function. The tissue which recovers its function after reperfusion is said to be viable tissue.

However, some myocardial tissue may have undergone a necrotic process, and the tissue is said to be scarred. In this case, even a successful revascularization will not help to improve the left ventricular function.

The aim of viability imaging is to identify those patients in whom revascularization is likely to improve the left ventricular function, in order to do a pre-surgical assessment of the risk to benefit ratio [310, 259]. If there is a large amount of viable, hibernating tissue,

revascularization will be performed. Conversely, a patient having mainly non-viable tissue will not profit from this high-risk intervention and will suffer increased operative mortality, so that alternative therapeutic options must be considered.

Perfusion	Glucose metabolism	Contractile function	Classification
Normal	Normal	Normal	Normal
Normal	Normal/increased	Impaired	Stunned
Reduced	Normal/increased	Impaired	Hibernating
Reduced/absent	Reduced/absent	Impaired	Scarred

Table 2.6: Classification of the myocardial tissue according to its perfusion, glucose metabolism and contractile function. Since most dysfunctional segments of the LV contain a mixture of fibrotic/necrotic and viable tissue, a continuum of values is seen in the examinations.

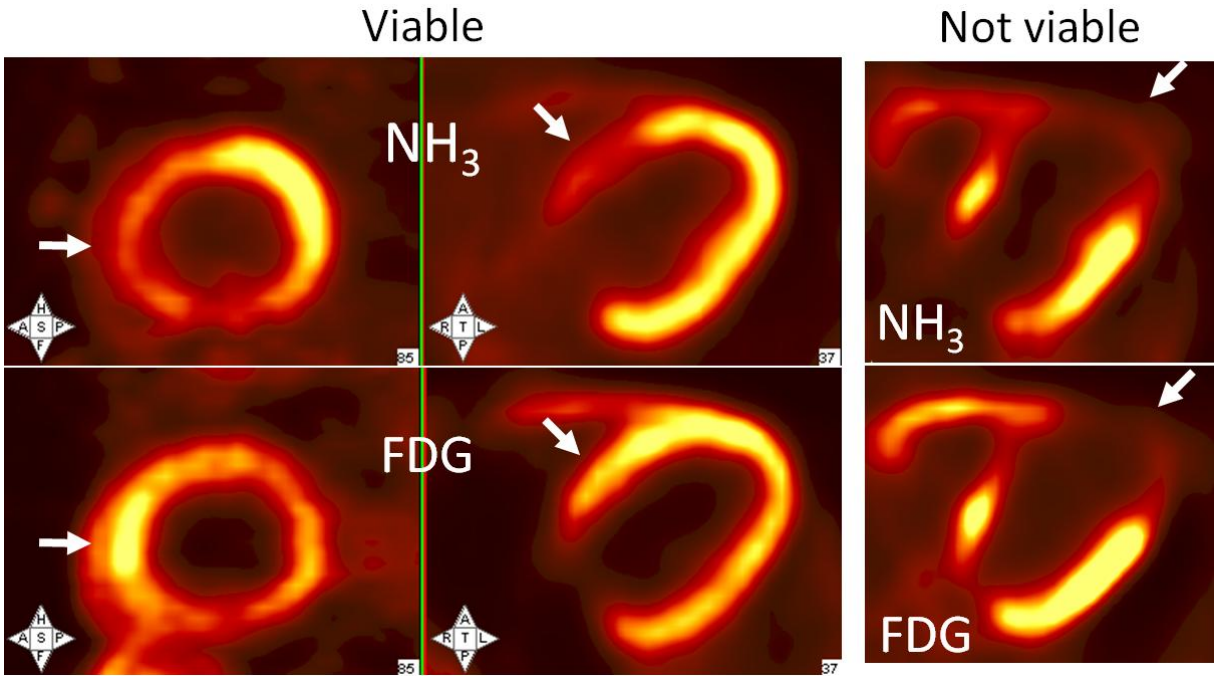

Figure 2.10: PET viability scans with ^{13}N-NH_3 and ^{18}F-FDG from two different patients. On the left, patient with viable tissue showing increased glucose metabolism (arrow). On the right, patient with severely reduced glucose metabolism, indicating scarred tissue.

PET is generally accepted as the gold standard for viability assessment. In PET, it is the amount of residual metabolic activity which helps distinguishing between viable and non-viable tissue in the hypoperfused myocardium [194, 18, 153]. In the fasting state and under resting conditions, the myocardium uses free fatty acids as its primary source of energy, with glucose in second place; in ischemic conditions, by contrast, glucose becomes the predominant source of energy.

Although assessment of the oxidative metabolism using tracers such as ^{11}C-acetate has been investigated, the most common approach is the evaluation of enhanced glucose utilization using ^{18}F-FDG. Therefore, a typical viability examination with PET consists in two scans, a rest perfusion scan and a glucose metabolism scan (Table 2.6). Hypoperfused regions with preserved or even increased glucose metabolism indicate viable tissue which will benefit from revascularization (Fig 2.10).

2.3.5 Calcium score

One of the most common findings in patients with CAD has been calcification within atherosclerotic plaques.

With the improvements in temporal and spatial resolution of multislice CT, the presence and extent of calcium in the coronary arteries can be evaluated with a relatively low associated radiation. Calcium has a high radiodensity and is therefore easily recognizable in the CT images (Fig 2.11). Scoring methods such as the Agatston score [1] or the measurement of calcium mass or volume [294] serve to quantitatively assess its extent.

Figure 2.11: Transaxial slice of a CT for evaluation of the coronary artery calcium. A calcium score is computed by identifying the calcium within the coronaries, which is segmented by means of its high radiodensity.

Coronary artery calcium (CAC) has been shown to provide independent incremental information in addition to traditional risk factors for the prediction of cardiac events and all-cause mortality [72, 240, 160, 272, 257]. Measurement of CAC is therefore a

powerful prognostic tool and can be used as gatekeeper for myocardial perfusion imaging or conventional angiography in chest-pain patients with intermediate risk for CAD [263].

2.3.6 Computed Tomography Angiography

Conventional invasive coronary angiography by means of catheterization is currently considered to be the reference for the clinical evaluation of CAD, allowing visualization of obstructions in the coronary tree. However, the method is invasive, it implies a non-negligible risk of adverse events (1.8% complication rate, 0.1% mortality rate) and discomfort for the patient [255, 16], as well as a high economic cost.

Figure 2.12: View of a CTA showing a high-degree stenosis produced by a soft coronary plaque (red circle).

Computed Tomography Angiography (CTA) is emerging as a potential non-invasive alternative to conventional non-interventional angiography. The basic idea of coronary CTA is to introduce a contrast agent in the blood in order to delineate the lumen of the coronary arteries (Fig 2.12). However, their small diameter and the cardiac motion make the procedure technically very demanding [227].

With the current technology, to acquire a CTA with optimal quality, the patient should ideally have a slow and regular heart rate. For that purpose, beta-blockers are often administered before the examination if the heart rate is over 65 beats per minute. The acquisition must be performed ECG-gated, since the images are acquired over several cardiac cycles; therefore, patients with arrhythmia might show CTA with suboptimal quality. Newer CT scanners with improved temporal resolution are becoming less sensitive to these effects.

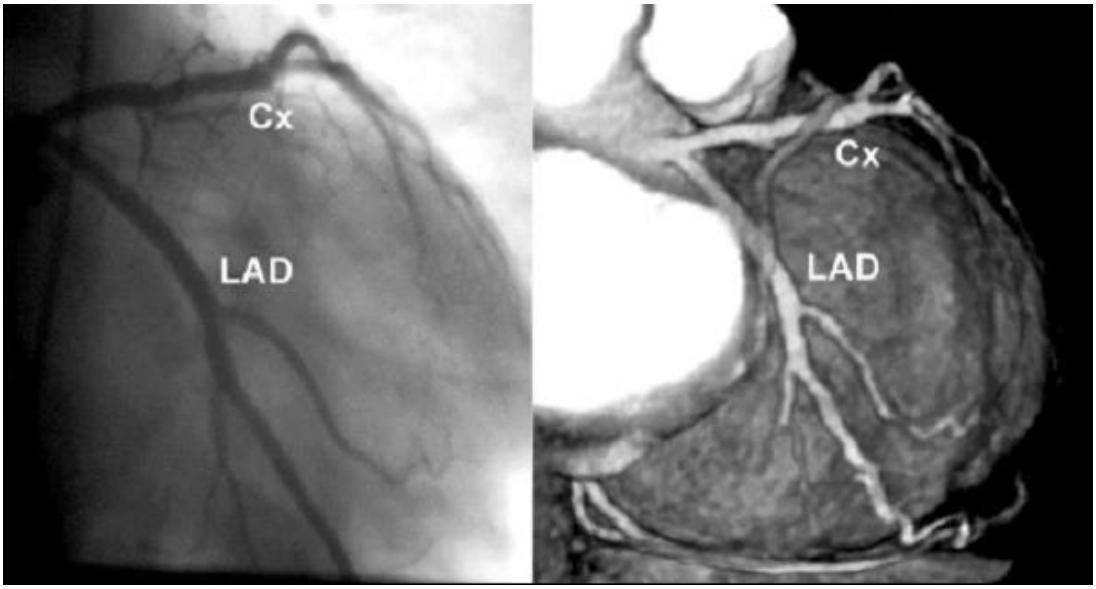

Figure 2.13: Comparison of conventional angiography and volume-rendering of a CTA acquired with a 4-rows CT. The coronaries are well delineated, but small branches are not visible in the CTA. Scanners with 64 or more rows allow to further improve the quality of the resulting CTA, providing a quality which is comparable to that of conventional angiography. Image reprinted from [266] with permission granted by the copyright holder (Radiological Society of North America) and by the author.

All recent developments in CT technology have resulted in a high level of reliability and accuracy in the visualization of the coronary tree. With the appropriate expertise, the diagnostic accuracy of CTA with 64 or more rows is already very close to that of conventional angiography [87, 108, 201] (Fig 2.13). Drawbacks of CTA are occasional reactions to contrast medium [201] as well as the associated radiation dose [81, 40, 132, 112]. Regarding the radiation dose, state-of-the-art scanners allowing prospective ECG gating [123, 250] can reduce the dose by more than 70%, so that a high-quality CTA can be obtained with a dose below 5 mSv [76, 126]. Furthermore, CTA is a purely diagnostic test and does not allow immediate intervention, in contrast to conventional angiography.

The greatest potential of CTA might be in symptomatic patients at intermediate risk; also patients with equivocal rest-stress perfusion studies. In these patients, CTA can help rule out the presence of obstructive CAD and be a gatekeeper for invasive coronary angiography [32, 59]. For patients at low-risk, CTA should not be used as a screening tool because of the associated radiation dose. Neither should CTA be performed on symptomatic patients with a high pretest likelihood, since they are likely going to require invasive angiography and intervention anyhow.

CTA and myocardial perfusion imaging provide complementary information about CAD: on the one hand, CTA shows the anatomy of the coronaries, allowing the detection and evaluation of stenotic coronary arteries as well as the definition of the individual vessel territories [216]. Perfusion imaging, on the other hand, allows to assess the functional relevance of the stenoses (Fig 2.14). Therefore, combined PET/CT or SPECT/CT scanners

Figure 2.14: Color-coded fusion of a CTA with an ^{13}N-NH_3-PET perfusion study. Combined PET/CTA can allow identification of the stenosis and the assessment of their functional impact.

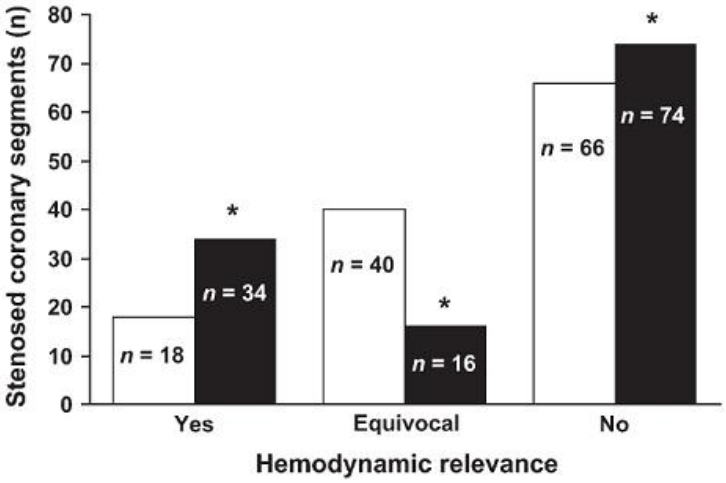

Figure 2.15: Interpretation of stenosed coronary segments with regard to hemodynamic significance on SPECT-CT side-by-side (white columns) or fused (black columns) analysis. Confidence in the assessment is increased through analysis of the fused data. Image reprinted by permission of the Society of Nuclear Medicine from [91].

show great potential for assessment of CAD [213, 268]. A study using separate 64-row CTA and ^{99m}Tc-tetrofosmin SPECT rest/stress perfusion scans acquired on different days

made this potential clear [91]: the fusion of SPECT/CT data resulted in a significantly better interpretation of the stenoses as compared to side-by-side analysis (Fig 2.15).

CHAPTER 3

Advances in PET respiratory gating

3.1 State of the art and method of respiratory gating

The spatial resolution of PET scanners has been progressively improving over time, with current commercial whole-body scanners achieving a spatial resolution below 5 mm [38]. However, most examinations cover the thorax and abdominal area, and the effective spatial resolution is markedly reduced due to respiratory motion. Indeed, PET requires a sufficient number of detected events in order to perform a reconstruction with enough signal to noise ratio, so that the acquisition of the PET data has to extend over several minutes; the resulting images appear therefore blurred due to respiratory motion, presenting consequently degraded diagnostic value.

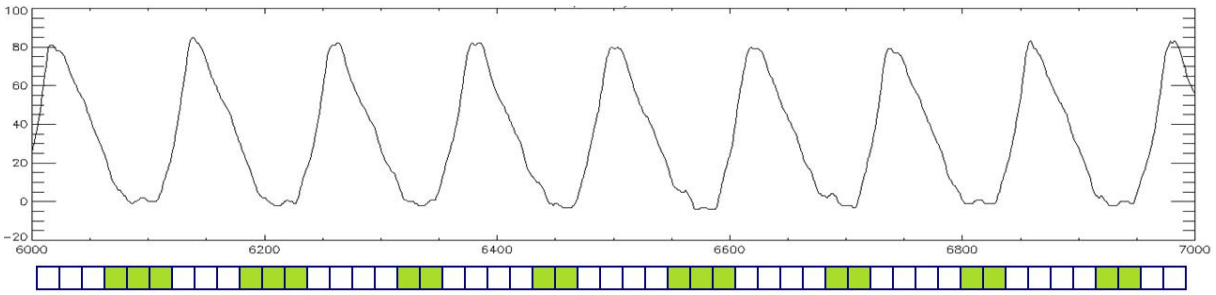

Figure 3.1: The respiratory signal (top) synchronized with the acquired data (represented as square array in the bottom) can be used to perform respiratory gating. For instance, by selecting only the data acquired at expiration (green squares) and using it for reconstruction, the image would show the patient at the expiratory phase.

To reduce the degradation of the image quality due to the respiratory motion, respiratory gating was developed. Gating consists in acquiring a physiological signal (ECG or respiratory signal) synchronized with the imaging data, which is acquired over several

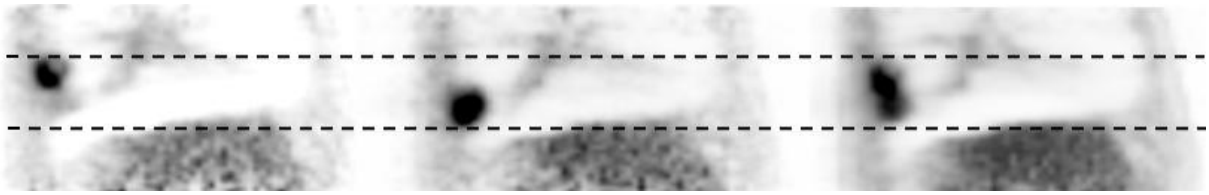

Figure 3.2: Effect of respiratory motion on PET data from a patient with an FDG-avid lung tumor (sagittal images). On the left, image acquired at the expiratory phase. On the middle, image acquired at inspiration. On the right, static image showing the average of all respiratory phases, as it is usually acquired. The image blurring produced by the respiratory motion results in degraded diagnostic value: the tumor volume is usually overestimated and its maximum metabolic activity underestimated, since the tracer uptake appears distributed over a larger volume. (Image courtesy of Ralph Bundschuh)

physiological cycles (Fig. 3.1). The data is then sorted so that all data belonging to a same physiological phase can be reconstructed separately, thus obtaining nearly motion-free images for each phase (Fig. 3.2).

As a matter of fact, scintigraphy was the first imaging modality which resolved physiological motion by performing gated acquisitions. The first ECG-gated cardiac blood-pool scintigraphic acquisitions were performed in the early 1970's [281, 318, 228, 270, 23, 102] (Fig. 3.3), showing great potential to assess the ventricular ejection fraction and segmental contraction. The possibility of performing cardiac gating to temporally resolve the heart beating and improve the image quality was soon extended to CT [251, 24, 207], MRI [117, 297, 163] and PET [120, 97, 312].

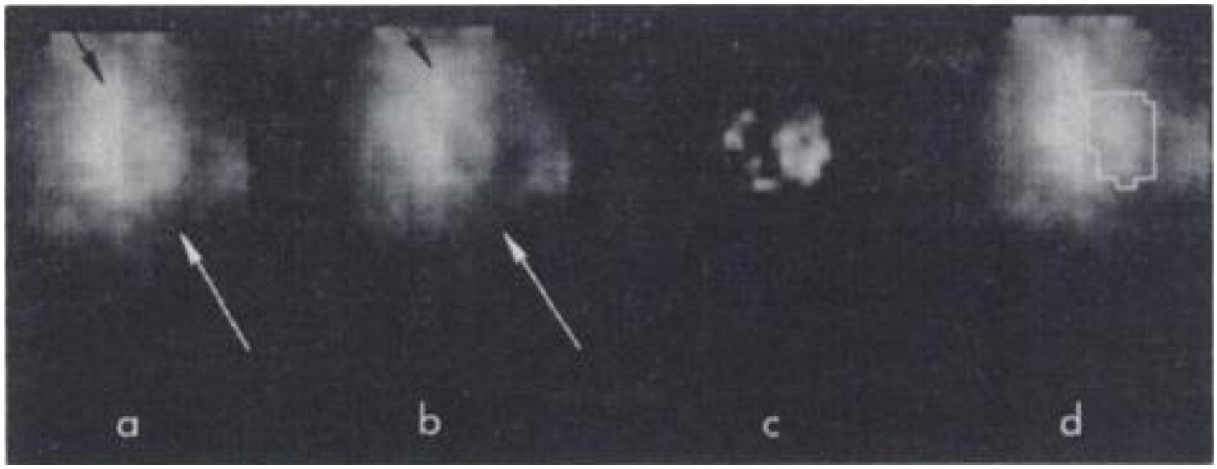

Figure 3.3: One of the first cardiac gated acquisitions, showing blood-pool scintigraphic images of ^{99}Tc-human serum albumin (^{99}Tc-HSA) in end-diastole (a), end-systole (b), end-diastole minus end-sytole (c) and outlined region of the ventricular blood-pool (d). The left-ventricular ejection fraction was derived from the images by comparing the measured counts in diastolic and systolic images. Reprinted by permission of the Society of Nuclear Medicine from [270].

ECG gating provides a significant clinical advantage by allowing evaluation of the cardiac function and parameters such as the ejection fraction and local myocardial contraction. But gating might also be interesting in order to obtain motion-free images rather than analyzing the motion itself. This is the case for respiratory gating. The influence of respiratory motion in the degradation of image quality was soon acknowledged [33, 4, 287]; the first implementations of respiratory gating were developed for nuclear imaging [140, 299] and extended to other imaging modalities such as MRI [249, 80] and CT [138, 300, 208].

Clinical evaluation of respiratory gating in PET showed an improvement in detectability, delineation and quantification of lung metastases [215, 214, 36]. Most respiratory gating systems for PET in use until 2006 were developed in-house and not supported by the PET manufacturer. Also in this clinic, equipped with a Siemens Biograph 16 by this time, respiratory gating was implemented in-house (implementation details are provided at section 3.3.1.3 in this chapter).

The major PET vendors learned from the experience of the different centers: whereas no commercial PET systems included respiratory gating in 2004, they all offer respiratory gating in their current scanners.

The contribution of this work to the problem of respiratory gating in PET was twofold:

- Different ways to acquire a respiratory signal for gating in PET were investigated and compared
- A dual cardiac-respiratory gated acquisition was developed and its potential clinical impact was evaluated

3.2 Measuring a respiratory signal

In order to perform respiratory gating, it is necessary to have a temporal signal providing information about the current respiratory phase of the patient. Two different approaches are possible:

- Extracting the respiratory signal using the imaging data itself
- Acquiring the respiratory signal with an external device

Extracting the respiratory signal from the imaging data is a well-known technique in MRI. There, a one-dimensional image navigator located at the interface between the liver and the lung is sometimes used to monitor respiration [79]. For such an approach to work, it is necessary to have a high temporal resolution (well below 1 second) and sufficient data to determine the respiratory phase of the patient. Such a technique was first investigated in PET by [150, 302]. Although the initial results were promising, the method was not implemented by the major PET manufacturers.

Acquiring the respiratory signal with an external device is the most commonly used method to perform respiratory gating. There, however, several sensors with different properties are available, and no consensus exists on the best suited system for respiratory gating in PET. For gated radiotherapy, however, one study reported the use of three different sensors [155]; the results of the study indicated that all three different sensors were potentially able to acquire a suitable respiratory signal, but other factors like patient comfort should also be considered, so that the use of a temperature sensor for the respired air or a strain gauge to measure the chest expansion appeared to be the best adapted.

The contribution of this work is to investigate which is the most suitable way to acquire a respiratory signal for PET, comparing the different existing sensors as well as a data-driven method.

3.2.1 Methods

We investigated four different sensors for the acquisition of a respiratory signal [242, 188], as well as a sensor-less approach [49] using the PET image data. Following is a summary of each of the methods investigated.

3.2.1.1 Anzai respiratory belt

The AZ-733V by Anzai Medical (Tokyo, Japan, `http://www.anzai-med.co.jp`) is a commercial system designed for respiratory triggering in radiotherapy. It is constituted by a pressure transducer which is positioned inside a pocket on an elastic belt, itself placed on the upper abdomen of the patient (Fig. 3.4). The pressure transducer is connected to a device comprising all acquisition electronics (Anzai Wave Deck) which samples the respiratory signal every 25 ms and delivers it to a separate laptop which stores it into a formatted text file using comma separated values.

Figure 3.4: Anzai respiratory belt.

Figure 3.5: PMM spirometer: the air flow going through the nasal cannula is measured and used to estimate the changes of the volume of the lungs.

3.2.1.2 PMM spirometer

The PMM spirometer is a prototype developed by Siemens Medical Systems (Erlangen, Germany, `http://www.medical.siemens.com`). Even though it was still an early prototype, it was included in the evaluation to provide feedback to Siemens for potential improvements. It consists in a nasal cannula (Fig. 3.5) plugged to an electronic box measuring the air flow. The acquisition system uses the air flow to provide the relative progression of the volume of air present in the lungs. These data are recorded in a text file at a frequency of 50 Hz.

Figure 3.6: Thermoprobe from BioVet: setup in a volunteer measurement, with the temperature probe located in front of the nostrils. The image shows in addition the placement of the Anzai belt with infrared markers attached on top of it.

3.2.1.3 BioVet temperature sensor

An early work on PET respiratory gating [36] proposed the use of a fast temperature sensor to measure the temperature of the air flowing in front of the nostrils, and deduce the respiratory phase of the patient out of this information. Such a setup was reproduced using a thermoprobe belonging to the BioVet CT1 by Spin Systems (Brisbane, Australia, `http://www.spinsystems.com.au`), a device initially designed to monitor the body temperature of small rodents (Fig. 3.6). The temperature is provided with a precision of 0.1° and a sampling rate of 1 kHz, storing the data in a comma separated file.

3.2.1.4 ART Stereo Infrared Camera

Tracking of infrared markers for monitoring respiratory motion was previously reported for application during nuclear cardiac examinations [19]. In this work, this approach was evaluated using the smARTrack1 infrared stereovision system from Advanced Realtime Tracking GmbH (Weilheim, Germany, `http://ar-tracking.de`). Passive infrared markers were placed on top of the thorax (Fig. 3.7), and the 3D location of each of the markers with respect to the PET/CT scanner were computed as described in Appendix D. In order to extract a single one-dimensional signal, two possibilities were investigated: using the average of the anterior-posterior coordinate of all markers, or computing principal component analysis (*PCA*, see [232, 134]) on all data from the markers.

(a) (b)

Figure 3.7: ART stereovision system (a) and placement of the markers in the thorax and upper abdomen (b).

3.2.1.5 Sensor-less approach

The PET listmode data records each detected coincidence with a high temporal resolution (1 ms). Therefore, it is theoretically possible to extract a respiratory signal out of the periodical displacement of the detected activity within the field of view. This approach was investigated by sorting the listmode data in short temporal frames of 500 milliseconds and reconstructing each of these frames. A cuboid Volume of Interest (VOI) was manually defined around the structure whose movement had to be investigated; within this volume, the craniocaudal coordinate of the center of the activity distribution (Fig. 3.8) was calculated using the following formula:

$$z_{COM}(t) = \frac{\sum_i z_i \cdot A_i}{\sum_i A_i} \tag{3.1}$$

where t is the time of the short frame, i covers all voxels inside the VOI, z_i is the z-coordinate of the i-th pixel, and A_i is its activity value. $z_{COM}(t)$ delivers the respiration curve as a function over time. To reduce noise in the signal, the Savitzky-Golay filter [254] was used, which performs a local polynomial regression and has the advantage of preserving the local maxima and minima of the signal. Further details on this approach can be found in [49].

3.2.1.6 Measurements with volunteers and patients

The external sensors were evaluated in 10 healthy volunteers. Volunteers lied in supine position and were asked to breathe normally for two minutes, then to simulate some

(a)

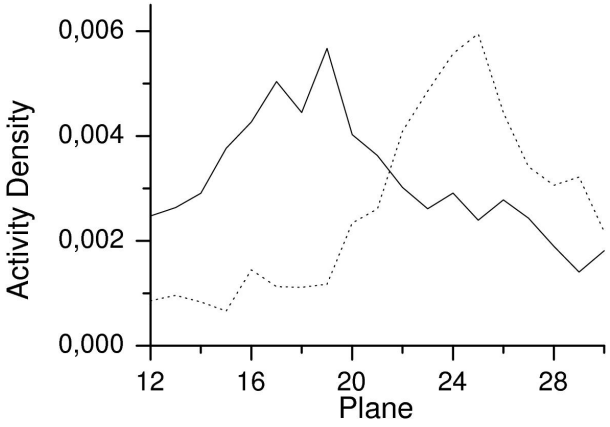

(b)

Figure 3.8: (a) Example showing the definition of a VOI around a lung tumor (red rectangle on the sagittal view). (b) Corresponding activity distribution within the VOI for two different 500 ms frames: one in expiration state (solid) and one in inspiration state (dotted line). The craniocaudal displacement of the tumor with respiration results in a change of the z-coordinate of the center of the activity distribution. Image b reprinted by permission of the Society of Nuclear Medicine from [49].

behavior common to patient acquisitions such as breath-holds, speaking, coughing, or slight repositioning. A total of 3-5 minutes of signal were acquired for each volunteer. The suitability of the sensors to measure a respiratory signal and their robustness to respiratory artifacts were qualitatively evaluated. The PMM prototype was used only in the first 3 acquisitions (as shown in the results, it appeared to be too unreliable for clinical use and was therefore discarded for further testing).

After the measurements with volunteers, only the Anzai and ART sensors appeared suitable for patient measurements. Three patients following a cardiac rest-stress protocol with ^{13}N-NH_3 in the Biograph 16 PET/CT scanner were monitored using both the Anzai and ART systems. The total examination time was 60-90 minutes. The respiratory

signals provided by the Anzai and ART systems were then compared in each of the two acquisitions at rest and stress for each patient.

Moreover, comparison between the Anzai sensor and the sensor-less approach was performed on 10 patients who underwent a routine protocol for oncological staging or restaging. Patients were injected between 320 and 507 MBq of ^{18}F-FDG and, after the routine protocol (∼100 minutes after injection), an additional 10 minutes listmode acquisition was performed. Only patients with a focal lesion in the lung or upper abdominal organs were selected for this comparison. The listmode data were processed as described in the previous subsection.

3.2.2 Results

3.2.2.1 Measurements with volunteers

All evaluated sensors were able to acquire a suitable respiratory signal during normal breathing. The only exception was the PMM spirometer: although most of the time it delivered a correct respiratory signal, as shown in Fig. 3.9, it was always more sensitive to irregular breathing than the other sensors; furthermore, due to its prototype stage, it presented some significant drawbacks, such as unreliable software which sometimes crashed during the acquisition and occasional jittering, resulting in a variable temporal resolution and the impossibility to synchronize it with other sensors. Therefore, the PMM prototype was discarded for further testing.

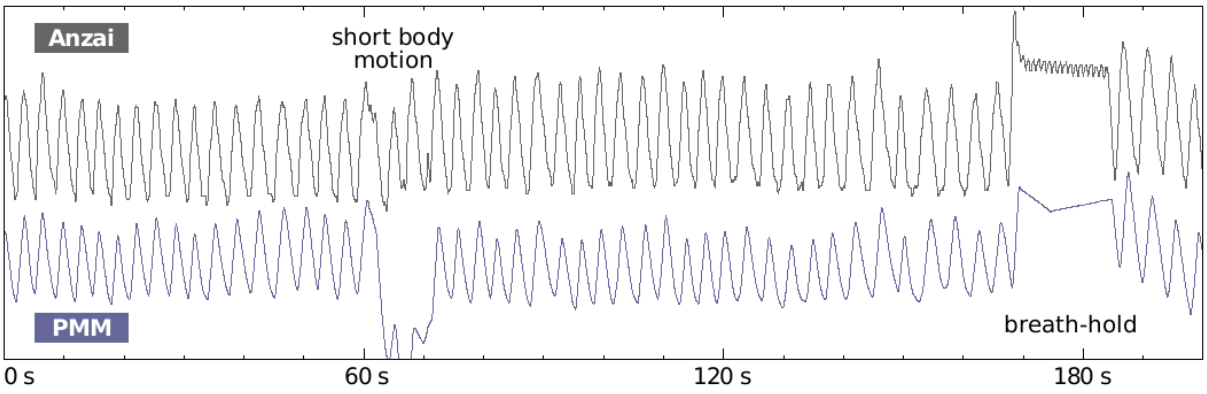

Figure 3.9: Comparison of the respiratory curves acquired with the PMM and Anzai systems. Example where the PMM provides a good respiratory signal, but needs some seconds to automatically recalibrate after abnormal events such as motion and breath-hold.

The BioVet thermoprobe worked more robustly and recovered faster from irregular breathing. Since the temperature of the respired air is higher during expiration, the signal from the BioVet thermoprobe was always inverted as compared to the rest of the sensors (Fig. 3.10). One drawback of the system was that the temperature signal was not synchronized with respiration but it had some variable delay, explained by the time needed between the change in the respiratory phase and the effective detection of the

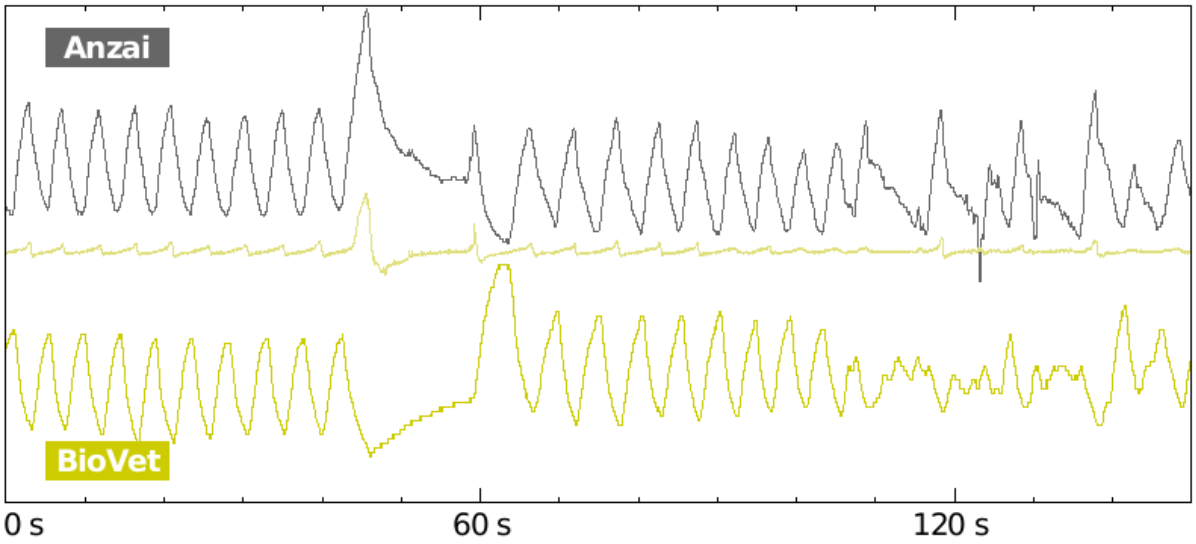

Figure 3.10: Comparison of the respiratory curves aquired with the BioVet and Anzai systems. The small signal in the center corresponds to an additional pressure pad from BioVet used only for temporal synchronization.

change in temperature by the thermoprobe. Variables such as the temperature of the breathed air do potentially influence this delay, making it challenging to find a general correction and an accurate synchronization for the system.

After the tests with volunteers, the Anzai and ART systems appeared as the best suited sensors. Further measurements with patients allowed a better evaluation.

3.2.2.2 Measurements with patients

The respiratory signals provided by Anzai and by ART showed good agreement on all 3 cardiac patients acquired (Fig 3.11), independently on whether the ART signal was computed as an average of the anterior-posterior coordinate or as the first component of the PCA.

The correlation between both signals in the 6 patient acquisitions (3 in rest, 3 under pharmacological stress) was 0.75 ± 0.26 (Fig. 3.12). More importantly, the signals resulted in the same respiratory gate for $85 \pm 14\%$ of the time, with the gates computed using the algorithm detailed in section 3.3. Therefore, similar definition of the gates and similar gated images were obtained using both approaches. One patient acquisition (the first stress acquisition in Fig. 3.12), showed a low correlation factor between both signals, but still resulted in a fair correspondence between the derived gates.

3.2.2.3 Sensor-less approach

In 7 out of 10 patients, the respiratory signal derived from the PET listmode data agreed well with that obtained using the Anzai belt (Fig. 3.13(a)). In 3 of the patients, however, the data-driven signal did not correlate with the breathing cycle (Fig. 3.13(b)). Two of

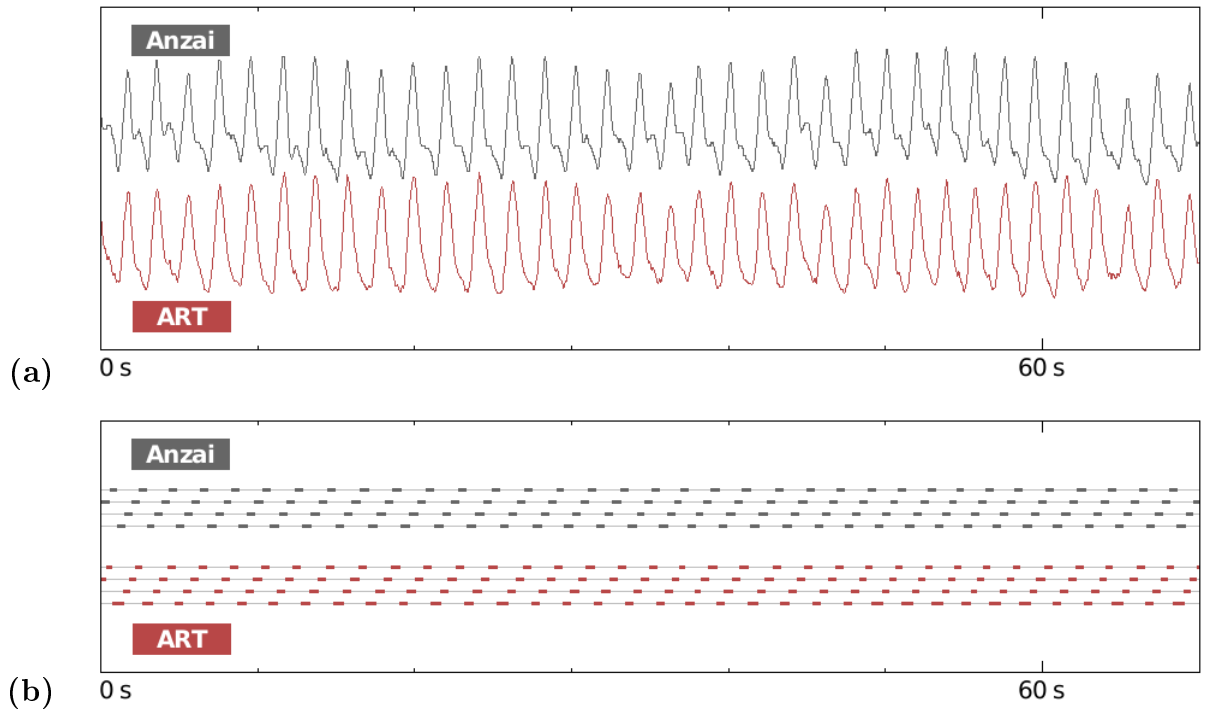

Figure 3.11: Respiration curves acquired during a stress PET scan with Anzai and ART (a), and the resulting respiratory gates (b).

these 3 patients had tumors located in the upper part of the lungs (upper lobe), region which is known to have notably less respiratory motion than the mid and lower part.

3.2.3 Discussion

Although all evaluated sensors were able to provide a correct respiratory signal during normal breathing conditions, the Anzai and ART systems appeared to be the most robust and both equally suitable for respiratory gating in PET. However, other factors have to be considered for the decision on the best sensor to monitor respiration. In particular, two drawbacks have to be mentioned for the ART system:

- It was technically very demanding, requiring advanced post-processing of the data to extract the respiratory signal
- It is rather cumbersome in the examination room, occupying much space. Moreover, one of the patients manifested some discomfort because of the presence of the infrared cameras

By contrast, the ART system presents the advantage that it can measure bulk patient motion in addition to respiratory motion. As an example, fig. 3.14 shows the average patient motion computed using the centroid of all infrared markers during the rest examination, the stress examination, and the complete examination (approx. 60 minutes).

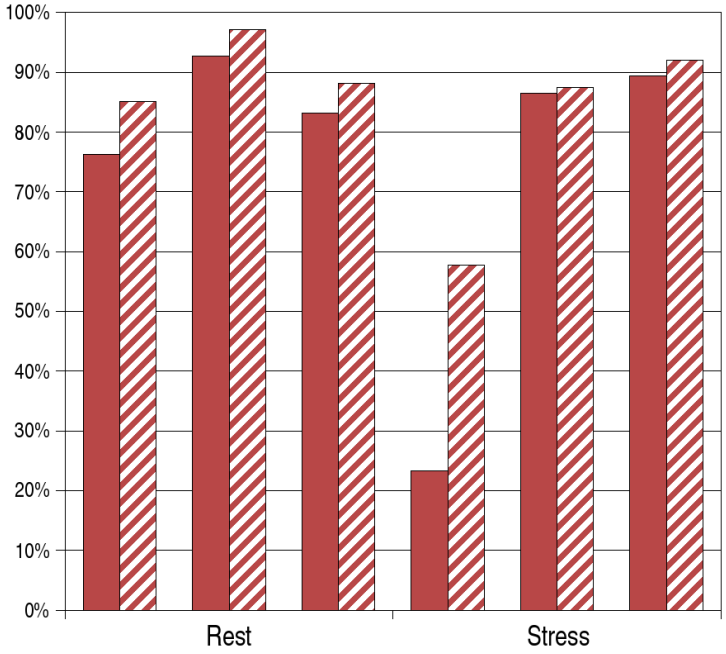

Figure 3.12: Quantitative comparison of the Anzai and ART measurements in the 6 patient acquisitions. Solid bars indicate correlation between the signals, dashed bars indicate percentage of time with matching respiratory gates.

Using this information provided by the stereovision system, more sophisticated motion correction techniques could be potentially implemented [19, 242]. Despite this potential advantage, if no additional motion correction techniques are to be used, the Anzai system appears as the most convenient for use in clinical routine.

The sensor-less approach appears as an attractive alternative. The results with patients indicate an apparent "failure" of the method in 3 tumors which showed no correlation with Anzai and a noisy signal, but these cases could actually correspond to tumors showing nearly no motion with respiration. This possibility is reinforced by the fact that two of the 3 tumors were located in the upper lung, region showing only minor respiratory motion.

The sensor-less approach would bring significant advantages:

- No additional hardware is required during the PET acquisition, improving the clinical workflow and patient comfort.

- The measurement is done on the structure of interest, so that the internal motion is measured and it can be directly used for motion correction approaches [47].

However, some drawbacks should also be noted:

- The method works well for focal isolated lesions, but might fail for more complex structures with high background.

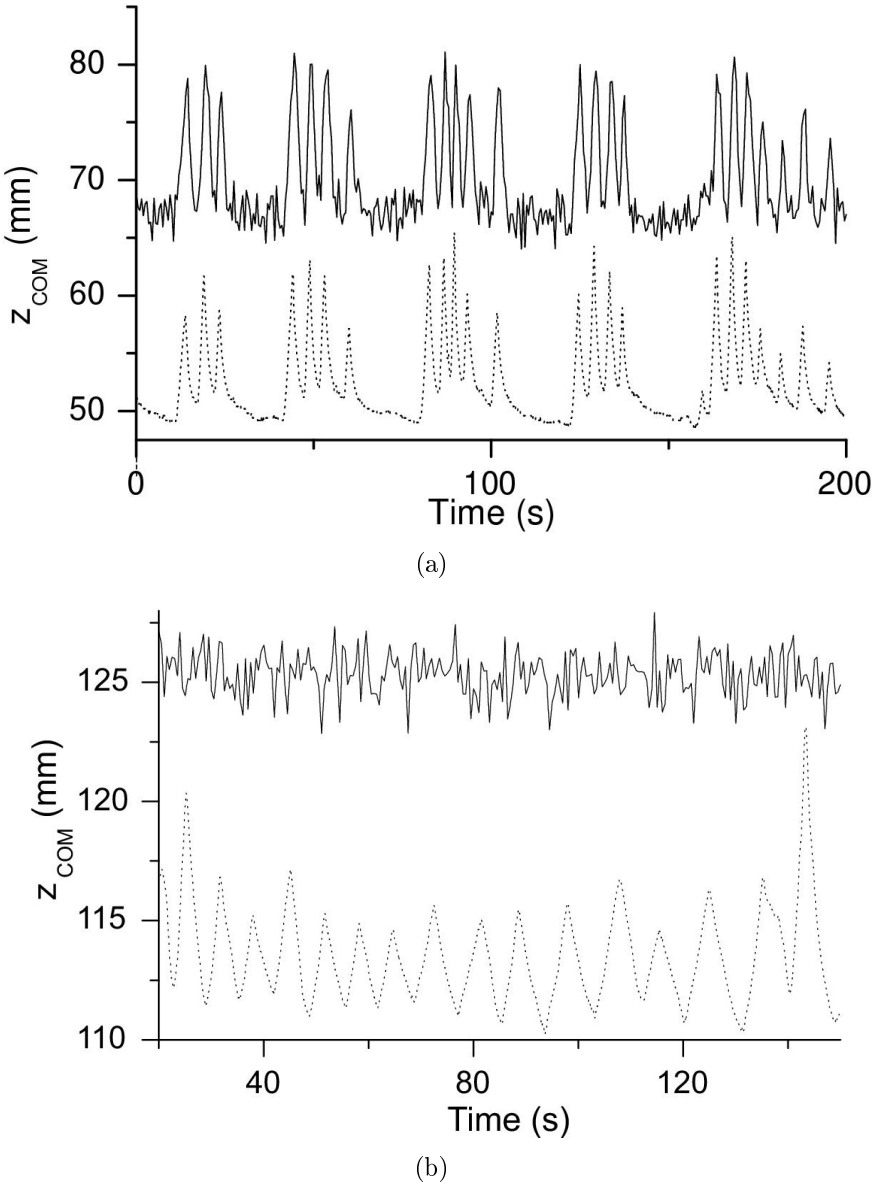

Figure 3.13: Data-driven curves of two patients (solid curves) compared with curve obtained using the Anzai respiratory sensor (dotted line). (a) Patient showing a good agreement. (b) Patient showing no correlation due to a low-quality data-driven signal. Image reprinted by permission of the Society of Nuclear Medicine from [49].

- The operator must manually define the structure of interest for analysis of the respiratory motion, which is inconvenient in clinical routine, and complex in cases with several structures.

- Once the structure of interest is selected, the PET data must be reconstructed in many 500 ms frames, requiring a long processing time. Using a dual-core workstation, a 10 minutes listmode acquisition needed over 17 hours to be processed in

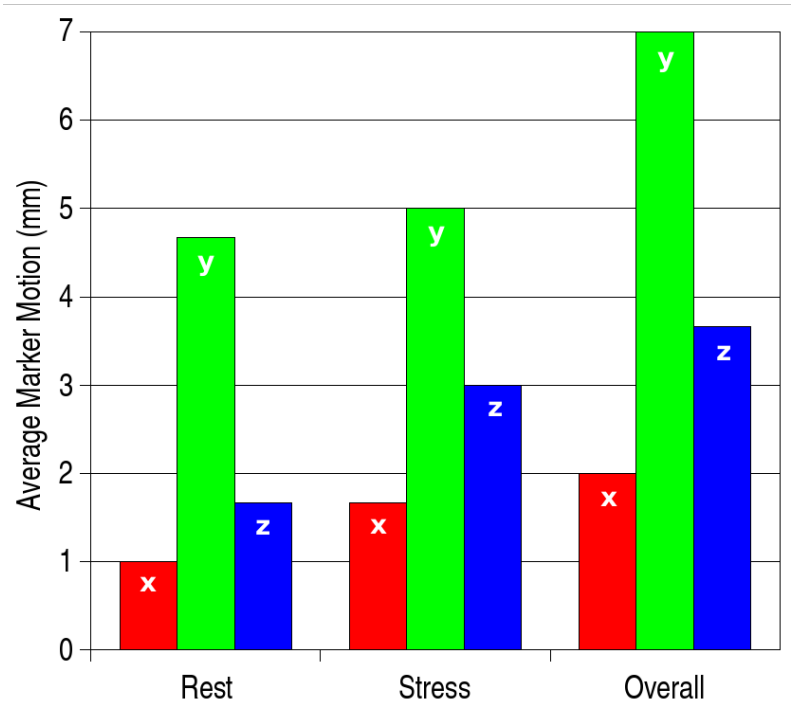

Figure 3.14: Average body motion observed during the rest and stress PET examinations, and during the complete examination. The motion was computed as the maximal distance between the temporally smoothed centroid of the 3D position of all infrared markers.

order to determine the respiratory signal.

In conclusion, the sensor-less approach is attractive but not yet convenient for clinical routine. The method should be further investigated, and ways to accelerate it should be considered. One possibility would be for instance to work directly on the sinogram space rather than reconstructing each frame [261, 45]; this would save a significant amount of computing time.

The Anzai respiratory sensor appears as the best suited method to acquire a respiratory signal for respiratory gating in PET from all the approaches studied. This is the method of choice for further experiments.

3.3 Dual cardiac-respiratory gating

The availability of a suitable respiratory signal is a prerequisite for performing respiratory gating, but it is only a part of the complete solution. An implementation of respiratory gating requires four steps:

1. Acquisition of a respiratory signal
2. Processing the respiratory signal to identify the respiratory gates
3. Histogramming[1] the PET listmode data according to the definition of the respiratory gates
4. Reconstructing the sinograms into respiratory gated images

Besides the basic implementation, additional information can be gained by using more sophisticated appraoches:

- Combination of respiratory and cardiac gating
- Correction of the respiratory motion in order to have one single frozen image containing the data from all respiratory gates after spatial alignment

For cardiac imaging with PET, both cardiac and respiratory motion contribute to the degradation of image quality. Therefore, cardiac PET can only exploit the spatial resolution available in state-of-the-art scanners with techniques to account for both motions simultaneously. A pioneering study indicated the feasibility of such an approach using dual cardiac-respiratory gating in phantoms [151], but technical limitations were reported (real-time definition of the gates, partial loss of data, maximum of 16 gates in total) and the method was not implemented in clinical practice.

In mouse imaging, recent implementation of combined cardiac-respiratory gating in the preclinical microPET II scanner overcame these limitations [313]. This methodological achievement, however, proved unnecessary in this animal model as mice remain in an end-expiratory state for more than 75% of the time. In contrast, the end-expiratory state represents only 25-50% of the human natural breathing cycle and respiratory motion could play a more significant role. Respiratory gating was also proposed for clinical cardiac PET [173], but the combination with ECG gating was not investigated.

In this section, the full implementation of respiratory gating is investigated as well as its combination with cardiac gating.

3.3.1 Methods

3.3.1.1 MRI acquisition for validation of the respiratory triggering

For respiratory gating, it is important that the signal provided by the respiratory sensor provides a surrogate signal for the internal organ motion. Therefore, the correlation

[1] Histogramming is the step necessary to process detected events and sort them into a sinogram containing the number of detected events for each Line of Response

between diaphragmatic excursion measured by real-time MRI and the expansion of the chest measured with an elastic belt was studied in six subjects.

The subjects were examined using a clinical 1.5-Tesla Philips ACS-NT MRI (Philips Medical Systems, Best, The Netherlands) equipped with a five-element cardiac coil and an advanced cardiac software package (R11). Real-time MRI of the lung-liver interface was performed in a coronal plane using a non-ECG triggered single-shot Cartesian steady state free precession (SSFP) sequence. Imaging parameters included: TR/TE 2.5 ms/1.25 ms, flip angle 50°, spatial resolution 3.2×3.2×8.0 mm^3, temporal resolution 182 ms, dynamics 100, and SENSE factor 2 (SENSitivity Encoding). Simultaneous with the MRI real-time measurement, the signal corresponding to the thorax expansion was measured with a small pressure pad placed within a stretchable belt on the upper abdomen. A respiratory signal was derived from the air flow variations and recorded into a log file in the MRI acquisition computer together with timing information necessary to synchronize the signal with the corresponding MRI acquisition. This system is standard equipment with the used MRI scanner.

The diaphragmatic excursion due to respiration has been shown to correlate with the respiratory motion of the heart with a patient-dependent linear factor [65, 305]. Thus, if an adequate trigger to monitor the diaphragm excursion can be measured with the external respiratory sensor, the trigger will equally serve for the respiratory motion of the heart, comparable to what is done for cardiovascular MRI using diaphragmatic navigators. The displacement of the diaphragm was measured from the sequence of images by quantifying the craniocaudal motion of the liver-lung interface within a two-dimensional region of interest (ROI), then compared with the respiratory signal obtained from the elastic belt by means of the linear Pearson correlation coefficient.

3.3.1.2 Patient population

Twelve patients belonging to two different groups were included in the study: six of the patients (age 61±13 years) were referred for diagnosis of coronary artery disease and underwent an ammonia (^{13}N-NH_3) perfusion examination, consisting of an acquisition at rest and one during adenosine-induced stress. The remaining six patients (age 67±6 years) were referred for an ^{18}F-FDG oncology examination and were included in the study owing to their intense cardiac uptake. Using these two groups of patients, the gating approach could be tested with short-lived perfusion radiotracers as well as with long-lived metabolic radiotracers and thus represents tracers typically used in cardiac PET imaging.

3.3.1.3 PET/CT acquisition

All 12 patients were scanned using a Biograph Sensation 16 PET/CT (Siemens Medical Solutions, Erlangen, Germany) for 10 min and the data were stored in listmode format, that is, each detected coincidence event was recorded with millisecond temporal resolution into a file as a 32-bit word representing the couple of crystals detecting the coincidence. The average injected dose was 256±35 MBq of ^{13}N-NH_3 for the rest acquisition and 295±61 MBq for the stress acquisition in the first patient group, and 400±62 MBq of ^{18}F-FDG in the second patient group. The PET acquisition was started synchronized

with the tracer injection for the ammonia patients and 60 min after injection for the FDG patients.

In parallel to the listmode acquisition, the ECG provided with the PET/CT scanner recorded the exact timing of the R waves in a binary log file on the PET acquisition computer. The respiratory signal of the patient was measured with the Anzai AZ-733V system, as described in section 3.2.1.1.

In order to achieve accurate temporal synchronization between the listmode and ECG acquired by the PET system and the respiratory signal acquired by the separate laptop, the PET terminal was programmed to send an output signal on the parallel port when the listmode acquisition started. This signal was then transferred via a customized parallel-serial converter to the Anzai Wave Deck and stored together with the respiratory signal.

For attenuation correction, a low-dose CT (120 keV, 20 mAs) was performed during shallow breathing. In order to reduce attenuation artifacts due to the misregistration of the PET and CT datasets [185], the alignment of the heart between the PET and CT volumes was visually controlled immediately after the PET acquisition, and in those patients presenting a misalignment, an additional ultra-low-dose CT (80 keV, 13 mAs) was acquired.

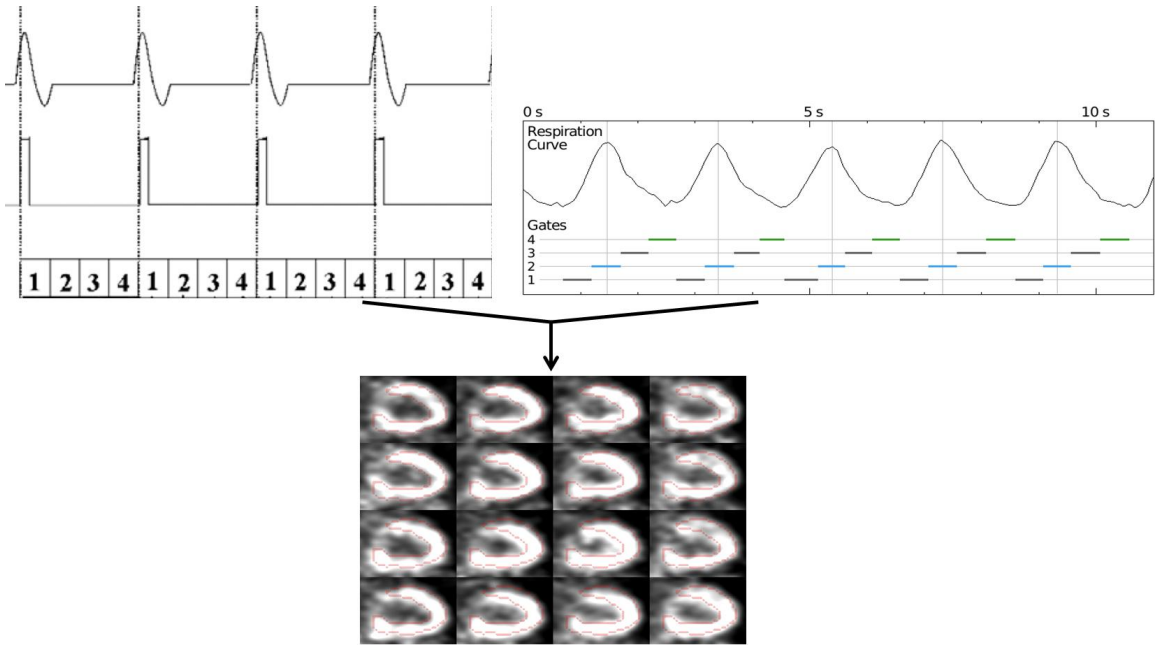

Figure 3.15: Combination of the m gates defined by the ECG (left) and by the n respiratory gates (right) results in m x n gates showing neither cardiac nor respiratory motion. Correspondingly, the detected events are sorted throughout all gates, decreasing the number of events for each gate.

All data required for the dual gated reconstruction (listmode file, ECG, respiratory signal and CT-based attenuation map) were transferred through the network to another computer for offline processing, so that the PET/CT scanner could be further used. Therefore, the dual gated acquisition had no effect on the usual clinical workflow other than

the addition of the elastic belt to measure the respiratory signal. The events contained in the listmode file were then sorted into the corresponding gates, taking into account both the cardiac and respiratory phase corresponding to the detection time of the event (Fig. 3.15).

Finally, the PET images were reconstructed using the attenuation-weighted ordered subsets expectation maximization (AW-OSEM) algorithm with four iterations and eight subsets and an in-plane zoom of 2.2 to a matrix of 128×128×47 voxels, each voxel with a size of 2.34×2.34×3.37 mm^3.

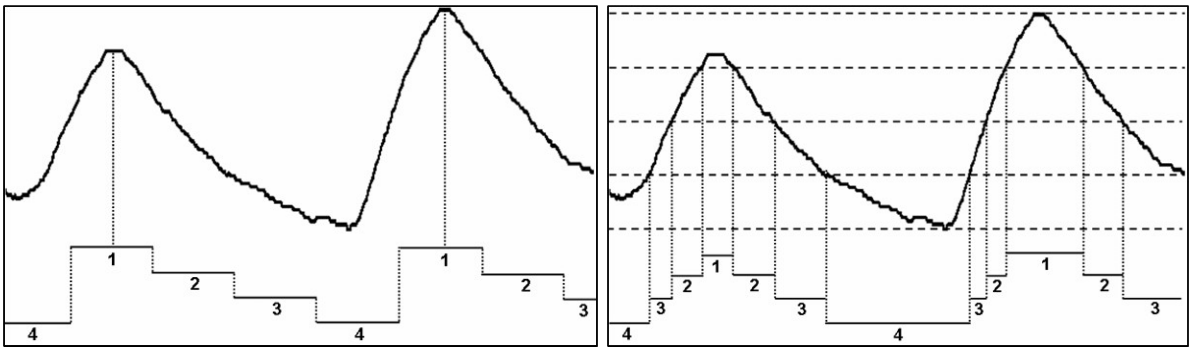

(a) (b)

Figure 3.16: Definition of the respiratory gates using two different algorithms: (a) based on equitemporal division of the respiratory cycles. (b) Based on the intensity division of the signal range. Image reprinted with kind permission from Springer Science+Business Media from [186].

3.3.1.4 Definition of the gates

The cardiac and respiratory gates were defined retrospectively using the Interactive Data Language (IDL, ITT Visual Information Solutions, Boulder, CO). The definition of the cardiac gates was achieved by dividing the interval between two consecutive R-waves into n frames of the same duration, n being the desired number of gates. The computation of the respiratory gates out of the respiratory signal required some additional signal processing. The noise in the acquired signal was reduced by means of a bandpass filter (0.05Hz - 0.6Hz) and a gating algorithm comparable to the one for cardiac gating was applied: the maximum inspiratory peaks were identified as those having first derivative equal to zero and a negative second derivative. The interval between two consecutive inspiration peaks was divided into m frames of the same duration, m being the number of respiratory gates (Fig 3.16(a)). As compared to an intensity based gating algorithm (Fig. 3.16(b)), which was also tested but discarded for this study, this gating approach presents two significant advantages: it delivers equitemporal gates, which have therefore similar count statistics, and it is robust to changes in the baseline of the signal, as will be discussed later in this chapter. However, an intensity based gating algorithm might be able to better capture the full amplitude of the motion, as reported in [66].

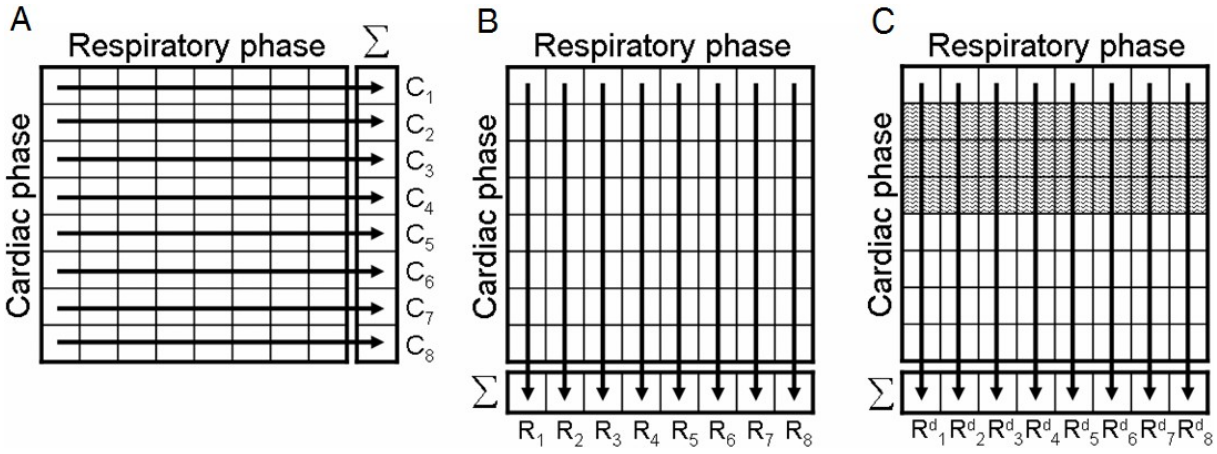

Figure 3.17: Different combinations to sort a dual gating matrix with eight cardiac and eight respiratory gates. (a) Cardiac gated series. (b) Respiratory gated series. (c) Respiratory gated series after exclusion of the systolic phase. Image reproduced with kind permission from Springer Science+Business Media from [186].

Thus, a matrix of $n \times m$ gates was obtained, with one dimension corresponding to the cardiac beating motion and the other to the respiratory motion (Fig 3.17). Finally, these gates could be combined flexibly during the sorting process. For example, if 8 cardiac gates were defined, the user could define a diastolic inspiratory image consisting in the cardiac gates 1 and 5-8 combined with gate 1 from the respiratory dimension (Fig. 3.17C).

3.3.1.5 Motion analysis

In order to quantify exclusively the respiratory motion of the heart, the systolic phase of the heart was discarded as indicated in Fig. 3.17C. The images corresponding to maximum inspiration and maximum expiration were registered using the deformable registration algorithm described in the following paragraph and the resulting motion was evaluated for each of the myocardial walls. The analysis was performed using both four and eight respiratory gates.

The used deformable registration algorithm was developed by Darko Zikic [322]. It is an intensity-based and fully automatic method employing a variational method for deformable registration and yielding a dense displacement field. It utilizes the sum of squared differences as a dissimilarity measure and a diffusion regularization term to enforce smooth results [204]. The resulting non-linear elliptic partial differential equation (PDE) was solved by a modified fixed-point iteration where a linear elliptic PDE arose in every iteration. The linear PDE was solved numerically by applying an efficient multigrid algorithm [41]. In order to improve the computation time and account for large displacements, a multi-resolution pyramid was employed [7]. The pyramid was computed by reducing the resolution by a factor of 2 along each dimension from level to level by applying a discrete approximation to the Gaussian filter. On every level of the pyramid, the deformable registration was performed using the result of the next coarser level as initial guess. The registration algorithm was implemented in C++ and the runtime for

a pair of PET volumes of size 128x128x47 was 6-7 seconds on a Pentium M 1.8 GHz computer.

3.3.2 Results

3.3.2.1 Validity of the respiratory trigger

The correlation between the image derived excursion of the diaphragm extracted from the real-time MRI and the signal from the stretchable belt was excellent (mean R^2 of 0.91, range 0.88 – 0.94), indicating the ability of the belt to provide a suitable respiratory trigger signal (Fig. 3.18).

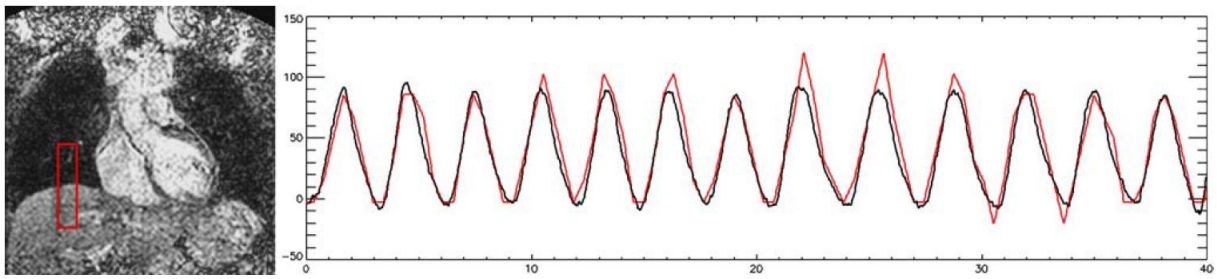

Figure 3.18: MRI coronal image (left) showing the definition of the ROI at the liver-lung interface and comparison of both signals: red signal obtained from the diaphragmatic excursion in the ROI, black signal obtained from the stretchable belt. The amplitude ranges of both signals were adjusted to similar values in order to facilitate visual comparison. Image reproduced with kind permission from Springer Science+Business Media from [186].

3.3.2.2 Variability of the respiratory signals

The respiratory patterns from the PET patients showed a very large interindividual variability (Fig. 3.19) for both the ammonia and FDG patients. This variability had not been observed during previous measurements performed on young healthy volunteers, indicating that several patients could have respiratory abnormalities probably related to their health condition. Moreover, small irregularities in the respiratory signals were common, including very deep breathings, occasional speaking or coughing, and sudden or progressive changes in the baseline.

The employed gating algorithm was robust to the different patterns and irregularities observed in the signals; in particular, changes of the baseline during the examination (Fig. 3.19B) were handled efficiently by the temporal division of the breathing cycles, whereas the approach using intensity division failed to account for these changes.

3.3.2.3 Respiratory motion of the heart

The respiratory motion of the heart is observable in Fig. 3.20 on both the PET images and the activity profiles. The activity profiles show that the myocardial wall in the static

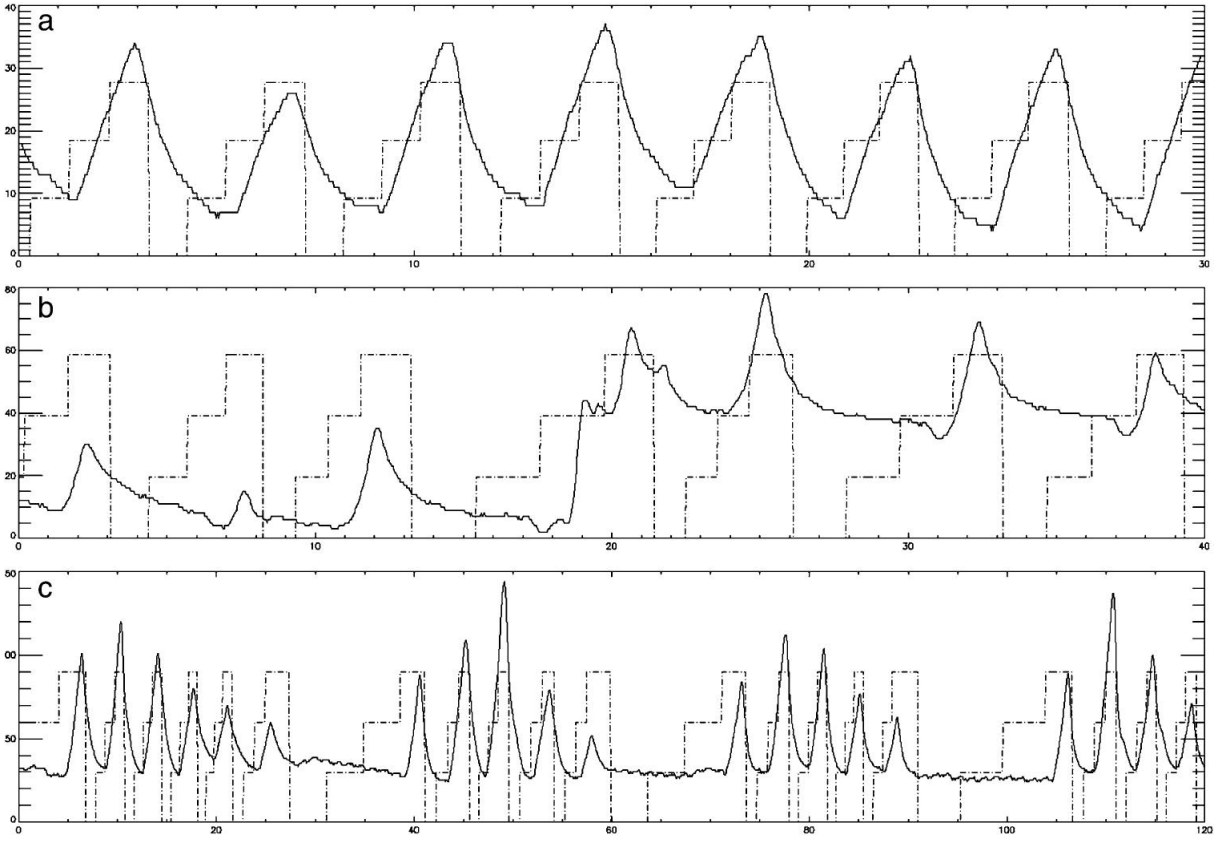

Figure 3.19: Fragments of three respiratory signals acquired from patients (solid curves) and the corresponding respiratory gates (m=4) as defined by the applied algorithm. Half of the patients had a respiratory pattern fairly similar to (a), but the other half had rather unusual patterns, two of which are presented in (b) and (c). Signal (b) also shows a sudden change of the baseline, probably introduced by a slight repositioning of the patient. Image reprinted with kind permission from Springer Science+Business Media from [186].

image appears thicker and with reduced maximum activity as a result of the motional blurring, indicating the potential improvement of spatial resolution that can be achieved by means of respiratory and dual gating.

Results of the non-rigid registration are presented in Fig. 3.21, showing that the heart followed mainly a craniocaudal displacement with respiration. The average respiratory motion of each myocardial wall for all examinations is shown in Table. 3.1. The average motion of the entire heart for each group of patients was 4.9±1.3 mm for the ammonia rest acquisitions, 5.0±2.7 mm for the ammonia stress acquisitions and 4.6±1.3 mm for the FDG acquisitions. The motion for all 18 examinations averaged 4.8±1.8 mm. Changing the number of respiratory gates used from four to eight produced a significant increase in the motion extent (3.92 vs. 4.82 mm average motion, $p<0.001$) as a consequence of the better temporal resolution of the gates.

Combined with the craniocaudal displacement, a deformation of the heart during respiration was observed, with the inferior wall presenting a significantly larger motion

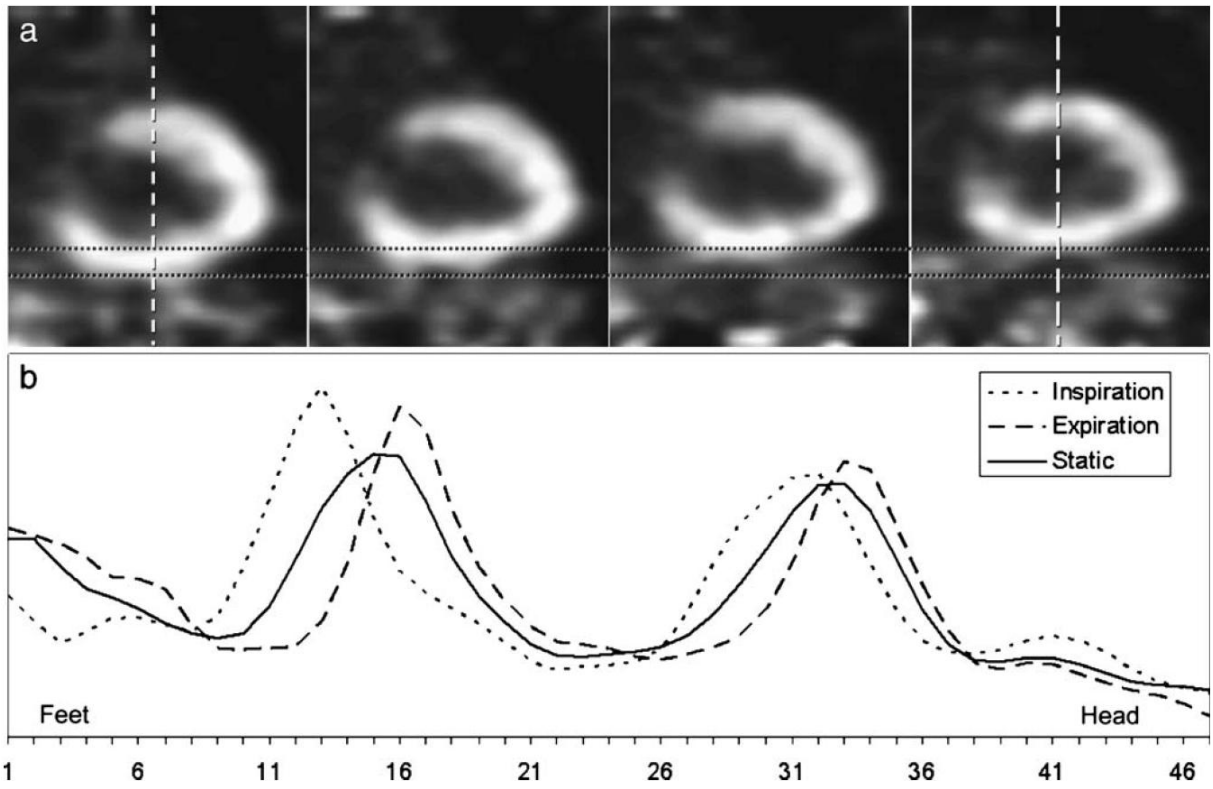

Figure 3.20: Data from an examination with 10-mm feet-head respiratory motion at the inferior segment of the heart. (a) Coronal view of the respiratory gated images in the diastolic phase. (b) Craniocaudal activity profile through the left ventricle showing the displacement of the myocardial walls with respiration. Image reproduced with kind permission from Springer Science+Business Media from [186].

than the anterior wall (5.84 vs. 4.16 mm average motion, $p<0.001$).

3.3.3 Discussion

The reported results showed the feasibility of acquiring dual cardiac-respiratory gated PET data using a clinical PET/CT scanner. The quantification using the deformation field resulting from the non-rigid registration resulted in an average respiratory motion of the heart of 4.8 mm, which is comparable to the spatial resolution of current clinical PET scanners. The motion showed significant local differences: the inferior wall of the heart moved 5.8 mm on average, 40% more than the anterior wall, indicating that the heart is not only moving craniocaudally with respiration, but also deforming.

The observed average respiratory motion of the heart (4.8 mm) is a rather low value as compared with other data in the literature. This is a consequence of important differences in the methodology: one essential factor is how breathing is performed. Some MRI studies have reported respiratory motion measured comparing breath-holding at inspiration and expiration [197], motion which is known to be higher than that observed during free breathing, as in the case of the present study. A second difference is the population

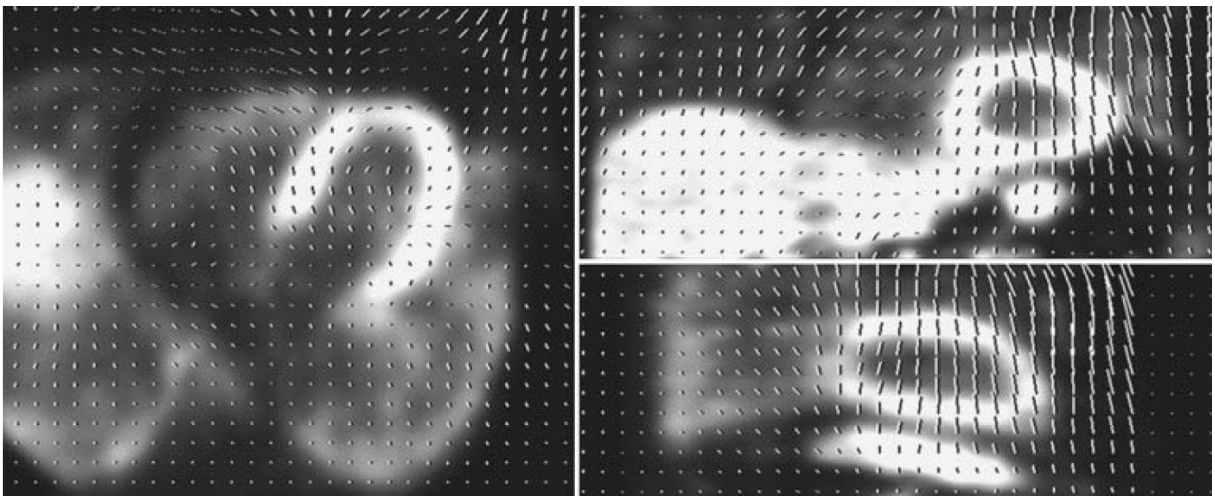

Figure 3.21: Displacement field resulting from the non-rigid image registration between inspiratory and expiratory phases. The displacement vectors are plotted on top of the image in the axial, coronal and sagittal views. Image reproduced with kind permission from Springer Science+Business Media from [186].

examined. Reports from MRI studies are frequently based on young healthy volunteers, whereas the population included in this study consisted of CAD and cancer patients with an average age of 64 years; clear differences between motion in volunteers and patients can be seen in [197], where young volunteers showed an average craniocaudal motion of 16 mm and patients (age 56±9 years) a motion of 8 mm. Finally, in this study the average motion for the entire heart is reported, but it is also observed that this motion is not homogeneous and, in particular, the inferior wall shows a higher motion (5.8 mm); for comparison, a recent study including eight young healthy subjects showed an average motion at the infero-apical extreme of the heart of 6.7 mm [36].

A study which compares well in the patient population (65±11 years) and also uses free-breathing acquisition is that by Shechter et al. [273]; during free-breathing coronary

		Myocardial segment				
		Anterior	Septal	Inferior	Lateral	Apex
4 gates	CC motion	3.2±1.6	3.8±1.6	4.4±2.0	3.7±2.1	3.1±1.5
	3D motion	3.4±1.6	4.1±1.5	4.7±2.0	4.0±2.1	3.4±1.6
8 gates	CC motion	4.0±1.5	4.5±1.8	5.5±2.2	4.6±2.1	3.8±1.8
	3D motion	4.2±1.5	4.9±1.8	5.8±2.2	4.9±2.2	4.3±1.7

Table 3.1: Average respiratory motion (mean ± standard deviation) in millimeters for the 18 PET examinations. CC indicates motion only in the craniocaudal direction, whereas the 3D motion refers to the Euclidean distance taking into account also motion in the anterior-posterior and lateral directions. Table reproduced with kind permission from Springer Science+Business Media from [186].

angiograms, the heart was reported to have an average craniocaudal motion of 4.9±1.9 mm, in agreement with the measurements reported here.

Dual gating suffers from the problem of low statistics: the gain achieved by the reduction of motion blurring involves a significant loss of count statistics. If the same histogramming approach as for single gating is used, image quality is significantly reduced: for instance, when using eight cardiac gates and eight respiratory gates, the total counts are divided by 64. The reduction of count statistics derived from dual gating can potentially be overcome by spatial registration. That is, all respiratory gates can be registered to the expiratory gate and summed into one respiratory-free image with high counts. Although rigid registration has been proposed for this purpose [174], the results from this study indicate that the motion is not uniform across the left ventricle, a finding which is supported by previous studies [197, 150, 182]. Thus, a non-rigid correction will provide greater accuracy. However, the PET gated images are noisy and any error in the registration could result in biased summed PET images and eventually diagnostic errors.

As an alternative to image registration, the selection of only those parts of the cardiac and respiratory cycles where minimal motion is present provides a suitable approach. Respiratory patterns suggest that end-expiration may be the most suitable part of the respiratory cycle as it has the longest period without motion. Thus, approximately 25-50% of the data could be considered to have nearly no respiratory motion. The same applies for ventricular diastole, which represents more than 60% of the cardiac cycle in most patients, depending on the degree of ventricular dysfunction. By combining both, 15-30% of the total acquired data could be considered to have virtually no motion, cardiac or respiratory, so that a motion-free image of the heart could be obtained without the use of any registration technique.

A limitation of this study is that only the PET acquisition was gated, and one single CT was used for attenuation correction of all PET gates. This approach inherently involves some misregistration between the PET and CT datasets and could potentially introduce artifacts due to a biased attenuation correction [185, 224], as will be discussed in chapter 4. Although the possibility of acquiring respiratory gated or respiratory averaged CT for attenuation correction has been proposed [226], its clinical benefit has not yet been established, and it was decided to perform a single CT in order to avoid the substantial additional radiation for the patients.

The incremental value of dual gating and the associated gain in effective spatial resolution is still undetermined and should be further investigated. The effects observed in this study do not seem to justify its use for routine perfusion and metabolic examinations in this clinical setting. However, dual gated acquisitions are likely going to gain importance with the continuous improvement of PET spatial resolution, and it might be speculated that the correction for respiratory motion could be standard in future cardiac applications as it is in cardiac MRI. Furthermore, such an approach can be a determinant point for successful hot spot imaging of vulnerable coronary plaques [247, 69], where the imaged target might be smaller than the combined cardiac-respiratory motion itself.

3.4 Conclusion

During the course of this PhD, substantial progress was done in the area of respiratory gating. At the start of this work, respiratory gating was not commercially available in PET/CT tomographs; available hardware was used and the necessary software was developed in order to be able to perform respiratory gating with the clinical PET/CT scanner present at this clinic.

Other research institutions followed parallel paths, and the potential impact of respiratory gating for managing PET patients was soon demonstrated. Still, it was not clear how to implement it at best, especially regarding the method to acquire a respiratory signal. The results of this work led to the conclusion that the use of an elastic belt with a pressure sensor is optimally suited for PET acquisitions, performing reliably and with minimal impact on the clinical workflow.

An additional finding regards the difficulty of detecting and defining the respiratory gates for the patient population undergoing PET examinations. The measurements performed on healthy volunteers showed always regular respiratory signals, following a well-defined pattern, and this was also the case for nearly half of the patients. But it was also observed that the respiration for many of the patients was extremely irregular, with variations probably related to their health condition, resulting in additional challenges for the detection and definition of the respiratory gates.

Finally, this work explored the combination of respiratory and cardiac gating in a clinical setup and showed that this combination could be achieved successfully. However, it could not be demonstrated that dual gating provides a clinical gain with the PET scanner employed for routine clinical applications. New developing applications such as hot spot imaging may pose higher requirements regarding the quality of the acquired images, better exploiting the increasing spatial resolution of state-of-the-art scanners and needing motion-correction techniques such as dual gating in order to achieve its full potential.

CHAPTER 4

Cardiac PET/CT misregistration

4.1 Introduction

Since the introduction of hybrid PET/CT tomographs, CT has replaced external rotating sources (e.g. ^{68}Ge or ^{137}Cs) for the measurement of the transmission scan used for attenuation correction. The use of CT has several advantages:

- The CT scan is significantly faster, improving patient comfort and throughput
- It contains much lower statistical noise
- It can be acquired post-injection without bias from the injected tracer
- It eliminates the need for periodical replacement of the external rotating sources
- It provides anatomical information which complements the functional data provided by PET

CT has been validated for attenuation correction of cardiac images even when low tube currents are used [154, 278]. However, CT-based attenuation correction potentially suffers from a non simultaneous acquisition as well as differences in scanning time between PET and CT: the latter is acquired in a few seconds, covering only a fraction of the respiratory cycle, whereas PET shows an image averaged over several respiratory cycles.

These differences result in PET-CT misregistration in the thorax and upper abdomen. Since the CT scan is used for attenuation correction of the PET data, artifacts can potentially appear in the PET image due to this misregistration. For oncological imaging, such artifacts have been previously reported [223, 224, 99, 26], and they can eventually compromise the correct localization of lesions in the thoracic area (Fig. 4.1).

By the start of this work, and despite the fact that the heart is closely coupled with the diaphragm and thus shows a significant respiratory motion [197], no studies had reported

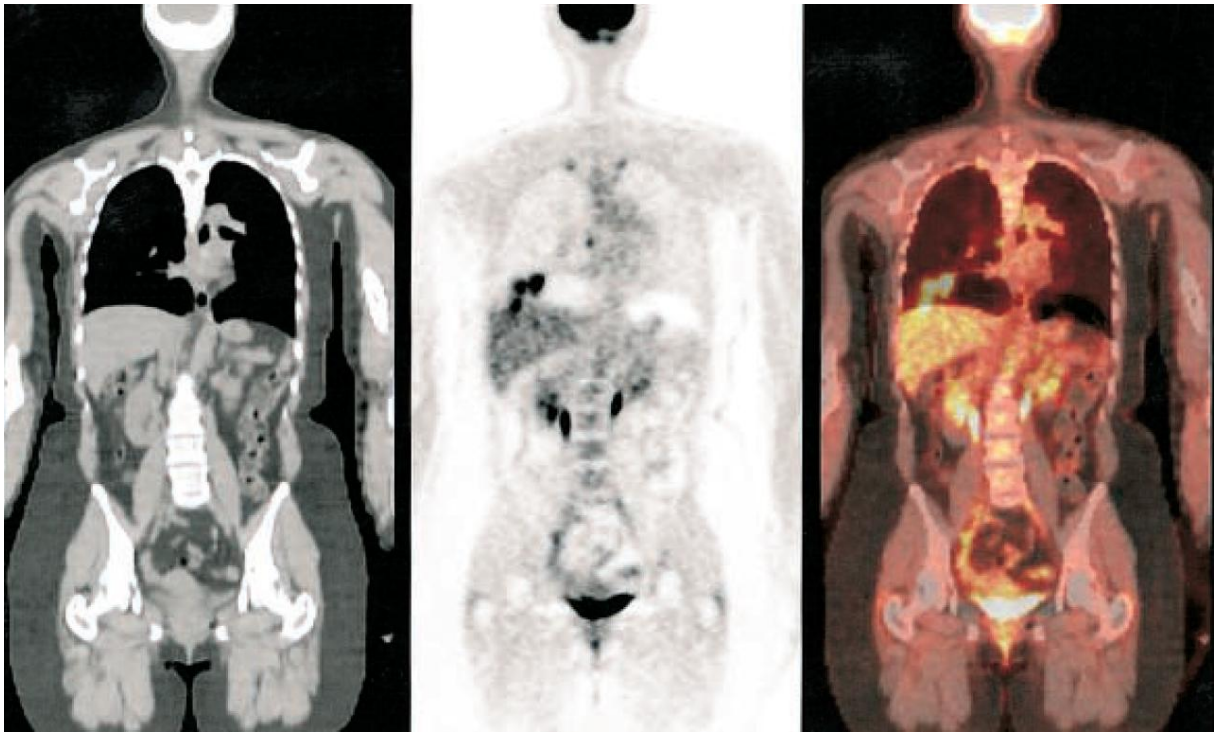

Figure 4.1: Coronal CT (left), PET (middle) and PET/CT (right) images of a 39 year old woman with breast cancer and CT-proven liver lesions but no lung lesion. Lesions are mislocalized to right lung base on fused PET/CT. Image reprinted and adapted by permission of the Society of Nuclear Medicine from [223].

on the effects of this misregistration for cardiac PET/CT. By contrast, the problem of emission-transmission misalignment in cardiac imaging –due to pharmacological stress, breathing or other patient motion– had been previously investigated using PET with rotating sources [176, 196], SPECT [193] and SPECT/CT [88].

Despite the lack of reports on this issue in combined PET/CT scanners, several perfusion studies acquired with the PET/CT at this clinic showed moderate to severe PET-CT misregistration, and apparent perfusion defects were observed in spatial coincidence with the misregistered segments (Fig. 4.2). Therefore, it was investigated whether these defects could be artifactual and originated from a wrong attenuation correction in presence of emission-transmission misregistration. The severe difference between the attenuation factor of the lung and that from the heart tissue was assumed to be the underlying reason for reduced uptake in the misregistered cardiac segments.

The purpose of this study was to understand the effects of PET-CT misalignment on the measured tracer distribution and to investigate possible solutions such as image registration and an automatic algorithm based on the adjustment of the cardiac outline in the attenuation map.

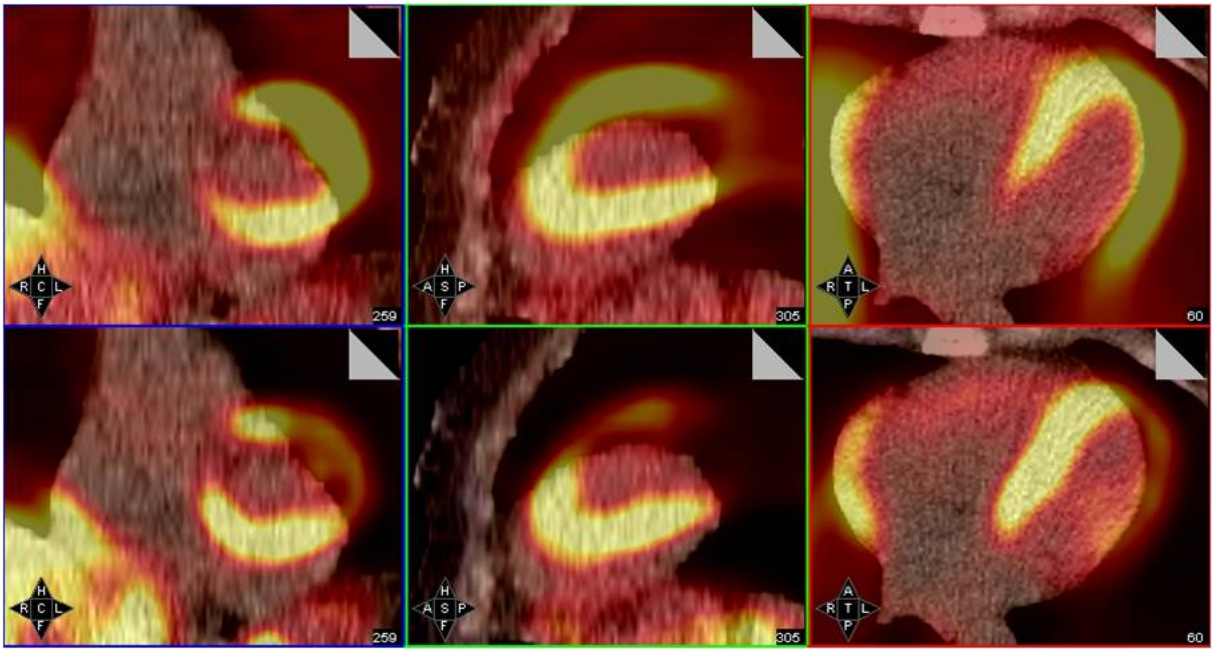

Figure 4.2: Fused PET/CT images of a myocardial perfusion ^{13}N-NH_3 study with a severe misregistration. On the top, the PET images were reconstructed without performing attenuation correction (coronal, sagittal and transaxial planes). On the bottom, the PET images were reconstructed with CT-based attenuation correction. There is an evident decrease of observed uptake in the misaligned regions produced by the attenuation correction.

4.2 Methods

4.2.1 Patient population

A total of 28 consecutive patients (20 men and 8 women, age 63±12y) referred for evaluation of coronary artery disease were enrolled in this study. All patients underwent a PET/CT rest/stress ^{13}N-NH_3 perfusion study.

4.2.2 Protocol

The patients were examined using a Siemens Biograph 16 PET/CT (described in appendix C). Transmission data for the thorax were acquired with a low-dose CT scan (120kV, 26mAs) performed in shallow breathing. After that, patients received a 300 to 500 MBq injection of ^{13}N-NH_3 synchronized with the start of the PET acquisition. The PET rest examination lasted for 10 min and 30 min later pharmacological induced stress was achieved by a 6-min infusion of adenosine at 0.14 mg/min/kg of body weight. Patients received a second 300 to 500 MBq ^{13}N-NH_3 injection and the PET stress examination was acquired for 10 min. Image data from 5 min post-injection to 10 min post-injection was summed and used for further analysis. Both CT and PET were acquired in the arms down position to improve patient comfort and reduce the probability of motion.

4.2.3 Data analysis

The acquired PET data were reconstructed using the ordered-subsets expected maximization (OSEM) algorithm [125] with 4 subsets and 8 iterations. The attenuation map, image containing the attenuation factor for each voxel which is used for AC, was obtained from the CT image after the necessary transformations including scaling from X-rays to attenuation factors at 511 keV and smoothing to match PET spatial resolution [149].

In order to investigate whether emission-transmission misregistration was at the origin of perfusion defects, the CT data were realigned to the PET data and the PET reconstruction was repeated with the aligned CT-based attenuation map. For this purpose, a registration program was developed using IDL (Interactive Data Language, RSI Inc., Boulder, CO, USA), allowing three different possibilities to realign the PET and CT examinations: manual registration, automatic registration, and an *emission driven* in-house developed correction method to modify the heart outline based on the PET data (Fig. 4.3). Details on each of the realignment techniques are provided in the following sections.

For each PET examination acquired, all three realignment techniques were separately applied. PET rest and stress scans were processed independently, as motion could potentially happen in only one of both scans. Using each of the realigned attenuation maps, the PET raw data were reconstructed again. The tracer uptake was quantified before and after realignment by spatially sampling the left ventricle and projecting the measured activity on a polar map basis [218]. The polar map was then divided in 17 segments according to the AHA17 model [54] as shown in Fig. 4.4, normalized and compared to a

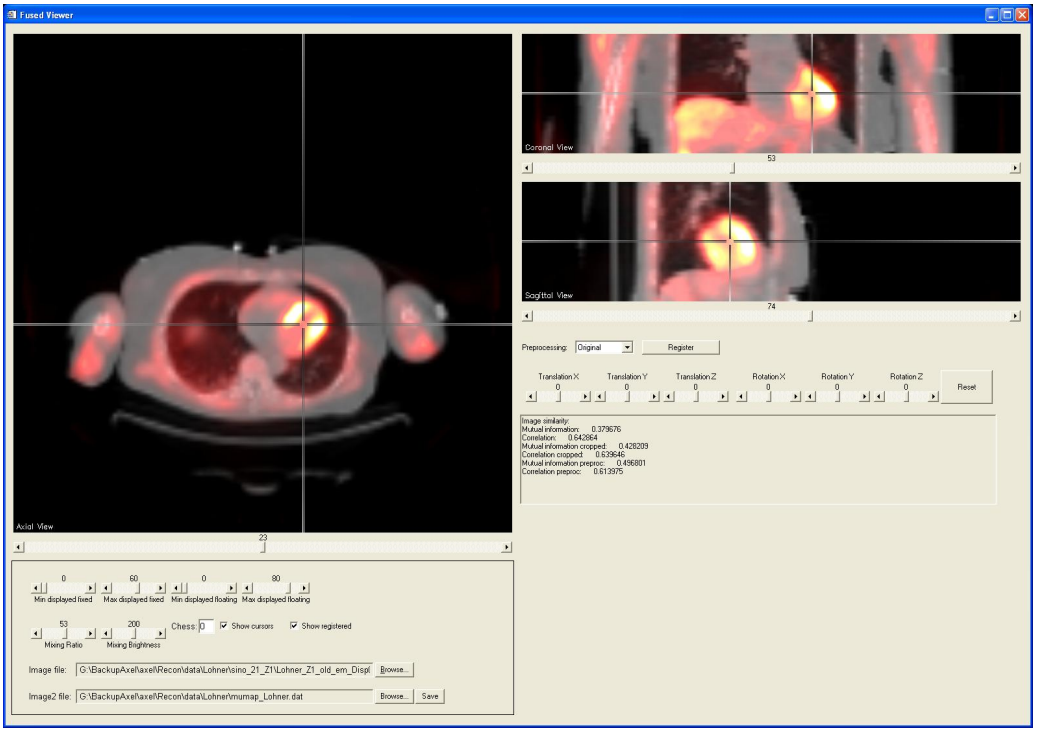

Figure 4.3: Screenshot of the IDL program to perform the PET-CT image registration, showing the fused images in transaxial, coronal and sagittal views.

normal ^{13}N-NH_3 perfusion map. Segments where the uptake differed by more than 2.5 standard deviations were considered as perfusion defects.

Furthermore, 7 patient PET/CT scans which were evaluated as being originally aligned were used to simulate the effects of misregistration in the different spatial directions. For this purpose, the CT was shifted by 1 to 4 voxels in each spatial direction (the voxel size being 5.1 x 5.1 x 3.4 mm^3), the PET image was reconstructed again using each of the shifted attenuation maps, and the tracer uptake in each segment of the myocardium was quantified.

4.2.3.1 PET-CT Registration

In both manual and automatic PET-CT registration, motion between the PET and CT scans was approximated as being a rigid translation, with no rotational component. Manual registration was done by interactively moving the CT image over the PET image and assessing the overlap in fused PET/CT images from coronal, sagittal and transaxial views. Careful manual registration required 30 to 60 seconds for a PET-CT dataset.

The principle of automatic image registration is to find the spatial transformation between both images providing the highest value for the similarity measure, and it is commonly achieved through the maximization of the similarity measure using an optimization algorithm. However, the most simple and robust algorithm, although the one which is by far the most computationally expensive, is to do an exhaustive search throughout all the

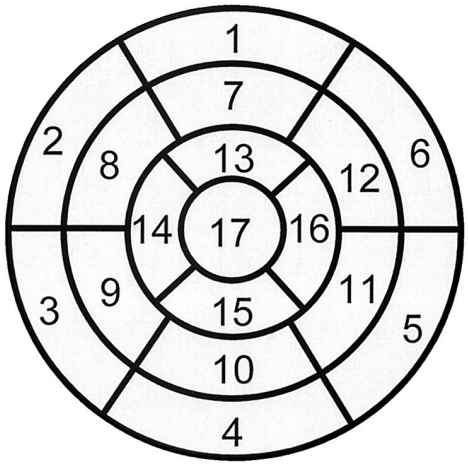

1. basal anterior
2. basal anteroseptal
3. basal inferoseptal
4. basal inferior
5. basal inferolateral
6. basal anterolateral
7. mid anterior
8. mid anteroseptal
9. mid inferoseptal
10. mid inferior
11. mid inferolateral
12. mid anterolateral
13. apical anterior
14. apical septal
15. apical inferior
16. apical lateral
17. apex

Figure 4.4: Polar map display showing the division of the left ventricle in 17 myocardial segments together with their recommended nomenclature. Image reproduced from [54] with kind permission from Wolters Kluwer Health.

transformation parameters, checking all possible spatial transformations to find the one providing the highest similarity measure. The advantage of such an approach is that the algorithm will not stop in the presence of local maxima, so that the absolute maximum of the function is going to be found in all cases. As the transformation was approximated to be purely translational, and with the additional assumption that the displacement in each direction could be no larger than 3 cm, registration using an exhaustive search required a runtime of approximately 20 seconds for each PET/CT dataset (Pentium M 1.8 GHz, 1 GB RAM). Mutual information was used as the metric to evaluate each pose [301, 179].

4.2.3.2 Emission Driven Correction

The emission driven correction was developed based on the following assumption: if there is tracer uptake corresponding to the left ventricle (LV) in the PET image, the corresponding voxel in the CT should contain cardiac tissue as well. However, in case there is an inconsistency and the voxel contains lung tissue and therefore nearly no attenuation, the value of the voxel in the CT is modified to match that of cardiac tissue.

As this operation is only to be applied in the LV, a fully automatic segmentation of the LV from the PET scan was required. The LV has always high ^{13}N-NH_3 uptake except for the infarcted or hibernated regions, but a simple histogram thresholding for the whole volume would have failed as other organs in the same bed position, e.g. the liver, may show higher uptake (Fig. 4.5(A)). The assumption that the heart is located on the left side of the patient allowed discarding half of the image. Furthermore, an a

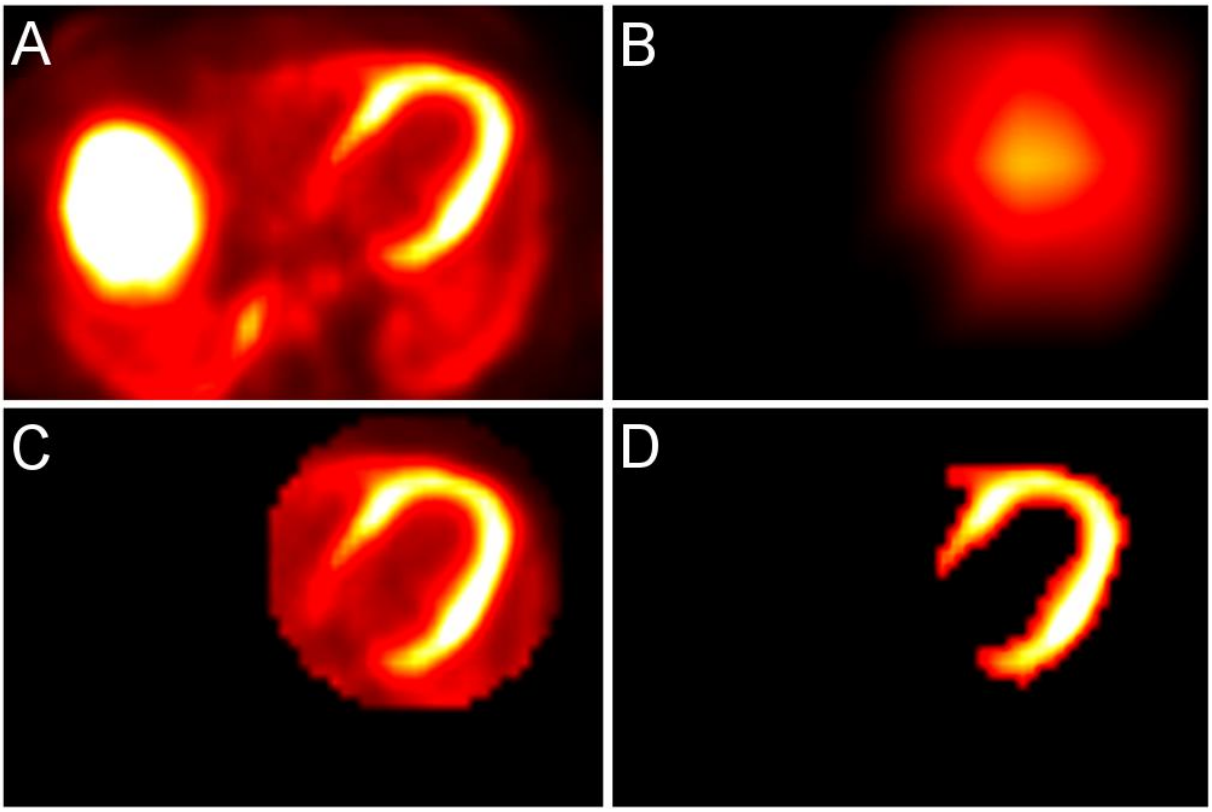

Figure 4.5: Segmentation of the left ventricle used by the emission-driven algorithm. (A) Central transaxial plane of the initial PET image. (B) Image after masking the left side and applying a strong smoothing filter; the spatial center of the LV is assumed to be roughly the point with maximum intensity in the image. (C) 3D ellipsoid defined around the spatial center; the 3D ellipsoid is a circle in each transaxial plane. (D) Segmentation results after histogram thresholding within the ellipsoid. Image reprinted by permission of the Society of Nuclear Medicine from [185].

priori knowledge of the acquisition was used: the bed position used for cardiac imaging was always selected so that the LV is located in the central transaxial slice, corresponding to the plane 23 out of 47 in the scanner used. A strong smoothing filter (boxcar average of 90 millimeters) was applied to this plane (Fig. 4.5(B)), so that the maximum value contained in it after the application of the filter was roughly the spatial center of the LV. A 3D ellipsoid approximating the shape of the LV (but slightly larger) was automatically defined around this point, and a binary mask was used to exclude all voxels outside of this ellipsoid (Fig. 4.5(C)). As the location of the LV was now defined, a local histogram thresholding within this area was able to classify the voxels as belonging or not belonging to the LV (Fig. 4.5(D)).

After the segmentation, the proposed correction was as follows: if a voxel was classified as belonging to the LV in the PET image, it was tested whether the CT-based attenuation factor corresponded to heart tissue, that is, if it was higher than 0.095 cm^{-1}, assuming 0.1 cm^{-1} is the reference cardiac tissue attenuation factor. If the attenuation factor was

lower, it was replaced by the average cardiac attenuation factor from all other voxels classified as belonging to the LV.

The segmentation and modification of the attenuation map required less than one second runtime on a Pentium M 1.8 GHz computer with 1 GB of RAM. Although the focus of this study were rest/stress ^{13}N-NH_3 perfusion examinations, the emission-driven correction could be applied to most tracers used in cardiac PET/CT such as FDG and Rubidium, with the only condition that the left ventricle can be segmented out of the PET data.

4.3 Results

4.3.1 Simulated misalignment

When shifting the attenuation map of originally aligned PET/CT scans to simulate emission-transmission misregistration, each region was differently affected by the displacement. The decrease in the average uptake of the lateral wall due to the motion was up to 42.5% when displacing the attenuation map by 4 voxels (21 mm) to the left direction. The application of the correction algorithm reduced this difference down to a 16.5% decrease (see Fig. 4.6). An example of the correction algorithm applied to a scan with a simulated misalignment of 15 mm is presented in Fig. 4.7.

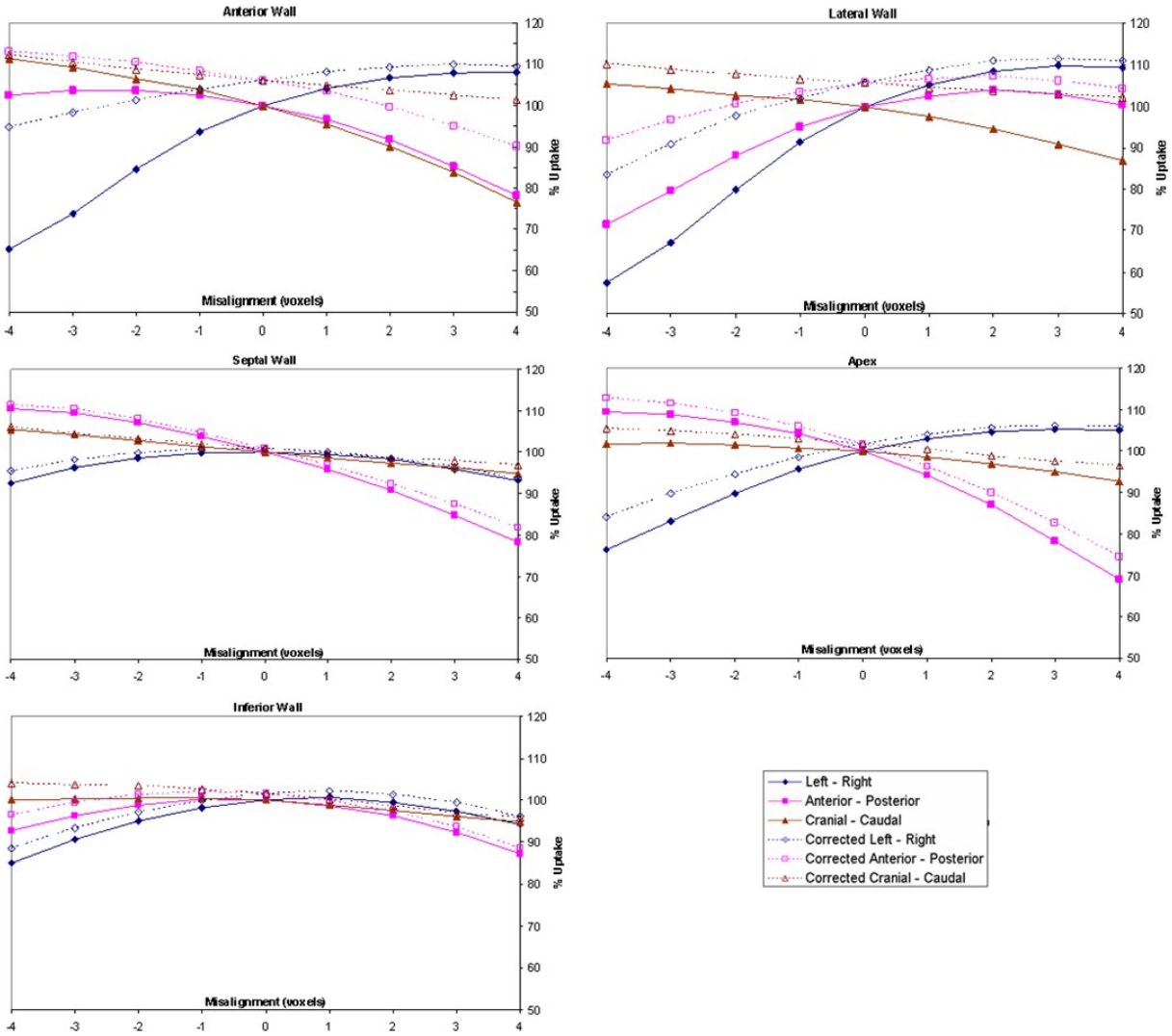

Figure 4.6: Change of uptake in the 5 myocardial segments produced by misaligning the emission and transmission images prior to performing the attenuation correction. The uptake after application of the emission-driven correction is shown with dashed lines.

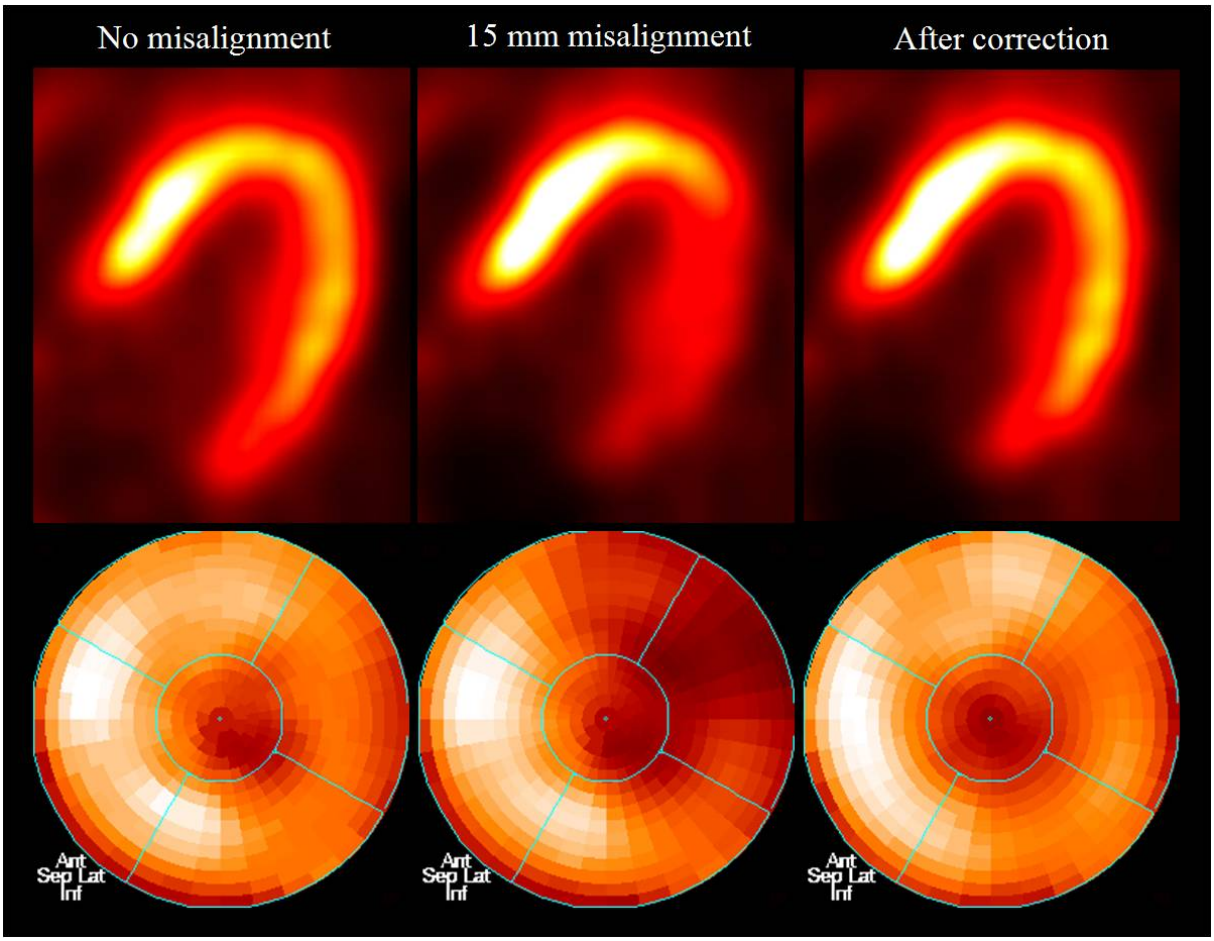

Figure 4.7: PET transaxial images and associated polar maps for: 1st column) data with no misalignment 2nd column) data reconstructed with simulated emission-transmission misalignment of 3 voxels (15 mm) to the left 3rd column) data reconstructed with the same emission-transmission misalignment after application of the emission-driven correction algorithm. The uptake in the anterior and lateral segments appears like a perfusion defect when no correction is applied, leading to potential errors in the image reading.

The results indicate that the anterior and lateral wall suffered at most from the misregistration, with a decrease in uptake of over 30% in some cases, in particular for left-right misalignment. On the other hand, the septal and inferior wall appeared to be quite robust to misregistration. The sensitivity of the anterior and lateral segments to misregistration-induced artifacts could be explained by the fact that these two segments are in direct contact with the lungs, so that a misregistration can lead to a completely biased attenuation factor at this region.

4.3.2 Manual registration

The misalignment between the PET and CT datasets was quantified following manual registration using the Euclidian distance between the original and the registered pose,

that is, as the square root of the sum of the misalignments in each individual direction. The misalignment averaged 6.1±7.0 mm for the 28 rest acquisitions and 6.0±5.6 mm for the 28 stress acquisitions, revealing that the extent of observed misalignment is not increased despite the pharmacological stress and the delay in the acquisition.

The spatial distribution of the motion for all 56 examinations was as follows: left-right 1.3±2.2 mm (range: 0 - 5.1 mm), anterior-posterior 1.6±2.9 mm (range: 0 - 15.4 mm), head-feet 4.7±6.1 mm (range: 0 - 23.6 mm). Head-feet motion represented the major component of the misalignment, in agreement with the main direction of the breathing motion. The maximum value of the misalignment for an examination was 29 mm.

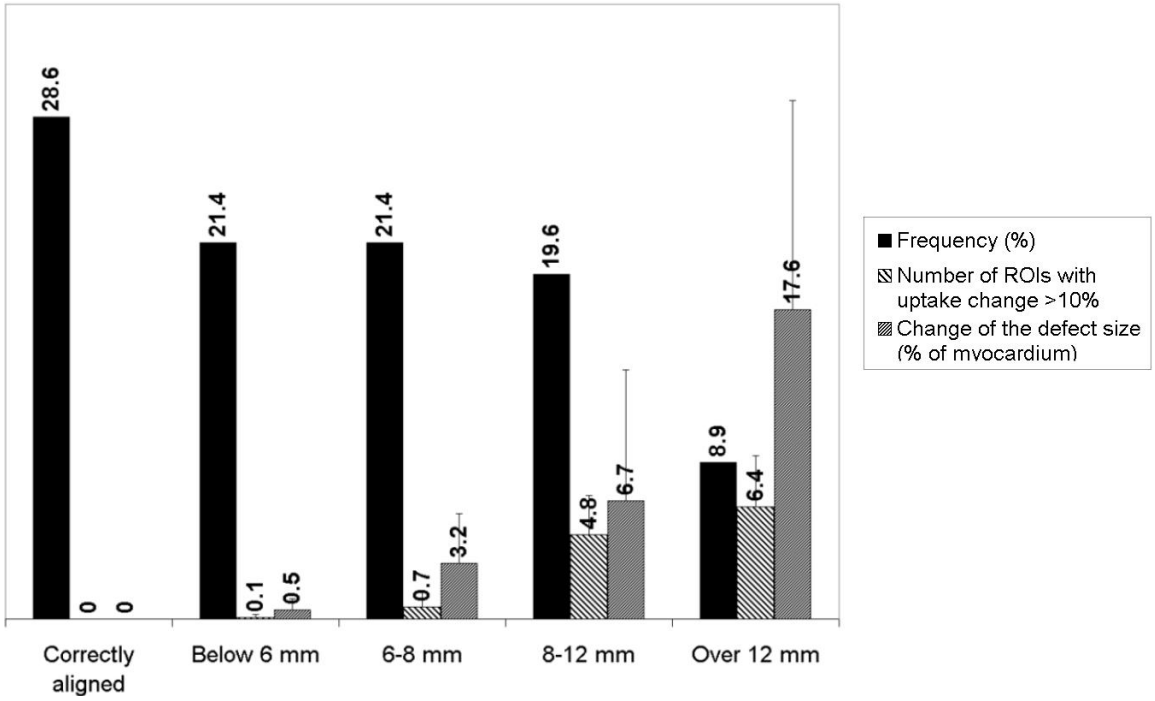

Figure 4.8: Classification of the 56 scans according to the degree of misalignment. For each group, two parameters indicating the effects resulting from manual registration are shown: the average number of segments from the AHA17 model which suffered an uptake change superior than 10% and the change of the defect size in % of the myocardium. Image reprinted by permission of the Society of Nuclear Medicine from [185].

Figure 4.8 shows the distribution of the misalignment according to its magnitude, as well as the changes on measured tracer uptake and defect size observed after reconstruction with the manually registered CT for attenuation correction. The registration had noticeable effects when the misalignment was greater than six millimeters, which occurred in half of the examinations. When the misalignment was greater than 8 mm (29% of the scans), the effects on the tracer uptake were severe, resulting in notable changes of the defect size (average of 10.1 %LV) assessed by comparison to a normal ^{13}N-NH_3 database.

The mean local differences of normalized uptake between the original studies and the studies after manual registration are shown in Fig. 4.9A. Significant differences were observed in the anterior and anterolateral segments, suggesting that a bias due to misreg-

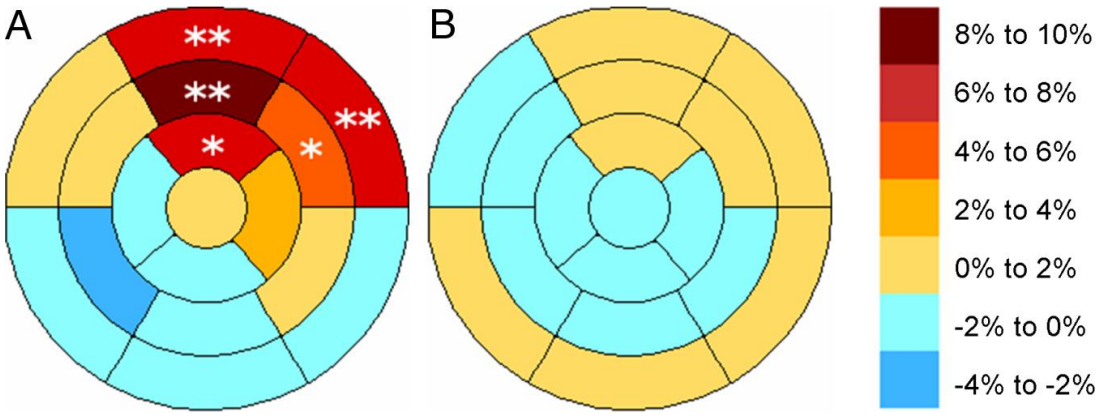

Figure 4.9: Polar map plots showing the mean differences in normalized uptake: (A) between studies with and without manual registration, (B) between studies with manual registration and with emission-driven correction. * denotes $p < 0.10$, ** $p < 0.05$. Image reprinted by permission of the Society of Nuclear Medicine from [185].

istration could exist in PET/CT perfusion studies showing up as slightly reduced uptake in these segments.

The defect size of 6 out of 28 patients (21.4%) changed by more than 10 %LV in either the rest or stress examinations, all of them following a manual realignment greater than 10 mm. From these 6 patients, 4 had a defect (15 to 46 %LV) located in the anterior or anterolateral segment which was completely artifactual and disappeared after reconstruction with the realigned CT, one patient had an artifactual defect (15 %LV) in the inferoapical wall, and another one had an increase of size (by 13 %LV) of a septal perfusion defect induced by the registration. This was the only case where the correction resulted in a modest increase of the defect size.

4.3.3 Automatic registration

Despite using an exhaustive search, the results from the automatic registration were disappointing. When the complete image (bed position corresponding to the heart) was used as input for the registration, the initial PET-CT pose was usually considered to be optimal by the registration algorithm, due to the presence of other dominant structures in the image which were correctly aligned, such as the body contour. In other words, the relevance of the local misalignment of the heart for the computation of the mutual information is too small as compared to the impact of the rest of the structures. Subsequently, a more regional approach was tested by manually defining a volume of interest around the heart and removing all other surrounding structures. Unfortunately, this approach did also not produce the desired result as the low correlation between the functional (only LV) and anatomical images (atria, ventricles, blood) in the heart made mutual information incapable of properly assessing the agreement between both poses.

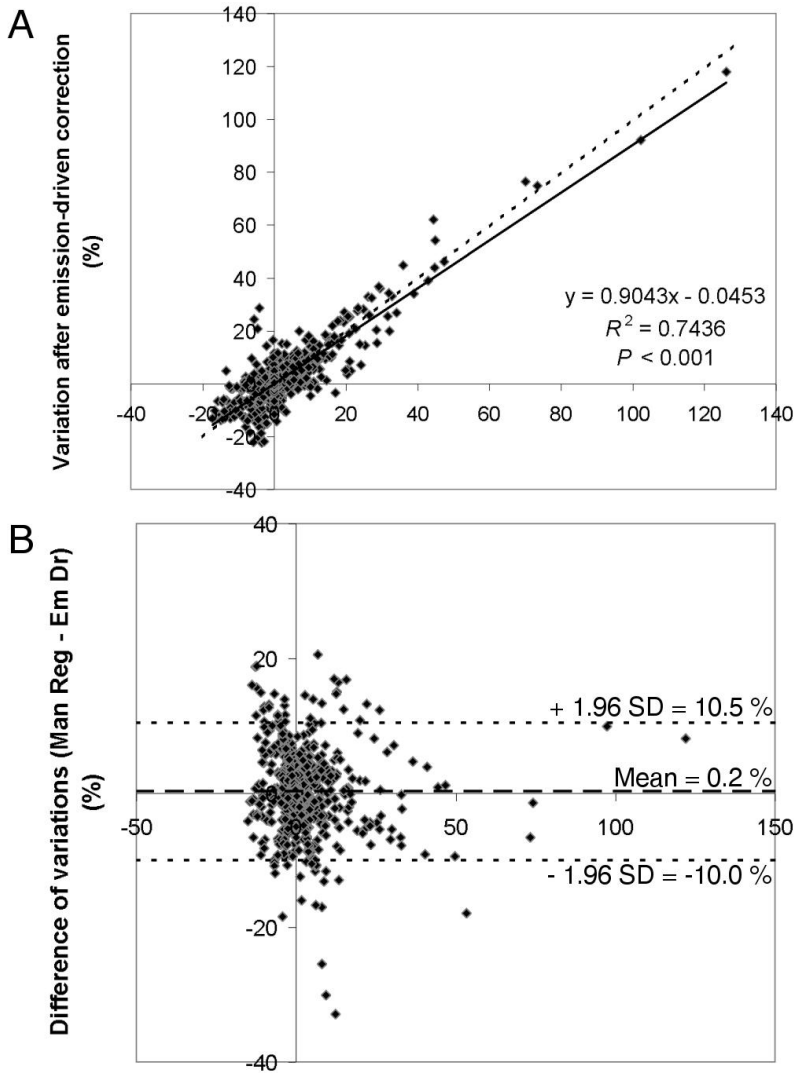

Figure 4.10: Comparison between correction methods. (A) Regression plot between variation of local measured uptake (in % of the original uptake) introduced by manual realignment and by the emission-driven algorithm. Each point corresponds to one segment of the AHA17 model from the perfusion examination of one patient. Regression line (solid line) and line of equality (dotted line) are shown. (B) Difference in the correction plotted against their average (Bland-Altman plot, see [29]), with mean difference (dashed line) and 1.96 SD intervals (dotted line). Image reprinted by permission of the Society of Nuclear Medicine from [185].

4.3.4 Emission-driven algorithm

Figure 4.10 shows the comparison between the variation of measured uptake produced by the emission-driven algorithm and by manual registration. Due to the reduced size of the regions considered in the AHA17 model, some local differences were observed. The correlation between both methods was high ($R^2 = 0.74$, $p < 0.001$) and good agreement was seen for large misregistration-induced defects. Mean local differences of

uptake between the studies corrected by manual registration and by the emission-driven algorithm were all non-significant and within a 2% interval (Fig. 4.9B), indicating good agreement between both approaches. Figure 4.11 shows an example of the emission-driven correction compared to manual registration for a patient with a severe misalignment.

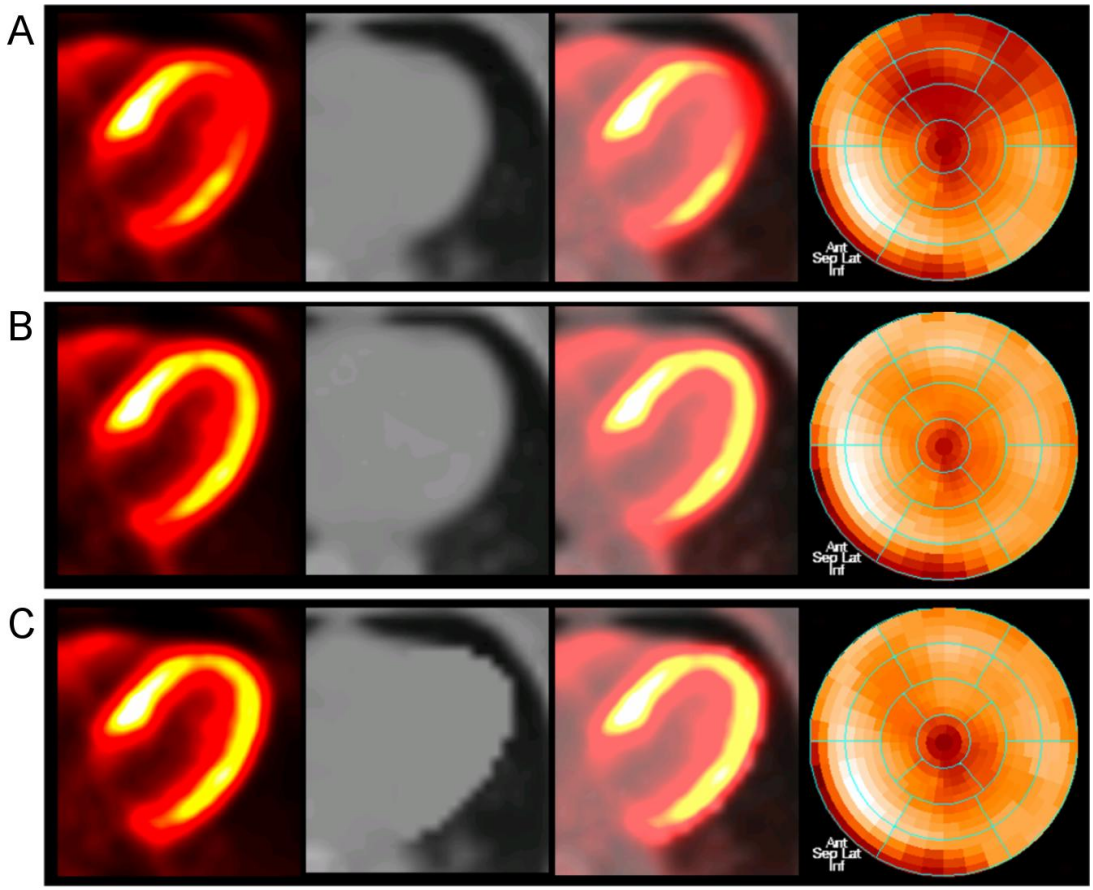

Figure 4.11: Study with a PET-CT misregistration of 11 millimeters. Columns from left to right: PET, CT, fused PET/CT and polar map. From top to bottom: (A) Original study. (B) Study after manual registration and reconstruction using the coregistered attenuation map. (C) Study after emission-driven correction and reconstruction using the modified attenuation map. Undercorrection for attenuation in the anteroapical and anterolateral segments produced reduced apparent uptake and was assessed as a perfusion defect (24% of the myocardium) after comparison with a normal database. Both correction methods had comparable results, recovering the uptake in these segments and demonstrating that the defect was completely artifactual. Image reprinted by permission of the Society of Nuclear Medicine from [185].

Although it was not observed in this study, one theoretical limitation of the emission-driven algorithm is as follows: for a severe perfusion defect located in a misaligned area, the uptake would probably be so low that the segmentation would not identify it as cardiac tissue and would therefore not perform any correction for this area. That is, the emission-driven algorithm would preserve this area as it initially was in the original study, where

the misregistered perfusion defect would likely appear more intense than it really is. This limitation is related to the segmentation step of the algorithm, which is currently based on thresholding of the image intensity. Improvements of the segmentation step by spatial constraints, model-based segmentation or use of the tracer dynamics of the myocardium could help overcome it.

4.4 Discussion

The results indicate that, despite the use of combined PET/CT hardware, emission-transmission misregistration occurs frequently in perfusion studies using PET/CT. Changes of the defect size larger than 10% of the myocardium were observed in 6 out of 28 patients (21.4%), in 5 of these patients being fully artifactual defects which completely disappeared after coregistration, results which are in agreement with previous studies [176].

The misregistration had larger effects in the anterior and anterolateral segments, producing a significant reduction of measured uptake in these areas. This supports the hypothesis that the severe difference in the attenuation factor of cardiac and lung tissue (0.1 cm^{-1} vs. 0.02 cm^{-1}) could be the core reason for the changes of measured uptake: indeed, the anterior and lateral segments have the largest common surface with the lungs, whereas the septal and inferior walls are in contact with other soft tissue (right ventricle, liver, etc.) so that a misalignment will produce only minor changes in the attenuation factors for these segments.

PET-CT misregistration can be minimized during acquisition with optimized protocols where patient comfort is maximized (e.g. arms down acquisition, short protocols) and with adapted breathing protocols [26, 100]. Despite these precautions, which were already adopted in this study, misalignment can still be present and needs to be corrected. A possible approach is modifying the CT acquisition protocol in order to reduce its temporal resolution to match that of the PET examination by using a slow CT averaged over the complete respiratory cycle [226, 6, 221]. Such an approach can indeed minimize the breathing-induced misalignment at the expense of increased radiation dose for the patient and/or longer acquisition times. However, misalignment resulting from other sources (e.g. patient motion or changes of the heart location due to pharmacological stress agents) will still not be corrected.

One further strategy which was explored was the analysis of the misalignment immediately after reconstruction of the PET images while the patient was still lying on the bed, in order to perform a second ultra low dose CT (80 kV, 13 mAs) if a moderate to severe misalignment was detected. This approach was not convenient for the regular workflow and increased slightly the radiation dose received by the patient. Moreover, the second CT scan could potentially present misalignment as well. Therefore, this approach was considered suboptimal and was interrupted.

Image registration would be a convenient post-acquisition approach to overcome the problem. If robust automatic registration was possible, this would certainly be a suitable solution: unfortunately, the initial tests revealed that mutual information was unable to register the cardiac contour on PET and CT images, probably due to the fact that the PET perfusion images show mainly the left ventricular mass, whereas CT does not distinguish between the myocardium and blood pool; alternative approaches must be investigated. Manual registration is a solid option, with the inconvenient of being time consuming and observer dependent. Alternatively to manual registration, the proposed emission-driven correction has the advantages of being fast and fully automatic, having therefore a high potential for clinical routine application. Its application yielded results comparable to

those achieved by manual registration. However, patients showing large perfusion defects in severely misregistered areas could represent a weakness of this approach as compared to manual registration. Furthermore, the CT data is modified so that it may be argued that this approach is physically incorrect.

More recently, this issue was further investigated by [145], who proposed a more sophisticated automatic registration approach. In their work, Khurshid et al. used the borders of the anterior and lateral myocardial walls in both PET and CT images to align them; the walls are identified in the PET image using fuzzy clustering and masking to isolate the cardiac region, and then applying a Canny edge detection algorithm [50] to obtain the cardiac border; this information is used as starting point to locate the borders in the CT image, and then the distance between the borders in each of the spatial directions is computed and used to correct for the misalignment. Although no numerical result was given to assess the accuracy of the registration or compare it to manual registration, the authors indicated that the automatic registration successfully aligned the PET and CT cardiac images independently of the respiratory phase in which the CT was acquired. The execution time was reported to be 6 minutes on a 2 GHz Intel Core 2 Duo machine with 2 GB of RAM for a couple of images. This approach could potentially suffer from the same limitation as the emission-driven approach presented above, since a strong perfusion defect could jeopardize the detection of the cardiac contour in the PET images and have an impact on the registration.

Moreover, researchers at Siemens have also recently presented results of automatic cardiac SPECT-CT [35] and PET-CT [34] registration; by using mutual information on a cropped image around the left ventricle, they reported that automatic translation produced visually acceptable results for 95% of the SPECT-CT cases and 98% of the PET-CT cases. Mean distances of 12 mm (SPECT-CT) and 8±4 mm (PET-CT) as compared to manual registration were reported. Since 3 CTs were available for each patient, the consistency of the registration was evaluated using each separate CT, and for both SPECT-CT and PET-CT the consistency of automatic registration was reported to be comparable to that of manual registration.

Registration of cardiac PET and CT data to avoid potential attenuation-related artifacts appears therefore to be a topic still under research, and although automatic tools have not reached the commercial software packages yet, they will surely be part of clinical routine in the coming years.

Lastly, the method presented here can also be extended to account for emission-transmission misregistration in areas other than cardiac imaging [48]. For example, the method was applied on the images of a patient with an adenocarcinoma of the oesophagogastric junction showing a clear PET-CT misregistration (Fig 4.12). The SUV suffered an important change after the correction (Fig 4.13), relevant enough to have an effect on the patient management.

4.4.1 Limitations

A limitation of this study is the lack of a gold standard to confirm that the defects which disappeared after PET-CT registration were artifactual defects and not real per-

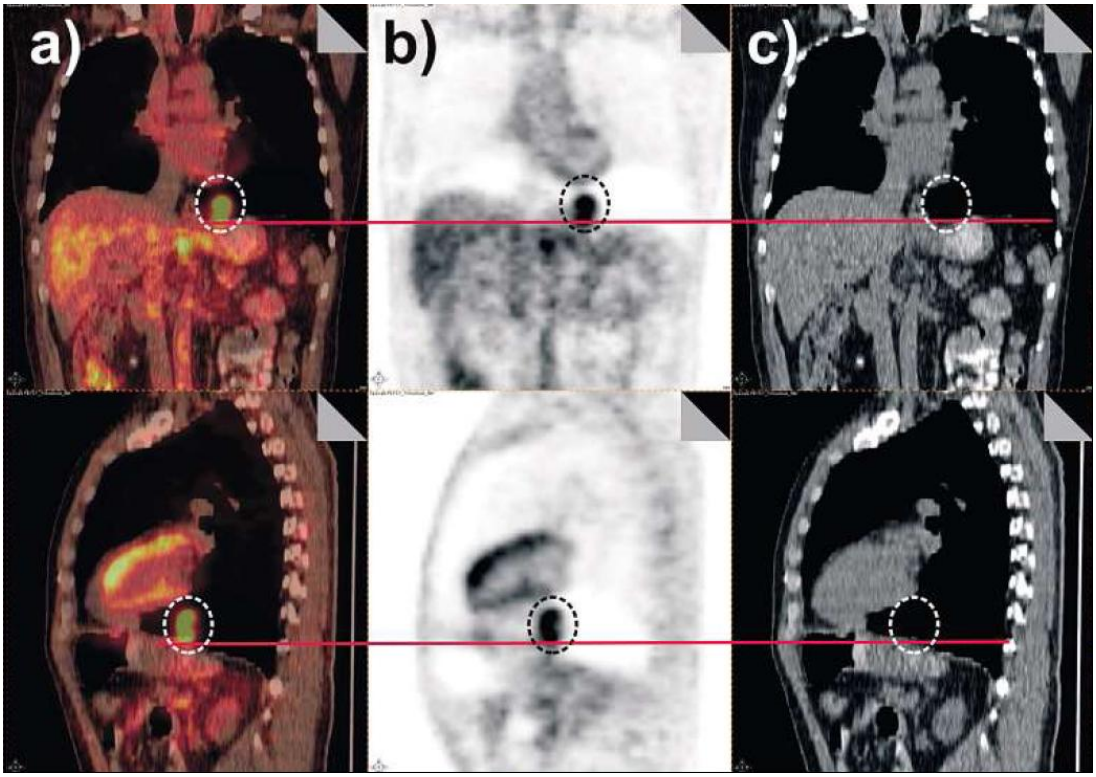

Figure 4.12: Patient with an adenocarcinoma of the adenocarcinoma of the oesophagogastric juntion juntion showing a notable PET-CT misregistration. Fused PET/CT (a), PET (b) and CT (c) images, showing that the focal uptake in the tumor corresponds to lung tissue in the CT. Reproduced from [48] with permission from Schattauer.

fusion defects; coronary angiography of the patients would have helped to confirm and support the results. However, the primary motivation for this study was the observation that rest/stress studies presenting moderate to severe emission-transmission misregistration had apparent perfusion defects in spatial coincidence with the misregistered segments. This, combined with the conclusions from previous works which observed significant changes of local uptake following a simulated emission-transmission misalignment in PET and SPECT [196, 193], provided confidence that the apparent defects were due to the observed misregistration. The fact that the defects disappeared completely after manual registration by an expert firmly supported the hypothesis that the defects were artifactual and due to a biased attenuation correction.

Another limitation of the study is that only one observer performed manual registration of the PET and CT data, and inter-observer variability was not studied. Indeed, registration of PET/CT cardiac data can be challenging because of the lack of anatomical landmarks which can be identified in both images. One recent study which further investigated this issue [277] reported an average difference between observers of 3.4 mm (see Fig. 4.14).

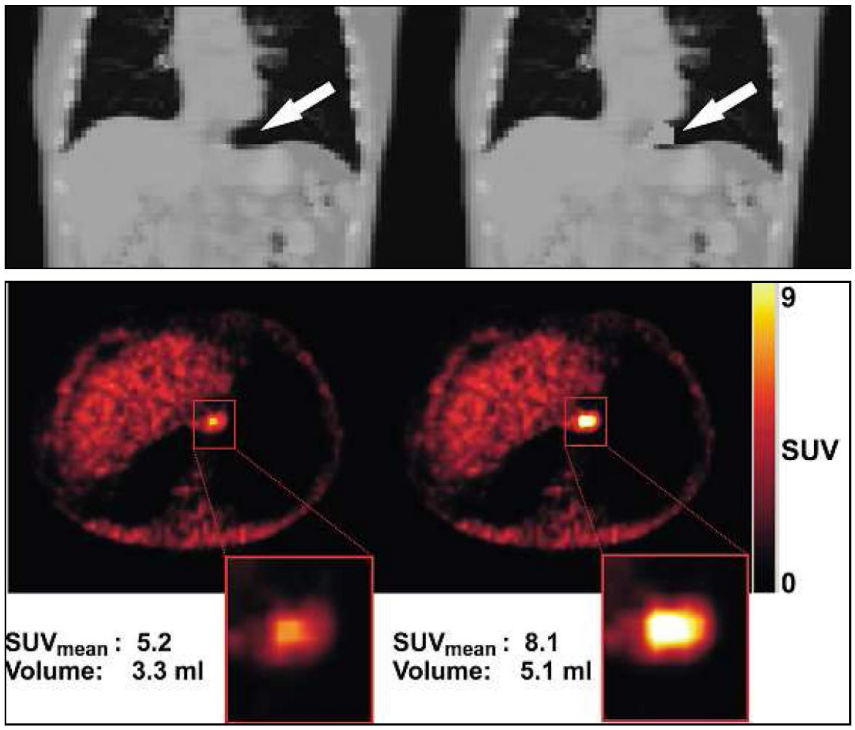

Figure 4.13: Top: CT image before (left) and after correction (right), using a similar emission-driven algorithm as for the heart. Bottom: Transaxial PET image reconstructed with the original (left) and the corrected attenuation map (right), showing a 56% increase in SUV after correction (from 5.2 to 8.1) and a 55% increase in lesion volume. Reproduced from [48] with permission from Schattauer.

Study	Direction (mm)			Magnitude (mm)
	x	*y*	*z*	
Rest	2.16 ± 2.06	3.24 ± 3.50	2.16 ± 2.97	3.18 ± 3.52
Stress	2.49 ± 2.91	2.91 ± 3.28	2.35 ± 3.14	3.61 ± 3.95
Rest and Stress	2.33 ± 2.51	3.07 ± 3.38	2.25 ± 3.05	3.39 ± 3.71

Data are average differences between 2 observers in visual PET/CT alignment verification in all 3 directions.

Figure 4.14: Interobserver variability in PET/CT manual alignment. Table reprinted by permission of the Society of Nuclear Medicine from [277].

4.5 Conclusion

This work served to better understand the problem of PET-CT misregistration in cardiac imaging and acknowledge its relevance. Indeed, when a part of the myocardium in PET appears to be within the lung in the CT image, the biased attenuation factors result in undercorrection of photon attenuation and decreased apparent uptake, potentially resulting in false perfusion defects and therefore decreased specificity of PET for myocardial perfusion imaging. It was shown that manual registration of the PET/CT datasets followed by a new PET image reconstruction was able to avoid this artifact.

These results underline the relevance of this issue and the potential decrease of diagnostic accuracy for cardiac imaging using combined PET/CT scanners. The image-readers must be aware of the misregistration-induced artifact and know that, when no correction technique is implemented, they cannot be confident on their diagnosis if misregistration is present. The implementation of a correction technique is therefore a requisite.

The publication of the results from this investigation [189, 192, 190, 185] was followed by further studies confirming these findings also with different perfusion tracers and supporting the urgent need of correction techniques [198, 101, 221, 6, 166, 277]. By the end of this thesis, within three years of the publication of the first results, all major PET/CT vendors had added software to manually register the PET and CT data and to repeat the PET reconstruction afterwards, acknowledging the potential artifact and offering a solution in order to preserve the otherwise excellent diagnostic accuracy of PET for the assessment of myocardial perfusion.

There is no consensus yet regarding the optimal correction technique. Manual registration is of definite help, but it is also time-consuming and operator dependent. The emission-driven algorithm proposed here seems promising but would need to undergo further validation before introduction in clinical routine, and could potentially fail in the case of a strongly hypoperfused and misregistered area, which would not be properly corrected. The initial tests with automatic registration based on maximization of the mutual information did unfortunately not provide satisfactory results. Recent studies [145, 34] have further investigated the possibility of performing automatic cardiac PET-CT registration reporting positive results. It is expected that such automatic tools will be further tested and integrated in commercial software for combined PET/CT and SPECT/CT scanners in the coming future.

CHAPTER 5

Attenuation correction in combined MRI/PET scanners

5.1 Strengths and challenges of combined MRI/PET

Hybrid MRI/PET scanners are technologically very challenging, mainly due to the sensitivity of the usual PET design to strong magnetic fields. The idea of building combined MRI/PET scanners was discussed in the 1990's, with the motivation of reducing the effects of the positron range using the magnetic field to achieve improved spatial resolution [107]. The focus has progressively shifted to clinical and research applications exploiting the simultaneous acquisition of MRI and PET data. Development of combined MRI/PET scanners has recently received renewed attention due to the success of combined PET/CT scanners, which have made standalone PET scanners virtually obsolete. Hardware manufacturers such as Siemens and Philips have announced plans to develop combined MRI/PET scanners in the coming years.

Besides providing an anatomical reference for the PET functional data, the same way as CT does in combined PET/CT acquisitions, a combined MRI/PET could provide other advantages as compared to a combined PET/CT scanner, such as:

Improved soft tissue contrast MRI provides better tissue contrast than CT, allowing the distinction of several tumor entities which cannot be identified based on CT.

Reduced ionizing radiation MRI uses no ionizing radiation, making it better suited for serial follow-up examinations and pediatric imaging [42].

True simultaneous acquisition As opposed to combined PET/CT scanners, where the acquisition is done sequentially, integrated MRI/PET scanners would allow true simultaneous acquisition. This makes new applications possible, as for instance measuring neurological activation and deactivation processes simultaneously with PET and MRI.

MRI-based motion correction for PET Acquisition of navigator signals to measure breathing and heart beating are already available in clinical MRI acquisitions of the thorax [79]. Due to the simultaneous acquisition and the lack of ionizing radiation, real-time MRI data could be used to account for the patient motion during the PET acquisition as well. More advanced correction techniques including 3D models of motion could also be used for this purpose.

Availability of advanced MRI sequences The large variety of possible MRI measurements, including functional MRI, diffusion and perfusion imaging as well as MR spectroscopy, could provide important complementary information to the PET functional measurements.

The complementary value of PET and MRI has already been pointed out for application in neurology [113, 13, 260, 53, 103, 141, 159, 283], cardiology [217, 284, 109, 21, 20, 119, 144, 286] and oncology [11, 10, 9, 170, 114, 180, 248, 220, 252, 265, 264]. Therefore, combined scanners are expected to be advantageous for many research and clinical applications.

However, the development of combined MRI/PET scanners faces several technological challenges, among them:

- Sensitivity of the PET detector technology to strong magnetic fields
- Spatial integration of the PET components within the magnet
- Influence from the PET components on the MRI image quality and vice versa
- Photon attenuation and scatter correction of PET data

The major difficulty is the fact that the photomultiplier tubes (PMTs), used in most PET scanners to read the light output generated by the scintillation crystals, cannot work within a strong magnetic field. Therefore, combined scanners must be completely redesigned [70, 304]. The first tests for combined MRI/PET measurements were done using optical lightguides to move the light output some meters away from the magnet [60, 93, 271, 84, 241], so that the PMTs were not disturbed by the magnetic field.

Although such a design is adequate for a moderate number of detectors and eventually feasible for animal PET scanners, the burden of the lightguides is inconvenient for a clinical MRI/PET scanner. A different approach was undertaken by researchers at this institution, who investigated replacing the PMTs by other light readout systems, and found the Avalanche Photodiodes (APDs) to be a potential alternative [262], proving that their performance was unaffected even by strong magnetic fields [235]. Prototype small animal PET systems based on this design have already been built [169, 320]. Several academic and corporate research groups are focusing on the development of hybrid MRI/PET tomographs using APD technology, and the first preclinical and clinical results appear very promising [52, 236, 135].

More recently, Silicon Photomultipliers (SiPMs) have also demonstrated to provide efficient light readout unaffected by magnetic fields [2, 225, 74] and appear also as potential

candidates for their use in combined MRI/PET scanners [205, 279, 175]. Further information on the different PET detector technologies and their application for MRI/PET imaging can be found in [168].

In future combined scanners, the influence of the MRI components on the PET image quality and of the PET components on the MRI image quality still needs to be established. The first studies on this topic concluded that the MRI data are nearly unaffected by the presence of the PET detectors [276, 236], but the influence of the MRI components on the image quality of the PET data still has to be better investigated based on the design of the scanner; redesign of many MRI components which can heavily interact with 511 keV photons (e.g. patient bed and coils), is also necessary to minimize its impact on the PET image quality.

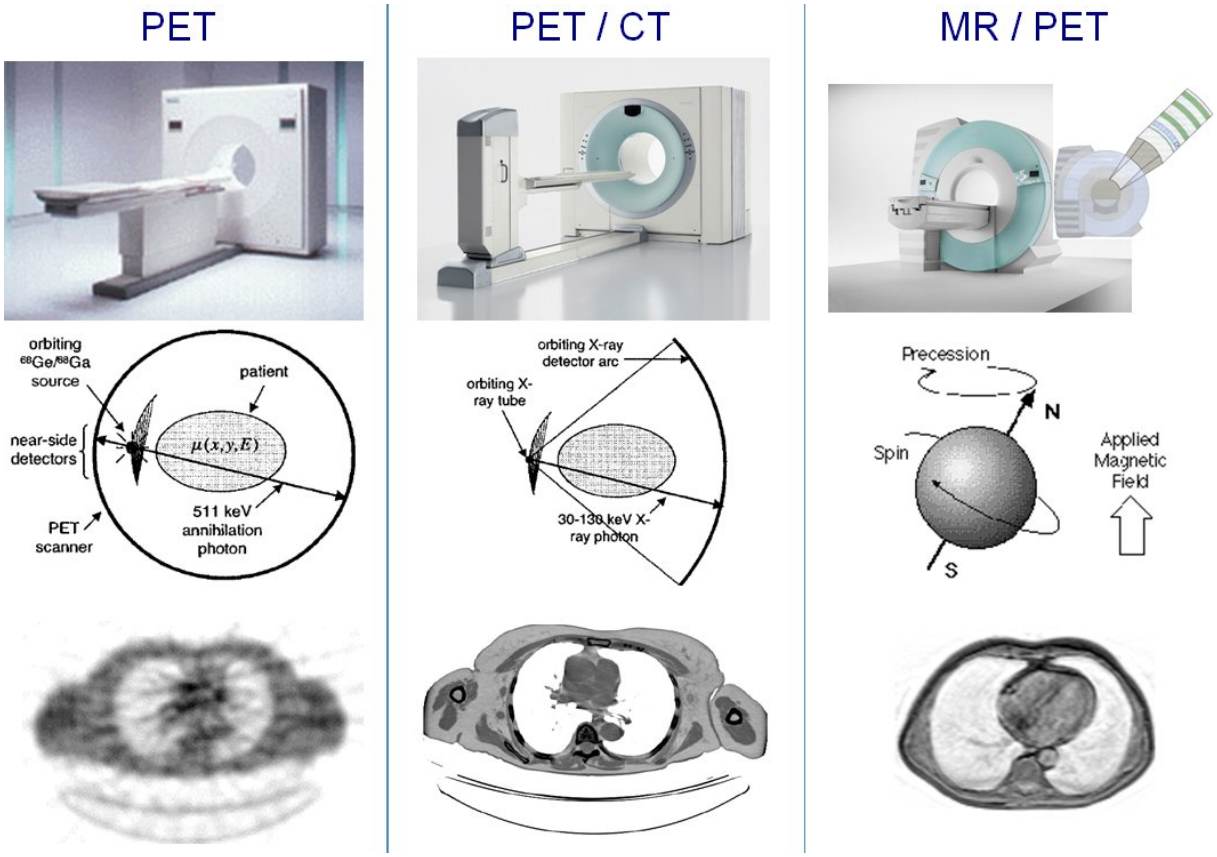

Figure 5.1: Different solutions adopted to determine the attenuation map: in standalone PET scanners, the attenuation map is determined by means of a rotating radionuclide source (left column); in PET/CT scanners, by means of a transform to bring the CT intensity values to attenuation at 511 keV (middle column); in hybrid MRI/PET tomographs, MRI data are not based on the transmission of photons throughout the body and therefore different approaches must be investigated (right column). Rows from top to bottom: picture of a representative scanner, sketch of the acquisition physics, and representative transaxial slice of the image acquired at the thorax.

The last challenge indicated above is correction of attenuation and scatter of photons in

the PET data. In order to account for these effects, it is necessary to have an attenuation map with the radiodensity of each volume element for 511 keV photons. For whole-body PET imaging, there are currently two approaches to obtain an attenuation map: either by using a radionuclide source rotating around the patient to obtain a transmission image, or by using spatially registered CT data after conversion of the attenuation factors to PET energies, as it is usually done in combined PET/CT scanners (Fig. 5.1).

Since hybrid MRI/PET tomographs will most likely neither include a radionuclide source nor an x-ray source, none of these approaches can be used and alternative solutions must be developed. Using the MRI data to generate an attenuation map appears therefore as an interesting option [315]. Unlike CT or radionuclide-based transmission scans, MRI is not measured by transmitting high-energy photons through the body and its signal is therefore not related to the radiodensity of the tissue. One example is cortical bone, which shows nearly no signal in MRI despite having a high attenuating power. Therefore, a simple scaling approach such as the one used for generating CT-based attenuation maps is not suitable for MRI data, and new approaches must be investigated.

The attenuation map, and also an eventual MRI-based attenuation map, should include the attenuation produced from the body of the patient as well as the attenuation produced by any hardware component present between the patient and the PET detectors, such as the patient bed, body and surface coils from the MRI scanner and eventual ECG or respiratory sensors. Hardware components can be accounted for by having precomputed attenuation models of the components and placing them at the appropriate location within the attenuation map (Fig. 5.2); however, correction for hardware components will not be investigated in this work. The rest of this chapter will concentrate only on attenuation due to the body of the patient.

Figure 5.2: Example of the creation of attenuation models for the hardware components: CT acquisition of an MRI head coil. The acquisition was performed by Siemens Healthcare. Once a 3D model of the components is available and those can be spatially localized in the MRI acquisition, the model can be added to the attenuation map.

5.2 State of the art

The use of MRI data to evaluate photon attenuation was first mentioned in [246], who questioned the at that time constant attenuation factor of 0.12 cm^{-1} used in Technetium-99m SPECT in the upper thorax. Rowell et al. used the anatomical images provided either by CT or MRI to geometrically measure the length of the path traveled by the photons through each tissue type (lung, bone, soft tissue), as shown in Fig. 5.3, and computing the additive attenuation suffered by the photons by assigning well-known attenuation factors for each type of tissue. This way, they demonstrated that the attenuation factor should be lower than the constant used due to the presence of the lungs.

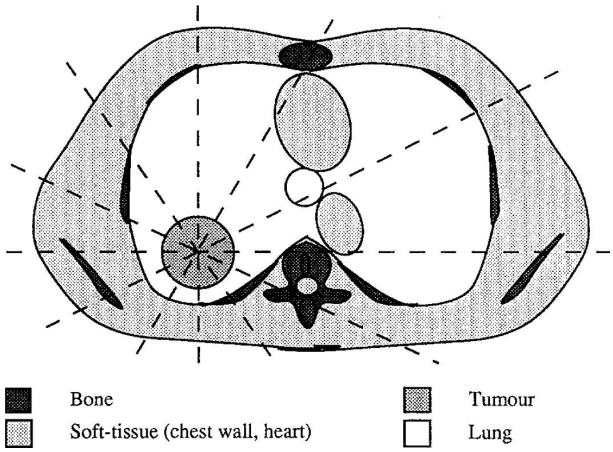

Figure 5.3: Determination of attenuation coefficients using topographical information from computed tomography (CT) scans. Diaphragmatic representation of CT image showing bone, soft tissue, tumor and lung. Dashed lines represent photons emitted from the tumor center. The authors did not use an algorithm to derive attenuation values directly from the images, but rather performed geometrical measurements on the images to estimate the attenuation suffered by the lines of response. Image reprinted with kind permission from Springer Science+Business Media from [246].

In 2000, Stodilka et al. proposed an indirect use of MRI for attenuation correction of SPECT neurological data [280]. Their method consisted in registering a SPECT atlas to the patient's SPECT image and apply the transformation matrix to an MRI-based head atlas on which attenuation factors for each voxel had been assigned. A few years later, Zaidi et al. [317] pointed out that most patients undergoing a neurological PET were also examined using MRI, and proposed skipping the radionuclide-based transmission image and using an MRI-derived attenuation map instead; for this purpose, they segmented T1-weighted images of the patients in five regions: air, skull, nasal sinuses, brain and scalp, with the last two regions having the same attenuation factor. The segmentation process was complex, involving a fuzzy clustering algorithm combined with a contour detection algorithm, a technique to identify the nasal sinuses and manual intervention to improve the segmentation of the skull. The same group later proposed the registration of the patient's brain MRI to an MRI atlas in order to apply well-known attenuation factors from the atlas and avoid the segmentation step [206].

All investigations targeted applications for neurology, for which atlas-based approaches based on registration techniques appeared to work reliably. At this institution, the investigation on the topic of MRI-based attenuation correction was started by a Master thesis by Diego Vivancos Gallego [303] and two Interdisciplinary Projects by Darko Zikic [321] and Loren Schwarz [269], all carried out in collaboration between the Department of Nuclear Medicine Department and the Department of Computer Science. Although these projects mainly focused on application for animal imaging and the problem of image registration, interesting results were observed.

In particular, [321] investigated the use of an intensity-based segmentation algorithm on a proton-weighted image of a human foot, observing that the fat and soft tissues could be distinguished. It was also noted that cortical bone was incorrectly identified as air due to its low signal, so that improvements were needed. Moreover, use of a joint histogram was also explored. The basic idea is to combine the information from two different MRI acquisitions, so that if a sequence shows a common intensity for two tissue types, the other sequences helps distinguish between them. The joint histogram between the proton-weighted and T1 sequences was computed and clustered using the K-means algorithm [110]. The resulting segmentation was equivalent to the intensity-based segmentation (see Fig. 5.4), so in this case no advantage was found by using this additional information. This preliminary study of possible segmentation approaches was visually evaluated, and no comparison to CT or numerical assessment on PET data was performed.

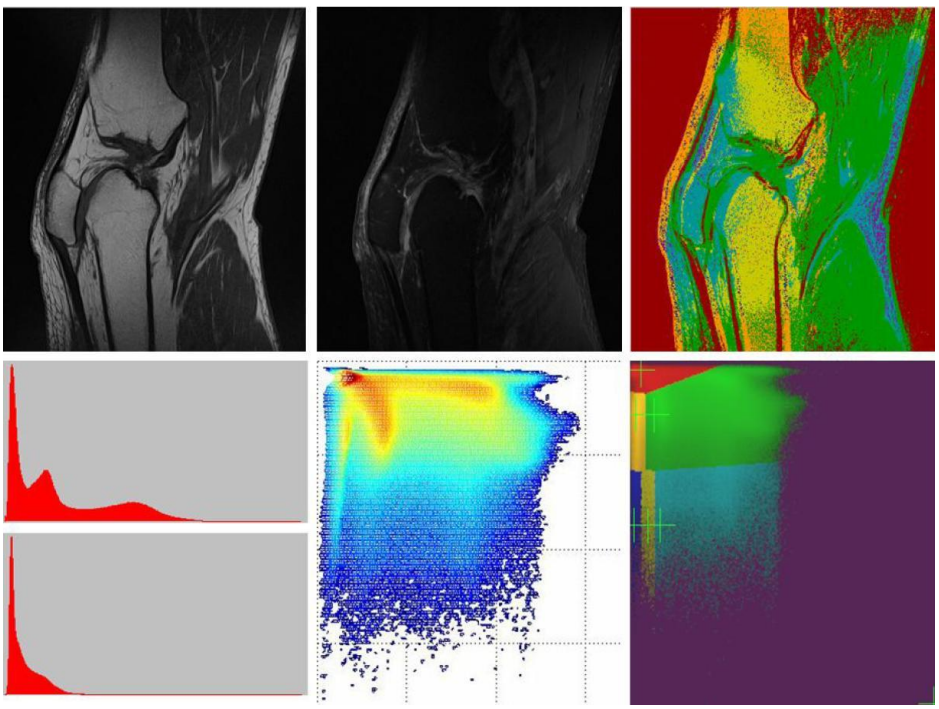

Figure 5.4: Results of the joint histogram clustering of a proton-weighted and T1 images, with the segmented image shown in the top right frame. Reproduced from [321] with permission from the author.

For clinical whole-body imaging, no results had been reported on the use of MRI-based attenuation maps by the start of this work. With the growing interest for the development of MRI/PET scanners, also for whole-body imaging, research on this topic was triggered and several centers started to focus on this issue as well.

5.3 Initial investigation and observations

As indicated above, an attenuation map should show the attenuation factor of each voxel for 511 keV photons. CT is well adapted for that: it operates at a lower energy but a scaling can be used to provide an excellent approximation for most biological tissues. MRI images are not related to radiodensity of the tissue but show information on the relaxation times of the nuclear spins; obtaining a perfectly accurate MRI-based attenuation map is comparable to acquiring a CT image using an MRI scanner, being therefore a virtually impossible objective. Consequently, MRI-based attenuation maps cannot be 100% accurate, but they should provide sufficient accuracy so that their clinical purpose is not compromised.

Using a joint histogram is a powerful approach since eventually some features can be shown only in some sequences and not in others. However, eventual motion, even of a few millimeters, could lead the method to completely biased results, so that the acquisition of a single scan would be preferable. A single scan requires also less acquisition time and is more convenient for the clinical workflow. For these reasons, it was decided to first investigate the limits of using a single sequence, and whether this could be sufficient for a clinical use.

To know the requirements for a suitable attenuation map, the attenuation maps used clinically in the available scanners were analyzed. As mentioned above, two different ways of determining the attenuation map are used clinically. In standalone PET scanners, the attenuation map is derived from transmission measurements performed using a rotating radionuclide source; one example of such an attenuation map with its corresponding histogram is shown in Fig. 5.5A. For workflow reasons, this scan is typically acquired within a few minutes and segmented to differentiate mainly between the background, lungs and soft tissue [311].

A second way to derive attenuation maps is by using spatially registered CT data. A bilinear transformation serves to convert from CT Hounsfield units, which measure the radiodensity at x-ray energies (60-140 keV), to attenuation factors at 511 keV [148]. This is the most commonly used approach in PET/CT scanners. As compared to radionuclide-based attenuation maps, CT provides much higher spatial resolution and improved statistics (see also section 4.1), being able to distinguish between the radiodensity of fat (0.086 cm^{-1}) and soft tissue (0.1 cm^{-1}), which appear clearly separated on the histogram (Fig. 5.5B). Also, a small fraction of voxels show an attenuation factor above 0.105 cm^{-1}, corresponding to bones or to a mixture of bone and soft tissue. It is worth mentioning that the resolution provided by CT is eventually too high for correction of the PET data, so that the CT image undergoes a 3D Gaussian filtering of 5 mm after the energy scaling for use in attenuation correction.

Both radionuclide-based and CT-based attenuation maps are used in clinical routine. Although CT-based attenuation maps have some drawbacks such as metal artifacts, they are commonly considered to result in better PET image quality, mainly because they contain much less statistical noise, which is otherwise propagated into the PET image. Thereafter, CT-based attenuation maps were considered the gold standard for this work and MRI-based attenuation factors which are as close as possible to the CT-based atten-

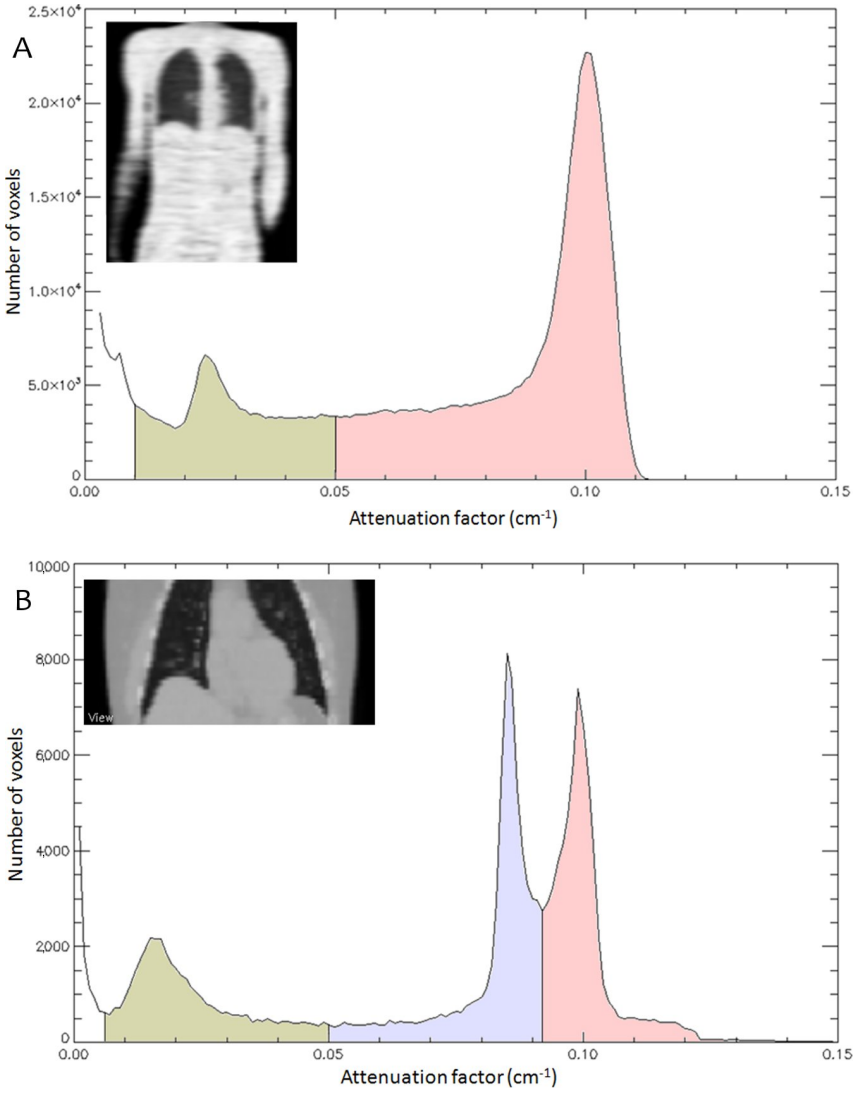

Figure 5.5: Histograms of an attenuation map acquired with a transmission source (A), and with low-dose CT (B). The tissue classes which can be clearly separated are color-coded on the histogram: lungs (green), fat (blue) and soft tissue (pink). The peak for the background (white area on the left with the lowest attenuation factor) has been cropped for improved visibility. Image reprinted by permission of the Society of Nuclear Medicine from [184].

uation factors were sought.

For that, the features of CT-based attenuation maps were analyzed, identifying five attenuation classes with their respective factors (Table 5.1).

The attenuation factors for the background, fat and soft tissue are well defined and similar in all patients. But the attenuation factor for the lung tissue is dependent on the patient and his respiratory state; after analysis of the CT-based attenuation map from over a dozen patients, a value of 0.018cm^{-1} was found to represent the average attenuation. Moreover, cortical bone is reported to have a higher attenuation factor,

Tissue	Attenuation factor (cm^{-1})
Background	0
Lungs	0.01 - 0.03
Fat	0.086
Soft tissue	0.1
Bones	0.105 - 0.14

Table 5.1: Attenuation factors observed for each type of tissue in CT-based attenuation maps. The values observed for bones in CT and reported here are smaller than the real attenuation value of cortical bone due to partial volume effect, so that only a fraction of cortical bone is present in each voxel.

about 0.15 cm^{-1} [317], but the values observed for bones in the CT-based attenuation maps are usually lower ($<0.12cm^{-1}$) due to partial volume effect; indeed, the cortical bone is a thin structure (see Fig. 5.6) and the CT-based attenuation map is blurred to adjust it to the spatial resolution of PET. Moreover, the bone radiodensity and attenuation are also dependent on the patient's age and eventual diseases such as osteoporosis, so that a unique attenuation factor cannot be assigned for bone in all patients.

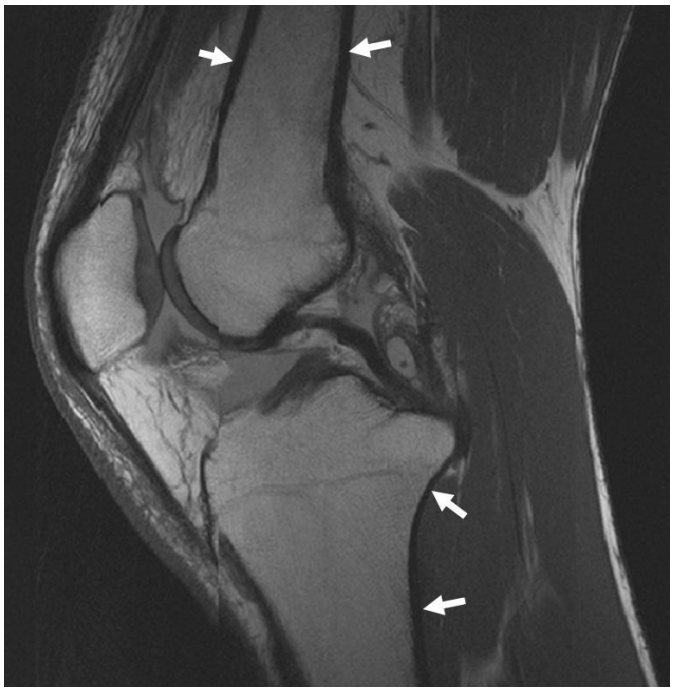

Figure 5.6: Slice from a magnetic resonance acquisition of a human's knee. In the image, the two main components of the bone are visualized: cortical bone, seen as a thin dark rim (with white arrows), and trabecular bone, the inner part, which appears brighter in this acquisition. Trabecular bone (also called spongy bone) occupies a much larger space, but it is less dense and has an attenuation factor comparable to that of fat. Cortical bone is thinner but has a higher attenuation factor.

Ideally, an MRI-based attenuation map should precisely identify these five classes. It is important to note that no additional classes need to be identified (e.g. single muscles, organs or specific tissue types); the objective is limited to the assignment of attenuation factors, so that the different intensities in the MRI image have to be all mapped to the 5 classes referred above.

5.3.1 Limited MRI Field of View

MRI tomographs are designed to have a very homogeneous B_0 magnetic field within a limited region. In most MRI scanners, the transverse diameter of the region with homogeneous field is below 45 centimeters, and it drops quickly after this limit. This means that, for rather large patients or for most patients acquired with arms-down, some parts of the body will be located out of the field of view (Fig. 5.7).

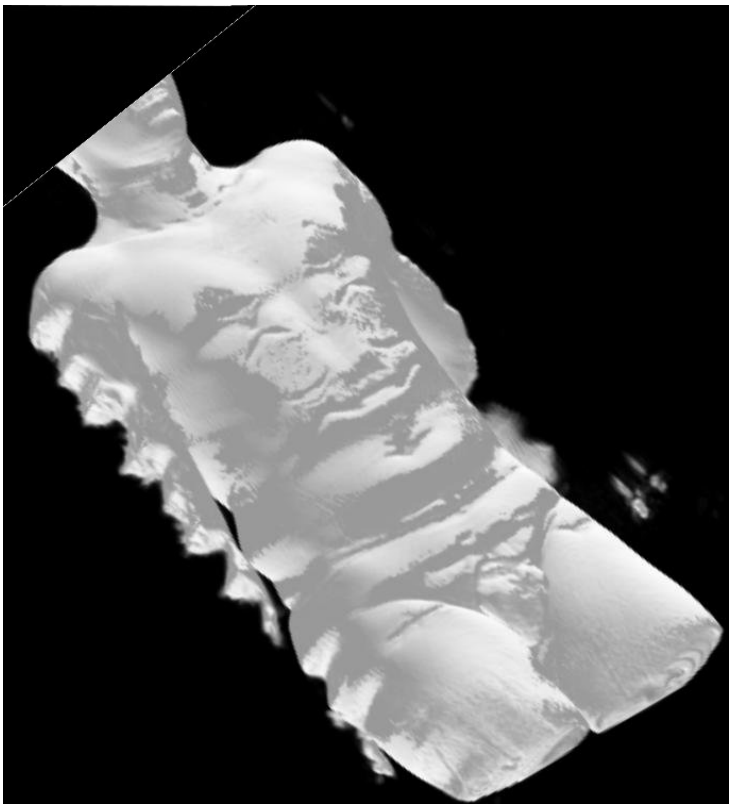

Figure 5.7: Volume rendering of an MRI acquisition performed arms-down showing the limited MRI field of view, with a significant part of the arms and parts of the hips missing.

In order to extend the field of view, it is necessary to increase the size of the main magnet and of the complete scanner, with a consequent increase in its price. At least for the first generation of combined MRI/PET scanners, this possibility is not viable.

If a part of the patient is outside the field of view, the attenuation correction is biased even if the segmentation of the attenuating classes present in the field of view was perfect [68], as shown in a reconstruction using PET/CT data in Fig. 5.8. A somewhat similar

problem was observed in PET/CT scanners: most CT systems provide a transverse field of view of 50 cm, occasionally resulting in some parts of the body extending beyond the field of view [27]. The solution adopted for PET/CT imaging was to use an extended field of view (eFOV), which consists in an extrapolation of the CT projections followed by a cosine roll-off filter to force them to converge to zero at the limits of the field of view [222].

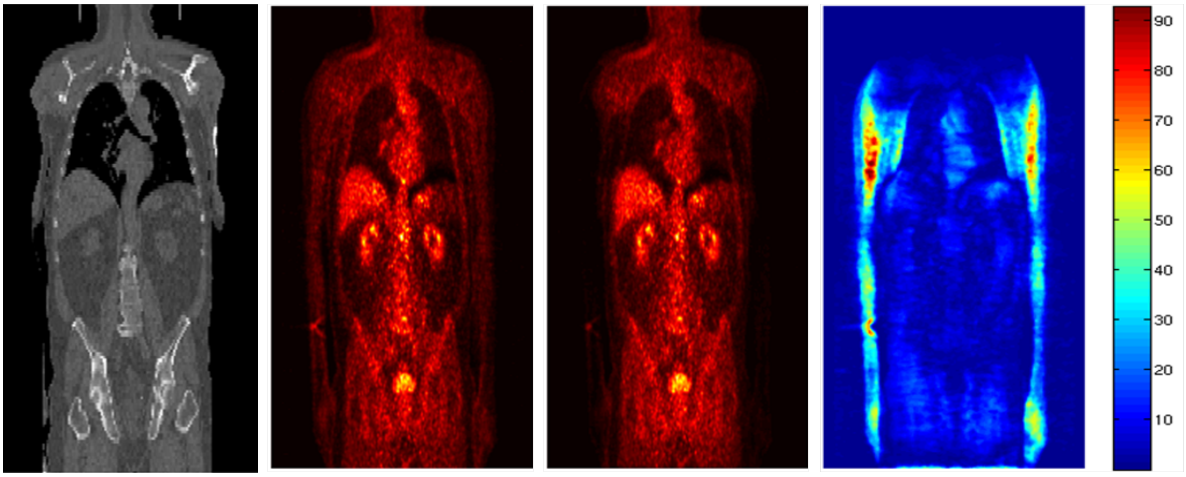

(a) (b) (c) (d)

Figure 5.8: Data from a PET/CT patient acquired with arms-down, coronal view. a) CT data after cropping the borders simulating a limited field of view as observed in MRI. b) PET data reconstructed using the original CT-based attenuation map. c) PET data reconstructed using the cropped CT-based attenuation map. d) Normalized error (in %) between both PET reconstructions. Besides strong errors at the regions located close to the arms, also the mediastinum and heart show errors over 30%, inacceptable for clinical use. Image courtesy of Dr. Gaspar Delso.

A similar solution is not possible using the acquired MRI data, and alternative approaches must be explored in order to account for the parts of the patient which are not visible within the field of view. Possible solutions are to include additional sensors (e.g. laser systems) which detect the body contour, or to use the content of the PET image to deduce some information about where there is radiotracer uptake and therefore tissue must be present [68].

Although this problem is out of the scope of this research, it is necessary to acknowledge its importance for the implementation of a complete solution for MRI-based attenuation correction in combined MRI/PET scanners.

5.3.2 Cortical bone in MRI

For the intensity-based segmentation, an MRI sequence was needed which allows mapping of each MRI intensity into one of the 5 classes. Initial research led to the conclusion that a

robust segmentation of bone in whole-body MRI images would not be feasible. The signal produced by cortical bone in conventional MRI sequences is very low and unspecific, as explained in [75]:

> On clinical scanners TE is typically several milliseconds or longer, which works well for signals with long T2*. But the water present in cortical bone has a very short T2* of about 200 to 500 μs in the mature skeleton, so the MRI signal from it decays to near zero before the receive mode of clinical MRI systems can be enabled and the signal can be encoded. As a result, bone has zero signal with all conventional pulse sequences on clinical MRI systems.

Bone segmentation in MRI is useful in a number of applications in orthopedics and rheumatology, and automated segmentation has attracted the attention of several research groups [63, 89, 37]. Research is mostly done in specific applications (e.g. knee imaging) and the use of information from several sequences has occasionally been suggested; still, automated segmentation is application-specific and error-prone. Currently, a solution for robust bone segmentation in whole-body images does not seem possible. Sequences such as ultra-short echo time (UTE) could help for this purpose [95, 243, 75, 293], but further research is still needed.

Since MRI-based attenuation correction is to be used clinically, robustness is a major requisite, and automated bone segmentation must be excluded. It is then justified to ask: is it accurate enough for clinical application to perform attenuation correction ignoring the specific influence of cortical bone? If it is not the case, alternative approaches must be explored.

In this work, a method suitable for whole-body MRI-based attenuation correction of PET data was investigated, using a segmented attenuation map with four different classes: background, lungs, fat and soft tissue. The proposed method can be used with any MRI acquisition which allows segmentation in these four classes.

5.4 Segmentation of the attenuation map on PET/CT data

Quantitative validation of the attenuation map using PET and MRI acquisitions performed on separate scanners is challenging, because the spatial registration might be compromised despite the use of non-rigid registration techniques. The misregistration might lead to errors in the attenuation corrected images which could potentially be larger than the approximation done by the segmentation itself [28, 185] and would as a consequence not fully reflect the results expected in a combined scanner. Therefore, PET/CT data was used to assess the impact and accuracy of the proposed segmentation.

5.4.1 Methods

5.4.1.1 Patient population

The study population was comprised of 35 patients referred for whole-body ^{18}F-FDG PET/CT for clinical staging of malignancy. The patients were retrospectively selected in order to study only cases where the technical challenge to the proposed approach was high. Therefore, only patients with bone metastases, lung nodules or neck lesions with focal pathological FDG uptake were selected. On one hand, the lesions located in the bones are expected to be the most sensitive to the absence of bone in the attenuation map, as well as lesions in the neck due to the significant fraction of bones for these areas. The lung lesions, on the other hand, are sensitive to the variable lung density in each patient.

The only condition for patient selection was the presence and localization of an FDG avid lesion in the aforementioned regions. No other factors (age, weight, malignancy, etc.) were considered. Altogether, 35 patients with 52 lesions were included in the study. Bone metastases were present in 9 of these patients (21 lesions: 12 in the pelvic bone, 8 in the spine, 1 in the sternum), lung nodules were present in 14 patients (15 lesions), and neck lesions were present in 12 patients (16 lesions).

5.4.1.2 PET/CT acquisition

All patients underwent the routine clinical ^{18}F-FDG protocol for oncological staging in the Siemens Biograph Sensation 16 PET/CT. Patients were injected 350 to 500 MBq of ^{18}F-FDG, depending on their weight. The acquisition started 90 minutes after tracer injection. For attenuation correction (AC), a low-dose CT (120 keV, 20 mAs) without intravenous contrast agent was performed.

5.4.1.3 Data processing

The attenuation maps were obtained from the CT data by a bilinear transformation [148]. The CT-based attenuation maps were then segmented based on the intensity of each voxel in the 4 aforementioned classes and predefined attenuation factors were assigned as observed in the CT-based attenuation maps. The intensity mapping was as follows:

voxels in the range 0-0.005 cm^{-1} were assigned to background (0 cm^{-1}), voxels in the range 0.005-0.05 cm^{-1} were assigned to lung (0.018 cm^{-1}), voxels in the range 0.05-0.093 cm^{-1} were assigned to fat (0.086 cm^{-1}), and voxels over 0.093 cm^{-1} were assigned to soft tissue (0.10 cm^{-1}). The Interactive Data Language (IDL, ITT Visual Information Solutions, Boulder, CO, USA) version 6.4 was used for all data processing. It is important to note that the segmentation was only based on the intensity at each voxel, so that no assumptions were done regarding the location of the tissues or organs. For example, due to partial volume effect, a voxel at the skin could potentially be classified as lung with its corresponding attenuation factor. Similarly, a mass in the lung would be classified as soft tissue rather than lung.

In addition, the specific importance of bone for AC of PET data was evaluated. For this, all bones were removed from the original CT-based attenuation maps by replacement of all voxels with attenuation factors above 0.105 cm^{-1} to values of 0.1 cm^{-1}, corresponding to soft tissue.

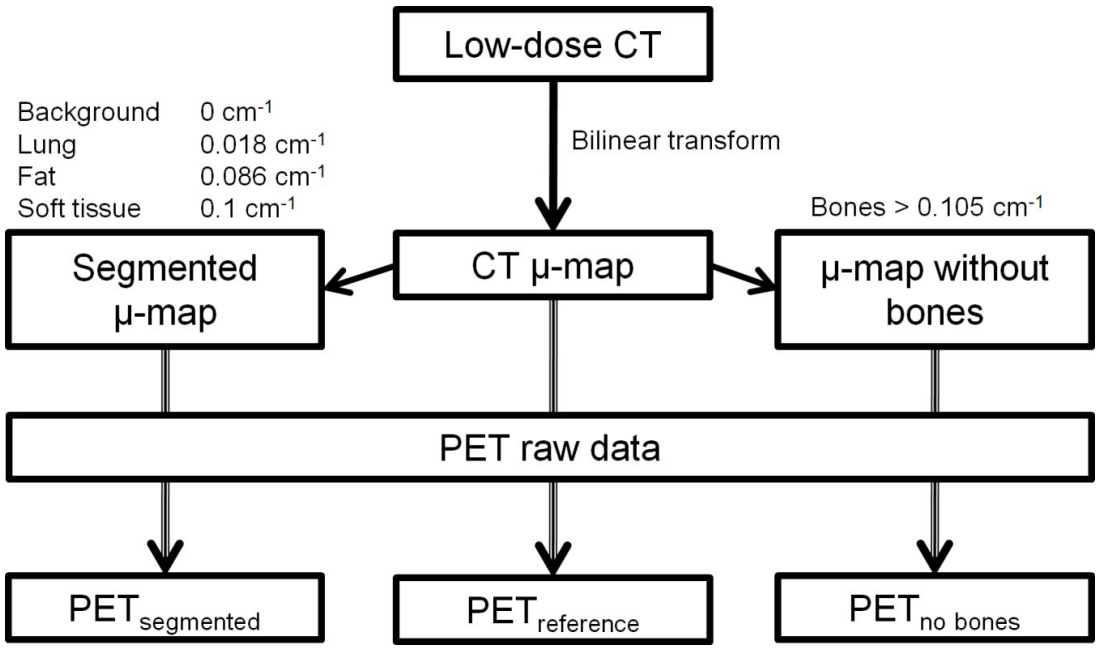

Figure 5.9: Diagram showing the three different PET reconstructions obtained with different processing of the attenuation map. On the left, segmented attenuation map using predefined attenuation factors. On the center, standard CT-based attenuation map as used routinely. On the right, attenuation map after replacement of bones by soft tissue. Image reprinted by permission of the Society of Nuclear Medicine from [184].

PET sinogram data were reconstructed using the original CT-based attenuation map, the attenuation map segmented in four classes, and the attenuation map without bones, as summarized in Fig. 5.9. PET reconstruction software from Siemens Molecular Imaging (e7 tools, Knoxville, TN, USA) was used for this purpose. The images were reconstructed using the Ordered Subsets Expectation Maximization (OSEM) algorithm with 4 iterations and 8 subsets.

5.4.1.4 Image Analysis

A Volume of Interest (VOI) was manually defined on the lesions. The VOI was defined on a fused view of the PET data reconstructed with the original attenuation map and the CT data, and the same VOI was used to assess the SUV in all three PET reconstructions. The effects of the different modifications of the attenuation map were quantified as percentage of change as compared to the original Standard Uptake Value (SUV).

In addition, an experienced observer interpreted the images reconstructed using the original and segmented attenuation map and evaluated whether there was a difference in the clinical interpretation of the studies. The observer was blinded to the attenuation map used for the reconstruction.

5.4.2 Results

The SUV changes resulting from the modification of the attenuation map depended largely on the location of the lesion considered, as summarized in Fig. 5.10. The absence of bones in the attenuation map resulted in undercorrection for bone attenuation, causing the SUV of the lesions to be generally inferior than the SUV from the images reconstructed using the original attenuation map.

The SUV_{max} in the PET images reconstructed with the segmented attenuation map decreased at most for osseous lesions, with an average decrease of 8.0±3.3%. The SUV of lesions in the neck suffered an average decrease of 3.8±2.0%, and that of lung lesions decreased by 1.9±2.3%. The SUV variations in the PET images reconstructed with the attenuation map without bones were comparable, indicating that the absence of bones was the main reason for these variations. The largest change observed in the 52 lesions considered was an underestimation of the SUV by 13.1%, which occurred in a lesion in the pelvic bone and is presented in Fig. 5.11.

Examination of the PET images by an observer blinded to the attenuation map used for reconstruction revealed no differences in the clinical interpretations of the PET scans of all patients. Neither false-positive nor false-negative findings as compared to the original reconstruction were observed. Although visual inspection of the complete PET image did not reveal noticeable changes in the activity distribution after segmentation of the attenuation map, detailed quantitative inspection revealed that the relative change of SUV for background regions with low uptake could be significantly higher than for high uptake lesions. Although clinically irrelevant, regions with very low SUV (<0.2) could occasionally show SUV variations of up to 50%. Such variations in very low uptake regions could be related to numerical instability in the reconstruction algorithm. Furthermore, the correlation coefficients between the original and segmented attenuation maps, as well as between the reconstructed PET images using each attenuation map, were found to be over 0.98 in all cases.

5.4.3 Discussion

Use of a segmented attenuation map with the 4 described classes resulted in most cases in a slight decrease of the SUV, in particular in bone lesions, which suffered most from the

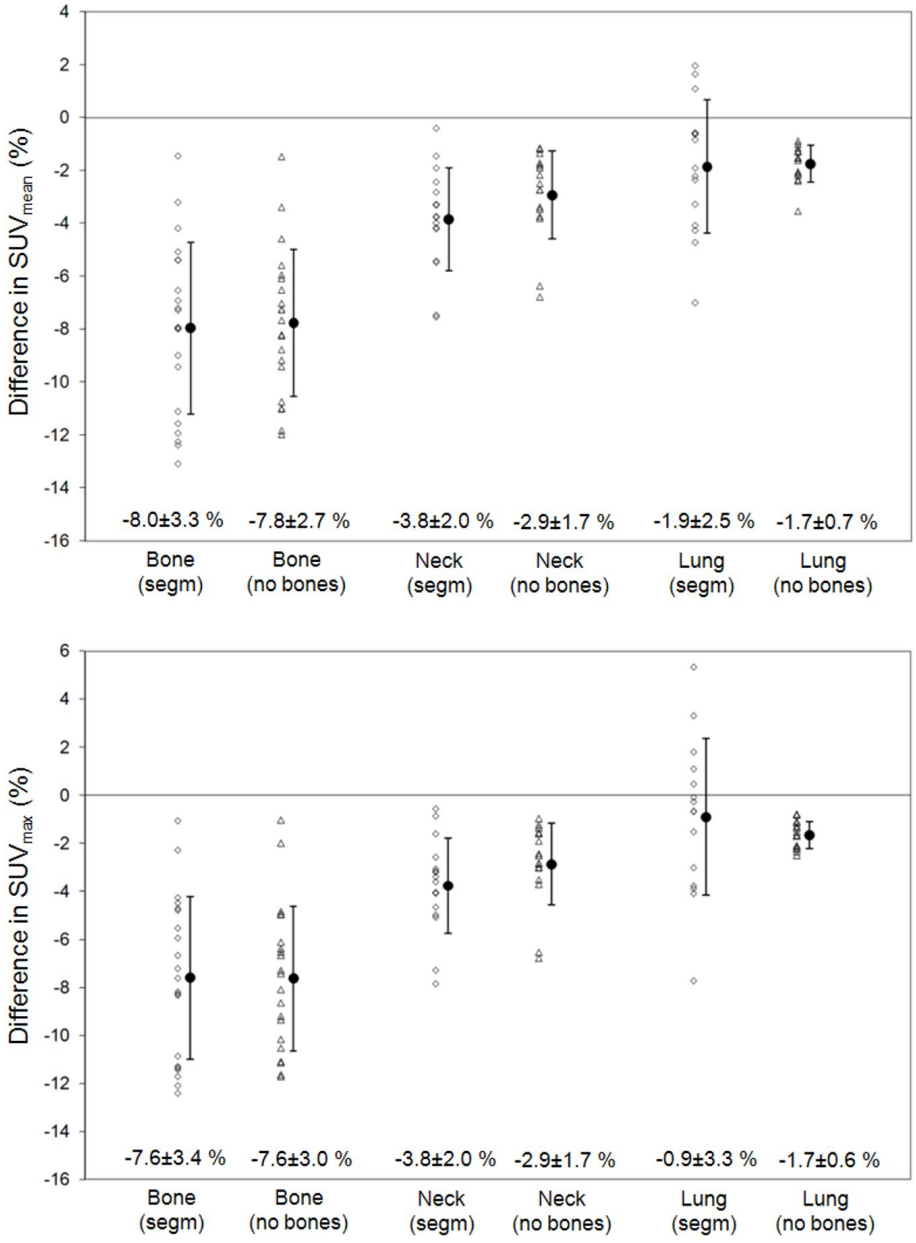

Figure 5.10: Changes in SUV_{max} (top) and SUV_{mean} (bottom) in each group of lesions produced by attenuation correction using the segmented attenuation map (segm) and the attenuation map with the bones removed (no bones) as compared to the original map. • = mean ± standard deviation. Image reprinted by permission of the Society of Nuclear Medicine from [184].

absence of bones in the attenuation map. Lung and neck lesions suffered only minor SUV changes (<8%). Reconstruction using the segmented attenuation map had no impact on the clinical interpretation of the images for all patients.

Even small SUV changes as reported here can be critical in the context of patient follow-up. An SUV change (before and shortly after start of therapy) of -25% can result

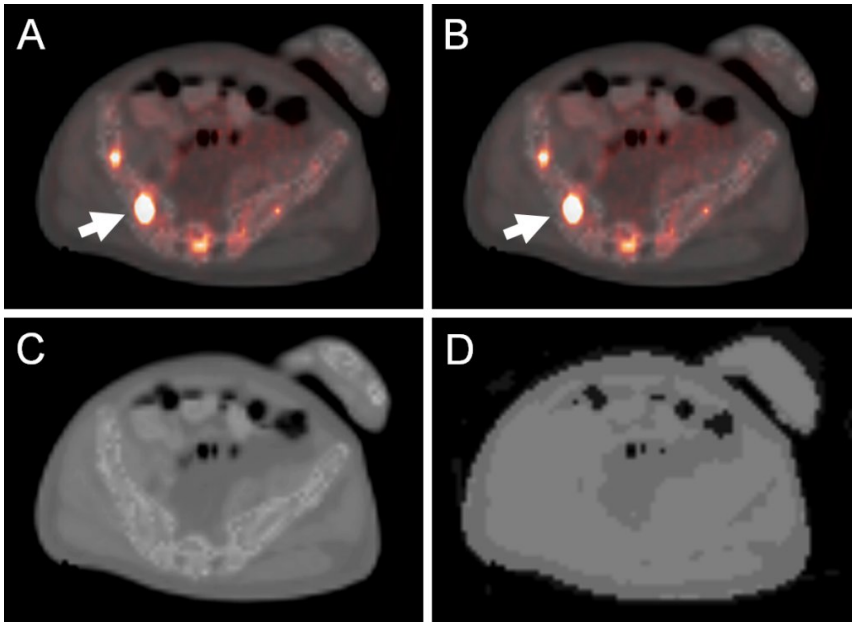

Figure 5.11: Lesion in the pelvic bone (arrow) which showed the largest SUV variation (13%) when reconstructed using a segmented attenuation map. It is difficult to note any visual differences. a) Original PET/CT image. b) PET image reconstructed using a segmented attenuation map fused to the original CT. c) CT-based attenuation map. d) Segmented attenuation map used to reconstruct image (b). Image reprinted by permission of the Society of Nuclear Medicine from [184].

in different conclusions regarding tumor responsiveness to the current therapy as compared to an SUV change of -35%, therefore having an impact on patient management. Therefore, it is important to note that the variation observed when using the segmented attenuation map as compared to the CT-based attenuation map would not prevent the segmented map and a potential MRI/PET scanner using this technique to be accurate for patient follow-up. Indeed, the SUV variation introduced by the segmented attenuation map should remain constant for a tumor throughout examinations at several time-points.

The decrease in SUV for bone lesions using the segmented attenuation map agrees with the finding by Nakamoto et al. [212], who warned, shortly after the emergence of PET/CT scanners, that calculated radioactive concentrations in osseous lesions were higher when corrected with CT as compared to Germanium based AC (average of 11% difference). As with fast transmission measurements, bones cannot be reliably segmented in whole-body MRI data. The results presented in this thesis work also indicated that the absence of bones has an impact on lesion quantification, but this impact was small for all lesions, even for those located in the pelvic bone and lumbar vertebrae. However, the influence of bones could be higher in neurological studies due to the skull, which all photons must pass before they reach the detectors. Therefore, the proposed segmented attenuation map is not suitable for neurological PET.

For the other body regions, the observed deviations should be put in perspective by considering further aspects: first, the transition from radionuclide-based attenuation to

CT-based attenuation resulted in a comparable variation for osseous lesions [212]. Second, larger variability (10%) is observed in repeated patient measurements as a result from all factors affecting the acquisition and data processing [306, 202]. And last, CT enhanced with iodinated contrast media is being used for AC of PET data in many centers despite its acknowledged bias [195, 314, 211]; these studies report that when CT scans with intravenous contrast agents are used for AC, it results in average variations of SUV_{max} of 6% for the liver, 17% for the heart, 27% for the subclavian vein and 8% for the site of primary malignancy. However, these variations did not result in differences in the clinical interpretation of the PET scans in any of the studies.

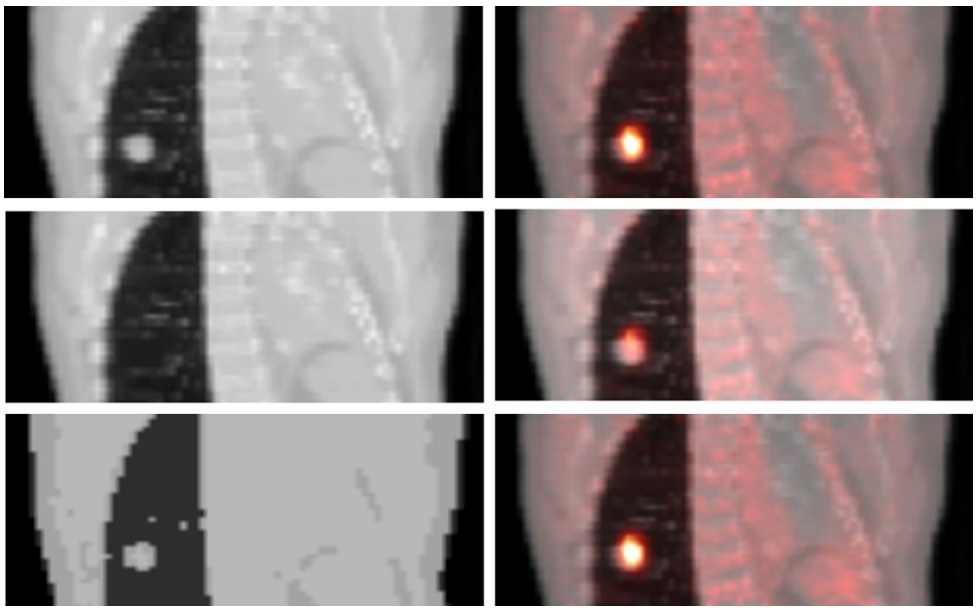

Figure 5.12: Patient with a tumor in the right lung and a pulmonary edema in the left lung. Attenuation maps used for the reconstruction (left), and reconstructed PET image fused to the original CT (right) are shown. Upper row: original CT-based attenuation map. Middle row: CT-based attenuation map with lung tumor manually removed from the map. Bottom row: segmented attenuation map. While the segmented attenuation map results in a ΔSUV of +1.6%, the deletion of the lung tumor results in a ΔSUV of -35%, indicating potential pitfalls for atlas based approaches. Image reprinted by permission of the Society of Nuclear Medicine from [184].

An alternative approach for MRI-based AC is an atlas-based registration, where the known distribution of attenuation factors of the atlas can be applied to the patient data after registration. This would have the benefit of taking bone into account for photon attenuation. While this approach performs well for neurological studies, the registration of whole-body images to an atlas is much more demanding and error-prone, since the thorax and abdomen do not have the same rigidity as the head. So far, the experience with PET/CT shows that even small emission-transmission misregistration can have an impact on the diagnostic [185, 26]. Moreover, anatomic variation cannot be regarded by an atlas while being common in the cancer patient population and often essential for AC.

Fig. 5.12 illustrates this with a patient having a lung tumor and a pulmonary edema, abnormalities which cannot be taken into account by an atlas. The potential absence of the lung tumor in the attenuation map results in a variation of the tumor's SUV by 35%. In contrast, the segmented attenuation map would reflect the real tissue distribution being therefore more robust to unusual anatomies.

5.5 MRI-derived attenuation maps

The results from the previous section indicate that an attenuation map distinguishing between four different attenuation factors (background, lungs, fat, soft tissue) would provide sufficient accuracy for clinical use. However, an MRI sequence for that purpose was not described, neither was it indicated how the MRI data should be processed in order to obtain these four classes.

For an MRI sequence to be convenient for the derivation of an attenuation map, several conditions should be ideally fulfilled:

- Good contrast between the 4 above mentioned classes
- Fast acquisition (less than 20 seconds for each bed-position to enable breath-hold)
- Enough spatial resolution (below 4 mm in each spatial direction)
- Tolerant to unavoidable physiological patient motion
- Reduced geometric distortion [282, 15]

It is difficult to accomplish these requirements simultaneously. In particular, the contrast between the 4 classes can be jeopardized by common artifacts which can arise in MRI due to e.g. inhomogeneities in the main magnetic field and physiological patient motion. Therefore, the MRI sequence was optimized together with a segmentation algorithm so that the combination of both would provide satisfactory results.

5.5.1 Methods

The procedure applied for each patient examination can be divided in 7 steps:

1. Acquisition of the PET/CT
2. Acquisition of the MRI
3. MRI-CT spatial registration
4. Segmentation of the registered MRI and conversion to attenuation factors
5. Addition of the PET/CT patient bed to the MRI-based attenuation map
6. Re-reconstruction of the PET data using the MRI-based attenuation map
7. Comparison of the PET images with MRI-based and CT-based AC

5.5.1.1 Acquisition of the PET/CT

The patients included in the study were referred for an oncological PET/CT examination. The PET/CT protocol was the usual protocol for oncological scanning with ^{18}F-FDG as described in section 5.4. The patients were pre-selected in order not to have intravenous iodinated contrast agent in the CT examination for attenuation correction, since this would have biased the results and made the CT-based attenuation correction invalid as gold standard. Furthermore, patients without oral contrast agent were preferred, although this was not always possible due to the time constraints for the scanners.

Patients provided informed consent and were then brought to the MRI tomograph to perform the additional acquisition.

5.5.1.2 Acquisition of the MRI

Three different MRI sequences were investigated. In all cases, the sequences were first tested and optimized on volunteers before proceeding to perform patient acquisitions. Each patient was examined using only one of the sequences, since the three sequences used respond rather to a progressive improvement towards more suitable MRI-based attenuation maps. Here is a short description of each of the sequences:

Proton-weighted Proton-weighted fast gradient echo sequence with fat saturation, acquired on a Philips ACS-NT scanner. Image matrix of 128x128, with 3.5x3.5 mm voxel size and a slice thickness of 5 mm.

VIBE Dixon A volume interpolated breath-hold examination (VIBE) two-point Dixon sequence [73, 62, 177] was used, acquired on a Siemens Espree scanner. Image matrix of 256x256, with 1.8x1.8 mm voxel size and a slice thickness of 5 mm. With this acquisition, in-phase and opposed-phase images are obtained, allowing the reconstruction of fat-only and water-only images.

Dual-echo Dixon A dual echo one-point Dixon sequence [178] was used, acquired on a Siemens Espree scanner. Image matrix of 128x128, with 3.5x3.5 mm voxel size and a slice thickness of 4 mm. Short and long echo are acquired, and, similarly to the VIBE Dixon, they allow to derive fat-only and water-only images.

In both Dixon sequences, the patients were covered with two surface coils. Moreover, a pressure pad to monitor the respiration of the patients was placed on the abdomen.

The patients were usually asked to place their arms in the same position as for the PET/CT examination, which is mostly performed with the arms up. Breath-holding was performed for the *stations* (bed positions) corresponding to the thorax and abdomen.

Due to time constraints, only one or two stations could be acquired for each patient with the proton-weighted sequence. In contrast, the Dixon sequences required only 14-18 seconds per station, so that 4 to 5 stations could be acquired in a reduced time and composed afterwards to obtain one single image.

5.5.1.3 MRI-CT Spatial registration

At the start of this study, the proton-weighted sequence was used, and the MRI-CT spatial registration was performed only as a translation, and applied separately to individual PET bed positions (covering only 15 cm in the craniocaudal direction). However, many problems were observed in the registered images: the position of the patient was not the same in both images, partially due to different bed curvature in each scanner; the respiratory position was different; and even if the examinations were done within less than one hour, occasional internal motion (stomach, bowel) was observed.

For that, a non-rigid registration was used, implemented as a combination of a rigid registration algorithm based on the maximization of mutual information [301, 179] and a dense non-rigid registration method. The non-rigid deformation was modeled as a vector field obtained by composition of small displacements minimizing a statistical measure of similarity between the images, following the approach described in [56]. The computation time of the non-rigid registration on a dual-core PC at 3.0 GHz ranged between 30 seconds and 1 minute, depending on the size of the images and the amplitude of the misalignment. Manual tuning of the registration parameters was needed for each patient in order to obtain successful results.

The MRI-CT non-rigid registration was applied on the MRI in-phase image (for the two-point Dixon) or on the short echo image (for the one-point Dixon). It was not applied retrospectively on the proton-weighted data after discarding this sequence for further use.

5.5.1.4 Segmentation of the registered MRI

The implementation of the MRI segmentation was different for each sequence used. With the proton-weighted approach, a binary segmentation was initially performed, classifying each voxel only as air or soft tissue based on a fixed threshold [191]. This was due to a poor histogram distribution in the first tests (Fig. 5.13). This binary segmentation was tested before the work reported in the previous section analyzing the requirements for an attenuation map (see section 5.4). After the simulations reported in the last section and improvement of some acquisition parameters, segmentation in four classes based on the intensity distribution of the histogram appeared possible in some cases (Fig. 5.14). However, the peaks were not always as clearly separated as in this last example, so that the segmentation was prone to error, and no further tests with such a segmentation were done.

With the use of the Dixon sequence, the segmentation approach was changed in order to identify four compartments (air, lungs, fat, soft tissue). The image processing steps were as follows: the fat and water images were thresholded in order to identify the voxels corresponding to fat and soft tissue and separate them from the background; voxels representing a mixture of fat and soft tissue were also used when the values in both images were above the thresholds. The lungs were identified by connected component analysis of the air in the inner part of the body [245], with application of morphological operators in order to avoid any possible connection with the external air. It was observed that some voxels containing cortical bone were occasionally identified as air due to the absence of MRI signal, as well as some voxels in the heart and aorta due to artifacts resulting from

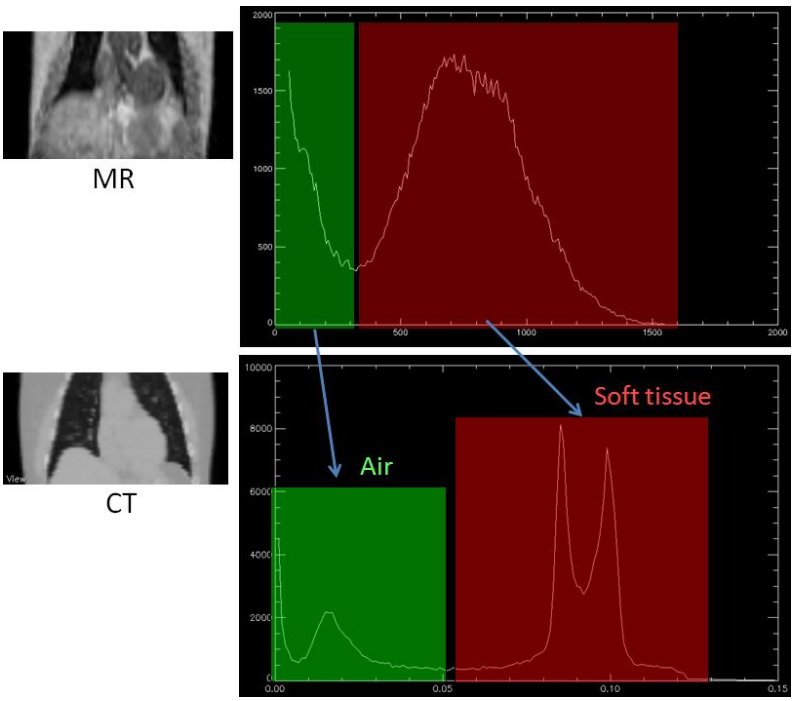

Figure 5.13: In the first proton-weighted acquisitions, the MRI histogram showed two different peaks for air (including the lungs) and soft tissue.

blood flow. This was addressed by means of a morphological closing filter (5 mm in each spatial direction) applied on the binary tissue/air image.

5.5.1.5 Addition of the PET/CT patient bed to the MRI-based attenuation map

Since the MRI-based attenuation map is used in this study for attenuation correction of the PET data acquired in a PET/CT scanner, the attenuation corresponding to the PET/CT bed must also be present. For that, after spatial registration, the region of the CT-based attenuation map corresponding to the patient bed was semi-automatically determined and copied to the MRI-based attenuation map.

The last processing step before using the map for attenuation correction was done by the tomographic reconstruction software (e7 tools), consisting in a 3D Gaussian filtering of 5 mm, the same way as it is done for CT-based attenuation maps.

5.5.1.6 Re-reconstruction of the PET data using the MRI-based attenuation map

The PET data were reconstructed with the original CT-based attenuation map as well as with the MRI-based attenuation map. In all cases, the reconstruction parameters from clinical routine were used, namely the AW-OSEM algorithm with 4 iterations and 8 subsets (see section 2.1.6). The e7 tools reconstruction software from Siemens Molecular Imaging was used for this purpose.

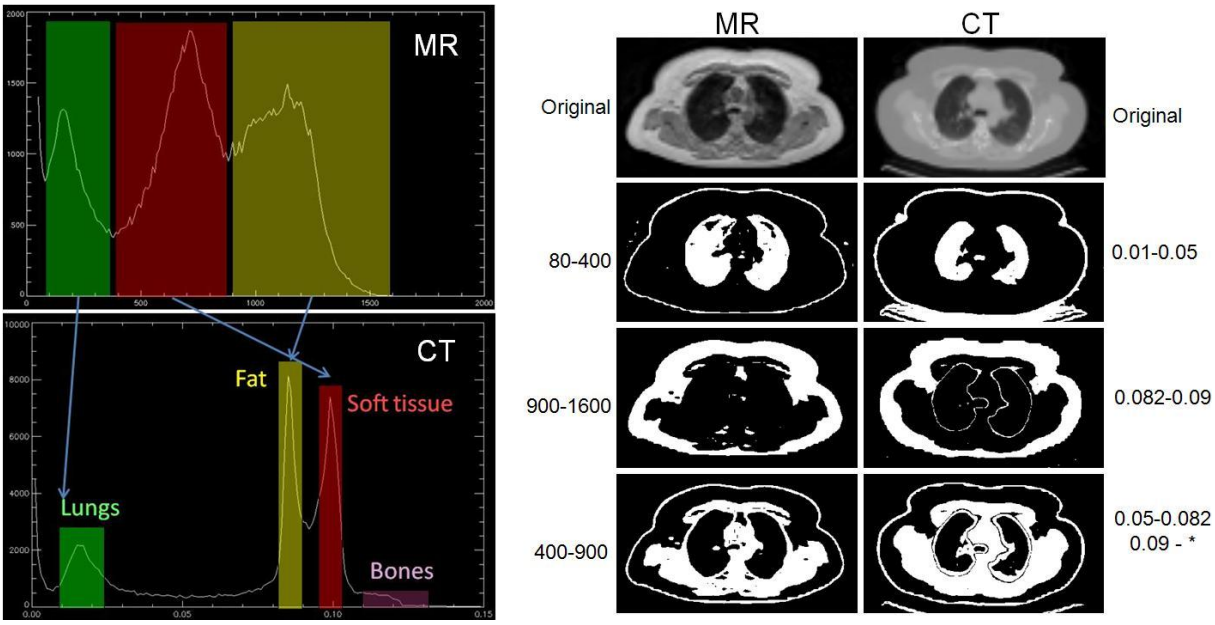

Figure 5.14: On the left, best case histogram acquired using the proton-weighted sequence. Here, four peaks can be easily separated, corresponding to each of the main four peaks observed in the CT histogram. On the right, intensity-based separation shown on the image space. A reasonable agreement between both segmentations can be observed despite an incorrect spatial registration. From top to bottom: original image, lung, fat, and soft tissue compartments.

5.5.1.7 Comparison of the PET images with MRI-based and CT-based AC

Comparison of the reconstructed images was done qualitatively (visual assessment) and quantitatively. For quantitative assessment, VOIs were manually defined on clinically relevant regions (tumors for the Dixon sequences, cardiac regions for the proton-weighted data) and their attenuation-corrected uptake was evaluated.

5.5.2 Results

5.5.2.1 Proton-weighted sequence

The rigid registration initially used with the proton-weighted sequence was far from optimal. Seven patients were acquired with both PET/CT and proton-weighted MRI, two bed positions for each. From these data, one bed position corresponding to the heart of a patient showed a good MRI-CT registration. The other datasets showed severe misregistration and were not used. As described in the methods section, the attenuation map derived from the proton-weighted sequence included only two classes: air (including lungs) and tissue, including both fat and soft tissue.

The bed position with a correct registration could be then processed, and the results from the binary MRI-based attenuation map are shown in Fig. 5.15. This was the first MRI-based attenuation correction performed in this investigation and also the first

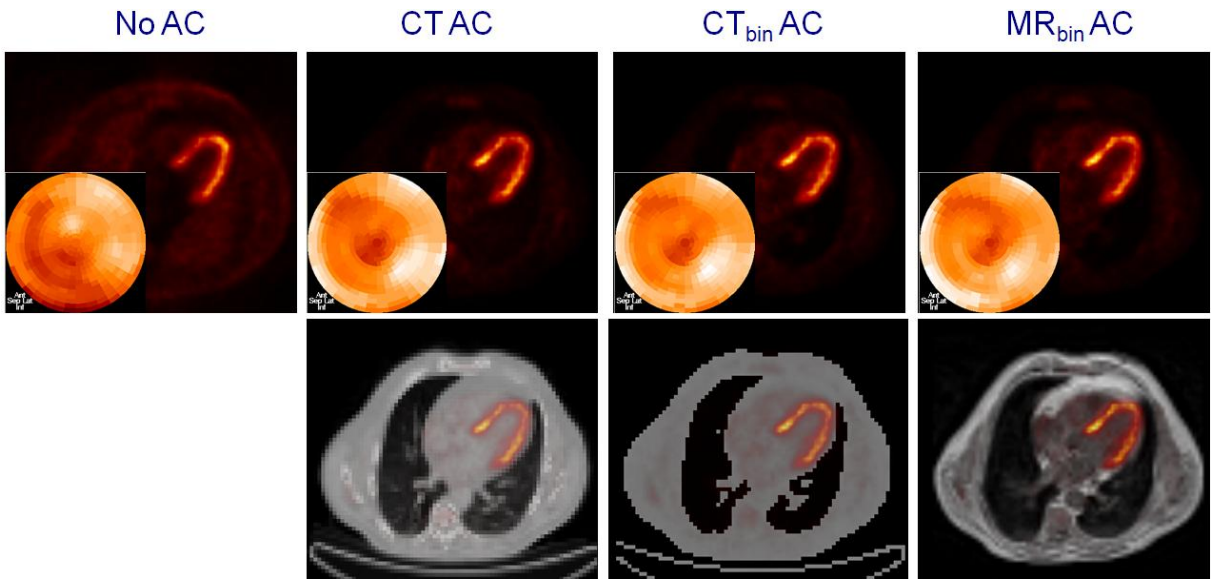

Figure 5.15: Cardiac transaxial slice and polar map showing the myocardial ^{18}F-FDG uptake (top) observed using the attenuation maps showed in the bottom row. From left to right: data without attenuation correction, with standard CT-based attenuation correction, with binary CT-based attenuation correction, and with binary MRI-based attenuation correction.

MRI-based attenuation correction reported for a non-neurological human study. The quantitative analysis indicated that the method was moderately biased. For example, the septal wall activity (determined using the polar map) was 79.5% of the maximum in the CT-AC data, 79.6% in the binary CT-AC, and 83.7% in the binary MRI-AC. That is, the MRI-based AC resulted in a 5% difference as compared to the CT-based AC. Still, these scarce results were far from being conclusive.

Since the MRI-CT misregistration would not allow to assess the effects of a binary attenuation map, it was decided to segment the CT-based attenuation map itself; that is, assess the effects of such a binary segmentation in the case of a perfect registration. This assessment was done before the results reported in the previous section (section 5.4) and served to establish the methodology used in it. In this case, the results showed a positive correlation between the change of uptake and the patient's weight (Fig. 5.16). This correlation was the consequence of ignoring the difference in the attenuation coefficient between fat and soft tissue, which resulted in an overcorrection of the attenuation produced by fat and therefore in an increased measured uptake.

Although the results from the proton-weighted approach were scarce and poor due to the initial registration problems, they were important since they led to the more accurate investigation of the requirements for the attenuation map and the development of the four-tissue model presented in the previous section.

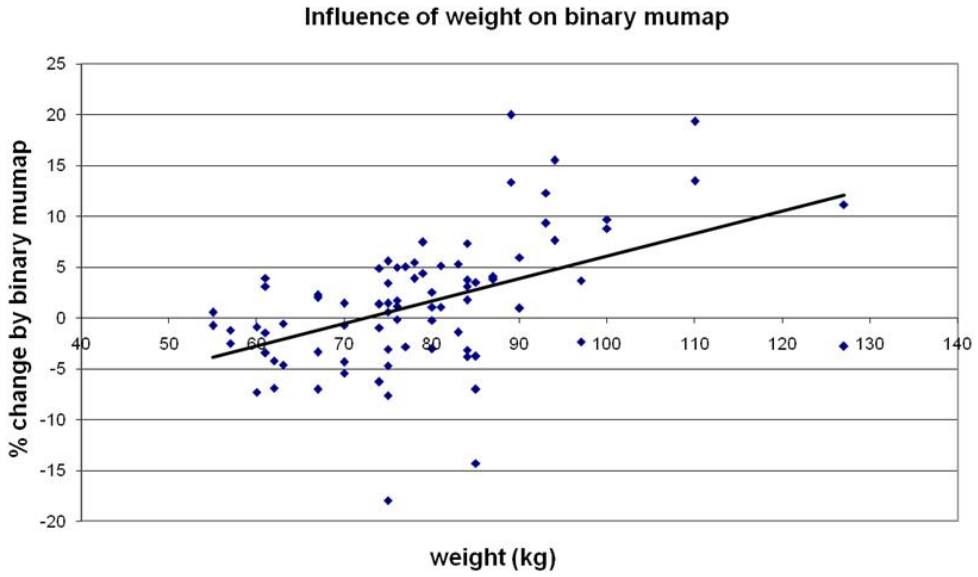

Figure 5.16: Change in uptake at manually defined VOIs between original CT-based attenuation map and binary CT-based attenuation map, shown as a function of the patient's weight. The regression line indicates a positive correlation between uptake change and patient weight.

5.5.2.2 VIBE Dixon

The VIBE Dixon approach allowed the segmentation in all four tissue classes, as shown in Fig. 5.17. Although 20 patients were acquired with this sequence, most cases could not be successfully used due to several practical issues. One of the most important issues is that the acquisition performed did not allow suitable composing of the different MRI stations, so that very often the PET bed positions could be reconstructed efficiently. Moreover, some patients showed no PET lesions, the position of the arms was occasionally different in both acquisitions, and the non-rigid registration did not always succeed. Finally, some patients had intravenous contrast agent in the CT acquisition (required for the clinical protocol), so that the CT-based attenuation map was slightly biased and could not be considered as the gold standard anymore.

Despite these problems, the segmentation results based on the sequence were promising. The feasibility of the method can be seen in Fig 5.18, showing a PET dataset reconstructed using the CT-based and MRI-based attenuation maps. No visual differences can be observed between both reconstructions. Quantitative comparison of the lesion's measured uptake revealed a 4.6% difference. Later, the acquisition of further patients using this MRI sequence was interrupted, in order to use a more adapted sequence.

5.5.2.3 Dual-echo Dixon

After the initial experience, the VIBE Dixon sequence was replaced by a dual-echo Dixon sequence with some refinements adapted to the requirements of the method and solving some of the practical issues mentioned above. Seven patients were examined using the

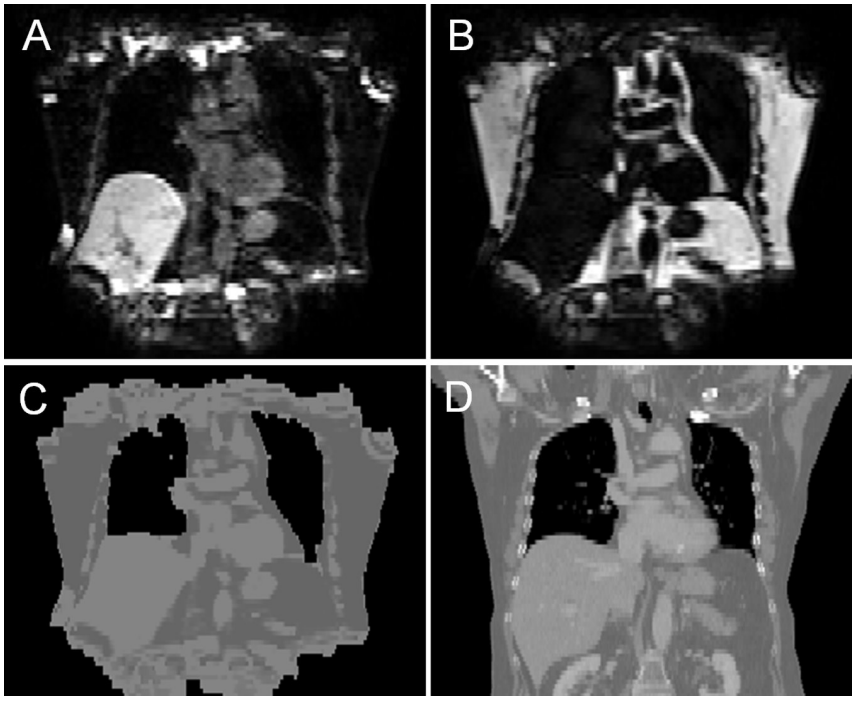

Figure 5.17: Segmentation of a VIBE Dixon sequence for attenuation correction purposes. The MRI water (A) and fat (B) images are combined and segmented to produce the MRI-based attenuation map (C). For comparison, CT-based attenuation map of the same patient (D).

dual-echo sequence. The acquisitions served to observe some weaknesses such as some motion-related artifacts appearing as signal outside of the body (Fig. 5.19) and also eventual misclassification of static fluids (e.g. bladder and eventual cysts) as air due to the small associated signal (Fig. 5.20). An enhancement of the signal from static fluids was then achieved through a stronger proton-density weighting in later acquisitions. Still, some of the practical acquisition problems as observed in the VIBE Dixon sequence remained unchanged, having sometimes contrast agent in the CT, strong differences in patient positioning, or absence of FDG-avid lesions.

Figure 5.21 shows the results of the segmentation for a patient with mediastinal and bihilar lymph node metastases. The resulting PET reconstructions (Fig. 5.22) demonstrated that suitable attenuation maps for large body regions can be obtained by means of MRI, achieving good visual and quantitative results. However, despite the use of a non-rigid registration, the exact values must be considered carefully because they represent a combination of variations resulting from 2 different sources, namely, the segmentation of the attenuation map and potential inaccuracy in the spatial registration between images.

5.5.3 Discussion

The work served to demonstrate the feasibility of MRI-based attenuation correction with a four-classes compartment ignoring the specific contribution of bone. MRI sequences

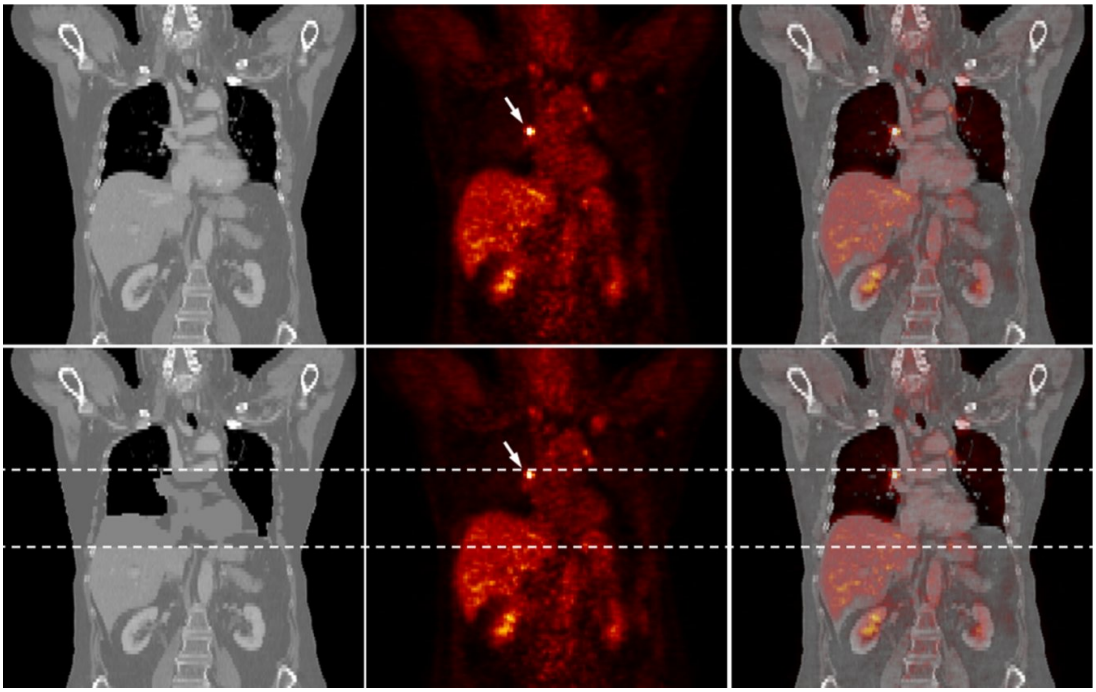

Figure 5.18: Attenuation map (left), PET images (center), and fused PET/CT images (right) of patient with an ^{18}F-FDG-avid mediastinal lymph node metastasis. On the top, original CT-based attenuation map and PET image reconstructed with this map. On the bottom, MRI-based attenuation map for region indicated by dashed lines and PET image reconstructed with this map. Use of MRI-based attenuation map resulted in a SUV change of -4.6% for the metastasis relative to results obtained with CT-based AC.

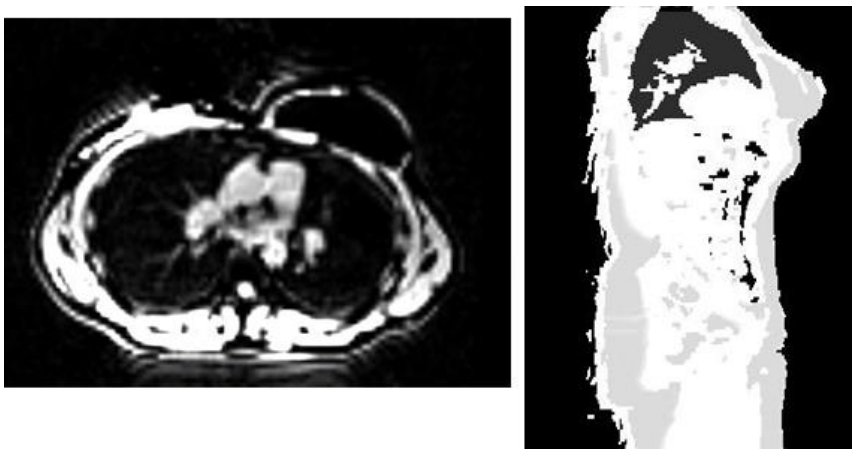

Figure 5.19: Shadowing artifacts were occasionally observed in the MRI image (left), producing signal outside the patient's body and misleading the segmentation of the body contour (right). The artifacts observed were likely related to patient motion.

with the required contrast properties are readily available.

The scarce results indicate the difficulty of validating the approach on a large number

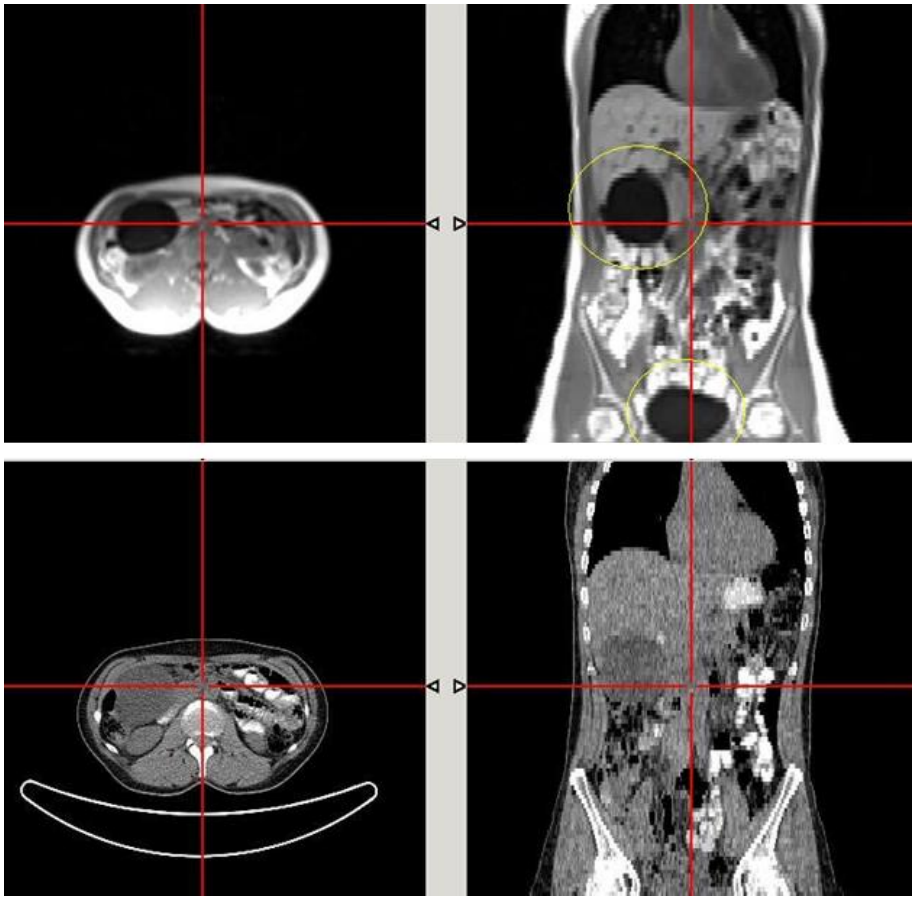

Figure 5.20: Transaxial (left) and coronal (right) views of the in-phase Dixon MRI (top) and CT (bottom) acquisitions of the same patient after spatial registration. Problematic regions (bladder and a large cyst located below the liver) showing very low signal due to the presence of static fluids are shown with a yellow circle on the MRI. These regions can eventually be misclassified as air by the segmentation approach. A stronger proton-density weighting helped increase this signal in the MRI data and improve the robustness of the segmentation.

of patients. On the one hand, it is difficult to coordinate the acquisition of PET/CT and MRI on the same patients because of logistical and workflow reasons: both scanners belong to different departments (nuclear medicine and radiology) and nearly-simultaneous free time slots must be available on both scanners; moreover, the patient has to agree to perform an acquisition which does not provide him/her any clinical benefit, and qualified staff is needed to perform and supervise the MRI acquisition. On the other hand, a large part of the patient data acquired has to be discarded because of many practical issues such as a failure of the non-rigid registration to recover the deformation for severe changes in patient positioning, parts of the patient's body located out of the field of view in the MRI acquisition or absence of FDG-avid lesions on the PET data. Also patients with contrast agent in the CT acquisition should be excluded, since the CT-based attenuation correction can then be biased.

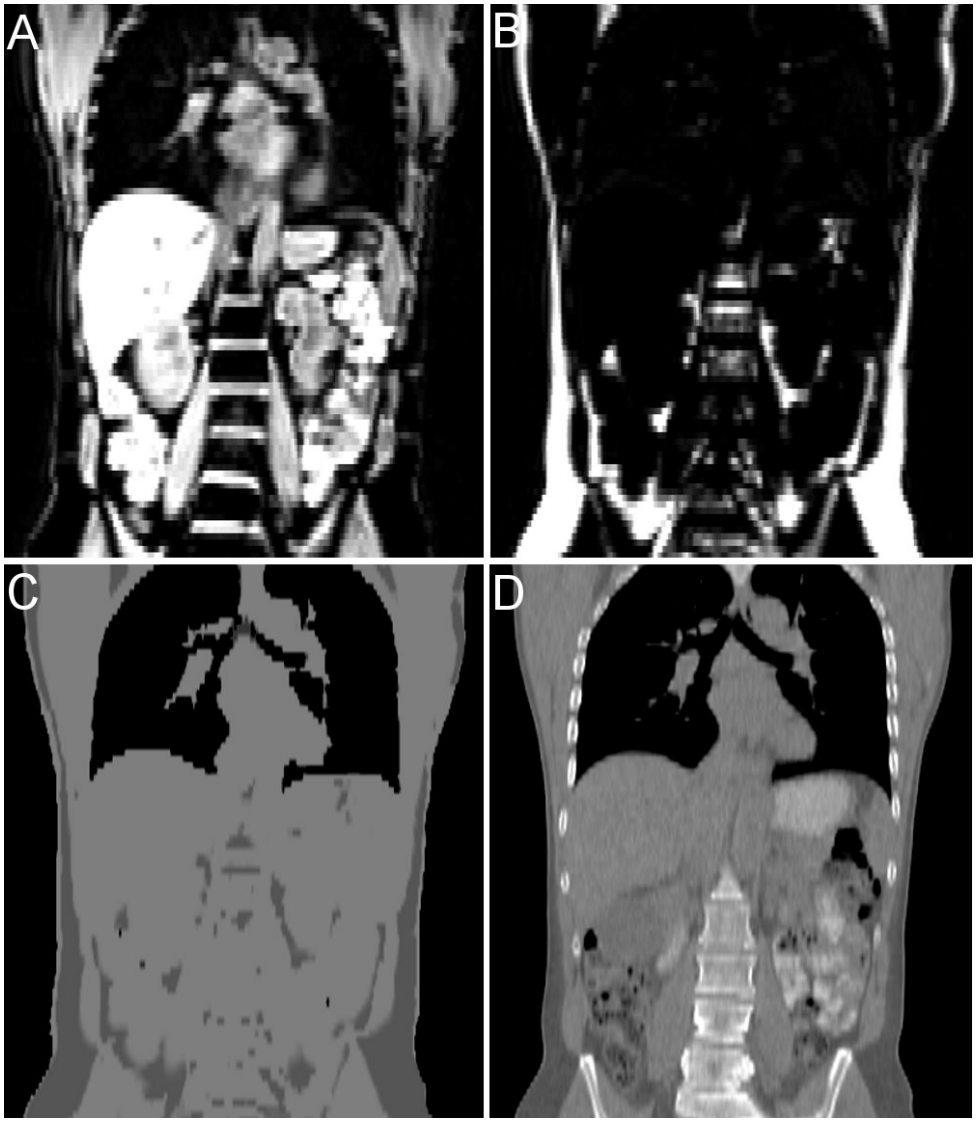

Figure 5.21: Segmentation of a two-point Dixon sequence for attenuation correction purposes, showing a larger field of view through composing of several MRI bed positions. The MRI water (A) and fat (B) images are used to produce the MRI-based attenuation map (C) as in Fig. 5.17. For comparison, CT-based attenuation map of the same patient (D). Image reprinted by permission of the Society of Nuclear Medicine from [184].

The measurements performed until now served also to underline the importance of an optimized and robust MRI acquisition. The segmentation approach cannot adequately deal with motion artifacts. The sequence must then be short enough to allow breath-holding and avoid other patient motion. Moreover, it is essential that the complete body is within the MRI field of view, since missing parts can have a dramatic effect on the attenuation correction; problems are likely to arise for large patients or acquisitions performed with the arms-down. The design of combined MRI/PET scanners should preferably include a large field of view for the MRI component. Otherwise, specific correction

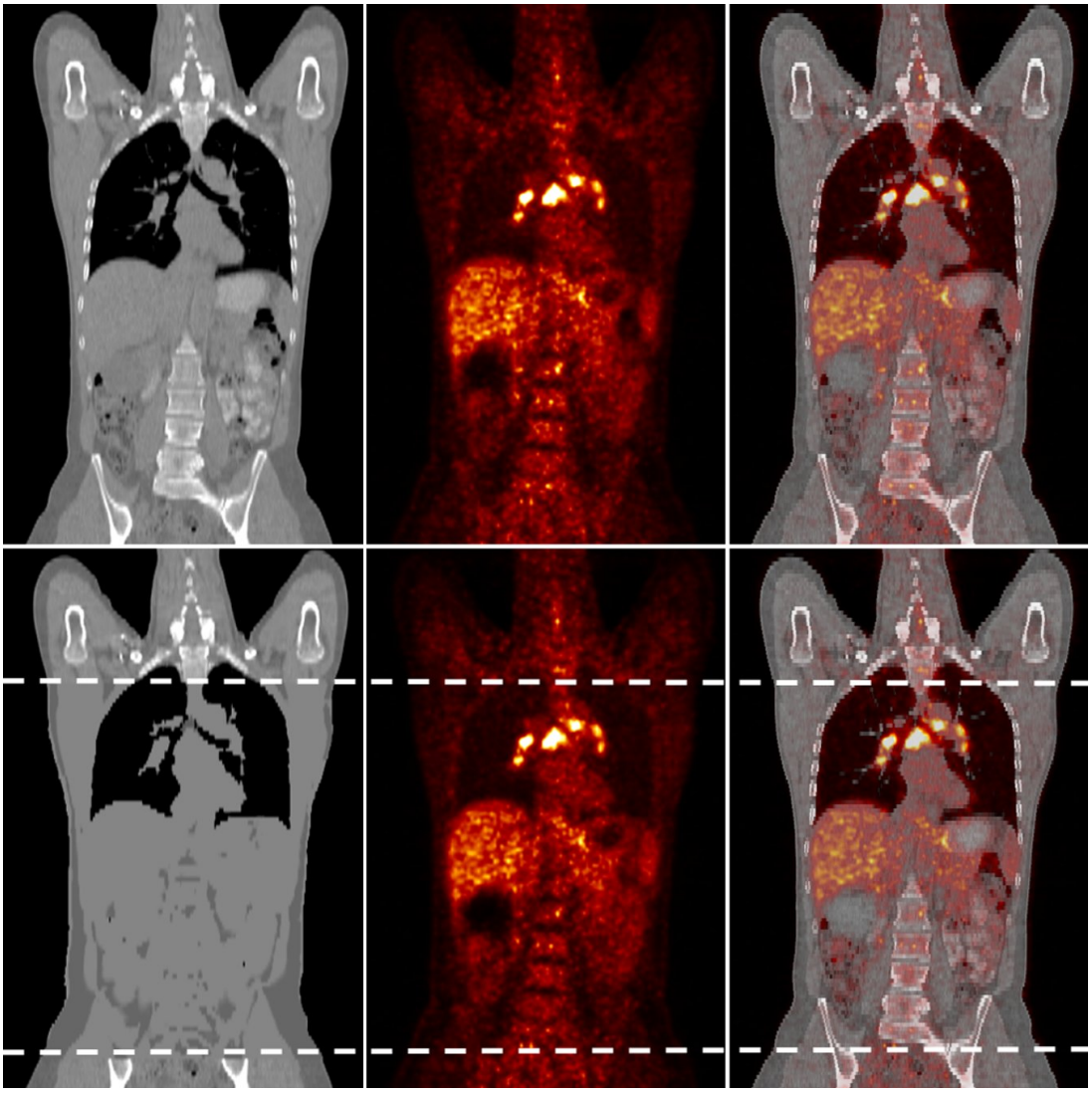

Figure 5.22: Attenuation map (left), PET images (center), and fused PET/CT images (right) of patient with multiple ^{18}F-FDG-avid mediastinal and bihilar lymph node metastases. On the top, original CT-based attenuation map and PET image reconstructed with this map. On the bottom, MRI-based attenuation map for region indicated by dashed lines and PET image reconstructed with this map. Use of MRI-based attenuation map resulted in average SUV change of 2.3% (range, -6%–+1%) for 6 lymph nodes metastases relative to results obtained with CT-based AC. Image reprinted by permission of the Society of Nuclear Medicine from [184].

techniques must be set up, such as using the uncorrected PET data to detect where the activity is arising from.

More patient measurements are needed in order to validate the method. Potential weaknesses of the sequence (such as the presence and misclassification of cysts or other eventual artifacts) can only be detected by scanning a large sample of individuals. The data acquired until now made clear that many practical issues make the validation com-

plex. But the project is still running and some promising results served as a proof of feasibility of the segmented attenuation map.

5.6 Conclusion

In a comment article in the Journal of Nuclear Medicine in 2007 [25], the development of hybrid MRI/PET tomographs was addressed by Thomas Beyer, one of the developers of combined PET/CT scanners, with a brilliant statement:

> A mere 2 y after the advent of commercial PET/CT, Johannes Czernin from UCLA, at the 2003 annual DGN meeting, commented that "PET/CT is a technical evolution that has led to a medical revolution." Today, at the dawn of PET/MRI, it may be said that "PET/MRI is a medical evolution based on a technical revolution."

The complementary value of PET and MRI makes combined MRI/PET scanners an appealing option for many research and clinical applications. Although there is still some uncertainty about the cost-efficiency of the procedure in the case of excessively expensive scanners, current expectations are high and the major hardware vendors are investing resources in its development. Still, a complete redesign of the current PET and MRI scanners is required and significant technical challenges must be overcome.

Correction for photon attenuation is part of this "revolution", being acknowledged as one of the main challenges. MRI-based attenuation correction was a nearly unexplored field when this investigation started. Novel solutions had to be developed, and approaches viable in a clinical setup were sought, where the maximum robustness is required.

Based on the previous experience with standalone PET and PET/CT, and considering the properties of MRI, a segmented attenuation map with four tissue classes was proposed, with the target of deriving it from one single MRI acquisition. It was shown on PET/CT data that such a segmentation would provide adequate attenuation maps, with the acknowledged drawback of the undercorrection for bones; therefore, according to the results reported here, osseous lesions will show a slightly decreased SUV when using MRI-based AC with the segmentation approach as compared to CT-based AC. This SUV decrease did not change the diagnosis in all patients analyzed, and appeared to be acceptable for clinical routine. Still, the image-readers have to be aware of this fact when comparing examinations between both scanners.

PET/CT data were used to perform a preliminary assessment of the potential and limitations of a segmented attenuation map. However, MRI data is needed for the final validation, since it is necessary to demonstrate that the segmentation applied on the CT image can also be achieved based on MRI data. One example is the misclassification of bones: if bones were classified as soft tissue in the segmented CT attenuation map, it is necessary to show that segmentation of the MRI data would also result in bones being classified as soft tissue, and not as air or lung tissue.

The PET/CT and MRI data acquired from the same patients served to show that comparable segmentation could be achieved with a Dixon sequence. Limitations in the MRI field of view were not addressed: patients acquired with arms-down could not be used because of this reason. Despite the numerous practical issues, further PET/CT and MRI acquisitions on the same population are needed to fully validate the proposed approach and eventually indicate if any additional refinements are needed on the MRI sequence.

Furthermore, comparison of the segmented attenuation map to other approaches such as a combined atlas and pattern-recognition [121] would be certainly interesting, once a patient atlas is developed for this purpose.

With the currently available results, segmentation of the attenuation map in four classes appears to be accurate enough for implementation in future clinical MRI/PET scanners. A small decrease of the SUV for osseous lesions is predicted by the measurements reported here; although this difference was clinically irrelevant in all patients analyzed, the image-readers should be aware of it when comparing PET images obtained from an MRI/PET scanner to images from a PET/CT scanner. The data acquired serve to show the feasibility of an MRI-based segmentation, but further validation with a large number of patients is needed to demonstrate that the segmentation performs robustly enough for clinical use.

CHAPTER 6

Conclusions

Molecular imaging with PET offers a broad spectrum of possibilities. The development of new radiotracers and new therapeutic approaches makes it an exciting and dynamic area. And also an area with numerous new challenges.

The sensitivity of commercial PET tomographs has increased dramatically in the last decade mainly because of acquisition in 3D mode and the development of new scintillators. Diagnostic image quality in PET can be now obtained with an acquisition time below 2 minutes per bed position (about 20 cm). This has a direct impact on the observed spatial resolution for clinical acquisitions: the patient motion due to anxiety, fatigue, etc. is significantly reduced, and therefore sharper, less blurred images are obtained. This is to be added to improvements in intrinsic spatial resolution achieved by using smaller crystals, faster electronics and new reconstruction algorithms. Performance measurements with state-of-the-art PET scanners report a spatial resolution close to 4 mm at the center of the field of view.

Although an acquisition time below 2 minutes per bed position results in a significant reduction of the patient's voluntary motion during the acquisition, respiratory and cardiac motion are still present. Their contribution to the degradation of image quality is critical. Myocardial imaging suffers from both motions simultaneously, so that the observed spatial resolution in clinical examinations is far worse than the scanner's intrinsic resolution. In this work, respiratory sensors for use in PET imaging were evaluated, and a respiratory gating scheme which could be combined with cardiac gating was implemented. Dual gated acquisitions might play an essential role in cardiovascular imaging, with potential application to resolve transmurality of the perfusion defects and also for imaging the vulnerable coronary plaque with PET once suitable tracers are available. The main PET manufacturers decided to include respiratory gating in their commercial PET/CT scanners in the recent years, realizing its usefulness for both cardiac and oncologic imaging, and some of them also introduced the capability to perform dual gated acquisitions.

The recent evolution of PET reflects a clear trend towards multimodality imaging.

Standalone PET scanners are virtually not sold anymore and have been replaced by combined PET/CT scanners. CT undeniably helps the diagnosis, but it also allows faster acquisition by saving the time which was previously dedicated to transmission scans, needed to correct for patient specific photon absorption. CT-based attenuation maps can be acquired within seconds and provide better statistics, so that the resulting PET images are less noisy. However, the non-simultaneous acquisition and different temporal resolutions of PET and CT have resulted in misregistration problems which affect especially the thoracic area, due to differences in the respiratory state in both images.

This issue was investigated focusing particularly on cardiac imaging, and it was shown that it could often mislead the diagnosis and produce false-positive defects. Image-readers must be aware of this limitation when reading cardiac examinations performed in PET/CT scanners, and a quality control appears necessary. Manual registration is possible, but somewhat inconvenient and operator-dependent. As alternative, an automatic emission-driven approach was developed and evaluated, showing potential for routine use. These findings, novel in cardiac PET/CT imaging, were soon confirmed by other studies, and the possibility of correcting the misregistration after the acquisition has been since then included in all commercial scanners.

The success of multimodality imaging with PET/CT scanners has recently renewed the interest in combined MRI/PET scanners. Its development faces many challenges. Among those, the necessity of achieving a satisfactory MRI-based attenuation correction, which is essential for the scanner to be clinically viable.

MRI is not based on the transmission of high-energy photons throughout the body; due to the fundamentally different physics, it is not possible to directly measure an attenuation map with MRI. Based on previous approaches for attenuation correction in PET, a segmented attenuation map which can be derived from a single MRI acquisition and differentiates between four different attenuation classes was proposed. Simulations based on PET/CT data showed that such an approach would be suitable and not change diagnosis as compared to CT-based attenuation correction, although an undercorrection for osseous lesions was observed. The patient data acquired so far with PET/CT and MRI served to show the feasibility of this method and to set the basis for use in combined whole-body scanners. Further acquisitions should help validate the method before its introduction for routine clinical use.

In summary, the work presented serves to overcome some of the current limitations of PET imaging and finally to improve the diagnostic value of PET and contribute therewith to the benefit of the patient.

APPENDIX A

Computed Tomography

Computed Tomography (CT) in modern scanners is usually acquired by rotating an x-ray source around the patient, having x-ray sensors positioned on the opposite side, and moving the patient's bed continuously, in the so called helical acquisition mode (Fig. A.1).

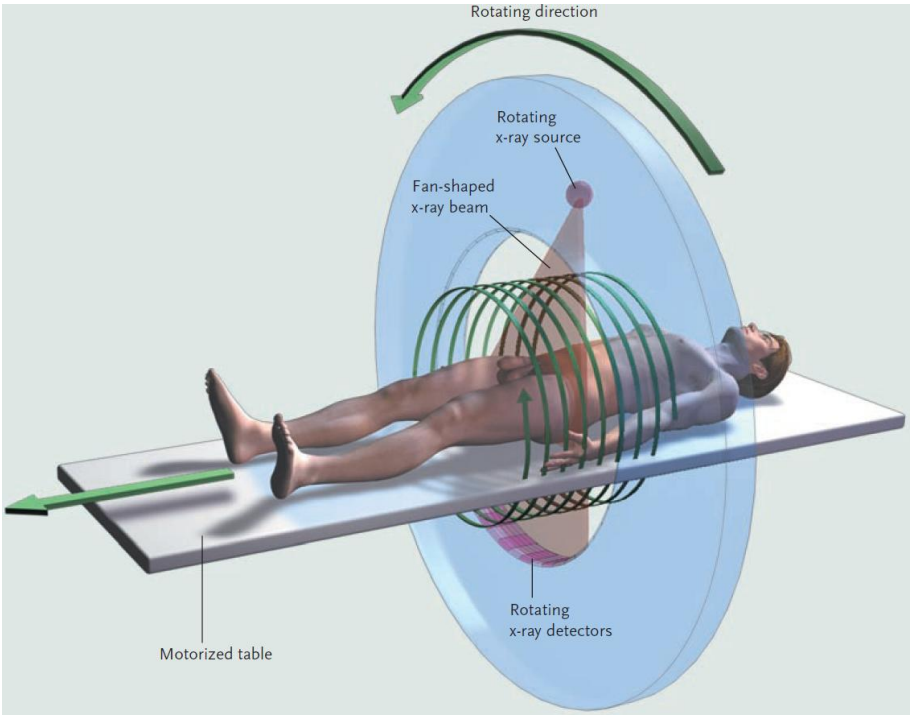

Figure A.1: Principle of the helical CT, with an x-ray source on one side and x-ray sensors on the other side. Both rotate simultaneously while the patient's bed is displaced. Image reproduced from [40] with permission from the Publishing division of the Massachusetts Medical Society.

The data acquired are a forward projection of the radiodensity of the imaged object, so that tomographic reconstruction techniques are used (similarly to PET). Most often, reconstruction is achieved by means of the filtered backprojection algorithm described in section 2.1.6 together with techniques to account for the helical acquisition geometry.

After reconstruction, the CT images reflect the radiodensity of each voxel according to the scale proposed by Hounsfield, where air has a radiodensity of −1000 Hounsfield Units (HU) and distilled water a radiodensity of 0 HU. For any material X, the radiodensity in HU is computed as:

$$\frac{\mu_X - \mu_{H_2O}}{\mu_{H_20} - \mu_{air}} \times 1000$$

With μ being the linear attenuation coefficient of the materials. The radiodensity of some relevant human tissues according to Hounfield's scale is shown in Tab. A.1.

Material	HU
Air	−1000
Lungs	−900 – −600
Fat	−120
Water	0
Muscle	40
Contrast agent	> 100
Bone	> 100

Table A.1: Radiodensity of materials and human tissues according to Hounsfield's scale.

CT provides high resolution morphological images of the body (Fig A.2), with an excellent contrast beween air, adipose tissue, soft tissue and bone. Contrast agents may additionally be used to highlight some regions, such as the gastrointestinal tract or the blood vessels. However, the soft tissue contrast is poor if compared to other imaging modalities such as MRI.

CT technology has impressively evolved in the last 20 years [90, 227, 86]. The spiral acquisition mode was introduced in 1989 [139], allowing continuous volume scanning. This was followed in the late 1990's by a major breakthrough with multi-slice systems [12, 171, 124], resulting in improved spatial and temporal resolutions and faster acquisition times; systems with 256 slices are commercialized nowadays. Moreover, 2005 saw the advent of dual source CT [85, 233, 200], which makes it possible to halve the temporal resolution (Fig A.3) and is capable of providing dual-energy images acquired simultaneously.

State-of-the-art CT scanners have a temporal resolution below 100 ms and an isotropic spatial resolution below 0.4 mm. These features make CT able to assess the coronary tree with an accuracy comparable to that of conventional angiography, as will be discussed in more detail in section 2.3.

CT images can suffer from different artifacts resulting from the physics of the acquisition, the scanner and the patient motion. Most artifacts can be efficiently corrected by software, but some are still be present in the images. Despite the speed of modern scanners, motion artifacts are sometimes observed, appearing as shadowing or eventually

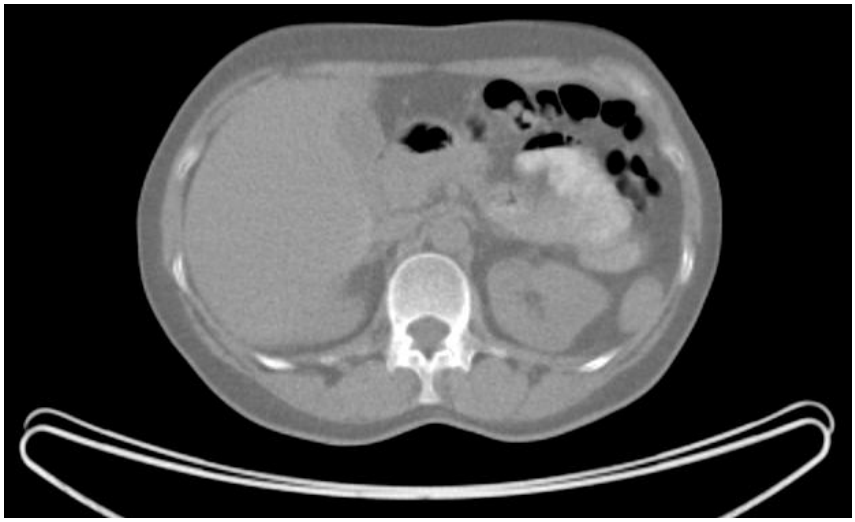

Figure A.2: Example of a CT transaxial slice of the abdomen acquired with a Siemens 64-slice CT. A good contrast can be observed between air, adipose tissue (fat), soft tissue and bone.

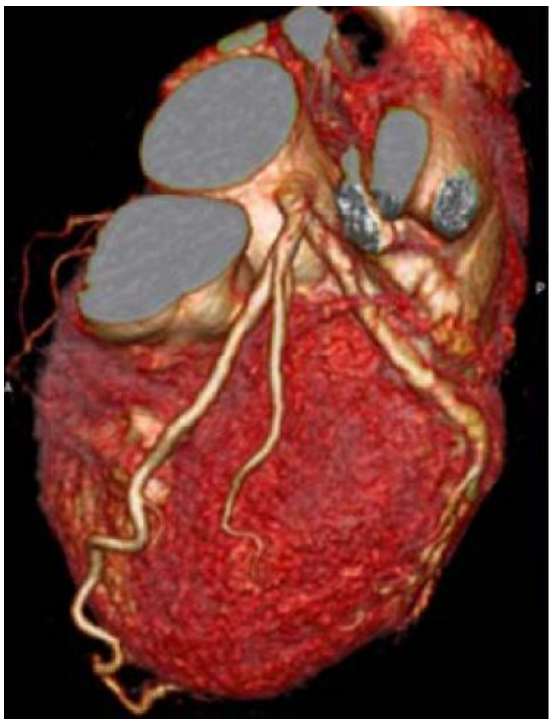

Figure A.3: Volume rendering of a dual source CT angiography, showing high spatial resolution and clearly depicted coronary arteries without motion artifacts. Reproduced with kind permission from Springer Science+Business Media from [85].

as deformed anatomy. Furthermore, metal objects or implants can also lead to streaking artifacts, because of the high attenuation produced by metal, making it difficult to assess

the regions in its proximity.

One important drawback of CT is its associated ionizing radiation [40]. The patient dose depends strongly on the purpose of the exam and the acquisition parameters, but can be above 15 mSv for acquisitions such as coronary angiography (CTA). However, dose reduction techniques have been implemented and improved in the last years, making it possible to acquire a high-quality CTA with a dose below 5 mSv.

APPENDIX B

Magnetic Resonance Imaging

The Nobel prize in physics in 1952 was awarded to Felix Bloch and Edward Purcell for the development in 1946 of Nuclear Magnetic Resonance (NMR), the scientific principle behind Magnetic Resonance Imaging (MRI). In 1971 Damadian proposed measuring the relaxation time of the spin of the hydrogen protons in water to get information about biological tissues, reporting that normal tissue and tumors studied in vitro had different relaxation times [64]. Due to the high concentration of hydrogen protons in the human body (e.g. in water and fat), application for clinical detection of diseases could be envisioned.

In 1973 Paul Lauterbur made a fundamental proposal on how to form an NMR image: in addition to the static magnetic field, a magnetic field gradient also had to be applied, allowing spatial localization of the signals [167]. For this, he was awarded the Nobel prize in physiology and medicine in 2003 together with Sir Peter Mansfield, who patented the method of selectively exciting and defining a slice across a sample [94] and made essential advances on echo-planar fast pulse sequences [183], allowing much faster imaging. Shortly after the publication of the work from Lauterbur, phase and frequency encoding and the Fourier transform started being used [158, 78], establishing the basis of modern MRI acquisition and for which Richard Ernst would get the Nobel Prize in Chemistry in 1991. Finally, in the early 1980s, MRI entered the clinical arena, quickly becoming a mainstream imaging modality.

The basic idea of MRI is to study the response of the magnetized tissue to radio frequency (RF) signals and deduce the underlying properties of the tissue. An MRI system consists mainly of three hardware components (Fig B.1):

Main magnet The main magnet produces a high magnetic field B_0 which is used to magnetize the tissue. The higher the magnetic field, the higher the SNR which can be potentially achieved with the scanner [258]. It is essential that it is homogeneous over the imaging volume in order to avoid distortions in the acquisition; additional shim coils are used to guarantee the homogeneity even after the introduction of the

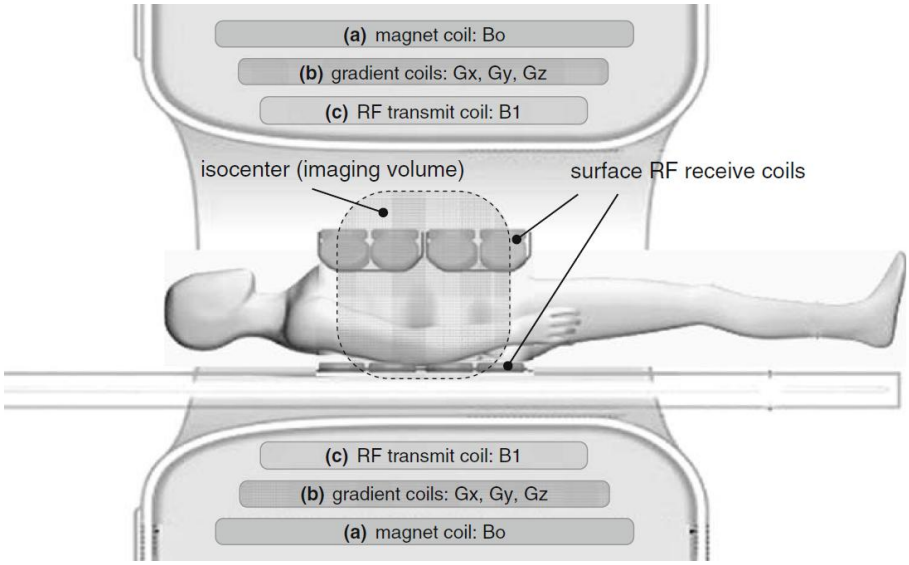

Figure B.1: Schematic view of an MRI scanner, with the main magnet producing a strong homogeneous magnetic field (a), the gradient coils responsible for the spatial localization of the signal (b), and a RF transmit coil (c), with the signal response from the excited spins within the patient being measured by local surface coils placed on the imaging volume. Reproduced from [209] with permission from the authors.

patient in the bore. Other than some open MRI scanners using permanent magnets, most clinical scanners use a cylindrical superconducting magnet consisting of a solenoid of wire (typically niobium-titanium), which operates within liquid helium at 4 kelvin in order to have superconducting properties and not offer resistance to the flowing current. Therefore, the magnetic field always stays on even when the scanner is not being operated. Modern clinical MRI scanners have a main magnet producing a field strength of typically 1.5 or 3 Tesla, although preclinical and research scanners can use 7 Tesla and above. For comparison, the Earth's magnetic field strength is about 0.00005 Tesla.

Gradient coils The gradient coils allow the spatial localization of the signal. Usually, three pairs of coils are used to generate magnetic field gradients in the x, y and z directions, but they can also be combined to generate oblique gradients for imaging any off-axis plane. The coils generate a less intense magnetic field which is added on top of that from the main magnet, and which varies linearly throughout the imaging field of view. As opposed to the main magnet, these coils are normal electromagnets and the current which flows through them can be modified within a short time. Both scan speed and image quality are influenced by the gradient coils: they should have a high gradient amplitude (in mT/m) and a fast gradient slew rate (in mT/m/ms) for optimal performance. However, these parameters are also limited by safety concerns over peripheral nerve stimulation [256].

Radiofrequency system The radio frequency system is responsible for creating a mag-

netic field B_1 which selectively excites the spins of the nuclei in the tissue by varying at their Larmor (resonance) frequency, and for measuring the magnetic field produced as a response by the tissue, which can be measured by induction of a current flow in the coils. For that, some coils are transmit coils, some coils are receive coils, and some coils can operate in both modes. Usually, a so called body coil is permanently integrated into the MRI housing, which can operate as transmit and receive coil. Additionally, local surface coils positioned directly over the imaged areas of the patient can be used, allowing to achieve a higher SNR at the expense of an eventual loss of signal homogeneity. Furthermore, several coil elements can be combined as phased-array coils to cover larger regions and speed up the acquisition, in the so called parallel imaging mode [128, 164].

MRI cannot be understood without the concept of *spin*, first proposed by Wolfgang Pauli in 1924 [230]. Individual unpaired protons, neutrons and electrons each possesses a spin of 1/2. However, two or more particles can pair up to eliminate the manifestations of their spin. MRI can use the nuclei of the atoms with a non-zero net spin, such as ^{1}H, ^{2}H, ^{31}P and ^{13}C. Due to the non-zero spin, these nuclei have a magnetic moment in the direction of the spin axis, behaving like a tiny magnet rotating around this axis.

For clinical imaging, only those nuclei with non-zero spin which are abundant enough within the human body can be used. For this reason, hydrogen nuclei are most often used, since hydrogen represents over 60% of the atoms in the body. Furthermore, they have the advantage of having a strong magnetic moment since they have one single proton. From now on, for reasons of simplicity, imaging will be described using protons, with protons referring specifically to the nuclei from the hydrogen atoms. However, the explanations can be extrapolated to any other nuclei with non-zero spin.

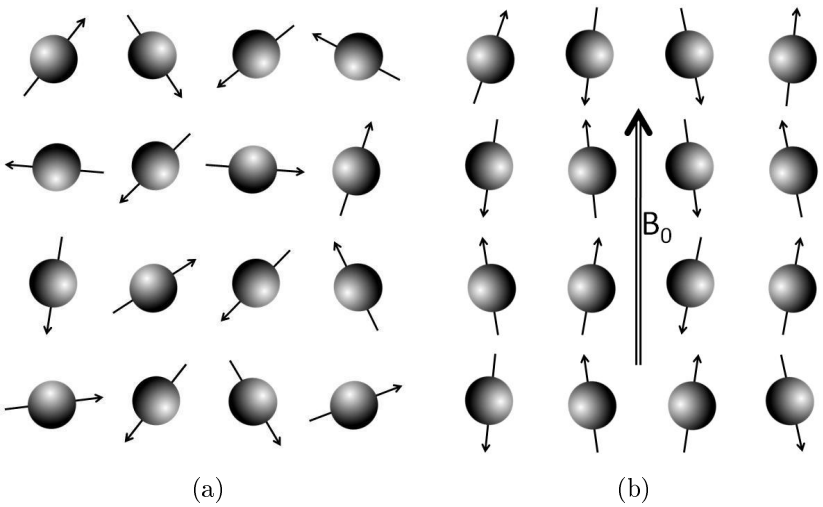

Figure B.2: a) In the absence of a magnetic field, the spins are arbitrarily oriented, with a net magnetization equal to zero. b) Within a strong magnetic field, the spins tend to align with the direction of the field, with a small excess of spins in the parallel state.

In the absence of a magnetic field, each proton aligns in an arbitrary orientation, and therefore the net magnetization M (the sum of the magnetic moment of all spins) is zero. However, when placed in a strong magnetic field B_0, protons tend to align with the field, the same way a magnet would (Fig B.2). They can align in a low energy state (parallel state), with the north face of the proton towards the south face of the magnet, and in a high energy state (antiparallel state), with the north face towards the north face. At absolute zero temperature, all protons would align in the parallel state, but at room temperature, due to thermal agitation, the spins are distributed in both states, with a very small excess of spins in the parallel state, only a few per million. The excess of spins in the parallel state depends linearly on the strength of the magnetic field applied. Since only this excess is used to produce a signal in MRI, as will be described below, higher SNR can potentially be achieved by using stronger magnetic fields.

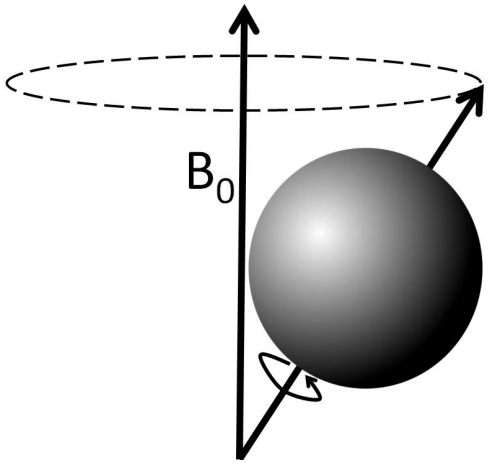

Figure B.3: Schematic representation of a precessing proton, showing the wobbling around the direction of B_0 and spinning simultaneously around its axis.

Even though the net magnetization of an ensemble of protons is parallel to the magnetic field B_0, single protons have a rotation axis which precesses around the direction of the magnetic field (Fig B.3). The frequency of the precession is called the *Larmor frequency*, and depends mainly on the strength of B_0 and on the nuclear species. For example, in a 1.5 Tesla magnetic field, the protons from the hydrogen nuclei have a Larmor frequency of about 64 MHz.

When radio frequency energy at the Larmor frequency is provided by the transmitter coil, creating a rotating magnetic field B_1, some of the exceeding spins in the parallel state swap to the antiparallel state, that is, to a state with higher energy. The strength and duration of the RF signal applied will determine the energy available for the spins to achieve transitions between both states. For example, the RF signal can be adjusted in order to rotate the net magnetization vector M by 90° (to be perpendicular to the direction of the magnetic field) or by 180°. The angle of the tilt is referred to as the *flip angle*.

After the RF transmitter coil is shut off, the magnetization vector M goes back to its equilibrium state M_0, in the original parallel state, in a process known as relaxation. The

relaxation of the magnetization M with time is mathematically described by the Bloch equations [31]. Two components of the relaxation can be distinguished, which are both characterized by an exponential process:

T_1 relaxation T_1 relaxation indicates how the longitudinal component of M, M_Z (parallel to B_0), goes back to the equilibrium state M_0, dissipating the excess energy of the spins as heat to the surrounding tissue (or *lattice*). Each tissue will be characterized by a value T_1, which is the time to reduce the difference between M_Z and its equilibrium state M_0 by a factor of e (that is, to approx. 37% of the original difference), according to:

$$M_Z = M_0 \cdot (1 - e^{-t/T_1})$$

T_1 is also called the spin-lattice relaxation time or the longitudinal relaxation time. For the tissues in the human body, T_1 values in the range of 200 ms to 1000 ms are usually observed at 1.5 T, but they can be above 2 seconds for some fluids such as cerebrospinal fluid.

T_2 relaxation T_2 relaxation indicates how the magnitude of the transverse magnetization M_{XY} (perpendicular to B_0) decreases to 0, which is its equilibrium state. Transverse relaxation is due to two reasons: to the interaction between the magnetic moments of the protons within the tissue, and to the inhomogeneity of the external magnetic field B_0, which makes protons at different locations precess with slightly different frequencies. These two effects contribute to the loss of the initial phase coherence achieved after e.g. a 90° pulse. T_2 is the time to decrease M_{XY0} (the transverse magnetization present after applying the RF signal) by a factor of e due exclusively to the interaction between the magnetic moments, according to:

$$M_{XY} = M_{XY0} \cdot e^{-t/T_2}$$

T_2 is also called the spin-spin relaxation time or the transverse relaxation time. For human tissues, T_2 values between 40 ms and 100 ms are typically observed at 1.5 T, but some fluids (such as cerebrospinal fluid) have T_2 values above one second. T_2 is always shorter or equal to T_1. Because of the inhomogeneities in B_0, a shorter value T_2^* is usually observed. Spin echo sequences can account for this effect and measure the T_2 value corresponding exclusively to the spin-spin relaxation.

The receiver coil serves then to measure -by induction of a voltage due to the moving magnetic field- the net transverse component of the magnetization which rotates around the direction of the main magnetic field B_0. The transverse component has a sinusoidal form, corresponding to the rotation of the spins with time at the Larmor frequency. Due to the progressive dephasing of the protons described by the T_2 relaxation, the amplitude of the transverse magnetization decays with time, resulting in a decaying sinusoidal waveform measured by the receiver, which is called *free induction decay* (FID). The FID after RF excitation is usually too rapid to generate an MRI image, because the system electronics do not allow to image after RF excitation within such a short time (for T_2 values usually below 100 ms). Therefore, a temporal separation between the RF pulse and the acquisition

is introduced, and a so called echo of the initial FID is measured. The delay between the RF excitation and the signal acquisition is called *echo time* (TE).

In MRI, each signal measured is a mixture of signals from all voxels in the sample. In order to perform spatial encoding, gradient coils are used. Three different gradients are used for spatial encoding: selection of the imaged slice by applying a gradient orthogonal to the slice during RF excitation (as an example, in the z-axis) which results in the resonance of only this slice of spins; phase encoding after RF excitation by applying a brief gradient (in the y-axis following the example) which dephases the different rows of spins; and frequency encoding, applied as a gradient (in the x-axis following the example) during signal readout which changes the frequency of each column of spins. In order to form a complete image, the phase encoding is stepped during the acquisition, with increasing strength of the phase encoding gradient. The time interval between the application of subsequent RF excitations while varying the phase encoding gradient is called *repetition time* (TR). In most standard scans, each repetition allows to fill a line in the so-called *k-space*. Once the complete k-space has been sampled, the MRI image can be obtained by applying a two-dimensional Fourier transform to it.

By varying acquisition parameters such as TR and TE, different contrasts can be obtained, such as T1-weighted (short TE and TR), T2-weighted (long TE and TR) and proton-density weighted images (short TE and long TR).

The signal intensity resulting at each voxel will depend on the sequence used as well as on the chemical composition of the tissue. This makes MRI so unique, in its ability to tailor the exam to the particular clinical question, being able to provide different images from the same organ depending on the parameters of the acquisition (Fig B.4). Moreover, paramagnetic contrast agents can be used, most of them employing chelated Gadolinium, which shorten the T_1 of the region where they are located. Contrast agents which are absorbed by specific tissues can be used to effectively produce new contrasts and better diagnose some pathological conditions.

MRI offers additional acquisition techniques, which are out of the scope of this appendix. Among them, it is worth pointing out MR spectroscopy. MR spectroscopy of the hydrogen nucleus, the most commonly used, works by suppressing the signal from water and identifying metabolites through the slightly different Larmor frequency resulting from the electron cloud surrounding the hydrogen nuclei. SNR and acquisition time still represent major limitations for MR spectroscopy, being therefore mainly used for research applications, but with increasing clinical use in areas such as brain, tumor and inflammatory imaging.

MRI finds application in a large number of clinical areas. As compared to CT, MRI provides an excellent soft tissue contrast, making it useful for diagnosing and monitoring several neurological, oncological and cardiovascular conditions, as well as many musculoskeletal diseases and post traumatic injuries. In addition, MRI is increasingly used intraoperatively for image-guided minimal invasive procedures.

MRI has the advantage of having no ionizing radiation associated with it; this is particularly relevant for pediatric imaging and makes it suitable for serial follow-up examinations. Still, there are some risks involved, which are harmless if basic precautionary measures are respected. These risks include:

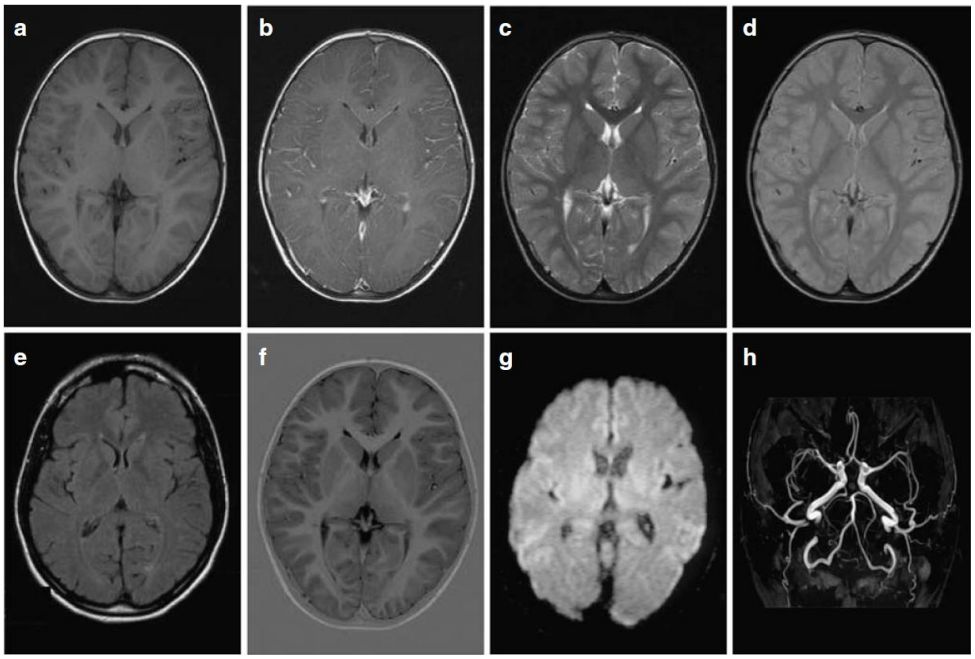

Figure B.4: Choice of multi-parameter soft tissue contrasts available with MRI. Repeated MRI imaging of an axial cross-section through the brain of a normal volunteer demonstrates how the soft tissue contrast can be varied simply through the appropriate choice of imaging sequences and corresponding sequence parameters. (a-d) show the basic MRI contrasts: (a) T1-weigthing (T1w), (b) T1w with contrast agent, (c) T2w, (d) proton-density-weighted. (e) and (f) show FLAIR and inversion recovery sequences, respectively. (g) Diffusion-weighted image of the brain, and (h) provides a maximum-intensity projection (MIP) of a non-contrast-enhanced 3D time-of-flight (TOF) angiogram of the intracranial vessels. Reproduced from [209] with permission from the authors.

- The energy introduced in the body by the RF system, which produces heating. This energy is usually measured as Specific Absorption Rate (SAR), in Watts/kg.
- The high acoustic level which might occur during the acquisition.
- The influence of the magnetic field on pacemakers and other devices.
- The eventual heating of the liquid helium in the case of a system failure, which stops the superconducting properties of the magnet and results in a sudden heating and a fast, explosive expansion of the helium gas.
- The attraction of ferromagnetic objects to the magnet, which can convert many objects in projectiles dangerous for the patient.

As indicated above, when MRI is correctly operated and basic precautions are taken, these risks are virtually inexistent.

For further information about MRI physics and its clinical applications, please refer to [111, 209].

APPENDIX C

Medical hardware used for the data acquisition

Here is an overview of the clinical scanners available at the Department of Nuclear Medicine that served to acquire the data used within this thesis together with some of their relevant parameters.

Biograph Sensation 16 PET/CT The Siemens Biograph 16 PET/CT (Fig. C.1) was available between 2004 and May 2008, prior to the installation of the Biograph TruePoint scanner. It combines an ECAT ACCEL PET and a 16-slice Somatom Emotion CT.

Regarding the PET component, it has an axial field of view of 16.2 cm and has no septa, so that all PET data is acquired in 3D mode (see section 2.1.5). Since 2005, it was also upgraded with improved detection electronics (Pico3D), allowing better energy and timing resolutions. The scanner contains approximately 11,000 Lutetium Oxyorthosilicate (LSO) crystals with a size of 6.45x6.45x20 mm^3, resulting in a spatial resolution of approximately 6 mm at the center of the field of view. The scanner's sensitivity is reported to be 4.5 %.

The CT component is a Siemens Somatom 16, with 16 rows of detectors made of ultra-fast ceramic and a rotation time of 500 milliseconds. The spatial resolution of the CT component is reported to be below 0.6 mm.

Biograph TruePoint PET/CT The Siemens Biograph TruePoint was installed at the department in May 2008, replacing the Biograph Sensation 16. It combines an LSO-based Hi-Rez PET scanner with a 64-slice CT.

Regarding the PET component, it has an axial field of view of 21.6 cm and has no septa, so that all PET data is acquired in 3D mode. It contains 32,448 LSO crystals with a size of 4x4x20 mm^3, resulting in a spatial resolution of approximately 4.2 mm at the center of the field of view. The scanner's sensitivity is reported to be 7.9 %.

Figure C.1: Siemens Biograph PET/CT architecture, with PET and CT scanners besides each other.

The CT component includes 64 rows of detectors made of ultra-fast ceramic. It has a rotation time of 330 milliseconds. The scanner's spatial resolution is reported to be 0.4 mm.

ECAT EXACT HR+ The Siemens ECAT EXACT HR+ (Fig. C.2) contains 18,432 bismuth germanate (BGO) crystals with a size of 4x4.4x30 mm^3 arranged in 32 rings and covering an axial field of view of 15.5 cm with a patient port of 56.2 cm. It has retractable septa, so that acquisitions can be done in 2D or 3D mode.

Figure C.2: Siemens ECAT EXACT HR+ PET scanner. Since the introduction of PET/CT scanners in the clinic and their clear advantage for oncological examinations, the HR+ scanner is used mainly for neurological and cardiac examinations.

Attenuation correction is performed by means of a transmission measurement done with a rotating ^{68}Ge rod source. Due to the reduced statistics of the transmission measurements, these can be segmented post-acquisition in order to reduce the noise

propagation into the reconstructed PET image [311].

The transaxial resolution of the scanner in 2D mode is 4.3 mm in the center of the field of view and the axial slice width 4.2 mm. In 3D mode, the observed spatial resolution at the center of the field of view is 4.4 mm (transaxial) and 4.1 mm (axial) [43].

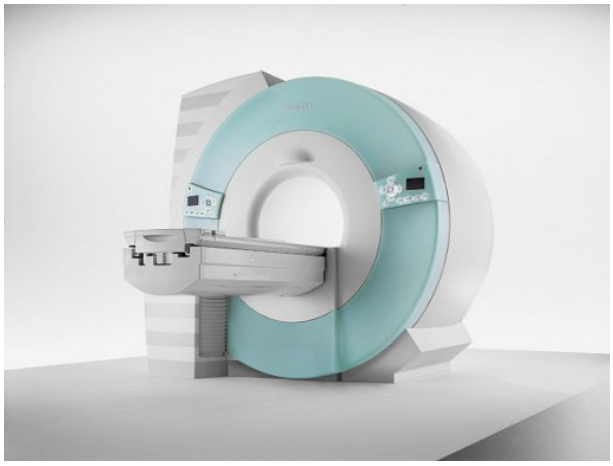

Figure C.3: Siemens Espree MRI.

Espree MRI The Siemens Espree (Fig. C.3) is a 1.5 Tesla MRI with open-bore (70 cm diameter) and a 125 cm magnet. It utilizes the Z-engine gradient system with 33 mT/m, slew rate of 100 T/m/s, and features the Total Imaging Matrix (Tim) technology.

Gyroscan ACS-NT MRI The Philips Gyroscan ACS-NT is a 1.5 Tesla MRI. It includes a 60 cm short bore magnet with 15 mT/m gradients.

APPENDIX D

Respiratory signal acquisition using an infrared stereovision camera

Since the ART stereovision system employed is an all-purpose tracking system, several in-house developments needed to be performed in order to adapt it for monitoring the patient's respiration. These developments were mainly performed within the frame of an interdisciplinary project [242]. They can be summarized in the following steps:

Camera setup It was verified that the system could be placed in the PET/CT examination room to monitor patients during the scans. The position of the cameras had to be adjusted in order to have a direct sight of the markers on the patient's torso during the acquisition, avoiding occlusion by the scanner's gantry and by the patient himself. In the clinical setup of this clinic, given the position of the PET scanner within the PET/CT gantry, it was decided that the camera would be placed one and a half meters apart from the bed-head. Moreover, this distance to the markers fitted well to the recommendations provided by the manufacturer of the infrared camera.

Calibration For logistical reasons, the camera system could not permanently stay in the examination room but had to be setup for every examination. In order to determine the position of the cameras with respect to the PET/CT scanner, a fix reference body consisting in a set of flat markers was attached to the scanner (Fig. D.1). Calibration of the system was achieved by measuring well-known displacements of markers using the motion of the PET/CT bed (see details in [242]), and provided the basis to get relative motion of the markers measured in the PET/CT coordinate system. After the calibration phase, a position vector $\vec{p}$ given in the raw ART marker data could be transformed to a position vector $\vec{p}'$ in coordinates of the PET/CT scanner following this equation:

$$\vec{p}' = \mathbf{C}^{-1}\mathbf{B}^{-1}(\vec{p} - \vec{b}).$$

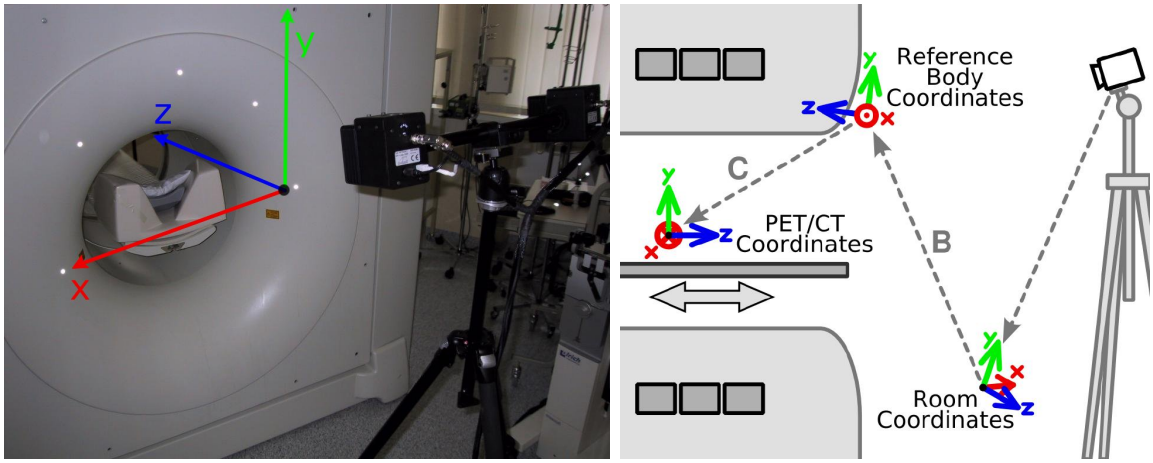

(a) (b)

Figure D.1: Set of flat markers attached to the PET/CT gantry used as reference body (a) and spatial transformations used to compute the motion in the PET/CT coordinate system (b). Image reproduced from [242].

Marker tracking A set of five separate markers was attached to the patient, as shown in Fig. 3.7, page 37. Three of the markers were placed on top of the Anzai elastic belt, whereas the other two were fixed to ECG electrodes. Having several markers served to increase the reliability of the system and its sensitivity to occlusion. The tracking data was recorded in a file using the DTrack software provided with the ART system with a sampling rate of 20 Hz. The file showed the position of each single marker as well as that of the calibration body with its 6 degrees of freedom (DOF). An occlusion handling algorithm was implemented by taking into account the location of the markers before and after occlusion, and the appropriate transformations were applied to go from the ART coordinate system to that of the PET/CT.

Data merging The output of the previous operations is an array with the three-dimensional position relative to the PET/CT scanner of each of the five markers at every time-point. Patient motion as well as displacements of the patient bed can be detected with a low-pass filter (frequency < 0.1 Hz) and removed from the signal. In addition, the data had to be combined in order to get a one-dimensional respiratory signal. Two different possibilities were investigated: 1) projecting of the marker locations to the anterior-posterior axis and computing its average. 2) Using *principal components analysis* (*PCA*, see [232, 134]) and assuming that the first component responds to the respiratory motion.

APPENDIX E

Authored and Co-Authored Publications

E.1 Publications in peer-reviewed journals

i. A. Martinez-Moller, M. Souvatzoglou, G. Delso, R. Bundschuh, C. Chefd'hotel, S. Ziegler, N. Navab, M. Schwaiger, S. Nekolla, *Tissue classification as a potential approach for attenuation correction in whole-body PET/MRI: evaluation with PET/CT data.* J Nucl Med 2009;50:520–526.

ii. S. Nekolla, A. Martinez-Moller, A. Saraste, *PET and MRI in cardiac imaging: from validation studies to integrated applications.* Eur J Nucl Med Mol Imaging 2009;36(1):121–130.

iii. R. Bundschuh, A. Martinez-Moller, M. Essler, M.J. Martinez, S. Nekolla, S. Ziegler, M. Schwaiger, *Local motion correction for lung tumours in PET/CT-first results.* Eur J Nucl Med Mol Imaging 2008;35:1981–1988.

iv. R. Bundschuh, A. Martinez-Moller, S. Ziegler, M. Schwaiger, K. Scheidhauer, *Misalignment in PET/CT: relevance for SUV and therapy management.* Nuklearmedizin 2008;47:N14–15.

v. R. Bundschuh, A. Martinez-Moller, M. Essler, M.J. Martinez, S. Nekolla, S. Ziegler, M. Schwaiger, *Postacquisition detection of tumor motion in the lung and upper abdomen using list-mode PET data: a feasibility study.* J Nucl Med 2007;48:758–763.

vi. A. Martinez-Moller, M. Souvatzoglou, N. Navab, M. Schwaiger, S. Nekolla, *Artifacts from misaligned CT in cardiac perfusion PET/CT studies: frequency, effects, and potential solutions.* J Nucl Med 2007;48:188–193.

vii. A. Martinez-Moller, D. Zikic, R. Botnar, R. Bundschuh, W. Howe, S. Ziegler, N. Navab, M. Schwaiger, S. Nekolla, *Dual cardiac-respiratory gated PET: implementation and results from a feasibility study.* Eur J Nucl Med Mol Imaging 2007;34:1447–1454.

E.2 Publications in conferences

viii. G. Delso, A. Martinez-Moller, R. Bundschuh, R. Ladebeck, D. Faul, S. Ziegler, *Study of MR head and neck coils for its use in an integrated MR/PET scanner*, Proceedings of the Annual Meeting of the Society of Nuclear Medicine (SNM 2009), Toronto, Canada, June 2009. J Nucl Med 2009;50(2):p294.

ix. J. Dinges, R. Bundschuh, N. Andratschke, S. Astner, A. Martinez-Moller, M. Bruegel, M. Schwaiger, S. Ziegler, M. Essler, *4D FDG-PET/CT and diffusion weighted MR for planning of stereotactic radiotherapy of liver metastasis from colorectal cancer*, Proceedings of the Annual Meeting of the Society of Nuclear Medicine (SNM 2009), Toronto, Canada, June 2009. J Nucl Med 2009;50(2):p56.

x. A. Martinez-Moller, M. Souvatzoglou, N. Navab, S. Ziegler, M. Schwaiger, S. Nekolla, *Influence of bones and constant attenuation factors in PET/CT: learning for MR-based attenuation correction in whole-body MR/PET*, Proceedings of the Annual Meeting of the European Association of Nuclear Medicine (EANM 2008), Munich, Germany, September 2008.

xi. G. Delso, A. Martinez-Moller, R. Bundschuh, S. Ziegler, M. Schwaiger, *Towards coronary atheroma vulnerability assessment with PET*, Proceedings of the Annual Meeting of the European Association of Nuclear Medicine (EANM 2008), Munich, Germany, September 2008.

xii. R. Bundschuh, A. Martinez-Moller, M. Essler, G. Delso, S. Nekolla, S. Ziegler, M. Schwaiger, *Local motion correction and influence of attenuation correction in PET/CT for lung tumors*, Proceedings of the Annual Meeting of the European Association of Nuclear Medicine (EANM 2008), Munich, Germany, September 2008.

xiii. R. Bundschuh, G. Delso, M. Herz, A. Martinez-Moller, M. Essler, S. Nekolla, S. Ziegler, M. Schwaiger, *Gradient-based algorithm are superior in segmentation of tumors with inhomogeneous activity distribution in positron emission tomography (PET) data*, Proceedings of the Annual Meeting of the European Association of Nuclear Medicine (EANM 2008), Munich, Germany, September 2008.

xiv. A. Martinez-Moller, R. Bundschuh, N. Navab, S. Ziegler, M. Schwaiger, S. Nekolla, *MR-based attenuation correction for whole-body MR/PET*, Proceed-

ings of the Annual Meeting of the Society of Nuclear Medicine (SNM 2008), New Orleans, USA, June 2008. J Nucl Med 2008;49(1):p65b.

xv. A. Martinez-Moller, B. Jensen, N. Navab, M. Schwaiger, S. Nekolla, *Automatic cardiac PET-SPECT and SPECT-SPECT registration*, Proceedings of the Annual Meeting of the Society of Nuclear Medicine (SNM 2008), New Orleans, USA, June 2008. J Nucl Med 2008;49(1):p31.

xvi. G. Delso, A. Martinez-Moller, R. Bundschuh, S. Ziegler, S. Nekolla, M. Schwaiger, *Investigation of gating requirements for coronary plaque imaging in PET*, Proceedings of the Annual Meeting of the Society of Nuclear Medicine (SNM 2008), New Orleans, USA, June 2008. J Nucl Med 2008;49(1):p185a.

xvii. G. Delso, R. Bundschuh, A. Martinez-Moller, S. Nekolla, S. Ziegler, M. Schwaiger, *Impact of limited MR field-of-view in simultaneous PET/MR acquisition*, Proceedings of the Annual Meeting of the Society of Nuclear Medicine (SNM 2008), New Orleans, USA, June 2008. J Nucl Med 2008;49(1):p162b.

xviii. R. Bundschuh, G. Delso, A. Martinez-Moller, s. Nekolla, S. Ziegler, M. Schwaiger, *Segmentation of lesions with inhomogeneous activity distribution in PET*, Proceedings of the Annual Meeting of the Society of Nuclear Medicine (SNM 2008), New Orleans, USA, June 2008. J Nucl Med 2008;49(1):p381a.

xix. A. Martinez-Moller, R. Bundschuh, S. Ziegler, M. Schwaiger, S. Nekolla, K. Scheidhauer, *Potential pitfall of PET/CT therapy monitoring due to PET/CT misregistration*, Deutsche Gesellschaft für Nuklearmedizin (DGN 2008), Leipzig, Germany, April 2008.

xx. A. Martinez-Moller, R. Bundschuh, N. Navab, S. Ziegler, M. Schwaiger, S. Nekolla, *Determination of body surface area from a whole-body CT scan and its impact for SUV normalization*, Proceedings of the Annual Meeting of the Society of Nuclear Medicine (SNM 2007), Washington, D.C., USA, June 2007. J Nucl Med 2007;48(2):p44c.

xxi. A. Martinez-Moller, M. Souvatzoglou, R. Botnar, N. Navab, S. Ziegler, M. Schwaiger, S. Nekolla, *An approach for MR-based attenuation correction for combined MR/PET: effects of ignoring bones*, Proceedings of the Annual Meeting of the Society of Nuclear Medicine (SNM 2007), Washington, D.C., USA, June 2007. J Nucl Med 2007;48(2):p156.

xxii. A. Martinez-Moller, R. Bundschuh, M. Riedel, N. Navab, S. Ziegler, M. Schwaiger, S. Nekolla, *Comparison of respiratory sensors and its compliance for respiratory gating in emission tomography*, Proceedings of the Annual Meeting of the Society of Nuclear Medicine (SNM 2007), Washington, D.C., USA, June 2007. J Nucl Med 2007;48(2):p426b.

xxiii. R. Bundschuh, A. Martinez-Moller, M. Essler, M.J. Martinez, S. Nekolla, S. Ziegler, M. Schwaiger, *Local motion correction for lung tumors in PET/CT*. Proceedings of the Annual Meeting of the Society of Nuclear Medicine (SNM 2007), Washington, D.C., USA, June 2007. J Nucl Med 2007;48(2):p196a.

xxiv. R. Bundschuh, M. Essler, A. Martinez-Moller, M. Bazanez-Borgert, S. Nekolla, S. Ziegler, M. Schwaiger, *How does respiratory motion reduce the detectability of small lesions?*, Proceedings of the Annual Meeting of the Society of Nuclear Medicine (SNM 2007), Washington, D.C., USA, June 2007. J Nucl Med 2007;48(2):p407.

xxv. A. Martinez-Moller, N. Navab, M. Schwaiger, S. Nekolla, *Emission-transmission misregistration artifacts in cardiac PET/CT: extent and solutions*, Proceedings of the International Conference in Nuclear Cardiology (ICNC 2007), Prague, Czech Republic, April 2007. J Nucl Cardiol 2007;14(1):p60.

xxvi. A. Martinez-Moller, N. Navab, M. Schwaiger, S. Nekolla, *Photon Attenuation Correction in Misregistered Cardiac PET/CT*. Bildverarbeitung für die Medizin 2007;10:p227–231.

xxvii. A. Martinez-Moller, R. Bundschuh, W. Howe, M-J. Martinez, N. Navab, S. Ziegler, M. Schwaiger, S. Nekolla, *Dual gated PET for evaluation of the cardiac respiratory motion: Towards motion-free images*, Proceedings of the Annual Meeting of the Society of Nuclear Medicine (SNM 2006), Toronto, Canada, June 2006. J Nucl Med 2006;47(1):p250b.

xxviii. S. Nekolla, A. Jankauskas, A. Martinez-Moller, J. Hausleiter, K. Rahbar, M. Souvatzoglou, F. Bengel, M. Schwaiger, *Cardiac PET/CT for definition of individually derived vessel territories*, Proceedings of the Annual Meeting of the Society of Nuclear Medicine (SNM 2006), Toronto, Canada, June 2006. J Nucl Med 2006;47(1):p254.

xxix. A. Martinez-Moller, W. Howe, M. Schwaiger, S. Nekolla, *Motion free images by dual gating of PET listmode acquisitions*, Proceedings of the World Congress of Cardiology (WCC 2006), Barcelona, Spain, September 2006.

xxx. A. Martinez-Moller, R. Bundschuh, M-J. Martinez, W. Howe, S. Ziegler, M. Schwaiger, S. Nekolla, *Doppeltgetriggerte Herz-PET zur Evaluierung der Bewegung des Herzens während der Atmung*, Deutsche Gesellschaft für Nuklearmedizin (DGN 2006), Berlin, Germany, April 2006.

xxxi. A. Martinez-Moller, M. Souvatzoglou, M. Schwaiger, S. Nekolla, *Bewegungsartefakte in der Herz-PET/CT: Effekte auf der Tracerverteilung und Evaluierung eines Korrekturalgorithmus*, Deutsche Gesellschaft für Nuklearmedizin (DGN 2006), Berlin, Germany, April 2006.

xxxii. R. Bundschuh, A. Martinez-Moller, M.J. Martinez, S. Nekolla, S. Ziegler, M. Schwaiger, *Retrospektive registrierung von atembewegung mit hilfe von List Mode in PET/CT*, Deutsche Gesellschaft für Nuklearmedizin (DGN 2006), Berlin, Germany, April 2006.

xxxiii. A. Martinez-Moller, N. Navab, M. Schwaiger, S. Nekolla, *Photon Attenuation Correction in Misaligned PET/CT Cardiac Perfusion Images*, Proceedings of the International Conference in Medical Physics (ICMP 2005), Nuremberg, Germany, September 2005. Biomedizinische Technik 2005;50:p108-109.

xxxiv. A. Martinez-Moller, R. Bundschuh, N. Navab, S. Ziegler, M. Schwaiger, S. Nekolla, *Emission driven motion correction in PET/CT cardiac imaging*, Proceedings of the Annual Meeting of the Society of Nuclear Medicine (SNM 2005), Toronto, Canada, June 2005. J Nucl Med 2005;46(2):p163b.

References

[1] A. S. Agatston, W. R. Janowitz, F. J. Hildner, N. R. Zusmer, M. Viamonte, and R. Detrano, *Quantification of coronary artery calcium using ultrafast computed tomography*, J Am Coll Cardiol, 15 (1990), pp. 827–832.

[2] A. V. Akindinov, A. N. Martemianov, P. A. Polozov, V. M. Golovin, and E. A. Grigoriev, *New results on MRS APDs*, Nuclear Instruments and Methods in Physics Research Section A: Accelerators, Spectrometers, Detectors and Associated Equipment, 387 (1997), pp. 234–234.

[3] A. Alavi and M. Reivich, *Guest editorial: the conception of FDG-PET imaging*, Semin Nucl Med, 32 (2002), pp. 2–5.

[4] P. O. Alderson and B. R. Line, *Scintigraphic evaluation of regional pulmonary ventilation*, Semin Nucl Med, 10 (1980), pp. 218–242.

[5] A. Alessio and P. Kinahan, *Nuclear Medicine*, Elsevier, 2006, ch. PET Image Reconstruction.

[6] A. M. Alessio, S. Kohlmyer, K. Branch, G. Chen, J. Caldwell, and P. Kinahan, *Cine CT for attenuation correction in cardiac PET/CT*, J Nucl Med, 48 (2007), pp. 794–801.

[7] L. Alvarez, J. Weickert, and J. Sánchez, *Reliable estimation of dense optical flow fields with large displacements*, Int. J. Comput. Vision, 39 (2000), pp. 41–56.

[8] C. D. Anderson, *The positive electron*, Phys Rev, 43 (1933), pp. 491–494.

[9] E. J. C. Angtuaco, A. B. T. Fassas, R. Walker, R. Sethi, and B. Barlogie, *Multiple myeloma: clinical review and diagnostic imaging*, Radiology, 231 (2004), pp. 11–23.

[10] G. Antoch and A. Bockisch, *Combined PET/MRI: a new dimension in whole-body oncology imaging?*, Eur J Nucl Med Mol Imaging, 36 Suppl 1 (2009), pp. S113–S120.

[11] G. Antoch, F. M. Vogt, L. S. Freudenberg, F. Nazaradeh, S. C. Goehde, J. Barkhausen, G. Dahmen, A. Bockisch, J. F. Debatin, and S. G. Ruehm, *Whole-body dual-modality PET/CT and whole-body MRI for tumor staging in oncology*, JAMA, 290 (2003), pp. 3199–3206.

[12] J. S. Arenson, R. Levinson, and D. Freundlich, *Dual slice scanner.* US Patent Number 5228069, 1993.

[13] S. Arroyo and R. P. Lesser, *PET, MRI, and epilepsy*, Neurology, 43 (1993), p. 2156.

[14] C. Bai, P. E. Kinahan, D. Brasse, C. Comtat, D. W. Townsend, C. C. Meltzer, V. Villemagne, M. Charron, and M. Defrise, *An analytic study of the effects of attenuation on tumor detection in whole-body PET oncology imaging*, J Nucl Med, 44 (2003), pp. 1855–1861.

[15] L. N. Baldwin, K. Wachowicz, S. D. Thomas, R. Rivest, and B. G. Fallone, *Characterization, prediction, and correction of geometric distortion in 3 T MR images*, Medical Physics, 34 (2007), pp. 388–399.

[16] T. M. Bashore, E. R. Bates, P. B. Berger, D. A. Clark, J. T. Cusma, G. J. Dehmer, M. J. Kern, W. K. Laskey, M. P. O'Laughlin, S. Oesterle, J. J. Popma, R. A. O'Rourke, J. Abrams, E. R. Bates, B. R. Brodie, P. S. Douglas, G. Gregoratos, M. A. Hlatky, J. S. Hochman, S. Kaul, C. M. Tracy, D. D. Waters, W. L. Winters, and A. C. of Cardiology. Task Force on Clinical Expert Consensus Documents, *American College of Cardiology/Society for Cardiac Angiography and Interventions Clinical Expert Consensus Document on cardiac catheterization laboratory standards. A report of the American College of Cardiology Task Force on Clinical Expert Consensus Documents*, J Am Coll Cardiol, 37 (2001), pp. 2170–2214.

[17] T. M. Bateman, G. V. Heller, A. I. McGhie, J. D. Friedman, J. A. Case, J. R. Bryngelson, G. K. Hertenstein, K. L. Moutray, K. Reid, and S. J. Cullomc, *Diagnostic accuracy of rest/stress ECG-gated Rb-82 myocardial perfusion PET: comparison with ECG-gated Tc-99m sestamibi SPECT*, J Nucl Cardiol, 13 (2006), pp. 24–33.

[18] J. J. Bax, D. Poldermans, A. Elhendy, E. Boersma, and E. E. van der Wall, *Assessment of myocardial viability by nuclear imaging techniques*, Curr Cardiol Rep, 7 (2005), pp. 124–129.

[19] R. D. Beach, H. Pretorius, G. Boening, P. P. Bruyant, B. Feng, R. R. Fulton, M. A. Gennert, and M. A. King, *Feasibility of stereo-infrared tracking*

to monitor patient motion during cardiac SPECT imaging, IEEE Transactions on Nuclear Science, 51 (2004), pp. 2693–2698.

[20] F. M. Bengel, *Positron emission tomography and magnetic resonance imaging in heart failure*, J Nucl Cardiol, 13 (2006), pp. 145–149.

[21] F. M. Bengel, J. Lehnert, T. Ibrahim, C. Klein, H. P. Bülow, S. G. Nekolla, and M. Schwaiger, *Cardiac oxidative metabolism, function, and metabolic performance in mild hyperthyroidism: a noninvasive study using positron emission tomography and magnetic resonance imaging*, Thyroid, 13 (2003), pp. 471–477.

[22] F. M. Bengel and M. Schwaiger, *Assessment of cardiac sympathetic neuronal function using PET imaging*, J Nucl Cardiol, 11 (2004), pp. 603–616.

[23] D. S. Berman, A. F. Salel, G. L. DeNardo, H. G. Bogren, and D. T. Mason, *Clinical assessment of left ventricular regional contraction patterns and ejection fraction by high-resolution gated scintigraphy*, J Nucl Med, 16 (1975), pp. 865–874.

[24] W. H. Berninger, R. W. Redington, P. Doherty, M. J. Lipton, and E. Carlsson, *Gated cardiac scanning: canine studies*, J Comput Assist Tomogr, 3 (1979), pp. 155–163.

[25] T. Beyer, *PET: speed dating CT or MRI?*, J Nucl Med, 48 (2007), p. 331.

[26] T. Beyer, G. Antoch, T. Blodgett, L. F. Freudenberg, T. Akhurst, and S. Mueller, *Dual-modality PET/CT imaging: the effect of respiratory motion on combined image quality in clinical oncology*, Eur J Nucl Med Mol Imaging, 30 (2003), pp. 588–596.

[27] T. Beyer, A. Bockisch, H. Kühl, and M.-J. Martinez, *Whole-body 18F-FDG PET/CT in the presence of truncation artifacts*, J Nucl Med, 47 (2006), pp. 91–99.

[28] T. Beyer, M. Weigert, H. H. Quick, U. Pietrzyk, F. Vogt, C. Palm, G. Antoch, S. P. Müller, and A. Bockisch, *MR-based attenuation correction for torso-PET/MR imaging: pitfalls in mapping MR to CT data.*, Eur J Nucl Med Mol Imaging, 35 (2008), pp. 1142–1146.

[29] J. M. Bland and D. G. Altman, *Statistical methods for assessing agreement between two methods of clinical measurement*, Lancet, 1 (1986), pp. 307–310.

[30] R. Blasberg, *PET imaging of gene expression*, Eur J Cancer, 38 (2002), pp. 2137–2146.

[31] F. Bloch, *Nuclear Induction*, Physics Review, 70 (1946), pp. 460–473.

[32] D. A. Bluemke, S. Achenbach, M. Budoff, T. C. Gerber, B. Gersh, L. D. Hillis, W. G. Hundley, W. J. Manning, B. F. Printz, M. Stuber, and P. K. Woodard, *Noninvasive coronary artery imaging: magnetic resonance angiography and multidetector computed tomography angiography: a scientific statement from the american heart association committee on cardiovascular imaging and intervention of the council on cardiovascular radiology and intervention, and the councils on clinical cardiology and cardiovascular disease in the young*, Circulation, 118 (2008), pp. 586–606.

[33] H. G. Bogren, B. M. Lantz, R. R. Miller, and D. T. Mason, *Effect of respiration on cardiac motion determined by cineangiography. Implications concerning three-dimensional heart reconstruction using computer tomography*, Acta Radiol Diagn (Stockh), 18 (1977), pp. 609–620.

[34] S. L. Bond, T. Kadir, J. Hamill, M. Casey, G. Platsch, D. Burckhardt, R. Eisner, and N. Kausthubh, *Automatic registration of cardiac PET-CT for attenuation correction*, Proceedings of the IEEE Medical Imaging Conference, (2008), pp. M14–6.

[35] S. L. Bond, T. Kadir, A. H. Vija, X. Ding, G. Platsch, J. Kritzman, and J. Declerck, *Automatic registration of cardiac SPECT-CT for attenuation correction*, J Nucl Med, 49 (2008), p. 392P.

[36] L. Boucher, S. Rodrigue, R. Lecomte, and F. Bénard, *Respiratory gating for 3-dimensional PET of the thorax: feasibility and initial results*, J Nucl Med, 45 (2004), pp. 214–219.

[37] P. Bourgeat, J. Fripp, P. Stanwell, S. Ramadan, and S. Ourselin, *MR image segmentation of the knee bone using phase information*, Med Image Anal, 11 (2007), pp. 325–335.

[38] M. Brambilla, C. Secco, M. Dominietto, R. Matheoud, G. Sacchetti, and E. Inglese, *Performance characteristics obtained for a new 3-dimensional lutetium oxyorthosilicate-based whole-body PET/CT scanner with the National Electrical Manufacturers Association NU 2-2001 standard*, J Nucl Med, 46 (2005), pp. 2083–2091.

[39] E. Braunwald and R. A. Kloner, *The stunned myocardium: prolonged, postischemic ventricular dysfunction*, Circulation, 66 (1982), pp. 1146–1149.

[40] D. J. Brenner and E. J. Hall, *Computed tomography–an increasing source of radiation exposure*, N Engl J Med, 357 (2007), pp. 2277–2284.

[41] W. L. Briggs, V. E. Henson, and S. F. McCormick, *A multigrid tutorial (2nd ed.)*, Society for Industrial and Applied Mathematics, Philadelphia, PA, USA, 2000.

[42] G. Brix, E. A. Nekolla, D. Nosske, and J. Griebel, *Risks and safety aspects related to PET/MR examinations*, Eur J Nucl Med Mol Imaging, 36 Suppl 1 (2009), pp. S131–S138.

[43] G. Brix, J. Zaers, L. E. Adam, M. E. Bellemann, H. Ostertag, H. Trojan, U. Haberkorn, J. Doll, F. Oberdorfer, and W. J. Lorenz, *Performance evaluation of a whole-body PET scanner using the NEMA protocol. National Electrical Manufacturers Association.*, J Nucl Med, 38 (1997), pp. 1614–1623.

[44] G. Brownell and W. Sweet, *Localization of brain tumors with positron emitters*, Nucleonics, 11 (1953), p. 40.

[45] F. Büther, M. Dawood, L. Stegger, F. Wübbeling, M. Schäfers, O. Schober, and K. P. Schäfers, *List Mode-Driven Cardiac and Respiratory Gating in PET*, J Nucl Med, 50 (2009), pp. 674–681.

[46] T. F. Budinger and G. T. Gullberg, *Letter: Three-dimensional reconstruction of isotope distributions*, Phys Med Biol, 19 (1974), pp. 387–389.

[47] R. A. Bundschuh, A. Martínez-Möller, M. Essler, S. G. Nekolla, S. I. Ziegler, and M. Schwaiger, *Local motion correction for lung tumours in PET/CT-first results*, Eur J Nucl Med Mol Imaging, 35 (2008), pp. 1981–1988.

[48] R. A. Bundschuh, A. Martínez-Möller, S. I. Ziegler, M. Schwaiger, and K. Scheidhauer, *Misalignment in PET/CT: relevance for SUV and therapy management*, Nuklearmedizin, 47 (2008), pp. N14–15.

[49] R. A. Bundschuh, A. Martínez-Moeller, M. Essler, M.-J. Martínez, S. G. Nekolla, S. I. Ziegler, and M. Schwaiger, *Postacquisition detection of tumor motion in the lung and upper abdomen using list-mode PET data: a feasibility study*, J Nucl Med, 48 (2007), pp. 758–763.

[50] J. Canny, *A computational approach to edge detection*, IEEE Trans. Pattern Anal. Mach. Intell., 8 (1986), pp. 679–698.

[51] M. E. Casey and R. A. Nutt, *A multicrystal, two-dimensional BGO detector system for positron emission tomography*, IEEE Trans Nucl Sci, 33 (1986), pp. 460–463.

[52] C. Catana, D. Procissi, Y. Wu, M. S. Judenhofer, J. Qi, B. J. Pichler, R. E. Jacobs, and S. R. Cherry, *Simultaneous in vivo positron emission tomography and magnetic resonance imaging*, Proc Natl Acad Sci U S A, 105 (2008), pp. 3705–3710.

[53] A. O. Ceballos-Baumann, *Functional imaging in Parkinson's disease: activation studies with PET, fMRI and SPECT*, J Neurol, 250 Suppl 1 (2003), pp. I15–I23.

[54] M. D. Cerqueira, N. J. Weissman, V. Dilsizian, A. K. Jacobs, S. Kaul, W. K. Laskey, D. J. Pennell, J. A. Rumberger, T. Ryan, M. S. Verani, A. H. A. W. G. on Myocardial Segmentation, and R. for Cardiac Imaging, *Standardized myocardial segmentation and nomenclature for tomographic imaging of the heart: a statement for healthcare professionals from the Cardiac Imaging Committee of the Council on Clinical Cardiology of the American Heart Association*, Circulation, 105 (2002), pp. 539–542.

[55] M. Charlton and J. W. Humberston, *Positron physics*, Cambridge University Press, 2001.

[56] C. Chefd'hotel, G. Hermosillo, and O. Faugeras, *Flows of diffeomorphisms for multimodal image registration*, in Proc. IEEE International Symposium on Biomedical Imaging, 7–10 July 2002, pp. 753–756.

[57] G. P. Chen, K. R. Branch, A. M. Alessio, P. Pham, R. Tabibiazar, P. Kinahan, and J. H. Caldwell, *Effect of reconstruction algorithms on myocardial blood flow measurement with 13N-ammonia PET*, J Nucl Med, 48 (2007), pp. 1259–1265.

[58] S. Cho, S. Ahn, Q. Li, and R. M. Leahy, *Exact and approximate Fourier rebinning of PET data from time-of-flight to non time-of-flight*, Phys Med Biol, 54 (2009), pp. 467–484.

[59] B. J. Chow, A. Abraham, G. A. Wells, L. Chen, T. D. Ruddy, Y. Yam, N. Govas, P. D. Galbraith, C. Dennie, and R. S. Beanlands, *Diagnostic accuracy and impact of computed tomographic coronary angiography on utilization of invasive coronary angiography*, Circ Cardiovasc Imaging, 2 (2009), pp. 16–23.

[60] N. L. Christensen, B. E. Hammer, B. G. Heil, and K. Fetterly, *Positron emission tomography within a magnetic field using photomultiplier tubes and lightguides*, Phys Med Biol, 40 (1995), pp. 691–697.

[61] C. Comtat, P. E. Kinahan, M. Defrise, C. Michel, and D. W. Townsend, *Fast reconstruction of 3D PET data with accurate statistical modeling*, IEEE Trans Nucl Sci, 45 (1998), pp. 1083–1089.

[62] B. D. Coombs, J. Szumowski, and W. Coshow, *Two-point Dixon technique for water-fat signal decomposition with B0 inhomogeneity correction*, Magn Reson Med, 38 (1997), pp. 884–889.

[63] R. Dalvi, R. Abugharbieh, D. Wilson, and D. R. Wilson, *Multi-contrast MR for enhanced bone imaging and segmentation*, Conf Proc IEEE Eng Med Biol Soc, 2007 (2007), pp. 5620–5623.

[64] R. Damadian, *Tumor detection by nuclear magnetic resonance*, Science, 171 (1971), pp. 1151–1153.

[65] P. G. Danias, M. Stuber, R. M. Botnar, K. V. Kissinger, R. R. Edelman, and W. J. Manning, *Relationship between motion of coronary arteries and diaphragm during free breathing: lessons from real-time MR imaging*, AJR Am J Roentgenol, 172 (1999), pp. 1061–1065.

[66] M. Dawood, F. Büther, N. Lang, O. Schober, and K. P. Schäfers, *Respiratory gating in positron emission tomography: a quantitative comparison of different gating schemes*, Med Phys, 34 (2007), pp. 3067–3076.

[67] M. Defrise, M. E. Casey, C. Michel, and M. Conti, *Fourier rebinning of time-of-flight PET data*, Phys Med Biol, 50 (2005), pp. 2749–2763.

[68] G. Delso, R. Bundschuh, A. Martinez-Moller, S. Nekolla, S. Ziegler, and M. Schwaiger, *Impact of limited MR field-of-view in simultaneous PET/MR acquisition*, J Nucl Med, 49 (2008), pp. 162P–b–.

[69] G. Delso, A. Martinez-Moller, R. Bundschuh, S. Ziegler, and M. Schwaiger, *Towards coronary atheroma vulnerability assessment with PET*, in Proceedings of the European Association of Nuclear Medicine, 2008.

[70] G. Delso and S. Ziegler, *PET/MRI system design*, Eur J Nucl Med Mol Imaging, 36 Suppl 1 (2009), pp. S86–S92.

[71] A. P. Dempster, N. M. Laird, and D. B. Rubin, *Maximum likelihood from incomplete data via the EM algorithm*, Journal of the Royal Statistical Society, 39 (1977), pp. 1–38.

[72] R. Detrano, T. Hsiai, S. Wang, G. Puentes, J. Fallavollita, P. Shields, W. Stanford, C. Wolfkiel, D. Georgiou, M. Budoff, and J. Reed, *Prognostic value of coronary calcification and angiographic stenoses in patients undergoing coronary angiography*, J Am Coll Cardiol, 27 (1996), pp. 285–290.

[73] W. T. Dixon, *Simple proton spectroscopic imaging*, Radiology, 153 (1984), pp. 189–194.

[74] Dolgoshein, V. Balagura, P. Buzhan, M. Danilov, L. Filatov, E. Garutti, M. Groll, A. Ilyin, V. Kantserov, V. Kaplin, A. Karakash, F. Kayumov, S. Klemin, V. Korbel, H. Meyer, R. Mizuk, V. Morgunov, E. Novikov, P. Pakhlov, E. Popova, V. Rusinov, F. Sefkow, E. Tarkovsky, and I. Tikhomirov, *Status report on silicon photomultiplier development and its applications*, Nuclear Instruments and Methods in Physics Research Section A: Accelerators, Spectrometers, Detectors and Associated Equipment, 563 (2006), pp. 368–376.

[75] J. Du, G. Hamilton, A. Takahashi, M. Bydder, and C. B. Chung, *Ultrashort echo time spectroscopic imaging (UTESI) of cortical bone*, Magn Reson Med, 58 (2007), pp. 1001–1009.

[76] J. P. Earls, E. L. Berman, B. A. Urban, C. A. Curry, J. L. Lane, R. S. Jennings, C. C. McCulloch, J. Hsieh, and J. H. Londt, *Prospectively gated transverse coronary CT angiography versus retrospectively gated helical technique: improved image quality and reduced radiation dose*, Radiology, 246 (2008), pp. 742–753.

[77] W. C. Eckelman, *Positron emission tomography: radiochemistry*, Acad Radiol, 2 Suppl 2 (1995), pp. S96–S97.

[78] W. A. Edelstein, J. M. Hutchison, G. Johnson, and T. Redpath, *Spin warp NMR imaging and applications to human whole-body imaging*, Phys Med Biol, 25 (1980), pp. 751–756.

[79] R. L. Ehman and J. P. Felmlee, *Adaptive technique for high-definition MR imaging of moving structures*, Radiology, 173 (1989), pp. 255–263.

[80] R. L. Ehman, M. T. McNamara, M. Pallack, H. Hricak, and C. B. Higgins, *Magnetic resonance imaging with respiratory gating: techniques and advantages*, AJR Am J Roentgenol, 143 (1984), pp. 1175–1182.

[81] A. J. Einstein, M. J. Henzlova, and S. Rajagopalan, *Estimating risk of cancer associated with radiation exposure from 64-slice computed tomography coronary angiography*, JAMA, 298 (2007), pp. 317–323.

[82] P. H. Elsinga, *Radiopharmaceutical chemistry for positron emission tomography*, Methods, 27 (2002), pp. 208–217.

[83] G. E. Fakhri, P. A. Santos, R. D. Badawi, C. H. Holdsworth, A. D. V. D. Abbeele, and M. F. Kijewski, *Impact of acquisition geometry, image processing, and patient size on lesion detection in whole-body 18F-FDG PET*, J Nucl Med, 48 (2007), pp. 1951–1960.

[84] K. Farahani, R. Slates, Y. Shao, R. Silverman, and S. Cherry, *Contemporaneous positron emission tomography and MR imaging at 1.5 T*, J Magn Reson Imaging, 9 (1999), pp. 497–500.

[85] T. G. Flohr, C. H. McCollough, H. Bruder, M. Petersilka, K. Gruber, C. Süss, M. Grasruck, K. Stierstorfer, B. Krauss, R. Raupach, A. N. Primak, A. Küttner, S. Achenbach, C. Becker, A. Kopp, and B. M. Ohnesorge, *First performance evaluation of a dual-source CT (DSCT) system*, Eur Radiol, 16 (2006), pp. 256–268.

[86] T. G. Flohr, U. J. Schoepf, and B. M. Ohnesorge, *Chasing the heart: new developments for cardiac CT*, J Thorac Imaging, 22 (2007), pp. 4–16.

[87] M. Francone, A. Napoli, I. Carbone, M. Cavacece, P. G. Nardis, K. Lanciotti, S. Visconti, L. Bertoletti, E. D. Castro, C. Catalano, and R. Passariello, *Noninvasive imaging of the coronary arteries using a 64-row*

multidetector CT scanner: initial clinical experience and radiation dose concerns, Radiol Med, 112 (2007), pp. 31–46.

[88] H. Fricke, E. Fricke, R. Weise, A. Kammeier, O. Lindner, and W. Burchert, *A method to remove artifacts in attenuation-corrected myocardial perfusion SPECT Introduced by misalignment between emission scan and CT-derived attenuation maps*, J Nucl Med, 45 (2004), pp. 1619–1625.

[89] J. Fripp, S. Crozier, S. K. Warfield, and S. Ourselin, *Automatic segmentation of the bone and extraction of the bone-cartilage interface from magnetic resonance images of the knee*, Phys Med Biol, 52 (2007), pp. 1617–1631.

[90] T. Fuchs, M. Kachelriess, and W. A. Kalender, *Technical advances in multi-slice spiral CT*, Eur J Radiol, 36 (2000), pp. 69–73.

[91] O. Gaemperli, T. Schepis, I. Valenta, L. Husmann, H. Scheffel, V. Duerst, F. R. Eberli, T. F. Luscher, H. Alkadhi, and P. A. Kaufmann, *Cardiac image fusion from stand-alone SPECT and CT: clinical experience*, J Nucl Med, 48 (2007), pp. 696–703.

[92] S. S. Gambhir, *Molecular imaging of cancer with positron emission tomography*, Nat Rev Cancer, 2 (2002), pp. 683–693.

[93] P. B. Garlick, P. K. Marsden, A. C. Cave, H. G. Parkes, R. Slates, Y. Shao, R. W. Silverman, and S. R. Cherry, *PET and NMR dual acquisition (PANDA): applications to isolated, perfused rat hearts*, NMR Biomed, 10 (1997), pp. 138–142.

[94] A. N. Garraway, P. K. Grannell, and P. Mansfield, *Image formation in NMR by a selective irradiative process*, J Phys C: Solid State Phys, 7 (1974), pp. L457–L462.

[95] P. D. Gatehouse, R. W. Thomas, M. D. Robson, G. Hamilton, A. H. Herlihy, and G. M. Bydder, *Magnetic resonance imaging of the knee with ultrashort TE pulse sequences*, Magn Reson Imaging, 22 (2004), pp. 1061–1067.

[96] R. A. Gatenby and R. J. Gillies, *Why do cancers have high aerobic glycolysis?*, Nat Rev Cancer, 4 (2004), pp. 891–899.

[97] E. M. Geltman, R. Roberts, and B. E. Sobel, *Cardiac positron tomography: current status and future directions*, Herz, 5 (1980), pp. 107–119.

[98] R. J. Gillies, I. Robey, and R. A. Gatenby, *Causes and consequences of increased glucose metabolism of cancers*, J Nucl Med, 49 Suppl 2 (2008), pp. 24S–42S.

[99] G. W. Goerres, C. Burger, E. Kamel, B. Seifert, A. H. Kaim, A. Buck, T. C. Buehler, and G. K. V. Schulthess, *Respiration-induced attenuation artifact at PET/CT: technical considerations*, Radiology, 226 (2003), pp. 906–910.

[100] G. W. Goerres, E. Kamel, T.-N. H. Heidelberg, M. R. Schwitter, C. Burger, and G. K. von Schulthess, *PET-CT image co-registration in the thorax: influence of respiration*, Eur J Nucl Med Mol Imaging, 29 (2002), pp. 351–360.

[101] K. L. Gould, T. Pan, C. Loghin, N. P. Johnson, A. Guha, and S. Sdringola, *Frequent diagnostic errors in cardiac PET/CT due to misregistration of CT attenuation and emission PET images: a definitive analysis of causes, consequences, and corrections*, J Nucl Med, 48 (2007), pp. 1112–1121.

[102] M. V. Green, H. G. Ostrow, M. A. Douglas, R. W. Myers, R. N. Scott, J. J. Bailey, and G. S. Johnston, *High temporal resolution ECG-gated scintigraphic angiocardiography*, J Nucl Med, 16 (1975), pp. 95–98.

[103] J. V. Guadagno, E. A. Warburton, P. S. Jones, D. J. Day, F. I. Aigbirhio, T. D. Fryer, S. Harding, C. J. Price, H. A. Green, O. Barret, J. H. Gillard, and J.-C. Baron, *How affected is oxygen metabolism in DWI lesions? A combined acute stroke PET-MR study*, Neurology, 67 (2006), pp. 824–829.

[104] M. Habis, A. Capderou, S. Ghostine, B. Daoud, C. Caussin, J.-Y. Riou, P. Brenot, C. Y. Angel, B. Lancelin, and J.-F. Paul, *Acute myocardial infarction early viability assessment by 64-slice computed tomography immediately after coronary angiography: comparison with low-dose dobutamine echocardiography*, J Am Coll Cardiol, 49 (2007), pp. 1178–1185.

[105] R. Hachamovitch, D. S. Berman, L. J. Shaw, H. Kiat, I. Cohen, J. A. Cabico, J. Friedman, and G. A. Diamond, *Incremental prognostic value of myocardial perfusion single photon emission computed tomography for the prediction of cardiac death: differential stratification for risk of cardiac death and myocardial infarction*, Circulation, 97 (1998), pp. 535–543.

[106] R. Hachamovitch, S. W. Hayes, J. D. Friedman, I. Cohen, and D. S. Berman, *Stress myocardial perfusion single-photon emission computed tomography is clinically effective and cost effective in risk stratification of patients with a high likelihood of coronary artery disease (CAD) but no known CAD*, J Am Coll Cardiol, 43 (2004), pp. 200–208.

[107] B. E. Hammer, N. L. Christensen, and B. G. Heil, *Use of a magnetic field to increase the spatial resolution of positron emission tomography*, Med Phys, 21 (1994), pp. 1917–1920.

[108] M. Hamon, R. Morello, J. W. Riddell, and M. Hamon, *Coronary arteries: diagnostic performance of 16- versus 64-section spiral CT compared with invasive coronary angiography–meta-analysis*, Radiology, 245 (2007), pp. 720–731.

[109] J. Hartiala and J. Knuuti, *Imaging of the heart by MRI and PET*, Ann Med, 27 (1995), pp. 35–45.

[110] J. Hartigan and M. Wong, *A K-means clustering algorithm*, Appl Stat, 28 (1979), pp. 100–108.

[111] R. H. Hashemi, W. G. Bradley, and C. J. Lisanti, *MRI: The basics*, Lippincott Williams & Wilkins, 2004.

[112] J. Hausleiter, T. Meyer, F. Hermann, M. Hadamitzky, M. Krebs, T. C. Gerber, C. McCollough, S. Martinoff, A. Kastrati, A. Schömig, and S. Achenbach, *Estimated radiation dose associated with cardiac CT angiography*, JAMA, 301 (2009), pp. 500–507.

[113] W.-D. Heiss, *The potential of PET/MR for brain imaging*, Eur J Nucl Med Mol Imaging, 36 Suppl 1 (2009), pp. S105–S112.

[114] K. Herholz, D. Coope, and A. Jackson, *Metabolic and molecular imaging in neuro-oncology*, Lancet Neurol, 6 (2007), pp. 711–724.

[115] K. Herholz and W.-D. Heiss, *Positron emission tomography in clinical neurology*, Mol Imaging Biol, 6 (2004), pp. 239–269.

[116] R. J. Hicks, *Beyond FDG: novel PET tracers for cancer imaging*, Cancer Imaging, 4 (2004), pp. 22–24.

[117] C. B. Higgins, E. H. Botvinick, P. Lanzer, R. Herfkens, M. J. Lipton, L. E. Crooks, and L. Kaufman, *Cardiovascular imaging with nuclear magnetic resonance*, Cardiol Clin, 1 (1983), pp. 527–539.

[118] T. Higuchi, S. G. Nekolla, M. M. Huisman, S. Reder, T. Poethko, M. Yu, H.-J. Wester, D. S. Casebier, S. P. Robinson, R. M. Botnar, and M. Schwaiger, *A new 18F-labeled myocardial PET tracer: myocardial uptake after permanent and transient coronary occlusion in rats*, J Nucl Med, 49 (2008), pp. 1715–1722.

[119] T. Higuchi, S. G. Nekolla, A. Jankaukas, A. W. Weber, M. C. Huisman, S. Reder, S. I. Ziegler, M. Schwaiger, and F. M. Bengel, *Characterization of normal and infarcted rat myocardium using a combination of small-animal PET and clinical MRI*, J Nucl Med, 48 (2007), pp. 288–294.

[120] E. J. Hoffman, M. E. Phelps, G. Wisenberg, H. R. Schelbert, and D. E. Kuhl, *Electrocardiographic gating in positron emission computed tomography*, J Comput Assist Tomogr, 3 (1979), pp. 733–739.

[121] M. Hofmann, F. Steinke, V. Scheel, G. Charpiat, J. Farquhar, P. Aschoff, M. Brady, B. Schölkopf, and B. J. Pichler, *MRI-based attenuation correction for PET/MRI: a novel approach combining pattern recognition and atlas registration*, J Nucl Med, 49 (2008), pp. 1875–1883.

[122] G. N. Hounsfield, *Computerized transverse axial scanning (tomography): Part 1. Description of the system*, Br J Radiol, 46 (1973), pp. 1016–22.

[123] J. Hsieh, J. Londt, M. Vass, J. Li, X. Tang, and D. Okerlund, *Step-and-shoot data acquisition and reconstruction for cardiac x-ray computed tomography*, Med Phys, 33 (2006), pp. 4236–4248.

[124] H. Hu, H. D. He, S. Fox, S. Ackelsberg, G. Strong, and G. Seidenschnur, *Multi-slice helical CT: principles, imaging characteristics, and performance*, in Proc. 20th Annual International Conference of the IEEE Engineering in Medicine and Biology Society, vol. 2, 29 Oct.–1 Nov. 1998, pp. 637–639.

[125] H. M. Hudson and R. S. Larkin, *Accelerated image reconstruction using ordered subsets of projection data*, IEEE Trans Med Imaging, 13 (1994), pp. 601–609.

[126] L. Husmann, I. Valenta, O. Gaemperli, O. Adda, V. Treyer, C. A. Wyss, P. Veit-Haibach, F. Tatsugami, G. K. von Schulthess, and P. A. Kaufmann, *Feasibility of low-dose coronary CT angiography: first experience with prospective ECG-gating*, Eur Heart J, 29 (2008), pp. 191–197.

[127] R. Hustinx, R. J. Dolin, F. Bénard, A. Bhatnagar, D. Chakraborty, R. J. Smith, S. Jang, and A. Alavi, *Impact of attenuation correction on the accuracy of FDG-PET in patients with abdominal tumors: a free-response ROC analysis*, Eur J Nucl Med, 27 (2000), pp. 1365–1371.

[128] M. Hutchinson and U. Raff, *Fast MRI data acquisition using multiple detectors*, Magn Reson Med, 6 (1988), pp. 87–91.

[129] T. Ido, C.-N. Wan, V. Casella, J. S. Fowler, and A. P. Wolf, *Fluorination with F2. A convenient synthesis of 2-deoxy-2-fluoro-D-glucose*, J Org Chem, 42 (1977), pp. 2341–2.

[130] T. Ido, C.-N. Wan, V. Casella, J. S. Fowler, A. P. Wolf, and R. M, *Labeled 2-deoxy-D-glucose analogs. 18F-Labeled 2-deoxy-2-fluoro-D-glucose, 2-deoxy-2-fluoro-D-mannose and 14C-2-deoxy-2-fluoro-D-glucose*, J Label Cmpds Radiopharm, 14 (1978), pp. 175–83.

[131] C. J. Jaskowiak, J. A. Bianco, S. B. Perlman, and J. P. Fine, *Influence of reconstruction iterations on 18F-FDG PET/CT standardized uptake values*, J Nucl Med, 46 (2005), pp. 424–428.

[132] M. Javadi, M. Mahesh, G. McBride, C. Voicu, W. Epley, J. Merrill, and F. M. Bengel, *Lowering radiation dose for integrated assessment of coronary morphology and physiology: first experience with step-and-shoot CT angiography in a rubidium 82 PET-CT protocol*, J Nucl Cardiol, 15 (2008), pp. 783–790.

[133] F. Joliot, *Preuve expérimentale de l'annihilation des électrons positifs*, C R Acad Sci, 197 (1933), pp. 1622–1625.

[134] I. T. Jolliffe, *Principal component analysis*, no. ISBN 978-0-387-95442-4 in Series in statistics, Springer, 2nd ed. ed., 2002.

[135] M. S. Judenhofer, H. F. Wehrl, D. F. Newport, C. Catana, S. B. Siegel, M. Becker, A. Thielscher, M. Kneilling, M. P. Lichy, M. Eichner, K. Klingel, G. Reischl, S. Widmaier, M. Röcken, R. E. Nutt, H.-J. Machulla, K. Uludag, S. R. Cherry, C. D. Claussen, and B. J. Pichler, *Simultaneous PET-MRI: a new approach for functional and morphological imaging*, Nat Med, 14 (2008), pp. 459–465.

[136] M. E. Juweid and B. D. Cheson, *Positron-emission tomography and assessment of cancer therapy*, N Engl J Med, 354 (2006), pp. 496–507.

[137] K. Kacperski, N. M. Spyrou, and F. A. Smith, *Three-gamma annihilation imaging in positron emission tomography*, IEEE Trans Med Imaging, 23 (2004), pp. 525–529.

[138] W. A. Kalender, R. Rienmüller, W. Seissler, J. Behr, M. Welke, and H. Fichte, *Measurement of pulmonary parenchymal attenuation: use of spirometric gating with quantitative CT*, Radiology, 175 (1990), pp. 265–268.

[139] W. A. Kalender, W. Seissler, E. Klotz, and P. Vock, *Spiral volumetric CT with single-breath-hold technique, continuous transport, and continuous scanner rotation*, Radiology, 176 (1990), pp. 181–183.

[140] E. Kaplan, G. A. Gergans, T. Milo, A. M. Friedman, and J. T. Sharp, *Dynamic imaging of the respiratory cycle with 81mKr*, Chest, 81 (1982), pp. 312–317.

[141] J. Kassubek, F. D. Juengling, E. U. Nitzsche, and C. H. Lücking, *Limbic encephalitis investigated by 18FDG-PET and 3D MRI*, J Neuroimaging, 11 (2001), pp. 55–59.

[142] P. A. Kaufmann and P. G. Camici, *Myocardial blood flow measurement by PET: technical aspects and clinical applications*, J Nucl Med, 46 (2005), pp. 75–88.

[143] J. W. Keyes, *SUV: standard uptake or silly useless value?*, J Nucl Med, 36 (1995), pp. 1836–1839.

[144] H. P. Kühl, A. M. Beek, A. P. van der Weerdt, M. B. M. Hofman, C. A. Visser, A. A. Lammertsma, N. Heussen, F. C. Visser, and A. C. van Rossum, *Myocardial viability in chronic ischemic heart disease: comparison of contrast-enhanced magnetic resonance imaging with (18)F-fluorodeoxyglucose positron emission tomography*, J Am Coll Cardiol, 41 (2003), pp. 1341–1348.

[145] K. Khurshid, R. J. McGough, and K. Berger, *Automated cardiac motion compensation in PET/CT for accurate reconstruction of PET myocardial perfusion images*, Phys Med Biol, 53 (2008), pp. 5705–5718.

[146] Y. Kikuchi, K. Ishii, H. Yamazaki, S. Matsuyama, T. Yamaguchi, Y. Yamamoto, T. Sato, Y. Aoki, and K. Aoki, *Preliminary report on the development of a high resolution PET camera using semiconductor detectors*, Nuclear Instruments and Methods in Physics Research Section B: Beam Interactions with Materials and Atoms, 241 (2005), pp. 727 – 731.

[147] C. K. Kim, N. C. Gupta, B. Chandramouli, and A. Alavi, *Standardized uptake values of FDG: body surface area correction is preferable to body weight correction*, J Nucl Med, 35 (1994), pp. 164–167.

[148] P. E. Kinahan, B. H. Hasegawa, and T. Beyer, *X-ray-based attenuation correction for positron emission tomography/computed tomography scanners*, Semin Nucl Med, 33 (2003), pp. 166–179.

[149] P. E. Kinahan, D. W. Townsend, T. Beyer, and D. Sashin, *Attenuation correction for a combined 3D PET/CT scanner*, Med Phys, 25 (1998), pp. 2046–2053.

[150] G. Klein, B. Reutter, E. Botvinick, T. Budinger, and R. Huesman, *Fine-scale motion detection using intrinsic List Mode PET information*, in Proc. Mathematical Methods in Biomedical Image Analysis, 2001, pp. 71–78.

[151] G. Klein, B. Reutter, M. Hol, J. Reed, and R. Huesman, *Real-time system for respiratory-cardiac gating in positron tomography*, IEEE Trans Nucl Sci, 45 (1998), pp. 2139–43.

[152] R. A. Kloner, R. Bolli, E. Marban, L. Reinlib, and E. Braunwald, *Medical and cellular implications of stunning, hibernation, and preconditioning: an NHLBI workshop*, Circulation, 97 (1998), pp. 1848–1867.

[153] P. Knaapen and M. Lubberink, *Cardiac positron emission tomography: myocardial perfusion and metabolism in clinical practice*, Clin Res Cardiol, 97 (2008), pp. 791–796.

[154] P. Koepfli, T. F. Hany, C. A. Wyss, M. Namdar, C. Burger, A. V. Konstantinidis, T. Berthold, G. K. V. Schulthess, and P. A. Kaufmann, *CT attenuation correction for myocardial perfusion quantification using a PET/CT hybrid scanner*, J Nucl Med, 45 (2004), pp. 537–542.

[155] H. D. Kubo and B. C. Hill, *Respiration gated radiotherapy treatment: a technical study*, Physics in Medicine and Biology, 41 (1996), pp. 83–91.

[156] D. E. Kuhl and R. Q. Edwards, *Reorganizing data from transverse section scans of the brain using digital processing*, Radiology, 91 (1968), pp. 975–983.

[157] D. E. Kuhl, R. Q. Edwards, A. R. Ricci, and M. Reivich, *Quantitative section scanning using orthogonal tangent correction*, J Nucl Med, 14 (1973), pp. 196–200.

[158] A. Kumar, D. Welti, and R. Ernst, *NMR Fourier zeugmatography*, J Magn Reson, 18 (1975), pp. 69–83.

[159] K.-Y. Kwon, C. G. Choi, J. S. Kim, M. C. Lee, and S. J. Chung, *Comparison of brain MRI and 18F-FDG PET in the differential diagnosis of multiple system atrophy from Parkinson's disease*, Mov Disord, 22 (2007), pp. 2352–2358.

[160] M. J. LaMonte, S. J. FitzGerald, T. S. Church, C. E. Barlow, N. B. Radford, B. D. Levine, J. J. Pippin, L. W. Gibbons, S. N. Blair, and M. Z. Nichaman, *Coronary artery calcium score and coronary heart disease events in a large cohort of asymptomatic men and women*, Am J Epidemiol, 162 (2005), pp. 421–429.

[161] H. F. Langer, R. Haubner, B. J. Pichler, and M. Gawaz, *Radionuclide imaging: a molecular key to the atherosclerotic plaque*, J Am Coll Cardiol, 52 (2008), pp. 1–12.

[162] J. Langner, *Electron-positron annihilation*, March 2009. http://en.wikipedia.org/wiki/File:Annihilation.png.

[163] P. Lanzer, E. H. Botvinick, N. B. Schiller, L. E. Crooks, M. Arakawa, L. Kaufman, P. L. Davis, R. Herfkens, M. J. Lipton, and C. B. Higgins, *Cardiac imaging using gated magnetic resonance*, Radiology, 150 (1984), pp. 121–127.

[164] D. J. Larkman and R. G. Nunes, *Parallel magnetic resonance imaging*, Phys Med Biol, 52 (2007), pp. R15–R55.

[165] C. Lartizien, P. E. Kinahan, R. Swensson, C. Comtat, M. Lin, V. Villemagne, and R. Trébossen, *Evaluating image reconstruction methods for tumor detection in 3-dimensional whole-body PET oncology imaging*, J Nucl Med, 44 (2003), pp. 276–290.

[166] R. Lautamäki, T. L. Y. Brown, J. Merrill, and F. M. Bengel, *CT-based attenuation correction in (82)Rb-myocardial perfusion PET-CT: incidence of misalignment and effect on regional tracer distribution*, Eur J Nucl Med Mol Imaging, 35 (2008), pp. 305–310.

[167] P. C. Lauterbur, *Image formation by induced local interactions: examples employing nuclear magnetic resonance*, Nature, 242 (1973), pp. 190–1.

[168] R. Lecomte, *Novel detector technology for clinical PET*, Eur J Nucl Med Mol Imaging, 36 Suppl 1 (2009), pp. S69–S85.

[169] R. Lecomte, J. Cadorette, S. Rodrigue, D. Lapointe, D. Rouleau, M. Bentourkia, R. Yao, and P. Msaki, *Initial results from the Sherbrooke avalanche photodiode positron tomograph*, Nuclear Science, IEEE Transactions on, 43 (1996), pp. 1952–1957.

[170] H.-Y. Lee, Z. Li, K. Chen, A. R. Hsu, C. Xu, J. Xie, S. Sun, and X. Chen, *PET/MRI dual-modality tumor imaging using arginine-glycine-aspartic (RGD)-conjugated radiolabeled iron oxide nanoparticles*, J Nucl Med, 49 (2008), pp. 1371–1379.

[171] Y. Liang and R. A. Kruger, *Dual-slice spiral versus single-slice spiral scanning: comparison of the physical performance of two computed tomography scanners*, Med Phys, 23 (1996), pp. 205–220.

[172] P. Libby, *Current concepts of the pathogenesis of the acute coronary syndromes*, Circulation, 104 (2001), pp. 365–372.

[173] L. Livieratos, K. Rajappan, L. Stegger, K. Schafers, D. L. Bailey, and P. G. Camici, *Respiratory gating of cardiac PET data in list-mode acquisition*, Eur J Nucl Med Mol Imaging, 33 (2006), pp. 584–588.

[174] L. Livieratos, L. Stegger, P. M. Bloomfield, K. Schafers, D. L. Bailey, and P. G. Camici, *Rigid-body transformation of list-mode projection data for respiratory motion correction in cardiac PET*, Phys Med Biol, 50 (2005), pp. 3313–3322.

[175] G. Llosa, R. Battiston, N. Belcari, M. Boscardin, G. Collazuol, F. Corsi, G.-F. Dalla Betta, A. Del Guerra, N. Dinu, G. Levi, S. Marcatili, S. Moehrs, C. Marzocca, C. Piemonte, and A. Pozza, *Novel Silicon Photomultipliers for PET Applications*, Nuclear Science, IEEE Transactions on, 55 (2008), pp. 877–881.

[176] C. Loghin, S. Sdringola, and K. L. Gould, *Common artifacts in PET myocardial perfusion images due to attenuation-emission misregistration: clinical significance, causes, and solutions*, J Nucl Med, 45 (2004), pp. 1029–1039.

[177] J. Ma, *Dixon techniques for water and fat imaging*, J Magn Reson Imaging, 28 (2008), pp. 543–558.

[178] J. Ma, A. T. Vu, J. B. Son, H. Choi, and J. D. Hazle, *Fat-suppressed three-dimensional dual echo Dixon technique for contrast agent enhanced MRI*, J Magn Reson Imaging, 23 (2006), pp. 36–41.

[179] F. Maes, A. Collignon, D. Vandermeulen, G. Marchal, and P. Suetens, *Multimodality image registration by maximization of mutual information*, IEEE Trans Med Imaging, 16 (1997), pp. 187–198.

[180] A. Malesci, L. Balzarini, A. Chiti, and G. Lucignani, *Pancreatic cancer or chronic pancreatitis? An answer from PET/MRI image fusion*, Eur J Nucl Med Mol Imaging, 31 (2004), p. 1352.

[181] A. Mallon and P. Grangeat, *Three-dimensional PET reconstruction with time-of-flight measurement*, Phys Med Biol, 37 (1992), pp. 717–729.

[182] D. Manke, K. Nehrke, P. Börnert, P. Rösch, and O. Dössel, *Respiratory motion in coronary magnetic resonance angiography: a comparison of different motion models*, J Magn Reson Imaging, 15 (2002), pp. 661–671.

[183] P. Mansfield, P. G. Morris, R. J. Ordidge, I. L. Pykett, V. Bangert, and R. E. Coupland, *Human whole body imaging and detection of breast tumours by N.M.R.*, Philos Trans R Soc Lond B Biol Sci, 289 (1980), pp. 503–510.

[184] A. Martinez-Möller, M. Souvatzoglou, G. Delso, R. A. Bundschuh, C. Chefd'hotel, S. I. Ziegler, N. Navab, M. Schwaiger, and S. G. Nekolla, *Tissue Classification as a Potential Approach for Attenuation Correction in Whole-Body PET/MRI: Evaluation with PET/CT Data*, J Nucl Med, 50 (2009), pp. 520–526.

[185] A. Martinez-Möller, M. Souvatzoglou, N. Navab, M. Schwaiger, and S. G. Nekolla, *Artifacts from misaligned CT in cardiac perfusion PET/CT studies: frequency, effects, and potential solutions*, J Nucl Med, 48 (2007), pp. 188–193.

[186] A. Martinez-Möller, D. Zikic, R. M. Botnar, R. A. Bundschuh, W. Howe, S. I. Ziegler, N. Navab, M. Schwaiger, and S. G. Nekolla, *Dual cardiac-respiratory gated PET: implementation and results from a feasibility study*, Eur J Nucl Med Mol Imaging, 34 (2007), pp. 1447–1454.

[187] A. Martinez-Moller, R. Bundschuh, N. Navab, S. Ziegler, M. Schwaiger, and S. Nekolla, *Determination of body surface area from a whole-body CT scan and its impact for SUV normalization*, J Nucl Med, 48 (2007), pp. 44P–c–.

[188] A. Martinez-Moller, R. Bundschuh, M. Riedel, N. Navab, S. Ziegler, M. Schwaiger, and S. Nekolla, *Comparison of respiratory sensors and its compliance for respiratory gating in emission tomography*, J Nucl Med, 48 (2007), pp. 426P–b–.

[189] A. Martinez-Moller, M.-J. Martinez, S. Ziegler, N. Navab, M. Schwaiger, and S. Nekolla, *Emission driven motion correction in PET/CT cardiac imaging*, J Nucl Med, 46 (2005), pp. 163P–b–.

[190] A. Martinez-Moller, N. Navab, M. Schwaiger, and S. Nekolla, *Emission-transmission misregistration artifacts in cardiac PET/CT: extent and solutions*, Journal of Nuclear Cardiology, 14 (2007), p. 60.

[191] A. Martinez-Moller, M. Souvatzoglou, R. Botnar, N. Navab, S. Ziegler, M. Schwaiger, and S. Nekolla, *An approach for MR-based attenuation correction for combined MR/PET: effects of ignoring bones*, J Nucl Med, 48 (2007), pp. 156P–.

[192] A. Martinez-Moller, M. Souvatzoglou, M. Schwaiger, and S. Nekolla, *Bewegungsartefakte in der Herz-PET/CT: Effekte auf der Tracerverteilung und*

Evaluierung eines Korrekturalgorithmus, in Deutsche Gesellschaft für Nuklearmedizin, 2006.

[193] I. Matsunari, G. Böning, S. I. Ziegler, I. Kosa, S. G. Nekolla, E. P. Ficaro, and M. Schwaiger, *Effects of misalignment between transmission and emission scans on attenuation-corrected cardiac SPECT*, J Nucl Med, 39 (1998), pp. 411–416.

[194] I. Matsunari, J. Taki, K. Nakajima, N. Tonami, and K. Hisada, *Myocardial viability assessment using nuclear imaging*, Ann Nucl Med, 17 (2003), pp. 169–179.

[195] O. Mawlawi, J. J. Erasmus, R. F. Munden, T. Pan, A. E. Knight, H. A. Macapinlac, D. A. Podoloff, and M. Chasen, *Quantifying the effect of IV contrast media on integrated PET/CT: clinical evaluation*, AJR Am J Roentgenol, 186 (2006), pp. 308–319.

[196] M. E. McCord, S. L. Bacharach, R. O. Bonow, V. Dilsizian, A. Cuocolo, and N. Freedman, *Misalignment between PET transmission and emission scans: its effect on myocardial imaging*, J Nucl Med, 33 (1992), pp. 1209–14; discussion 1214–5.

[197] K. McLeish, D. L. G. Hill, D. Atkinson, J. M. Blackall, and R. Razavi, *A study of the motion and deformation of the heart due to respiration*, IEEE Trans Med Imaging, 21 (2002), pp. 1142–1150.

[198] L. L. Meunier, R. Maass-Moreno, J. A. Carrasquillo, W. Dieckmann, and S. L. Bacharach, *PET/CT imaging: effect of respiratory motion on apparent myocardial uptake*, J Nucl Cardiol, 13 (2006), pp. 821–830.

[199] R. S. Miletich, *Positron Emission Tomography for Neurologists*, Neurol Clin, 27 (2009), pp. 61–88.

[200] J. C. Miller, S. Abbara, W. S. Mamuya, J. H. Thrall, and R. N. Uppot, *Dual-source CT for cardiac imaging*, J Am Coll Radiol, 6 (2009), pp. 65–68.

[201] J. M. Miller, C. E. Rochitte, M. Dewey, A. Arbab-Zadeh, H. Niinuma, I. Gottlieb, N. Paul, M. E. Clouse, E. P. Shapiro, J. Hoe, A. C. Lardo, D. E. Bush, A. de Roos, C. Cox, J. Brinker, and J. A. C. Lima, *Diagnostic performance of coronary angiography by 64-row CT*, N Engl J Med, 359 (2008), pp. 2324–2336.

[202] H. Minn, K. R. Zasadny, L. E. Quint, and R. L. Wahl, *Lung cancer: reproducibility of quantitative measurements for evaluating 2-[F-18]-fluoro-2-deoxy-D-glucose uptake at PET*, Radiology, 196 (1995), pp. 167–173.

[203] M. Miyagawa, M. Anton, B. Wagner, R. Haubner, M. Souvatzoglou, B. Gansbacher, M. Schwaiger, and F. M. Bengel, *Non-invasive imaging of cardiac transgene expression with PET: comparison of the human sodium/iodide*

symporter gene and HSV1-tk as the reporter gene, Eur J Nucl Med Mol Imaging, 32 (2005), pp. 1108–1114.

[204] J. Modersitzki, *Numerical methods for image registration*, Oxford University Press, Oxford, UK, 2004.

[205] S. Moehrs, A. D. Guerra, D. J. Herbert, and M. A. Mandelkern, *A detector head design for small-animal PET with silicon photomultipliers (SiPM)*, Phys Med Biol, 51 (2006), pp. 1113–1127.

[206] M.-L. Montandon and H. Zaidi, *Atlas-guided non-uniform attenuation correction in cerebral 3D PET imaging*, Neuroimage, 25 (2005), pp. 278–286.

[207] C. C. Morehouse, W. R. Brody, D. F. Guthaner, R. S. Breiman, and G. S. Harell, *Gated cardiac computed tomography with a motion phantom*, Radiology, 134 (1980), pp. 213–217.

[208] M. Mori, K. Murata, M. Takahashi, K. Shimoyama, T. Ota, R. Morita, and T. Sakamoto, *Accurate contiguous sections without breath-holding on chest CT: value of respiratory gating and ultrafast CT*, AJR Am J Roentgenol, 162 (1994), pp. 1057–1062.

[209] E. Moser, A. Stadlbauer, C. Windischberger, H. H. Quick, and M. E. Ladd, *Magnetic resonance imaging methodology*, Eur J Nucl Med Mol Imaging, 36 Suppl 1 (2009), pp. S30–S41.

[210] W. W. Moses, *Recent advances and future advances in Time-of-Flight PET*, Nucl Instrum Methods Phys Res A, 580 (2007), pp. 919–924.

[211] Y. Nakamoto, B. B. Chin, D. L. Kraitchman, L. P. Lawler, L. T. Marshall, and R. L. Wahl, *Effects of nonionic intravenous contrast agents at PET/CT imaging: phantom and canine studies*, Radiology, 227 (2003), pp. 817–824.

[212] Y. Nakamoto, M. Osman, C. Cohade, L. T. Marshall, J. M. Links, S. Kohlmyer, and R. L. Wahl, *PET/CT: comparison of quantitative tracer uptake between germanium and CT transmission attenuation-corrected images*, J Nucl Med, 43 (2002), pp. 1137–1143.

[213] M. Namdar, T. F. Hany, P. Koepfli, P. T. Siegrist, C. Burger, C. A. Wyss, T. F. Luscher, G. K. von Schulthess, and P. A. Kaufmann, *Integrated PET/CT for the assessment of coronary artery disease: a feasibility study*, J Nucl Med, 46 (2005), pp. 930–935.

[214] S. A. Nehmeh, Y. E. Erdi, C. C. Ling, K. E. Rosenzweig, H. Schoder, S. M. Larson, H. A. Macapinlac, O. D. Squire, and J. L. Humm, *Effect of respiratory gating on quantifying PET images of lung cancer*, J Nucl Med, 43 (2002), pp. 876–881.

[215] S. A. Nehmeh, Y. E. Erdi, C. C. Ling, K. E. Rosenzweig, O. D. Squire, L. E. Braban, E. Ford, K. Sidhu, G. S. Mageras, S. M. Larson, and J. L. Humm, *Effect of respiratory gating on reducing lung motion artifacts in PET imaging of lung cancer*, Med Phys, 29 (2002), pp. 366–371.

[216] S. Nekolla, A. Jankauskas, A. Martinez-Moeller, J. Hausleiter, K. Rahbar, M. Souvatzoglu, F. Bengel, and M. Schwaiger, *Cardiac PET/CT for definition of individually derived vessel territories*, J Nucl Med, 47 (2006), pp. 254P–.

[217] S. G. Nekolla, A. Martinez-Moeller, and A. Saraste, *PET and MRI in cardiac imaging: from validation studies to integrated applications*, Eur J Nucl Med Mol Imaging, 36 Suppl 1 (2009), pp. S121–S130.

[218] S. G. Nekolla, C. Miethaner, N. Nguyen, S. I. Ziegler, and M. Schwaiger, *Reproducibility of polar map generation and assessment of defect severity and extent assessment in myocardial perfusion imaging using positron emission tomography*, Eur J Nucl Med, 25 (1998), pp. 1313–1321.

[219] S. G. Nekolla, S. Reder, A. Saraste, T. Higuchi, G. Dzewas, A. Preissel, M. Huisman, T. Poethko, T. Schuster, M. Yu, S. Robinson, D. Casebier, J. Henke, H. J. Wester, and M. Schwaiger, *Evaluation of the novel myocardial perfusion positron-emission tomography tracer 18F-BMS-747158-02: comparison to 13N-ammonia and validation with microspheres in a pig model*, Circulation, 119 (2009), pp. 2333–2342.

[220] S.-H. Ng, T.-C. Yen, J. T.-C. Chang, S.-C. Chan, S.-F. Ko, H.-M. Wang, L.-Y. Lee, C.-J. Kang, A. M.-C. Wong, and C.-T. Liao, *Prospective study of [18F]fluorodeoxyglucose positron emission tomography and computed tomography and magnetic resonance imaging in oral cavity squamous cell carcinoma with palpably negative neck*, J Clin Oncol, 24 (2006), pp. 4371–4376.

[221] J. A. Nye, F. Esteves, and J. R. Votaw, *Minimizing artifacts resulting from respiratory and cardiac motion by optimization of the transmission scan in cardiac PET/CT*, Med Phys, 34 (2007), pp. 1901–1906.

[222] B. Ohnesorge, T. Flohr, K. Schwarz, J. P. Heiken, and K. T. Bae, *Efficient correction for CT image artifacts caused by objects extending outside the scan field of view*, Med Phys, 27 (2000), pp. 39–46.

[223] M. M. Osman, C. Cohade, Y. Nakamoto, L. T. Marshall, J. P. Leal, and R. L. Wahl, *Clinically significant inaccurate localization of lesions with PET/CT: frequency in 300 patients*, J Nucl Med, 44 (2003), pp. 240–243.

[224] M. M. Osman, C. Cohade, Y. Nakamoto, and R. L. Wahl, *Respiratory motion artifacts on PET emission images obtained using CT attenuation correction on PET-CT*, Eur J Nucl Med Mol Imaging, 30 (2003), pp. 603–606.

[225] A. Otte, J. Barral, B. Dolgoshein, J. Hose, S. Klemin, E. Lorenz, R. Mirzoyan, E. Popova, and M. Teshima, *A test of silicon photomultipliers as readout for PET*, Nuclear Instruments and Methods in Physics Research Section A: Accelerators, Spectrometers, Detectors and Associated Equipment, 545 (2005), pp. 705–75.

[226] T. Pan, O. Mawlawi, S. A. Nehmeh, Y. E. Erdi, D. Luo, H. H. Liu, R. Castillo, R. Mohan, Z. Liao, and H. A. Macapinlac, *Attenuation correction of PET images with respiration-averaged CT images in PET/CT*, J Nucl Med, 46 (2005), pp. 1481–1487.

[227] H. K. Pannu, T. G. Flohr, F. M. Corl, and E. K. Fishman, *Current concepts in multi-detector row CT evaluation of the coronary arteries: principles, techniques, and anatomy*, Radiographics, 23 Spec No (2003), pp. S111–S125.

[228] J. A. Parker, R. Secker-Walker, R. Hill, B. A. Siegel, and E. J. Potchen, *A new technique for the calculation of left ventricular ejection fraction*, J Nucl Med, 13 (1972), pp. 649–651.

[229] J.-F. Paul, M. Wartski, C. Caussin, A. Sigal-Cinqualbre, B. Lancelin, C. Angel, and G. Dambrin, *Late defect on delayed contrast-enhanced multidetector row CT scans in the prediction of SPECT infarct size after reperfused acute myocardial infarction: initial experience*, Radiology, 236 (2005), pp. 485–489.

[230] W. Pauli, *Zur Frage der Theoretischen Deutung der Satelliten einiger Spektrallinien und ihrer Beeinflussung durch Magnetische Felder*, Naturwiss, 12 (1924), pp. 741–743.

[231] E. K. Pauwels, M. J. Ribeiro, J. H. Stoot, V. R. McCready, M. Bourguignon, and B. MazièrePauwels1998, *FDG accumulation and tumor biology*, Nucl Med Biol, 25 (1998), pp. 317–322.

[232] K. Pearson, *On lines and planes of closest fit to systems of points in space*, Philosophical Magazine, 2 (1901), pp. 559–572.

[233] M. Petersilka, H. Bruder, B. Krauss, K. Stierstorfer, and T. G. Flohr, *Technical principles of dual source CT*, Eur J Radiol, 68 (2008), pp. 362–368.

[234] I. Peñuelas, J. F. Boán, J. M. Martí-Climent, B. Sangro, G. Mazzolini, J. Prieto, and J. A. Richter, *Positron emission tomography and gene therapy: basic concepts and experimental approaches for in vivo gene expression imaging*, Molecular Imaging & Biology, 6 (2004), pp. 225 – 238.

[235] B. Pichler, E. Lorenz, R. Mirzoyan, W. Pimpl, F. Roder, M. Schwaiger, and S. Ziegler, *Performance test of a LSO-APD PET module in a 9.4 Tesla magnet*, Nuclear Science Symposium, 1997. IEEE, 2 (1997), pp. 1237–1239 vol.2.

[236] B. J. Pichler, M. S. Judenhofer, and H. F. Wehrl, *PET/MRI hybrid imaging: devices and initial results*, Eur Radiol, 18 (2008), pp. 1077–1086.

[237] B. J. Pichler and S. I. Ziegler, *Emission Tomography*, Elsevier Academic Press, 2004, ch. 14, pp. 255–267.

[238] J. Qi and R. M. Leahy, *Iterative reconstruction techniques in emission computed tomography*, Phys Med Biol, 51 (2006), pp. R541–R578.

[239] J. Radon, *Über die Bestimmung von Funktionen durch ihre Integralwerte langs gewisser Mannigfaltigkeiten*, Ber. Verh. Konigl. Sachs. Ges. Wiss. Leipzig, 69 (1917), pp. 262–277.

[240] P. Raggi, L. J. Shaw, D. S. Berman, and T. Q. Callister, *Prognostic value of coronary artery calcium screening in subjects with and without diabetes*, J Am Coll Cardiol, 43 (2004), pp. 1663–1669.

[241] R. R. Raylman, S. Majewski, S. S. Velan, S. Lemieux, B. Kross, V. Popov, M. F. Smith, and A. G. Weisenberger, *Simultaneous acquisition of magnetic resonance spectroscopy (MRS) data and positron emission tomography (PET) images with a prototype MR-compatible, small animal PET imager*, J Magn Reson, 186 (2007), pp. 305–310.

[242] M. Riedel, *Respiratory motion estimation: tests and comparison of different sensors*, master's thesis, TU Munich, April 2006.

[243] M. D. Robson, P. D. Gatehouse, G. M. Bydder, and S. Neubauer, *Human imaging of phosphorus in cortical and trabecular bone in vivo*, Magn Reson Med, 51 (2004), pp. 888–892.

[244] E. M. Rohren, T. G. Turkington, and R. E. Coleman, *Clinical applications of PET in oncology*, Radiology, 231 (2004), pp. 305–332.

[245] A. Rosenfeld and J. Pfaltz, *Sequential operations in digital picture processing*, J ACM, 13 (1966), pp. 471–494.

[246] N. P. Rowell, J. Glaholm, M. A. Flower, B. Cronin, and V. R. McCready, *Anatomically derived attenuation coefficients for use in quantitative single photon emission tomography studies of the thorax*, Eur J Nucl Med, 19 (1992), pp. 36–40.

[247] J. H. F. Rudd, E. A. Warburton, T. D. Fryer, H. A. Jones, J. C. Clark, N. Antoun, P. Johnström, A. P. Davenport, P. J. Kirkpatrick, B. N. Arch, J. D. Pickard, and P. L. Weissberg, *Imaging atherosclerotic plaque inflammation with [18F]-fluorodeoxyglucose positron emission tomography*, Circulation, 105 (2002), pp. 2708–2711.

[248] J. Ruf, E. L. Hänninen, M. Böhmig, I. Koch, T. Denecke, M. Plotkin, J. Langrehr, B. Wiedenmann, R. Felix, and H. Amthauer, *Impact of FDG-PET/MRI image fusion on the detection of pancreatic cancer*, Pancreatology, 6 (2006), pp. 512–519.

[249] V. M. Runge, J. A. Clanton, C. L. Partain, and A. E. James, *Respiratory gating in magnetic resonance imaging at 0.5 Tesla*, Radiology, 151 (1984), pp. 521–523.

[250] F. Rybicki, *Lower radiation dose coronary CT angiography with new imaging technologies*, Int J Cardiovasc Imaging, (2009).

[251] S. S. Sagel, E. S. Weiss, R. G. Gillard, G. N. Hounsfield, G. T. Jost, R. J. Stanley, and M. M. Ter-Pogossian, *Gated computed tomography of the human heart*, Invest Radiol, 12 (1977), pp. 563–566.

[252] D. V. Sahani, S. P. Kalva, A. J. Fischman, R. Kadavigere, M. Blake, P. F. Hahn, and S. Saini, *Detection of liver metastases from adenocarcinoma of the colon and pancreas: comparison of mangafodipir trisodium-enhanced liver MRI and whole-body FDG PET*, AJR Am J Roentgenol, 185 (2005), pp. 239–246.

[253] T. Sasano, M. R. Abraham, K.-C. Chang, H. Ashikaga, K. J. Mills, D. P. Holt, J. Hilton, S. G. Nekolla, J. Dong, A. C. Lardo, H. Halperin, R. F. Dannals, E. Marbán, and F. M. Bengel, *Abnormal sympathetic innervation of viable myocardium and the substrate of ventricular tachycardia after myocardial infarction*, J Am Coll Cardiol, 51 (2008), pp. 2266–2275.

[254] A. Savitzky and M. Golay, *Smoothing and differenciation of data by simplified least squares procedures*, Anal Chem, 36 (1964), pp. 1627–1639.

[255] P. J. Scanlon, D. P. Faxon, A. M. Audet, B. Carabello, G. J. Dehmer, K. A. Eagle, R. D. Legako, D. F. Leon, J. A. Murray, S. E. Nissen, C. J. Pepine, R. M. Watson, J. L. Ritchie, R. J. Gibbons, M. D. Cheitlin, T. J. Gardner, A. Garson, R. O. Russell, T. J. Ryan, and S. C. Smith, *ACC/AHA guidelines for coronary angiography. A report of the American College of Cardiology/American Heart Association Task Force on practice guidelines (Committee on Coronary Angiography). Developed in collaboration with the Society for Cardiac Angiography and Interventions*, J Am Coll Cardiol, 33 (1999), pp. 1756–1824.

[256] D. J. Schaefer, J. D. Bourland, and J. A. Nyenhuis, *Review of patient safety in time-varying gradient fields*, J Magn Reson Imaging, 12 (2000), pp. 20–29.

[257] M. P. Schenker, S. Dorbala, E. C. T. Hong, F. J. Rybicki, R. Hachamovitch, R. Y. Kwong, and M. F. D. Carli, *Interrelation of coronary calcification, myocardial ischemia, and outcomes in patients with intermediate likelihood of coronary artery disease: a combined positron emission tomography/computed tomography study*, Circulation, 117 (2008), pp. 1693–1700.

[258] F. Schick, *Whole-body MRI at high field: technical limits and clinical potential*, Eur Radiol, 15 (2005), pp. 946–959.

[259] A. F. L. Schinkel, D. Poldermans, A. Elhendy, and J. J. Bax, *Assessment of myocardial viability in patients with heart failure.*, J Nucl Med, 48 (2007), pp. 1135–1146.

[260] G. Schlaug, H. Hefter, V. Engelbrecht, T. Kuwert, S. Arnold, G. Stöcklin, and R. J. Seitz, *Neurological impairment and recovery in Wilson's disease: evidence from PET and MRI*, J Neurol Sci, 136 (1996), pp. 129–139.

[261] P. Schleyer, M. O'Doherty, S. Barrington, and P. Marsden, *Retrospective data-driven respiratory gating for PET/CT*, Phys Med Biol, 54 (2009), pp. 1935–1950.

[262] C. Schmelz, S. Bradbury, I. Holl, E. Lorenz, D. Renker, and S. Ziegler, *Feasibility study of an avalanche photodiode readout for a high resolution PET with nsec time resolution*, Nuclear Science, IEEE Transactions on, 42 (1995), pp. 1080–1084.

[263] A. Schmermund, S. Möhlenkamp, and R. Erbel, *Coronary artery calcium and its relationship to coronary artery disease*, Cardiol Clin, 21 (2003), pp. 521–534.

[264] G. P. Schmidt, A. Baur-Melnyk, A. Haug, V. Heinemann, I. Bauerfeind, M. F. Reiser, and S. O. Schoenberg, *Comprehensive imaging of tumor recurrence in breast cancer patients using whole-body MRI at 1.5 and 3 T compared to FDG-PET-CT*, Eur J Radiol, 65 (2008), pp. 47–58.

[265] G. P. Schmidt, A. R. Haug, S. O. Schoenberg, and M. F. Reiser, *Whole-body MRI and PET-CT in the management of cancer patients*, Eur Radiol, 16 (2006), pp. 1216–1225.

[266] U. J. Schoepf, C. R. Becker, B. M. Ohnesorge, and E. K. Yucel, *CT of coronary artery disease*, Radiology, 232 (2004), pp. 18–37.

[267] M. Schwaiger and J. Melin, *Cardiological applications of nuclear medicine*, Lancet, 354 (1999), pp. 661–666.

[268] M. Schwaiger, S. Ziegler, and S. G. Nekolla, *PET/CT: challenge for nuclear cardiology*, J Nucl Med, 46 (2005), pp. 1664–1678.

[269] L. A. Schwarz, *MR-based attenuation correction for PET*, tech. report, Technische Universität München (TUM), August 2006.

[270] R. H. Secker-Walker, L. Resnick, H. Kunz, J. A. Parker, R. L. Hill, and E. J. Potchen, *Measurement of left ventricular ejection fraction*, J Nucl Med, 14 (1973), pp. 798–802.

[271] Y. Shao, S. Cherry, K. Farahani, R. Slates, R. Silverman, K. Meadors, A. Bowery, S. Siegel, P. Marsden, and P. Garlick, *Development of a PET detector system compatible with MRI/NMR systems*, Nuclear Science, IEEE Transactions on, 44 (1997), pp. 1167–1171.

[272] L. J. Shaw, P. Raggi, T. Q. Callister, and D. S. Berman, *Prognostic value of coronary artery calcium screening in asymptomatic smokers and non-smokers*, Eur Heart J, 27 (2006), pp. 968–975.

[273] G. Shechter, C. Ozturk, J. R. Resar, and E. R. McVeigh, *Respiratory motion of the heart from free breathing coronary angiograms*, IEEE Trans Med Imaging, 23 (2004), pp. 1046–1056.

[274] L. A. Shepp and Y. Vardi, *Maximum likelihood reconstruction for emission tomography*, IEEE Trans Med Imaging, 1 (1982), pp. 113–122.

[275] T. Shiga, Y. Morimoto, N. Kubo, N. Katoh, C. Katoh, W. Takeuchi, R. Usui, K. Hirata, S. Kojima, K. Umegaki, H. Shirato, and N. Tamaki, *A new PET scanner with semiconductor detectors enables better identification of intratumoral inhomogeneity*, J Nucl Med, 50 (2009), pp. 148–155.

[276] R. B. Slates, K. Farahani, Y. Shao, P. K. Marsden, J. Taylor, P. E. Summers, S. Williams, J. Beech, and S. R. Cherry, *A study of artefacts in simultaneous PET and MR imaging using a prototype MR compatible PET scanner*, Phys Med Biol, 44 (1999), pp. 2015–2027.

[277] P. J. Slomka, L. Le Meunier, S. W. Hayes, W. Acampa, M. Oba, G. G. Haemer, D. S. Berman, and G. Germano, *Comparison of myocardial perfusion 82Rb PET performed with CT- and transmission CT-based attenuation correction*, J Nucl Med, 49 (2008), pp. 1992–1998.

[278] M. Souvatzoglou, F. Bengel, R. Busch, C. Kruschke, H. Fernolendt, D. Lee, M. Schwaiger, and S. G. Nekolla, *Attenuation correction in cardiac PET/CT with three different CT protocols: a comparison with conventional PET*, Eur J Nucl Med Mol Imaging, 34 (2007), pp. 1991–2000.

[279] V. C. Spanoudaki, A. B. Mann, A. N. Otte, I. Konorov, I. Torres-Espallardo, S. Paul, and S. I. Ziegler, *Use of single photon counting detector arrays in combined PET/MR: Characterization of LYSO-SiPM detector modules and comparison with a LSO-APD detector*, Journal of Instrumentation, 2 (2007), p. P12002.

[280] R. Z. Stodilka, B. J. Kemp, F. S. Prato, A. Kertesz, D. Kuhl, and R. L. Nicholson, *Scatter and attenuation correction for brain SPECT using attenuation distributions inferred from a head atlas*, J Nucl Med, 41 (2000), pp. 1569–1578.

[281] H. W. Strauss, B. L. Zaret, P. J. Hurley, T. K. Natarajan, and B. Pitt, *A scintiphotographic method for measuring left ventricular ejection fraction in man without cardiac catheterization*, Am J Cardiol, 28 (1971), pp. 575–580.

[282] T. S. Sumanaweera, G. H. Glover, T. O. Binford, and J. R. Adler, *MR susceptibility misregistration correction*, IEEE Trans Med Imaging, 12 (1993), pp. 251–259.

[283] X. Sun, M. Tanaka, S. Kondo, S. Hirai, and T. Ishihara, *Reduced cerebellar blood flow and oxygen metabolism in spinocerebellar degeneration: a combined PET and MRI study*, J Neurol, 241 (1994), pp. 295–300.

[284] A. Syrota and P. Jehenson, *Complementarity of magnetic resonance spectroscopy, positron emission tomography and single photon emission tomography for the in vivo investigation of human cardiac metabolism and neurotransmission*, Eur J Nucl Med, 18 (1991), pp. 897–923.

[285] Y. F. Tai and P. Piccini, *Applications of positron emission tomography (PET) in neurology*, J Neurol Neurosurg Psychiatry, 75 (2004), pp. 669–676.

[286] T. Y. Tang, R. R. Moustafa, S. P. Howarth, S. R. Walsh, J. R. Boyle, Z. Y. Li, J.-C. Baron, J. H. Gillard, and E. A. Warburton, *Combined PET-FDG and USPIO-enhanced MR imaging in patients with symptomatic moderate carotid artery stenosis*, Eur J Vasc Endovasc Surg, 36 (2008), pp. 53–55.

[287] M. M. Ter-Pogossian, S. R. Bergmann, and B. E. Sobel, *Influence of cardiac and respiratory motion on tomographic reconstructions of the heart: implications for quantitative nuclear cardiology*, J Comput Assist Tomogr, 6 (1982), pp. 1148–1155.

[288] J. Thibaud, *L'annihilation des positrons au contact de la matière et la radiation qui en resulte*, C R Acad Sci, 197 (1933), pp. 1629–1632.

[289] J. A. Thie, *Understanding the standardized uptake value, its methods, and implications for usage*, J Nucl Med, 45 (2004), pp. 1431–1434.

[290] J. A. Thie, K. F. Hubner, F. P. Isidoro, and G. T. Smith, *A weight index for the standardized uptake value in 2-deoxy-2-[F-18]fluoro-D-glucose-positron emission tomography*, Mol Imaging Biol, 9 (2007), pp. 91–98.

[291] C. A. Tobias, J. H. Lawrence, F. J. W. Roughton, W. S. Root, and M. I. Gregersen, *The elimination of carbon monoxide from the human body with reference to the possible conversion of CO to CO2*, Am J Physiol, 145 (1945), pp. 253–263.

[292] D. Townsend, P. Frey, A. Jeavons, G. Reich, H. J. Tochon-Danguy, A. Donath, A. Christin, and G. Schaller, *High density avalanche chamber (HIDAC) positron camera*, J Nucl Med, 28 (1987), pp. 1554–1562.

[293] D. J. Tyler, M. D. Robson, R. M. Henkelman, I. R. Young, and G. M. Bydder, *Magnetic resonance imaging with ultrashort TE (UTE) PULSE sequences: technical considerations*, J Magn Reson Imaging, 25 (2007), pp. 279–289.

[294] S. Ulzheimer and W. A. Kalender, *Assessment of calcium scoring performance in cardiac computed tomography*, Eur Radiol, 13 (2003), pp. 484–497.

[295] N. G. Uren, J. A. Melin, B. D. Bruyne, W. Wijns, T. Baudhuin, and P. G. Camici, *Relation between myocardial blood flow and the severity of coronary-artery stenosis*, N Engl J Med, 330 (1994), pp. 1782–1788.

[296] P. E. Valk, D. L. Bailey, D. W. Townsend, and M. N. Maisey, eds., *Positron Emission Tomography: basic science and clinical practice*, Springer-Verlag, 2003.

[297] P. van Dijk, *ECG-triggered NMR imaging of the heart*, Diagn Imaging Clin Med, 53 (1984), pp. 29–37.

[298] S. Vandenberghe, M. E. Daube-Witherspoon, R. M. Lewitt, and J. S. Karp, *Fast reconstruction of 3D time-of-flight PET data by axial rebinning and transverse mashing*, Phys Med Biol, 51 (2006), pp. 1603–1621.

[299] M. W. Vannier, *Respiratory gating by impedance plethysmography*, J Nucl Med, 25 (1984), pp. 1142–1143.

[300] J. A. Verschakelen, L. V. fraeyenhoven, G. Laureys, M. Demedts, and A. L. Baert, *Differences in CT density between dependent and nondependent portions of the lung: influence of lung volume*, AJR Am J Roentgenol, 161 (1993), pp. 713–717.

[301] P. Viola and I. Wells, W. M., *Alignment by maximization of mutual information*, in Proc. Fifth International Conference on Computer Vision, 20–23 June 1995, pp. 16–23.

[302] D. Visvikis, O. Barret, T. Fryer, A. Turzo, F. Lamare, C. C. L. Rest, and Y. Bizais, *A posteriori respiratory motion gating of dynamic PET images*, in IEEE Nuclear Science Symposium Conference Record, vol. 5, 2003, pp. 3276 – 3280.

[303] D. Vivancos-Gallego, *Development of pre-processing methods for attenuation correction algorithms in small animal PET/MR imaging*, master's thesis, Technische Universität München (TUM), October 2004.

[304] G. K. von Schulthess and H.-P. W. Schlemmer, *A look ahead: PET/MR versus PET/CT*, Eur J Nucl Med Mol Imaging, 36 Suppl 1 (2009), pp. S3–S9.

[305] Y. Wang, S. J. Riederer, and R. L. Ehman, *Respiratory motion of the heart: kinematics and the implications for the spatial resolution in coronary imaging*, Magn Reson Med, 33 (1995), pp. 713–719.

[306] W. A. Weber, S. I. Ziegler, R. Thödtmann, A. R. Hanauske, and M. Schwaiger, *Reproducibility of metabolic measurements in malignant tumors using FDG PET*, J Nucl Med, 40 (1999), pp. 1771–1777.

[307] K. A. Wood, P. J. Hoskin, and M. I. Saunders, *Positron emission tomography in oncology: a review*, Clin Oncol (R Coll Radiol), 19 (2007), pp. 237–255.

[308] F. Wrenn, M. Good, and P. Handler, *The use of positron emitting radioactive isotopes for the localization of brain tumors*, Science, 113 (1951), pp. 525–7.

[309] J. C. Wu, M. Inubushi, G. Sundaresan, H. R. Schelbert, and S. S. Gambhir, *Positron emission tomography imaging of cardiac reporter gene expression in living rats*, Circulation, 106 (2002), pp. 180–183.

[310] K. C. Wu and J. A. C. Lima, *Noninvasive imaging of myocardial viability: current techniques and future developments*, Circ Res, 93 (2003), pp. 1146–1158.

[311] E. Z. Xu, N. A. Mullani, K. L. Gould, and W. L. Anderson, *A segmented attenuation correction for PET*, J Nucl Med, 32 (1991), pp. 161–165.

[312] K. Yamashita, N. Tamaki, Y. Yonekura, H. Ohtani, H. Saji, T. Mukai, H. Kambara, C. Kawai, T. Ban, and J. Konishi, *Quantitative analysis of regional wall motion by gated myocardial positron emission tomography: validation and comparison with left ventriculography*, J Nucl Med, 30 (1989), pp. 1775–1786.

[313] Y. Yang, S. Rendig, S. Siegel, D. F. Newport, and S. R. Cherry, *Cardiac PET imaging in mice with simultaneous cardiac and respiratory gating*, Phys Med Biol, 50 (2005), pp. 2979–2989.

[314] Y.-Y. Yau, W.-S. Chan, Y.-M. Tam, P. Vernon, S. Wong, M. Coel, and S. K.-F. Chu, *Application of intravenous contrast in PET/CT: does it really introduce significant attenuation correction error?*, J Nucl Med, 46 (2005), pp. 283–291.

[315] H. Zaidi, *Is MR-guided attenuation correction a viable option for dual-modality PET/MR imaging?*, Radiology, 244 (2007), pp. 639–642.

[316] H. Zaidi and B. Hasegawa, *Determination of the attenuation map in emission tomography*, J Nucl Med, 44 (2003), pp. 291–315.

[317] H. Zaidi, M.-L. Montandon, and D. O. Slosman, *Magnetic resonance imaging-guided attenuation and scatter corrections in three-dimensional brain positron emission tomography*, Med Phys, 30 (2003), pp. 937–948.

[318] B. L. Zaret, H. W. Strauss, P. J. Hurley, T. K. Natarajan, and B. Pitt, *A noninvasive scintiphotographic method for detecting regional ventricular dysfunction in man*, N Engl J Med, 284 (1971), pp. 1165–1170.

[319] K. R. Zasadny and R. L. Wahl, *Standardized uptake values of normal tissues at PET with 2-[fluorine-18]-fluoro-2-deoxy-D-glucose: variations with body weight and a method for correction*, Radiology, 189 (1993), pp. 847–850.

[320] S. I. Ziegler, B. J. Pichler, G. Boening, M. Rafecas, W. Pimpl, E. Lorenz, N. Schmitz, and M. Schwaiger, *A prototype high-resolution animal positron tomograph with avalanche photodiode arrays and LSO crystals*, Eur J Nucl Med, 28 (2001), pp. 136–143.

[321] D. Zikic, *MR based PET attenuation correction in small animal PET imaging*, tech. report, Technische Universität München (TUM), February 2005.

[322] D. Zikic, W. Wein, A. Khamene, D.-A. Clevert, and N. Navab, *Fast deformable registration of 3D-ultrasound using a variational approach*, Medical Image Computing and Computer-Assisted Intervention (MICCAI), 4190 (2006), pp. 915–923.